Multiscale modelling of additively manufactured composite material behaviour

Gljuščić, Matej

UNIVERSITY OF RIJEKA
FACULTY OF ENGINEERING

Matej Gljušćić

MULTISCALE MODELLING OF ADDITIVELY MANUFACTURED COMPOSITE MATERIAL BEHAVIOUR

DOCTORAL DISSERTATION

Rijeka, 2022.

UNIVERSITY OF RIJEKA
FACULTY OF ENGINEERING

Matej Gljušćić

MULTISCALE MODELLING OF ADDITIVELY MANUFACTURED COMPOSITE MATERIAL BEHAVIOUR

DOCTORAL DISSERTATION

Thesis Supervisor: Prof. D. Sc. Marina Franulović
Thesis Co-supervisor: Prof. D. Sc. Domagoj Lanc

Rijeka, 2022.

SVEUČILIŠTE U RIJECI
TEHNIČKI FAKULTET

Matej Gljušćić

VIŠERAZINSKO MODELIRANJE PONAŠANJA ADITIVNO PROIZVEDENIH KOMPOZITNIH MATERIJALA

DOKTORSKA DISERTACIJA

Mentor: prof. dr. sc. Marina Franulović
Komentor: prof. dr. sc. Domagoj Lanc

Rijeka, 2022.

Thesis Supervisor:	Prof. D. Sc. Marina Franulović, University of Rijeka, Croatia, Faculty of Engineering
Thesis Co-supervisor:	Prof. D. Sc. Domagoj Lanc, University of Rijeka, Croatia, Faculty of Engineering

This doctoral thesis was discussed on December 15th, 2022 at the University of Rijeka, Croatia, Faculty of Engineering in front of the following Evaluation Committee:

1. Assoc. Prof. D. Sc. Kristina Marković, University of Rijeka, Faculty of Engineering, Croatia

2. Assoc. Prof. D. Sc. Marino Brčić, University of Rijeka, Faculty of Engineering, Croatia

3. Assist. Prof. D. Sc. Andrej Žerovnik, University of Ljubljana, Faculty of Mechanical Engineering, Slovenia

Acknowledgments

The research presented in this dissertation is the result of an extensive experimental campaign and numerical modelling conducted by the author, which would not have been possible without the support of the Croatian Science Foundation under project number IP-2019-04-3607, the University of Rijeka under project number uniri-tehnic-18-34 and many dedicated colleagues.

First and foremost, I would like to thank my supervisor, Prof. D. Sc. Marina Franulović, for her insightful comments on this material and our subsequent discussions. I would also like to acknowledge Prof. D. Sc. Domagoj Lanc for his guidance in all aspects of the mechanics of composite materials, and Assist. Prof. D. Sc. Andrej Žerovnik for his support in developing the experimental methods used.

Additional support came from David Howard, who helped to proofread the dissertation, and from D. Sc. Vedrana Špada of the Istrian University of Applied Sciences, METRIS Research Centre; from IB-CADDY d.o.o.; from the Institute of Metals and Technology (IMT) in Ljubljana; and from the Center for Advanced Computing and Modelling (CNRM) at the University of Rijeka, which provided technical support for the manufacturing and experimental procedures.

Finally, I would like to thank my parents Mario and Ivanka, my brothers Petar and Edi, and my immediate circle of colleagues and friends for their encouragement. I especially value my beloved Anna for her patience and inspiration. Thank you all

Abstract

Additive manufacturing is a process of joining material in successive layers in order to make objects from three-dimensional model data. Due to its versatility, the technology has initially been used only for rapid prototyping in research and development. However, recent improvements by introducing various types of reinforcing constituents in the fused deposition process expanded its application to geometrically complex, lightweight, and durable composites in engineering practice.

However, the main drawbacks of this approach are weakened intralaminar and interlaminar contact zones due to successive material deposition followed by reinforcement distribution irregularities and voids. Consequently, these deficiencies lead to the overall reduction of load-bearing capabilities in additively manufactured composites in comparison to their traditionally manufactured counterparts. Therefore, to model this behaviour, a systematic analysis of the state-of-the-art in additive manufacturing and composite material mechanics was conducted in this thesis, based on which a multiscale modelling approach was proposed. It starts with microstructural analysis based on homogenized representative volume elements designed according to microscopic inspections, followed by unidirectional and shear lamina properties identification through standardized destructive testing, while concluding with damage model calibration and validation on multidirectionally reinforced laminates. The microstructural investigation has been conducted on three distinctive cases of additively manufactured composites reinforced with continuous carbon, glass, and aramid fibers, respectively. The specimens have been produced using a Markforged-X7 3D printer utilizing a fused filament fabrication approach, while the microstructures have been inspected using SEM in cross-sections longitudinal and perpendicular to the fiber direction. The SEM images have been examined using machine-learning algorithms while the acquired results have been statistically analysed and compared with the relevant literature. The acquired data has been adopted to generate a representative volume element in Abaqus CAE environment for each of the test cases. The homogenization has been conducted using python scripting by adopting each of the constituent's constitutive models from the literature, while the cohesive interactions between the constituents have been calibrated according to the experimentally acquired data, acquiring good agreement between the experimental and numerical homogenization results for longitudinal, transversal, and in-plane shear behaviour. Consequently, further analysis of multidirectinally reinforced laminates on the

macroscale has been proposed. Therefore, three distinctive cases of additively manufactured carbon fiber reinforced laminates have been designed as standardized open-hole specimens, with the selection of lamina stacking sequences that enforce in-plane multiaxial stress state during uniaxial tensile loads. Subsequently, digital twins have been designed within the Abaqus CAE environment while the laminate constitutive behaviour has been described with a continuum damage model utilizing Puck failure theory implemented in the Abaqus CAE framework through the UMAT Fortran subroutine. The model has been modified for a better description of shear-influenced damage in AM composites and calibrated on a specific test case using response-surface algorithms of multiparametric central composite design of experiments. The results have been validated experimentally and compared with other damage models, confirming the significant influence of shear stress on the failure of AM composites which has been accounted for by the proposed modifications.

The performed research provides a significant scientific contribution to the field of additive manufacturing and material science, proposing a multiscale protocol for the identification of material properties in heterogenic and anisotropic composites produced by additive manufacturing, and the modification of failure criteria for a more accurate damage prediction and safer application of additive manufacturing technologies in engineering practice.

Keywords: additive manufacturing, fiber-reinforced composites, material behaviour modelling, material damage modelling, experimental assessment

Sažetak

Aditivna proizvodnja je proces izrade predmeta uzastopnim nanošenjem čestica u tankim slojevima na temelju trodimenzionalnih modela izrađenih pomoću računalnih CAD programa. Premda se postupci aditivne proizvodnje najviše koriste kod izrade prototipa u istraživanju i razvoju novih proizvoda, usvajanjem ojačanih materijala u procesu taložnog srašćivanja omogućeno je proširenje njihove primjene kod geometrijski kompleksnih te kompozita visokih performansi u inženjerskoj praksi. Međutim, pokazalo se da proces taložnog srašćivanja također uzrokuje nepravilnosti poput praznina te nekonzistentnosti distribucije ojačanja, što dovodi do oslabljenja kontaktnih zona, iz čega proizlazi smanjena nosivost aditivno proizvedenih komponenata u usporedbi s njihovim konvencionalnim ekvivalentima.

Stoga je u cilju interpretacije ponašanja takvih materijala, u ovoj disertaciji provedena sustavna analiza trenutnih tehnoloških dostignuća u procesima aditivne proizvodnje i mehanike kompozita, na temelju čega je usvojen višerazinski pristup modeliranja ponašanja materijala. Proces višerazinskog modeliranja je obuhvatio mikroskopsku analizu materijala na temelju čijih su rezultata modelirani reprezentativni volumni elementi te numerički homogenizirani i uspoređeni s rezultatima standardiziranih eksperimentalnih ispitivanja uslijed uzdužnog i poprečnog vlačnog, te smičnog opterećenja. Dobiveni su rezultati korišteni u modeliranju oštećivanja materijala, pri čemu su parametri materijalnog modela kalibrirani i validirani na temelju eksperimentalnih rezultata ispitivanja višesmjerno ojačanih laminata.

Ispitivanje mikrostrukture je provedeno na tri primjera aditivno proizvedenih kompozita ojačanih kontinuiranim ugljičnim, staklenim te aramidnim vlaknima. Uzorci su proizvedeni metodom taložnog srašćivanja koristeći 3D tisak Markforged-X7, dok je mikrostruktura materijala snimana u više poprečnih presjeka koristeći SEM uređaj. Snimke su analizirane pomoću algoritama strojnog učenja, a rezultati su statistički obrađeni i uspoređeni s dostupnim podacima iz literature te korišteni u svrhu modeliranja reprezentativni volumnih elemenata. Postupak mikromehaničke homogenizacije je automatiziran primjenom Abaqus CAD softveru koristeći programski jezik Python, pri čemu su materijalni modeli matrice i ojačanja usvojeni iz literature, dok su svojstva kohezivnih kontakata između uključaka kalibrirana sukladno odzivu ispitivanih materijala. Potvrdivši usklađenost rezultata eksperimentalnih ispitivanja te numeričkih rezultata homogenizacije na primjerima uzdužnog i poprečnog vlačnog te ravninskog smičnog opterećenja, istraživanje je prošireno na ispitivanje višesmjerno ojačanih aditivno proizvedenih

laminata ojačanih ugljičnim vlaknima s kružnim koncentratorom naprezanja, dok su usvajanjem specifičnih redoslijeda slaganja slojeva uzrokovana višeosna stanja ravninskog naprezanja tijekom jednoosnih vlačnih opterećenja. Digitalni ekvivalenti višesmjerno ojačanih ispitnih uzoraka su također modelirani koristeći Abaqus CAD softver, dok su za njihov konstitutivni odziv usvojeni principi mehanike kontinuuma i Puck-ova teorija oštećivanja materijala te implementirani pomoću UMAT subrutine. U svrhu interpretacije utjecaja smičnih opterećenja na oštećenje višesmjerno ojačanih aditivno proizvedenih kompozitnih laminata provedena je modifikacija i kalibracija Puck-ovog modela prema eksperimentalnim rezultatima koristeći algoritme više-parametarskog centralnog kompozitnog dizajna eksperimenata. Numerički rezultati su eksperimentalno validirani te uspoređeni s rezultatima sličnih modela oštećivanja dostupnim u Abaqus CAE softveru te originalnim Puck-ovim modelom preuzetim iz literature. Analiza je pokazala značajan utjecaj smičnih naprezanja na oštećivanje višesmjerno ojačanih aditivno proizvedenih kompozitnih materijala te pozitivan utjecaj usvojenih modifikacija kod analiziranih slučajeva.

Provedeno istraživanje pruža značajan znanstveni doprinos u područjima aditivne proizvodnje i znanosti o materijalima predlažući višerazinski protokol identifikacije svojstava heterogenih i anizotropnih kompozitnih materijala proizvedenih aditivnom tehnologijom na temelju mikroskopskih snimaka te modifikaciju i kalibraciju konstitutivnih modela u svrhu preciznijeg izračuna njihovog oštećenja i sigurnije uporabe aditivne tehnologije u inženjerskoj praksi.

Ključne riječi: aditivna proizvodnja, vlaknima ojačani kompoziti, modeliranje ponašanja materijala, modeliranje oštećivanja materijala, eksperimentalna mjerenja

TABLE OF CONTENTS

1. INTRODUCTION

The initial part of this work is dedicated to the presentation of general information about the research. A concise overview of scientific motivation is presented, followed by the main objectives and scientific contributions of the conducted research, concluding with a synopsis, where the thesis organization is delivered.

1.1. Scientific Motivation

Following the requirements of the EU Green Deal objective, with its tendency for climate neutrality and zero carbon emissions, this work has been focused on the research and evaluation of lightweight materials used in design within the novel 4.0 industry. Within this framework, the application of additive manufacturing (AM) offers huge potential in tailoring the material properties for specific design requirements by combining assorted renewable resins and fibers of various properties, thus enabling the manufacturing of strong, lightweight, and multifunctional composite materials. Incorporating multifunctionality, recycling possibilities, lightweight, cost-competitiveness and customization for specific applications, the additively manufactured polymer composite structures are the ideal response for increasing the competitiveness of the EU economy. Therefore, research into their behaviour and failure mechanisms is crucial. While the tendency of the recent development in additive manufacturing has been focused on surpassing the experimental rapid prototyping to the production of functional components, a variety of engineering polymers for structural applications (PA, PC, PET, PEEK) have been implemented. Regrettably, additive technology still struggles to deliver reliable components for engineering applications in comparison to conventional manufacturing methods, but the following could all benefit from the bottom-up approach: aeronautic, automotive, and space industries [63,171], wearable technologies [90], medical applications such as prosthetics, implants, and dentistry [15], as well as ergonomic [91] and biomimetic [47] designs, since each of them incorporates specific lightweight components. All things considered, the additive manufacturing of composites with continuous fiber-reinforced represents a new approach for the automated production of high-strength composites with a wide range of applications. While the specific load-bearing capability of AM CFRP composite structures is recognized, it is still not determined by constitutive material models, and the damage resistance to both uniaxial and multi-axial loads remains unknown.

Therefore, to predict the material behaviour and expand its potential industrial application, a better understanding of constitutive relations, damage initiation, propagation, and failure mechanisms is necessary.

1.2. Aims of the Work

Based on the outlined motivation, the goal of this thesis is to contribute to a better understanding of constitutive relations, damage initiation, progression, and failure mechanisms in additively manufactured continuous fiber reinforced polymer (AM-CFRP) composites. The thesis is particularly focused on multiscale analysis of AM composites by developing a Representative Volume Element (RVE) of unidirectionally reinforced (UD) CFRP composites in order to update the lamina properties in the continuum damage mechanic (CDM) model. For this purpose, several stages of experimental studies will be conducted. Initially, three cases of representative cross-ply laminates reinforced with carbon, glass, and aramid fibers respectively, will be designed and additively manufactured using Markforged-X7. The cross-section images have been extracted using SEM microscopy for each of the studied cases and analysed in FIJI using trainable WEKA segmentation algorithms. The resulting images will be processed to acquire content, sizes and misalignments of the constituents, as well as the lamina thickness and material deposition width, including the void and debris content. To calibrate the proposed RVE models, three distinctive specimens of carbon fiber reinforced composites will be designed in accordance with ASTM standards manufactured using Markforged-X7 3D and tested using an Instron servo-hydraulic testing system in quasistatic conditions. The unidirectionally reinforced specimens UD0 and UD90 will be designed and tested according to ASTM D3039 [204] standard to acquire longitudinal and transverse lamina properties, while the third group of specimens SH45 will be designed and tested according to ASTM D3518 [203] standard to acquire the shear properties. The material measurements will be conducted using full-field strain monitoring with the GOM-Aramis digital image correlation (DIC) system and implemented in the calibration protocol. To account for the bonding deficiency between constituents, a fiber/matrix interface utilizing cohesive elements will be implemented within the RVE model, while the cohesive zone model (CZM) properties will be calibrated according to the experimental results. The acquired calibration parameters for carbon fiber (C) reinforced RVE will be applied both to glass (G) and aramid (K) reinforced RVEs for validation. The resulting set of properties will

be adopted in order to update the experimentally acquired values of unidirectional lamina properties necessary in numerical analysis.

Since reinforced laminates are rarely used as unidirectional in engineering applications, the final experimental protocol will be focused on analyzing the behaviour of multi-directionally reinforced additively manufactured composites, following the guidelines presented in [163]. Hence, three cases of open-hole (OH) specimens, OH90, OH60, and OH45, corresponding to the laminate stacking sequences (LSS) of $[0/90_2/0/90_2]_S$, $[0/60_2/0/-60_2]_S$, and $[0/45_2/0/-45_2]_S$, will be designed according to the ASTM D5766 standard and tested uniaxially in quasistatic conditions. According to [163], these LSS-es manifest the biaxiality ratios of 0, 0.57, and 1.61 respectively, and simulate the multiaxial load conditions through uniaxial tests. The measurements will be carried out with the GOM-Aramis digital image correlation system, capturing both global and local strain fields around the stress concentration area.

Since fiber-reinforced composites are prone to fracture and brittle failure, their behaviour is best described using damage models. Because the suitability of existing damage models for composites to predict damage initiation and propagation in AM composites is still under research, progressive damage modelling has been proposed in this study. The applicable damage models used in the Worldwide Failure Exercise (WWFE) will be analysed, and a progressive damage model based on CDM and Puck-Schurmann failure criteria will be considered, due to its ability to distinguish between fiber and inter-fiber damage which could be correlated to local inter-raster weaknesses in AM structures. The damage model will be implemented as a Fortran subroutine and utilized in the FEA software Abaqus. The Puck-Schurmann failure criteria within the CDM framework will be adopted according to the acquired lamina properties, while accounting for the constrained layers' in-situ strength corrections. The model calibration will be conducted using response-surface algorithms based on the central composite design of experiments for multiple continuous factors, including the shear stress multiplier $m_{\tau f}$, effective fiber strength exponent ξ, and the moduli degradation parameters κ_{DEG} and n_{DEG}, targeting the minimal deviation between the numerically and experimentally acquired loads at failure for a specific test case and validated on all test cases. Upon validation, the guidelines for the safe application and damage modelling of AM CFRP composites will be proposed.

1.3. Contributions of the Thesis

The research performed within the framework of the doctoral thesis aims to provide a scientific contribution to the study of AM CFRP composites with promising benefits to the aeronautic and automotive industries, wearable technologies, medical applications, ergonomic, biomimetics, and structural health monitoring systems.

The contribution of this work comprises a thorough study of the effects of AM CFRP composites microstructure on the macro-mechanical response, along with establishing a suitable damage model and its calibration parameters. Firstly, the geometrical parameters of the RVE-s will be selected according to the data acquired from the microstructural inspection and followed by the calibration of the cohesive law in RVE fiber/matrix interface. The procedure will be validated with experimental results for lamina longitudinal, transverse and shear cases; these are seldom available in the literature. Furthermore, the multiaxial behaviour of AM CRTP composites will be assessed by conducting uniaxial tensile tests on multi-directionally reinforced AM CFRP composites with stacking sequences enforcing multiaxial stress states within the laminates. To inspect the engineering application of AM CFRP materials, the multi-directionally reinforced specimens will be designed with a circular stress concentrator in the gauge length centre, commonly encountered in a wide range of applications. The appearance of local strains and cracks around the hole edge will be monitored using the DIC system, analysed, and summarized in the load-strain diagrams, thus giving more insight into the materials' behaviour, and indicating appropriate guidelines for engineering applications.

Since CFRP composites are usually tailored for a specific function by adopting an optimal layer orientation, the outlined experimental results would be of limited value. Hence, this thesis focuses on validating a progressive damage model with the additional calibration parameters necessary to simulate the multi-directionally reinforced CFRP composite's behaviour accurately. The influence of four additional parameters related to effective fiber strength, shear influence on fiber failure, and stiffness degradation will be calculated using a response-surface algorithm based on the central composite design of experiments (DoE) and validated on experimental results. The thesis will conclude with observations of the acquired numerical solutions and guidelines for the safe implementation of AM CFRP composites in the design of lightweight structures within engineering applications.

1.4. Organization of the Thesis

The basic structure of the doctoral thesis is organized in sections, each covering one of the main parts of the research.

Section 1 describes the fundamental scientific motivation followed by the main research objectives and highlights the significant scientific contributions within the research field.

In Section 2 the basics of additive manufacturing are explained followed by a presentation of applicable AM methods for fiber reinforced polymer (FRP) production, highlighting the issues of its implementation. The state-of-the-art in multiscale modelling of FRP composites is also elaborated within this section, focusing on micro-, meso-, and macro-scale, respectively. The chapter concludes with the state-of-the-art in failure prediction of FRPs, where failure criteria, CDM and discrete damage mechanics (DDM) are elaborated in detail.

Section 3 provides an overview of the constitutive modelling of FRP composites focusing on the theoretical background for micro-, meso-, and macro- mechanical modelling, respectively. Furthermore, the theoretical concepts on failure predictions of FRPs are also covered within this chapter, explaining the failure criteria, CDM and DDM approaches in detail. Additionally, the mechanics of the adopted damage model are also categorically disclosed, highlighting calibration parameters and their potential influence on laminate behaviour predictions.

A summary of the experimental the procedures is presented in Section 4, along with a detailed outline of specimen design and manufacturing methods. Starting with the microscopic analysis of the composites' constituents, this section also covers the design and manufacturing of the specimens for longitudinal, transversal and shear properties acquisition, followed by the multi-directionally reinforced specimens with variable LSS-induced biaxiality ratios. The experimental results are also delivered within this section, starting with image analysis and the statistical constituent evaluation, which is followed by the lamina properties acquisition and damage monitoring in multi-directionally reinforced open-hole specimens using the DIC system.

The numerical modelling is presented in Section 5, beginning with the RVE development and followed by the theoretical background of micromechanical homogenization, highlighting the necessary assumptions for accurate model calibration. Additionally, the initial study of the influence of calibration parameters on the material behaviour prediction, as well as the detailed description of the used optimization process relying on DoE algorithms are critically assessed.

Subsequently, a comparison between the calibrated numerical model and the acquired experimental results is conducted and interpreted. The adopted RVE design assumptions are also implemented on similar materials and compared with the experimental data available in the literature. Moreover, the adopted damage model is also applied in the modelling of similar specimens with distinctive biaxiality ratios, ensuring good agreement between numerical and experimental results. The post-failure behaviour has also been critically assessed in this section, focusing on damage prediction accuracy, highlighting the necessity for a revision of shear influence on damage evolution.

The conclusion of the thesis presented in Section 6 contains the summary of essential observations, it presents the guidelines for modelling and safe application of AM CFRP composites, and proposes necessary steps for future research.

2. STATE-OF-THE-ART

An introduction to the additive manufacturing process as well as a review of the experimental observations of additively manufactured parts will be given in this section of the thesis, followed by a comprehensive overview of the state-of-the-art in heterogeneous material behaviour modelling.

2.1. Additive manufacturing

According to the ASTM F2792 standard [205], additive manufacturing (AM) is defined as a process of joining materials to make objects from three-dimensional (3D) model data, layer upon layer, as opposed to subtractive manufacturing technologies. The AM process begins with 3D modelling of the required object and its conversion to an intermediary neutral format [39]. The formatted geometry is then processed, accounting for the construction components, manufacturing operations, and AM machine settings. Finally, the 3D geometry is divided into 2D layers to be successively stacked over each other, hence generating a 3D printer toolpath [55]. In addition, the standard also classifies the AM technology into seven distinctive categories as follows:

In the process of Powder Bed Fusion, the thermal energy is used to selectively fuse regions of a powder bed. The process is used for metals and polymers, while implemented in technologies of Electron Beam Melting (EBM), Selective Laser Sintering (SLS), Selective Hot Sintering (SHS), and Direct Metal Laser Sintering (DMLS). The second category is Direct Energy Deposition (DED) where focused thermal energy is used to fuse materials by melting during deposition. The process is used for metals only, while implemented in the Laser Metal Deposition (LMD) process. Vat Photo Polymerization is a process where liquid photopolymer in a vat is selectively cured by light-activated polymerization. While this process is limited to photopolymers in Stereolithography (SLA) and Digital Light Processing (DLP) technologies, the binder jetting process enables the liquid bonding agent to be selectively deposited while joining the powder material, widening the application to polymers, metals and foundry sands used in Powder Bed and Inkjet Head (PBIH) and Plaster-based 3D Printing (PP) technologies. On the other hand, material jetting is based on the selective deposition of the building material droplets. The process is limited to polymers and waxes used in Multi-Jet Modelling (MJM). Furthermore, sheet lamination consists of bonding sheets of material to form an object. The process is used

in Laminated Object Manufacturing (LOM) and Ultrasonic Consolidation (UC) technologies for metals and paper. Due to its simplicity and versatility, material extrusion through a nozzle is one of the most widely spread AM technologies. The process is limited only to polymers and polymer matrix composites, and is commonly referred to as Fused Deposition Modelling (FDM) process.

2.1.1. Fused Deposition Modelling

The FDM process displayed in Figure 2.1 a) and b) was developed and patented in 1992 by Stratasys Inc. [42] and, since the patent expiration in 2009, has spread to a wide range of applications, attracting attention among scientists, engineers, and hobbyists due to its simplicity, versatility, and recyclability. Given the versatility, as well as its applicability in the rapid production of geometrically complex objects, FDM will also be used in the thesis framework to produce CFRP composites with automatized reinforcing while avoiding molding and a human labour factor. The FDM process is based on melting the polymer material within the heated extruder and enabling its flow through the delivery system using one or more nozzles, enabling multiple material interchangeability [55].

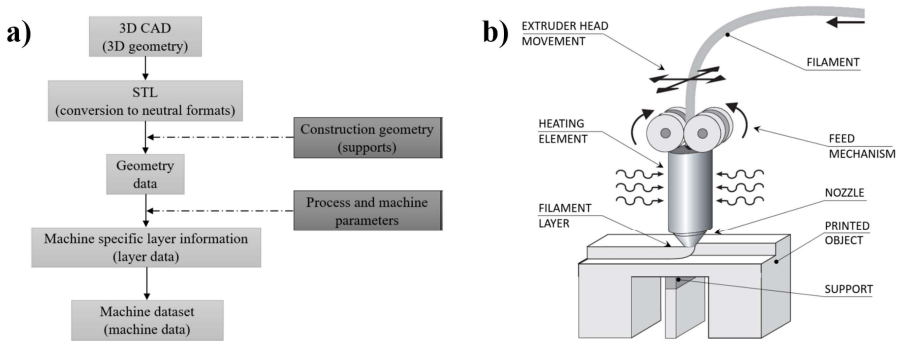

Figure 2.1 a) Simplified representation of a generalized data path for AM [55], b) Schematic representation of an FDM extruder head [55]

In most cases, the position of the FDM extruder is controlled along two horizontal and one vertical axis using linear guide rails, stepper motors, and leadscrews [55], or belt drivers [57] in the lower price range. Moreover, the FDM is safe for indoor usage since minimal harmful vapours are present during the process [55], while the printed thermoplastic polymers are fully recyclable, hence making the method sustainable. Moreover, the FDM approach supports various infill densities extended to hatch or honeycomb patterns often implemented to topology optimize lightweight structures, and also to increase the build speed [57].

There are flaws in the FDM method, including the positioning accuracy, limited build speed,

void content, uncontrolled heat dissipation, and inability to produce sharp features consequent to circular nozzle geometry, many of which are still unavoidable, as shown in Figure 2.2.

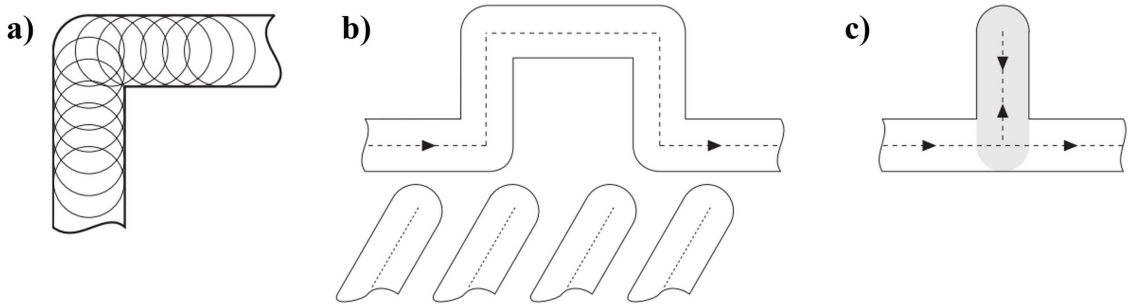

Figure 2.2 Fused deposition modelling: a) Corner detail, b) Intricate geometry detail, c) Fine web detail [55]

One of the features of FDM part is the printing orientation induced orthotropy, which affects the object stiffness and strength significantly, and must be accounted for during the product design. In addition, FDM parts also suffer from low interlaminar strength resulting in devastating effects from in-plane shear-induced delamination [86,137,176]. Despite the fast material solidification, the addition of support structures is often necessary to ensure object stability during manufacturing, especially when cantilevers are considered. In most slicing software, the support structures are automatically generated using the same material as the product, adopting a breakaway support system for its removal. Alternatively, a water-soluble polymer can be used for contactless removal. Initially supporting only polymers for general applications, like acrylonitrile butadiene styrene (ABS) and polylactic acid (PLA), machines utilizing FDM technology now support a wider range of open-source materials including engineering polymers for structural applications like polyamides (PA), polycarbonates (PC), and polyethylene terephthalate (PET), or recently introduced advanced polymers such as polyetheretherketone (PEEK), thus enabling the manufacturing of tailored objects for specific applications containing materials with distinctive mechanical, thermal and chemical properties. Among the additive technologies for polymer manufacturing, FDM method produces the structures with the best mechanical properties [57], while also being one of few technologies to support the addition of continuous reinforcements during the AM process.

2.1.2. Additively manufactured fiber-reinforced polymer composites

The rapid development in AM technology has extended to various applications, improving the process accuracy, and consequently the mechanical properties of 3D printed parts [51]. To boost competitiveness, various types of high-performance polymers and FRP composites

started to be adopted, enabling the additive manufacturing of lightweight objects with high specific strength and stiffness [51], while eliminating the human labour factor from the manufacturing process [137] by the automation of fiber placement. In general, a composite material is formed by combining two (or more) materials, one as a binding agent and the other as reinforcement, while their distinct properties are incorporated into a single improved material [51]. Therefore, the morphology of composite materials may also be considered an advantage because it enables the selection of the reinforcement content, positioning, and orientation to match the expected loads. Since FDM process is analogous to the composite layup configuration, the performance benefits of the combined processes are emphasized in the literature, along with advancements in AM materials, the introduction of various shape and type of reinforcements [128], and technological improvements in industrial applications [137].

The currently available FDM technology allows the production of low aspect ratio composites reinforced with short-fibers, macro-, micro-, or nano-particles, without significant modifications to the equipment, but due to the abrasive behaviour of reinforcing constituents, it is preferable to upgrade the nozzle material [167]. Furthermore, the presence of such reinforcements increases the polymer stiffness and reduces its expansion on deposition resulting in a more brittle filament and product, hence additives should be considered within the filament production process [177,202]. In addition, since the growing availability of thermoplastic filaments reinforced with nanoparticles, a specific category containing nanotubes and nanoparticles is also considered considering the aspect ratio at a nanoscale [51]. According to [114], such constituents are classified as low aspect ratio discontinuous reinforcements, while continuous fibers as high aspect ratio reinforcements with preferred orientation. Since the higher aspect ratio corresponds to higher fiber orientation and interface area, the continuous fibers result in stronger and stiffer composites in comparison to their discontinuously reinforced counterparts [51]. Unlike discontinuously reinforced composites, the successful implementation of continuous fibers requires specialized equipment, hence its application is still restricted.

2.1.3. Discontinuous fiber composites

Due to their simplicity and low machinery adaptation requirements, short fibers have been widely implemented in molding or extrusion processes to produce high-end products in various engineering applications [51]. Despite the simplicity in product manufacturing, the production of the material itself has to be carefully controlled and optimized since high fiber content may

lead to matrix thermal degradation, viscous dissipation and/or extruder clogging [51,94]. In general, short fiber composite feedstock is produced by mixing the matrix pellets with fiber powder, melting, and extrusion into a filament form. If the fiber distribution tolerance is not achieved, the process could be repeated through recycling as long as thermoplastic polymer is used as a matrix. Since AM short fiber composites are more dependable on feedstock production than the printing process itself, the optimization of mixture ratio, fiber size and orientation had been the major focus of most studies. A comprehensive survey on the effects of fiber content, expansion ratio, and extrusion rate on the filament diameter has been presented in [83]. The ABS polymer was mixed with 100μm carbon fibers in ratios of 0, 5, 10, and 15%, and extruded through a 3mm nozzle, showing decreasing diameter versus the increase of fiber content up to a 10% threshold, after which a decreasing trend has been observed. The study also reported nonlinear relation between the fiber content and the extrusion rate, reciprocal ratio for diameter/expansion ratio, and reverse reciprocity for diameter/extrusion rate, concluding a deeper study of feedstock fabrication influence on mechanical properties is necessary [51]. The thermo-mechanical properties of ABS polymer filled with iron and copper particles in 5, 10, 20, 30, 40% volume ratios have been studied in [138], confirming the constituents' interaction influences and reporting the best performance for a 30% mixture of 10μm copper particles [51] in cyclic loading conditions. The influence of fiber size and volume ratio on the mechanical behaviour of AM-ABS samples has been studied in [139]. The fiber content was varied between 3, 5, 7.5, 10 and 15%, with an average fiber length of 100-150μm, and a fiber diameter of 7.2μm. The specimens were designed and additively manufactured according to ASTM D638-10 and ASTM D790-10 for tensile and flexural testing, respectively, confirming better performance for longer fibers as expected, reaching an optimum for the volume ratio of 7.5%. In contrast, the authors also reported that further increase in fiber content diminished the reinforcement influence up to a complete negation at 15%, hence highlighting the necessity for additional research. Furthermore, the tensile and compressive behaviour of short fiber reinforced ABS composite has been studied in [184], while producing multiple mixtures of ABS matrix reinforced with 0.2 – 0.4mm long discontinuous carbon fibers in 10, 20, 30 and 40% ratios. The specimens were produced according to ASTM D638 and ASTM D4703 standards, using 0.5mm AM extruder nozzle and a compression molding method for comparison. Authors reported nozzle clogging at 40% fiber ratio, while voids generated between the deposited material caused a fiber ratio reduction in comparison to the compression molded counterparts. However, the AM specimens

have shown a higher level of fiber alignment in comparison to the compression-molded samples, followed by an increase of tensile strength and modulus by 115%, and 700%, respectively [51]. Additionally, the alignment effect of short fibers in epoxy-based resin was studied by [114], using a custom-developed method. Discontinuous carbon fibers 100μm in length and 7.2μm in diameter were mixed with the epoxy resin in a 14% ratio 20min before the extrusion process, additively manufactured using the *"nScrypt Smart Pump"* micro-extrusion system, and UV cured for 30-60s after the extrusion. To inspect the material behaviour, sets of longitudinally and transversely reinforced specimens were designed, manufactured, and tested according to ASTM D638-10, showing an increase in tensile stress and modulus by 44.12% and 42.67%, respectively, confirming the significant orientation influence. The influence of fiber volume fraction on thermal and mechanical properties in AM carbon fiber reinforced polyamide composites (C/PA) has been investigated in [104]. In the study, the PA12 matrix was reinforced with 15-20mm long carbon fibers in 2, 4, 6, 8 and 10 % volume ratios. Specimens for tensile, flexural and impact properties acquisition were designed, additively manufactured and tested according to the ASTM D638-10, ISO 14125 and ISO 180-2000 standard, respectively, while adopting the manufacturing conditions as 100% infill, 0.2mm layer height, a printing speed of 30mm/s, and the extruder temperature of 250°C with a bed temperature of 120°C [51]. Authors also reported a crystallization temperature increase by 3.5°C, an increase in thermal conductivity by 277.8%, and a decreased melt flow index by 10% [51,104]. In conclusion, the introduction of the reinforcement led to an increase in unidirectional tensile strength and stiffness by 102.2%, and 266%, while reaching a 250% and 346% increase in flexural strength and stiffness respectively. Additionally, there was a reduction in longitudinal elongation at break by 23.7 times, while impact resistance remained unaffected by the reinforcement presence. Furthermore, [77] considered the influence of orientation in the short fiber reinforced PLA. In the study, the PLA matrix was reinforced with 100μm long discontinuous carbon fiber in 15% ratio and extruded using a 0.4mm diameter nozzle. SEM images had been taken from the extruded material cross-section, showing good fiber/matrix cohesion. The material was also inspected after being additively manufactured, reporting ellipsoidal holes in the extrusion orientation, while the tensile tests showed 40% fiber pullouts upon specimen failure.The in-plane shear strength in ABS composites reinforced with 14% of short fibers and 8% of carbon nanotubes was studied in [201]. The specimens have been designed according to ASTM D3518/D3518M-13 standard and additively manufactured for raster orientations of 0°, +/-45°, and 90°, while adopting the +/-45° configurations according to ASTM D3039/D3039M-14 standard in double-notched

specimens. Moreover, layer thickness and printing speeds were also varied between 0.18/0.25/0.3 mm and 60/80/100 mm/s, respectively. For comparison, the specimens' duplicates were also manufactured as unreinforced counterparts. Inspecting the specimen's microstructure, the x-ray imaging revealed a distinctive microstructure and porosity level dependence on the raster angle, confirming its influence on the mechanical behaviour of the specimens. In conclusion, the authors reported that the in-plane strength benefits from the reinforcement presence significantly, while it is degraded with the increase in printing speed and layer thickness [201].

2.1.4. In-situ composites

In contrast to the discontinuous fiber reinforcement technology where the composite material is mixed prior to the manufacturing process, the in-situ process has the continuous fibers usually embedded within the extrusion head before the composite material is deposited [51]. In most cases, the matrix feedstock is delivered into the extruder as a filament, while the continuous reinforcement is fed as a fiber bundle. The constituents are mixed within the extruder's hot zone where the adjustments to fiber/matrix volume ratio can be achieved by calibrating the feed speed [51]. Regrettably, due to the fiber bundle brittleness and lack of process control, the resulting composite quality may be compromised due to defects arising from dust, air or humidity inclusions, low coefficient of embedding, or nozzle clogging [51,154].

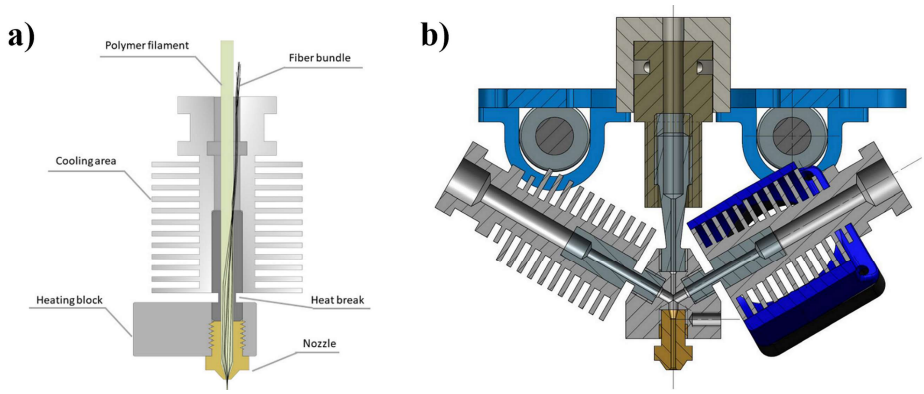

Figure 2.3 a) Continuous fiber composite mixing within the printing head [154], b) FFF printing head according to [51]

To account for the defects, authors studied the additive manufacturing process of continuous fiber fabrication (CFF), offering significant contributions [51]. The development of an extrusion nozzle with the capability of combining fiber and matrix constituents has also been presented in [52]. The adopted extruder geometry had a distinctively curved side channel developed for

the passing polymer matrix; this pulls the fiber bundle with a consistent feed rate, avoiding both the need for fiber feeding mechanisms and the defects caused by the bundle brittle fracture during mixing. The developed extruder was manufactured using selective laser melting (SLM) process and tested on 3K fiber in polyurethane thermoplastic elastomer showing good cohesion during the preliminary inspections [51,52]. A similar process, integrated into a three-sided extruder head shown on Figure 2.3, has also been proposed by [154]. In this example, polymer matrix is delivered through two of the side ports, while the fiber bundle is fed through the vertical port and mixed with the polymer within the central chamber, allowing a more uniform material impregnation. In addition, a similar process, without the additional feeding mechanism, has also been studied in [17], indicating the benefits of a modified commercial extruder. Despite achieving better control of the impregnation process, the authors reported the significance of processing parameter calibration on the resulting composite material. The study was conducted on PLA reinforced with carbon, glass, and aramid fibers, with only aramid bundles being the most applicable for the developed process, while the brittleness of carbon and glass caused frequent nozzle clogging. Nevertheless, the successfully printed materials showed an increase in tensile modulus up to six times in comparison to the unreinforced PLA counterparts [17,51]. Additional extruder design was also investigated in [102]. The study was performed on PLA reinforced with 1K continuous carbon fiber using a process analogous to [154] and [17]. Both constituents were supplied from a common extrusion head, using a conical nozzle, as shown on Figure 2.4 a), to improve the composite material homogeneity.

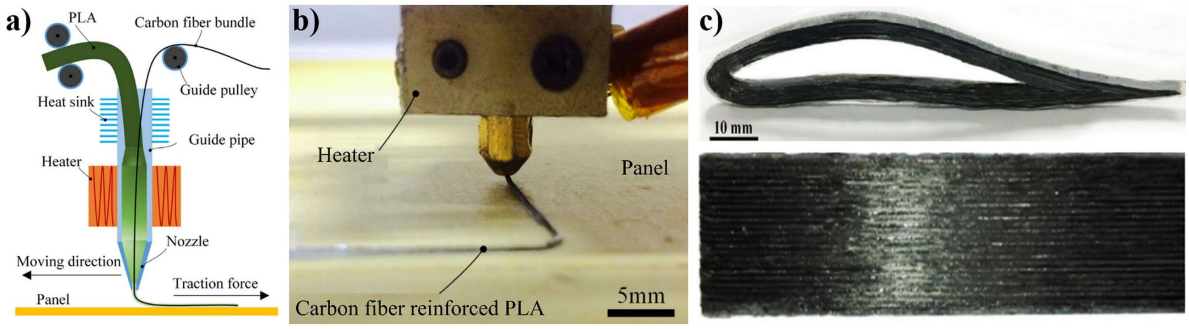

Figure 2.4 a) Extruder schematics [102], b) Composite deposition [102], c) Printed parts [102]

Hence, a performance comparison between the fiber/matrix, prepreg/matrix and unreinforced matrix has been conducted on unidirectional and on hollow profile specimens, as shown on Figure 2.4 c) and d), respectively [102]. In conclusion, the authors reported an increase of 13.8% and 164% for tensile and flexural strength in prepreg/matrix versus fiber/matrix composites. That indicates the importance of adhesion, as also confirmed with SEM imaging [51,102], for the improvement of flexural properties. The influence of processing temperature and thermal

bonding on the mechanical properties of AM parts was investigated in [129], highlighting the direct ties between the interfacial adhesion and the resulting part strength.

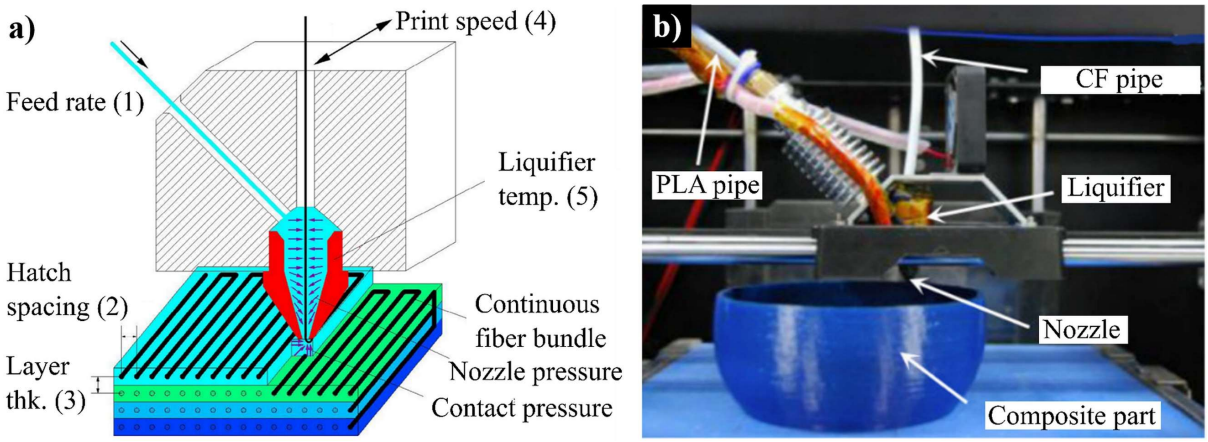

Figure 2.5 a) Process parameters for 3D printing of CFR-PLA composite [186] b) 3D printer setup [186]

The overall printing parameter influence on the mechanical properties of AM materials has been comprehensively studied in [186]. The authors were able to confirm a quasi-linear relation between the temperature and the mechanical properties in the range 180°C - 240°C, reporting a 40% and 150% increase in flexural strength and modulus between the minimal and maximal studied temperature, respectively. The flexural properties were also inspected for layer height between 0.3 to 0.8mm. The results confirmed the influence of the layer height on fiber content, with the layer height of 0.3mm confirmed as optimal [51]. The authors reported an increase of 161% and 204% in flexural strength and stiffness respectively, over the properties acquired for the 0.8mm value. These results accorded with the in-situ effects found in composite laminates [8,10] and other AM composites structures [79]. The authors also confirmed that the optimal properties are acquired with a feed rate of 80mm/min, and a hatching space of 0.4mm. Despite feed rate only having a limited effect on flexural properties, the hatching space of 0.4mm resulted in 162% and 383% strength and stiffness enhancement over the values acquired for 1.8mm [186], confirming the importance of pattern strategy.

2.1.5. Post extrusion composite

The post extrusion approach is based on embedding the fiber prepreg within the matrix on the printing bed, thus avoiding the problems of simultaneous extrusion but unfortunately creating interfacial adhesion problems due to temperature discrepancies during the polymer and fiber deposition phases [51]. Despite these problems, the approach was promising and underwent

further development. The first commercially available automated process of printing polymer matrix composites reinforced with continuous fibers was developed by Markforged® Inc. (Massachusetts, USA) in 2015. These machines were based on a post-extrusion approach, enabling the additive manufacturing of composites reinforced with continuous Carbon (C), Aramid (K) and Glass (G) fiber bundles delivered as filament with 400µm in diameter and combined with 1.75mm in diameter PA filament, resulting in a significant increase in mechanical properties. Similar to FFF extrusion of polymers, Markforged® Inc. also delivered a double-extrusion head system; one head is used for deploying the polymer matrix, and the other is used for the reinforced prepreg. Since continuous fiber deposition in AM requires frequent pausing and extruder repositioning, a fiber-cutting tool is essential as it enables the bottom-up build. This approach facilitates a multidirectional component reinforcement, while presenting minimal fiber/matrix adhesion problems due to the implementation of prepreg material. A similar approach has been developed by Anisoprint LLC; this utilizes two printing heads for matrix deposition and composite filament co-extrusion (CFC), respectively [6]. In contrast to other approaches, Anisoprint LLC uses a thermoset coating in the fiber bundles, thus ensuring superior fiber adhesion while significantly expanding the bonding capabilities with various matrix materials [7]. Furthermore, a multiphase approach has been studied in [129]. The printing has been done with the interruption for manual fiber placement, while the thermal bonding has been achieved using a microwave oven, as presented in Figure 2.6 c). The method was enhanced in [136]. The fibers were inserted in the middle of the extrusion process, as shown in Figure 2.6 a), and embedded in ABS during the transition from the heating block to extruder nozzle [51], achieving the thermal bonding and layer compression with a heated pin, as shown in Figure 2.6 d).

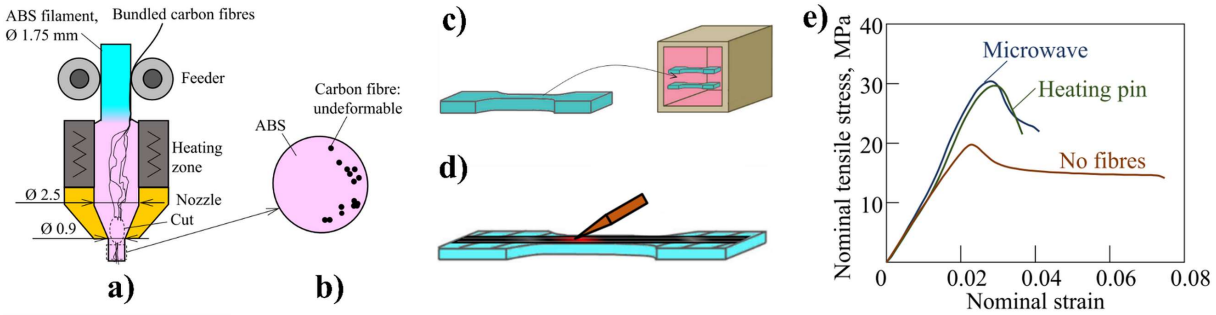

Figure 2.6 a) Extruder schematics [136], b) Carbon fiber inclusions in ABS [136], c) Thermal bonding using heated pin [136], d) Thermal bonding using microwave [136], e) Thermal treatment comparison [136]

By comparing the experimental results, the authors [129] and [136] reported that values of tensile strength for thermally treated specimens reached 30MPa, as presented in Figure 2.6 e),

outperforming both the unreinforced and untreated specimens, as shown in Figure 2.7 a). This confirms the bonding influence on the failure mode in Figure 2.7 b) and c), respectively.

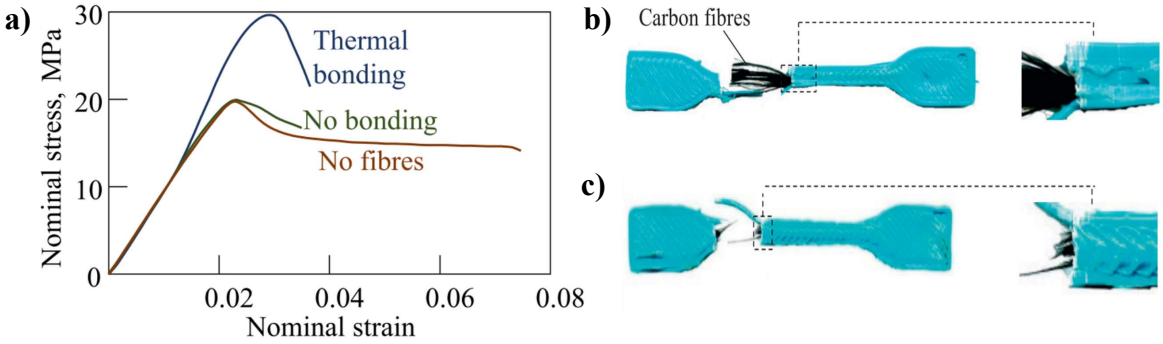

Figure 2.7 a) Comparison between thermally treated, untreated and unreinforced specimens [136], b) Untreated specimen failure mode, c) Thermally treated specimen failure mode

Since experimental data analysis shows only fiber detachment instead of rupture as the dominant failure mode, it can be concluded that these composites did not benefit significantly from the embedded fiber reinforcements due to their inferior bonding quality, despite having the advantage of a simplified manufacturing process. Despite its inferior mechanical response, the multiphase approach was utilized in structural health monitoring [196]; besides providing the structural integrity, fibers were also implemented as sensor components, measuring the changes in the fiber electric resistance during deformation. In this manufacturing process, the PAN 3K, 6K and 12K fibers were added manually in multiple ratios, while PLA was used as the matrix. The authors reported a 70% and 18.7% increase in tensile and flexural strengths, respectively. Moreover, analyzing the fiber fraction in unidirectionally reinforced laminates [96], it is clear that reinforcement content definition in AM materials is also crucial for a better result comparison with conventionally manufactured counterparts. The influence of the reinforcement content has been investigated in [96] by varying the number of reinforced layers. Three sets of concentrically reinforced specimens were designed according to the JIS K7073 standard, additively manufactured using a commercial Marforged® Inc. Mark One 3D printer and tested in tension, while maintaining the quasistatic conditions. The first set was reinforced with six carbon fiber layers and returned a tensile strength of 464 MPa at strain of 1.65%; for the second set reinforced with only two carbon layers, the tensile strength of 149 MPa at 1.05% strain was reported, while the unreinforced PA specimens reached values around 17 MPa at 5% strain, thus confirming significant fiber content contribution to the printed parts. The fiber content influence on the mechanical properties of AM composite materials was further studied in [122], where four sets of aramid reinforced PA composite specimens were designed according to the ASTM

D638-14 standard with 10% infill. The studied specimens included unreinforced and reinforced sets with two, four and five concentric rings, respectively. Upon confirming the positive effects of fiber content on specimen strength and stiffness, the authors developed a mathematical model to simulate the acquired behaviour, with good correlation for higher fiber contents. A more comprehensive study on mechanical and fracture behaviour of AM continuous fiber reinforced composites produced using the Markforged® MarkOne has been conducted in [61], encompassing microstructural inspections as well as experimental procedures on tensile, flexural and impact behaviour. The microstructural images were acquired using both SEM and micro-CT, highlighting the void formation between the adjacent deposited filament and pore size distribution, respectively. In addition, a density analysis has been conducted according to the ASTM D3171-15 standard, confirming 41% and 35% of reinforcement content in carbon and glass FRPs, respectively. Furthermore, the tensile specimens were designed according to the ASTM D3039 standard with 23 unidirectionally reinforced layers and tested statically in the direction of fiber orientation. The results showed lower values of tensile strength in comparison with the reported manufacturer's claims, but with higher values than the conventional UD composites [61]. Additionally, the flexural specimens were designed according to the ASTM D790 standard, reaching a significantly lower flexural strength in comparison with both manufacturer's claims and the conventionally manufactured counterparts [61]. Moreover, the indentation tests were performed in accordance with the ASTM D6264 standard, reporting slightly inferior results in comparison with traditionally manufactured FRPs. In conclusion, the authors agreed on the promising applications of AM technology for FRP manufacturing, but they stressed the necessity for a faster deposition rate. The mechanical behaviour of fully reinforced AM continuous carbon and glass-fiber-reinforced composites was studied in [88]. To acquire tensile, compressive and shear properties, the specimens were designed and additively manufactured using Markforged® Mark One, then tested according to ASTM D3039, ASTM D695, and ASTM D3518 standards, respectively. The experimental results acquired from the AM specimens were compared with the traditionally manufactured AS4 CF/Epoxy and E-glass/Epoxy prepregs with 69% and 65% fiber ratios, respectively. Based on the comparison, the authors concluded that the inferior behaviour of AM specimens versus traditionally manufactured counterparts could be mainly caused by the lower fiber content of 23% and 43% in AM carbon and glass fiber composites, respectively. These results were also influenced by the epoxy resin's cohesion superiority over the thermoplastic PA matrix, duly confirmed by the void content acquired from the microscopic inspections. In conclusion the authors proposed increasing the fiber content

and swapping the PA matrix to a more resilient one, like PEEK; the authors also implied the layer deposition should include a compaction stage to reduce the void content [88]. Further investigation on interlaminar bonding performance in AM continuous fiber reinforced composites has been conducted in [24]. Three sets of short-beam specimens reinforced with carbon, glass and aramid fibers, respectively, were designed according to the ISO 14130 standard and additively manufactured using Markforged® MarkTwo, varying the layer thickens and fiber content. The specimens were tested for acquiring the interlaminar shear strength using the 3-point bending technique and then compared to the data acquired for the unreinforced specimens. According to [24] the carbon-fiber-reinforced specimens showed the most significant enhancement from the reinforcement in comparison with the unreinforced PA, tripling its interlaminar shear strength; this was followed by the aramid composite with a 100% increase, whereas glass only showed 40% increase. Upon testing the specimens with lower fiber content, the authors [24] concluded that carbon fiber retained the best performance, reaching the double strength values, while the interlaminar shear strength of both glass and aramid composites increased by only 33%. The authors also confirmed the layer thickness did not influence the interlaminar shear strength significantly. This study was followed by [25], which investigated the impact performance influenced by the printing orientation, layer thickness and fiber content. The specimens were designed and tested following the ASTM D6110 standard, while keeping the component and printing parameters selection in accordance with [24]. In unreinforced specimens printed flat in the *x-y* plane, the authors reported improved impact resistance with the increase in layer thickness; the opposite was found for specimens printed on the edge. Moreover, all types of reinforced specimens benefited significantly from the increased fiber content, while edge printing resulted in an 11% and 80% increase for carbon and glass-reinforced composites, respectively. Meanwhile, aramid fiber composite surpassed the other variations with an order of magnitude, while having the impact strength increased for only 3% due to the edge printing. The authors concluded that the AM technology is still in development and, despite promising applications, it still delivers inferior components in comparison with conventional manufacturing when impact strength is considered.

2.1.6. Pre-impregnated composites

Traditionally, pre-impregnated (pre-preg) composite is a fiber-reinforced material where the fiber-embedding is prepared ahead of time or prior to molding, while the resin is kept partially

cured or thickened [10]. For pre-pregs, the fiber reinforcements can be arranged in a unidirectional tape, a woven fabric, or random chopped fiber sheets; there are additional costs due to the increased labour needs [10]. Pre-preg enables a high fiber ratio, but it also requires additional machinery, such as autoclave, to maintain the required quality [10]. In additive manufacturing, pre-pregs are specialized filaments with embedded continuous fibers, while their implementation requires specialized extruders, nozzles and fiber-cutting tools [51,137]. Analogous to the pre-preg approach, the authors in [188] proposed a pultrusion system to manufacture commingled filament using E-Glass reinforces PP matrix. The process is based on pulling the fiber yarn through a heated brass nozzle using a pull wheel and a servomotor, while being integrated with a FDM system with a cutting tool triggered by the movement without extrusion. Based on the material microstructure, the authors reported interlaminar void alignments, thus indicating insufficient material consolidation. Moreover, flexural test specimens were designed and tested according to the ISO 14125 standard, showing a flexural modulus of 12.37GPa using the reported printing parameters [188]. Furthermore, by discarding both in-situ and extrusion mixture approaches, the authors in [80] described the development of a prepreg AM feedstock which ensured a better fiber/matrix bonding during the extrusion. As presented in Figure 2.8, filament production is based on a single screw extruder and a coaxial extrusion mold, where the necessary pressure for fiber/matrix impregnation is achieved. The impregnated filament is submerged in water in order to achieve a proper solidification and subsequently dried at a constant rate [80].

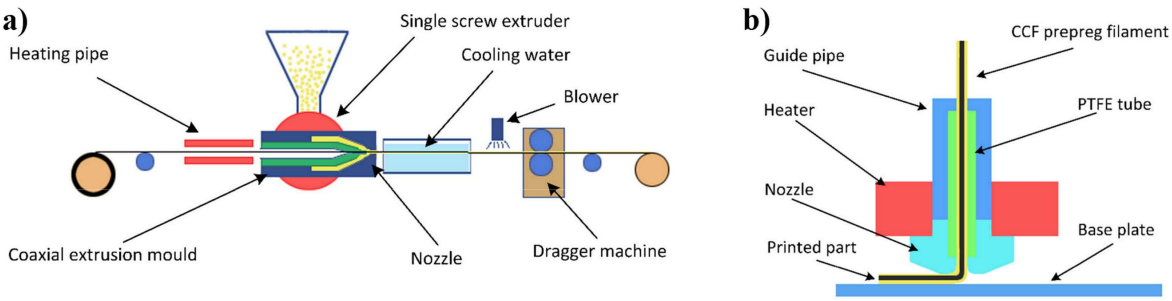

Figure 2.8 a) Pre-preg filament production process [80], b) Pre-preg extruder [80]

Material deposition was conducted using a simplified extruder, where pre-preg was delivered through a PTFE tube and extruded using a wider nozzle to avoid potential clogging and the fracture of filament during printing. In this process, the cutting tool is omitted.

DoE has been adopted for optimization of the printing parameters based on twelve sets of flexural specimens, and the authors confirmed there was a significant influence on flexural strength and stiffness.

2.1.7. Inherent defect in additive manufacturing

According to multiple studies, weak interlaminar and intralaminar bonds are inherent to the FDM process and are assumed to be major limiting factors in its engineering application. This has been reported in [26,144,161,182], where the authors investigated the effects of printing directions and confirmed the interlaminar and intralaminar void patterns' influence on the material behaviour. Furthermore, voids formation at inter-raster material deposition contact have also been reported in [73,84,111,144,181]. The authors agree on the origins of degraded mechanical properties in AM materials, however the authors in [180] also proposed a representative volume element (RVE) based mesoscale model for FDM polymers to account for these defects. Many researchers reported the potential difficulties arising from the additive manufacturing approach [122,126]. After analyzing the experimental data, researchers [4,19,195,197,69,86,95,102,144,150,161,173] agreed on the behavioural characteristics of AM fiber-reinforced composites, however, there are significant discrepancies between their studies. Moreover, the comparison between additively [84], and the conventionally [113] manufactured continuous fiber-reinforced composites shows superior mechanical properties in the conventional manufacturing of similar fiber/matrix compositions and fiber ratios. The processibility and performance ratio of short and continuous fiber-reinforced composites has been studied in [19]. The authors identified the negative effect of additional void formation during continuous fiber deposition, and they proposed the adoption of highly aligned short fibers instead. Similar to all laminated composites, AM components inherently suffer from low interlaminar shear strength (ILSS), which was studied in [84], while the experimental evaluation on the effects of layer thickness on ILSS was conducted in [24], emphasizing the necessity for further research. Although the technology of additive manufacturing is still under development and produces components with inferior mechanical properties due to a large number of factors, the application of additive manufacturing has significant potential through the tailoring of material properties for specific design requirements in a fully automated manufacturing process.

2.2. Material behaviour modelling

Together with the advancements in manufacturing processes, the development of novel matrix and fiber materials has resulted in novel composite systems which, supported by new design and analysis procedures, have expanded the industrial application of polymer composites [65]. These technological advancements have also been followed by the analytical and numerical

models, expanding the capabilities of commercial Finite Element Analysis (FEA) packages [8,9]. Most of the modelling approaches implemented in the analyses of composite material behaviour are phenomenological in nature, and could be based on: constitutive models developed for homogeneous materials, composition of isotropic or orthotropic phenomenological models, single- or multi-scale homogenization, isotropic/orthotropic phenomenological models, or kinematic formulations [65]. Moreover, to solve problems using computational mechanics, the understanding of the virtual domain is crucial, hence its separation into sub- and super-divisions is often necessary [141], as shown in Figure 2.9.

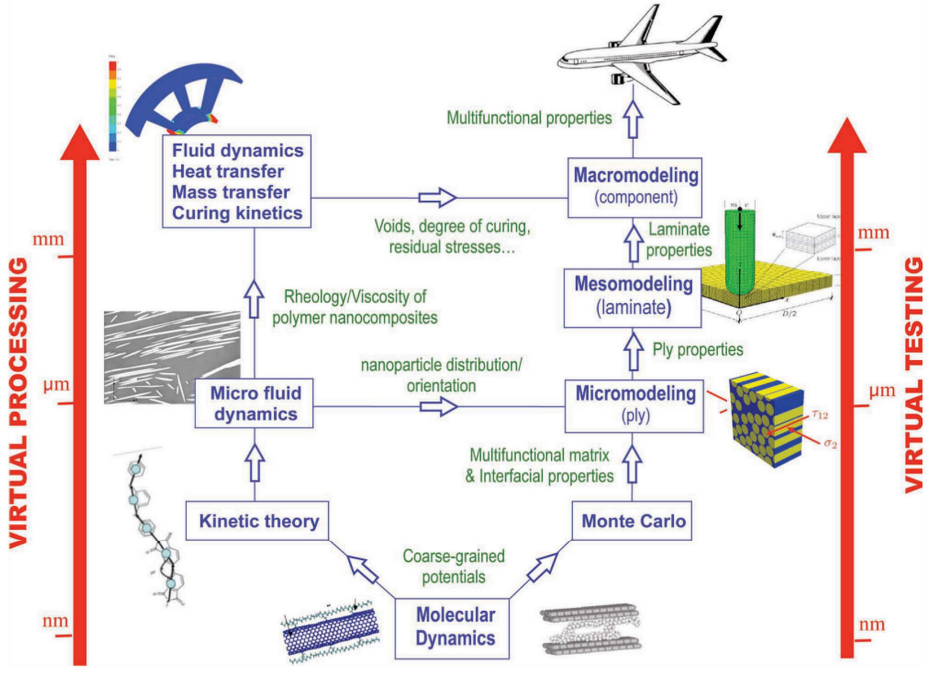

Figure 2.9 Multiscale simulation strategy for computational engineering of FRPs [107]

Considering the computational mechanics of fiber-reinforced composite materials, the most common division is between micro mechanics at the constituent's level, and continuum or discrete damage mechanics at the meso- and macro-scale [10,141]. In this section the state of the art involving the most commonly applied models will be briefly discussed.

2.2.1. Micro-scale mechanics

Micro-scale models are mathematical tools developed for analysis and differentiation of the constituents influence on the material behaviour at a measurement scale in the range of 10^{-6} m. Considering the material response, the analysis of material mechanical behaviour on the microscale is often referred as micromechanics. Depending on the material type, it can vary from the crystallographic and granular levels present in metallic materials, to the distinction between

the matrix and reinforcement in composite materials [10]. The micromechanical response of unidirectionally reinforced fiber composites is often computed based on two basic microscale models. The Voigt model, also referred as the Rule of Mixtures (RoM), is based on the iso-strain assumption, meaning that fiber and matrix strains are equal to the strain of the effective medium in longitudinally loaded composite, hence determining the upper bound of the effective elastic modulus [166], while the inter-phase boundaries are not in the equilibrium. In contrast, the Reuss model, also referred to as the inverse RoM, is based on iso-stress assumption transverse loading, meaning the stress in fiber is transferred to the matrix and is equal to that of the stress in the effective representative volume element, which is in conflict with the matrix/inclusion bonding and compatibility; better shear predictions could be achieved using higher-order shear stress distribution [166]. Voigt and Reuss models are simple tools for the determination of the upper and lower bounds of the effective material stiffnesses [1]. An improved method has been developed in [71,72] based on the concept of minimum potential energy, variational principle, and polarization. This model considers the strain energy of a homogeneous isotropic material as reference, for which the change in strain energy is calculated by the addition of inclusions with different elastic properties and then maximized with respect to the stress polarization tensor to obtain the bounds [166]. In contrast to Voigt and Reuss, the bounds in the Hashin-Shtrikman model are formulated based on the constituents' effective elastic properties, where the matrix is treated as the reference for the lower bounds, and the fiber for the upper bounds; instead of averaging stresses and strains, the strain energy is minimized [166]. A modification of the Voigt model for computing transverse and shear stiffness based on the distinctive fiber and matrix subregions has been developed by Hopkins and Chamis [78], assuming a rectangular fiber cross-section and utilizing the effect of fiber packing geometry [166]. The model has been validated in various fiber packing geometries in [85], showing consistent results. An additional approach has been proposed in [54], where the transverse stiffness in fiber-reinforced composites is calculated based on dividing the unit cell square packing into subregions. The results are consistent with the experimentally acquired data for fiber volume fraction less than 0.5 in [53]. Despite the geometrical similarities, the model [54] is based on continuum mechanics methods in contrast to the Chamis formulations which are based exclusively on geometrical parameters and fiber volume fraction. The model [54] is able to capture the effects of fiber geometric parameters, including fiber diameter, aspect ratio and inter-fiber spacing, therefore allowing more accurate stiffness predictions in comparison with the others shown in Figure 2.10 [166].

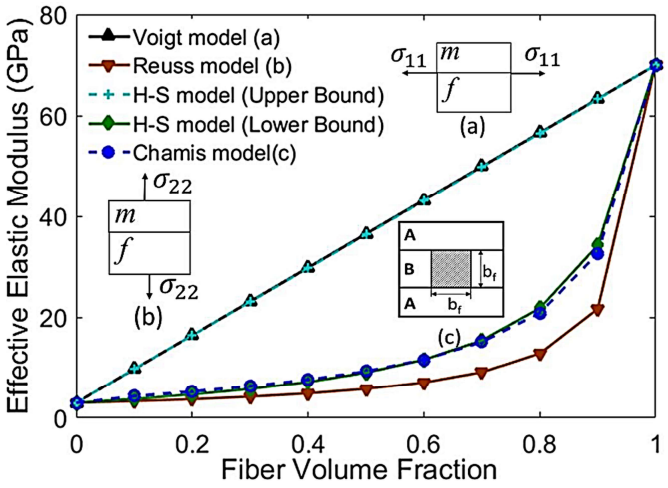

Figure 2.10 Micromechanical model comparison [166]

An empirically augmented generalized model has been developed in [66,67] based on the approximations of the effective properties in terms of matrix and fiber phases. Within the model framework, the geometry of the inclusions is quantified by the empirical parameter, which is calibrated on the experimental data as reported in [58,147]. The model was modified for in-plane shear predictions in [75], validated for higher volume fractions in [2,3], and implemented in the analyses of 3D woven composites with void inclusions [81]. All thing considered, the model gives an improved estimate of effective transverse and shear stiffnesses, however the empirical part is highlighted as a drawback due to the necessity for calibration [166]. Research on the application of eigenstrain theory for determination of internal stress in a matrix with inclusion has been conducted in [130], enabling the calculation of effective mechanical properties in composite materials [14,166]. The model was initially developed for ellipsoidal inclusions, while the analytical solutions for the composites containing spheroidal shapes, disks, needles, or penny shaped cracks were derived in later studies [16,50,194]. Moreover, the influence of aligned and randomly oriented cylindrical fibers has been studied in [38], as has the two-step homogenization of short fiber reinforced composites in [185]; there is agreement on the valid physical representation of the material constituents. In contrast, the study conducted on multi-phase composites has shown an inaccurate prediction for Mori-Tanaka based models [131]; inaccuracies arising from the dilute dispersion assumption were also confirmed in the analysis of particulate composites with higher volume fraction [103]. Therefore, the self-consistent model was developed in [20,76] to overcome the limitations of the existing models. It assumes there is equality between the matrix properties and the effective properties of the composite prior to the introduction of the single inclusion. The effective matrix properties simulate the multiple inclusion effect [166]. If a dilute dispersion equivalent to a single inclusion within

the infinite matrix medium is assumed, the method returns adequate predictions only for the low fiber fraction composites [166]. Additionally, the effective matrix properties simulate the interactions between the multiple inclusions hence the extended model discussed in [166] is applicable for the analysis of multi-phase composites. In this model extension, the calculation of the multi-phase composite materials' effective properties is based on volume fraction and the concept of iterative increase in inclusions. Within this framework, adopting a variable volume instead of the physically inconsistent fixed volume approach, the effective properties are calculated on every iteration until the desired volume fraction has been achieved. In contrast to the self-consistent models, the differential scheme enables a distinctive phase recognition, expanding the model applicability [121]. Similar to the attempt of modifying the rule of mixtures in [105], a revised model based on the Mori-Tanaka dilute dispersion approach has been discussed in [166]. The model is based on a differential scheme for obtaining the effective stiffness tensor for the desired volume fraction of inclusions, also enabling a multi-phase distinction. Within this framework, the information on the matrix background is applied to the new composite by rearranging the inclusions in the background mixture that follows the deformation state, thus only the volume fraction effect connects the state of inclusions between the background and the new state [166]. The authors also emphasize that the geometric arrangement of the inclusions causes a difficult nonlinear and process dependent problem, especially for the anisotropic cases, which still remains unsolved [166]. Following the increase of computational power, the finite element model is often used to capture the distributions of stresses and strains based on which a more accurate determination of effective properties can be made. Hence, a comparison between the theoretical, FEA, and experimentally acquired results has been conducted in [166], as shown in Figure 2.11 Model comparison for: a) Longitudinal response [166], b) Transversal response [166], c) Shear response [166]. It is concluded that, among theoretically based models, the predictions from the non-dilute self-consistent model and the revised Mori-Tanaka model are the closest to the numerically and experimentally acquired data.

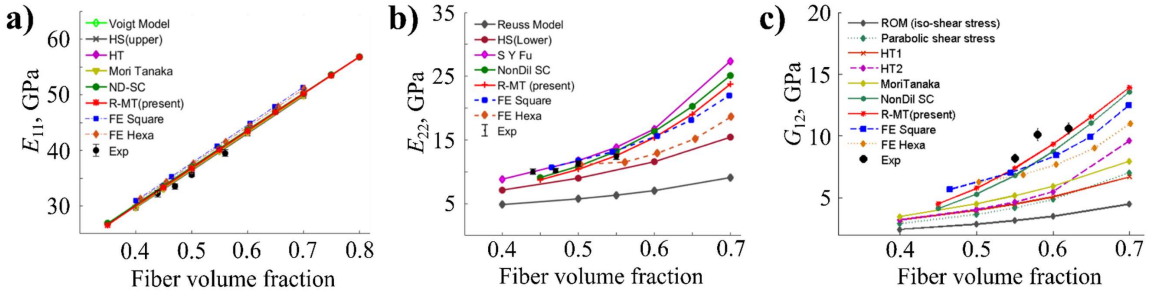

Figure 2.11 Model comparison for: a) Longitudinal response [166], b) Transversal response [166], c) Shear response [166]

Since the FEA became more applicable in engineering practice, a finite element based virtual framework for computing the full-field elastic response in unidirectionally reinforced composite materials, based on the 3D RVE domain, has been proposed in [5,142]. Using the case of through-the-thickness angle interlocked textile composite, the authors analysed the application of interpolation techniques for imposing periodic boundary conditions to arbitrary finite element meshes, computing the holistic range of effective mechanical and thermal properties of continuous fibre reinforced composite materials. The proposed boundary conditions are implemented within the commercial FEA software and validated on benchmark virtual tests, giving a comparison between the conventional techniques and experimentally acquired data. The authors demonstrate that predictions from the virtual framework compare closely with experimental data as well as with other numerical and analytical predictions in the literature. The authors state that the presented framework is suitable for holistic elastic properties acquisition based on virtual experiments with FRP composites, avoiding the necessity for assumptions on the macroscale behaviour.

Since only elastic behaviour is considered, the authors suggested further research on material plasticity and damage mechanics at the macro scale using a similar virtual framework. Subsequently, an Abaqus plug-in tool for periodic boundary conditions (PBC) placement and RVE homogenization of user customizable geometries has been developed in [143]. The concepts of a periodic RVE are automatically applied on the user-created geometry within the Abaqus CAE environment, followed by the homogenization concept by imposing uniform strains on the RVE in order to compute the effective elastic properties. The model has been validated on the experimental data from the literature showing consistent results, despite being limited to elastic behaviour. A method for numerical evaluation of material property degradation in composite RVEs due to fiber/matrix debonding and matrix cracking has been proposed in [135]. The authors studied the initiation and propagation of damage modes in various RVEs by implementing the cohesive zone model (CZM) to simulate fiber/matrix debonding. They used the extended finite element method (XFEM) to model matrix cracking while simultaneously studying its influence on the stiffness degradation. The method has been validated on the available data from the literature, upon which the authors concluded that the approach is applicable for macroscopic constitutive behaviour calculation, as well as for obtaining the required damage parameters of RVEs CDM analyses. A novel scheme for micromechanical simulation of fracture processes in composite materials has been developed in [74]. The author proposed a simulation based on linear elastic fracture mechanics (LEFM) of the displacement field around a crack tip acquired

during the mode I fracture tests and its application in virtual analysis of the interlaminar crack propagation in tension. He reported accurate characterization on interlaminar fracture energy and damage resistance. The resulting fracture response has been derived into softening laws applicable in higher scale modelling. A multiscale modelling approach has been proposed in [132], where authors investigated the micro- and meso-mechanical response of thermoplastic composites by computing the homogenized yarn behaviour at a microscale to allow the formulation of the representative constitutive model for predicting ply properties on the mesoscale. The RVE input properties have been acquired through in-situ constituent's micromechanical characterization and implemented in numerical analysis. The authors reported results consistent with the experimental data from the literature, documenting non-linear behaviour in transverse and shear directions prior to failure. All things considered, the FEA approach is unmatched by the analytical methods and has become a standardized methodology for calculation of material properties in heterogenous and orthotropic materials. Therefore, the FEA based virtual framework approach for holistic material properties acquisition has also been adopted in this thesis.

2.2.2. Continuum damage mechanics

Continuum damage mechanics represents the failure modes by the effect they have on the mesoscale behaviour of the material, calculating the degraded stiffness of the laminas in terms of continuum damage variables to predict the damage initiation based on the strength or fracture mechanics failure criteria [8]. The failure criteria often encountered in FEA packages [8,9] for fiber reinforced composites are based on linear elastic analysis and assume the lamina as an orthotropic continuum while calculating the failure index as a stress/strength ratio. Based on the stress interaction, these models can be characterized as noninteractive, partially interactive, and fully interactive; they don't account for the damage evolution process due to their phenomenological principles. Most commonly used are the Tsai-Hill [10] and the Tsai-Wu [187] failure criteria, developed to account for the stress interaction, but stresses in different directions are not decoupled and affect the lamina failure simultaneously. These criteria are independent of the failure mode and cannot be used to predict the mode of failure within the laminate accurately. Hence, the criteria with a more significant physical basis have been developed, including the Hashin [70], the Puck-Schurmann [157], and the Cuntze [44], with many more [31,46,115,153], which observe the stress interaction independence of the failure modes and

are consequently more applicable [21]. Physically-based, but simple enough for usage in engineering practice, the Puck failure criterion [48,49,156,157], distinguishes between fiber failure (FF) and matrix failure (MF) within multiple failure modes. Since damage in FRP composites can be manifested in multiple modes (including fiber breakage, matrix cracking, fiber-matrix debonding, and delamination) substantial effort had been invested in quantifying each of these damage modes and their evolution versus load, strain, time, and number of cycles, as well as the damage influence on the residual stiffness [8]. One comprehensive modelling approach is the stress-based CDM which represents all the failure modes by the effect they have on the lamina behaviour by calculating the degraded stiffness of the laminas in terms of continuum damage variables [8]. The damage is therefore detected using strength or fracture mechanics failure criteria, followed by an empirical damage evolution law controlled by calibration parameters.

2.2.3. Stress-based continuum damage mechanics

The stress-based CDM formulations have been in continuous development since the early works of [89,165], with improvements to their approach proposed in [34–37,65]. Based on [34], a mesoscale model for damage modelling in woven fabric-reinforced composites under compressive loads had been developed in [106], experimentally validating their results on load peak and crack propagation across fibers. Studying the elastic-brittle behaviour of fiber-reinforced composites, a constitutive model based on a homogenized continuum has been proposed in [119]. The model was developed for anisotropic damage analysis in fiber-reinforced composites and was later modified in [99]. Adopting the proposed framework in the LS-DYNA subroutine, the authors in [101] developed a numerical model for blast and fragmentation analysis in glass/epoxy composites. Furthermore, the authors in [134] proposed the stress tensor formulation and defined the theoretical foundations for anisotropic damage modelling, upon which the later work on 3D multi-directionally braided composites has been based [64]. The dynamic response of cross-ply laminates under low velocity impact has been studied in [200] by combining a CDM based FEA model with a damage-friction interface constitutive relation and the Hashin failure criteria within the Abaqus/Explicit environment. Another implementation of failure criteria within the CDM model has been proposed in [22] and experimentally validated in [23]. The model assumes four possible fracture planes in relation to tensile fracture, fiber kinking, matrix cracking within the range from 0° to 53°, versus lamina thickness direction.

The intralaminar failure mechanism is predicted by the LaRC04 failure criteria developed in [46,151]. The model has been developed with the ability of retaining tension-compression load histories, while also accounting for the ply thickness influence on the onset of matrix cracking by replacing the unidirectional strengths with the in-situ values in the failure criteria. The application of the model was also confirmed in the following studies on composite laminates [62], and variable-stiffness composite panels [112]. A comprehensive study on the composite materials was presented through a bottom-up multiscale approach in [107]. Within its framework, the authors distinguished between nano-, micro-, meso- and macro-mechanics, highlighting the advantages and disadvantages for each approach, respectively. Additionally, a three-dimensional continuum damage model applicable for the prediction of multiple failure mechanisms in laminated composites has been proposed in [116]; it also lays out a constitutive response, in accord with the formalism of the thermodynamics of irreversible processes, to ensure mesh-independent prediction of energy dissipation by crack band model implementation [116]. The prediction of delamination and matrix cracking without the implementation of cohesive elements has been validated on the experimental data and implemented in simulations conducted in [123], while further development on transverse and shear damage utilizing Gibbs energy has been proposed in [172]. A more accurate prediction of composite material behaviour has been achieved using fourth-order damage tensor in [36], which was extended in [124] by developing a parametrically homogenized CDM based progressive damage model, overcoming the excessive computational costs of homogenization methods. Additionally, a modified Puck's theory for 3D application was proposed in [48], where the authors developed a 3D degradation rule and implemented it into the FEA software Abaqus. According to Puck's theory, the model distinguishes between fiber and inter-fiber damage in both tension and compression, while tracing the fiber damage to its micromechanical origins. Model verification has also been conducted in [48] while also being confirmed in further studies [92,98,100]. The stress-based CDM approach has also been adopted in medical applications for composite-bone FEA in [45], by implementing the Hashin failure criterion for predicting microdamage initiation that triggers the nonlinear behaviour, thus accounting for the effect of physiological or non-physiological stress concentrators. Additionally a discrete crack-informed model for prediction of crack initiation and evolution, using failure criteria in a continuum element, has been proposed and validated in [149], showing consistency with the experimental data. The authors highlight the reduction in computational time in comparison with [116]. All things considered, the CDM phenomenological parameters need an experimental calibration based on a measurable effect of damage on the

macro-scale. Hence, most stress-based CDM models adopt stiffness reduction as the representative state variable of damage [8,65]. Therefore, the main disadvantage of the stress-based CDM approach is the necessity for additional experimental data to determine the calibration parameters; notwithstanding, the stress-based CDM is widely used in engineering design due to its calibration versatility [48,92,100,156].

2.2.4. Synergistic damage mechanics

While CDM homogenizes the damage and treats it phenomenologically [8,10], the alternative methods attempt to represent the actual geometry and discrete characteristics of damage [8]. Initially developed for the microscale, the Micro-Mechanic Damage model (MMD) is based on approximating an elastic solution for a laminate containing one or more discrete cracks [168,198], with the assumption of the kinematic laws [8]. The advantage of MMD over CDM is that the laminate stiffness reduction as a function of crack density is calculated without any empirical parameters [8]. The main disadvantage of MMD is that most of the available solutions are limited to symmetric laminates under membrane loads with only one or two laminas cracking [8,68,120,127,145]. On the other hand, the Synergistic Damage Mechanics (SDM) approach overcomes these restrictions since it combines the physics of discrete matrix cracking from MMD with the CDM modelling approach [8,11,12,41,189]. With that in mind, Discrete Damage Mechanics (DDM) is an approach based on discrete cracks in the matrix which grow parallel to fiber orientation, as shown in Figure 2.12, influencing laminate stiffness when accumulated [8,21]; its formulation is based on fracture mechanics invariants. As a result, many researchers recognized the prospects of DDM, proposing novel solutions. Among synergistic models, a versatile approach for material properties and damage evolution prediction in symmetric laminates with arbitrary LSS has been developed in [11,41]. Within the model framework, the elastic properties are predicted as a function of crack density, while the prediction of damage evolution is based on critical values of strain energy release rate (ERR) for modes I and II (G_{IC} and G_{IIC}), without the necessity for postulation and calibration of empirical parameters. The model validation shows significant computational efficiency, mesh independence and consistency with the experimental results. The model has also been extended for fatigue damage prediction, expanding its application [13].

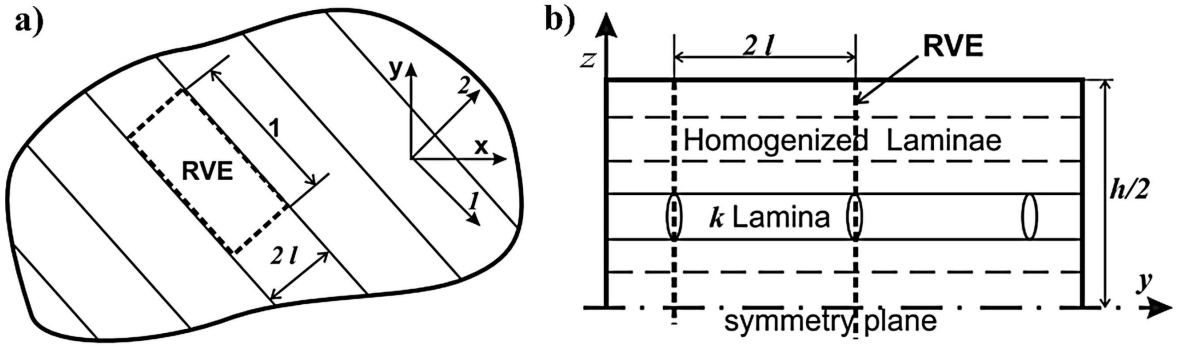

Figure 2.12 RVE in discrete damage mechanics [8]: a)Top view, b) Side view

The problem of the stiffness degradation in a cracked symmetric laminate with arbitrary LSS has also been studied in [28]. To compute the initial elastic properties in multidirectional symmetric laminate containing off-axis cracks in one layer, a bi-dimensional shear-lag analytical model has been developed in [28], calculating in-plane stresses, strains and displacements averaged over the thickness of each layer. Based on the proposed formulations, a compliance matrix of the damaged laminate is estimated as a function of the crack density. The model also accounts for the mutual crack interactions within and between layers by estimating the compliance matrix of a generic multidirectional symmetric laminate with cracks in multiple layers, using only elastic and geometric ply properties, the LSS and crack density. The model validation shows good computational efficiency and consistency with experimental data, while also confirming the effects of crack interactions on stiffness degradation through a parametric study, highlighting its importance in laminates with cracks in thick and neighbouring plies. In contrast to CDM, the advantages of synergistic methods reside in strain-based formulations governed by discrete fracture mechanics without the necessity for additional empirical parameters. In addition to the basic invariants of critical ERR values, elastic, and geometrical properties, the model requires the crack density master curves for each material; these are difficult to obtain experimentally [27,28].

Substantial research regarding the state-of-the-art methods of additive manufacturing and constitutive properties acquisition of continuous fiber composite materials has been presented in this chapter. Additionally, a comprehensive review of the most significant approaches in material modelling and damage analysis in composite materials has also been conducted. Subsequently, no reports have been found on constitutive response and damage modelling in multidirectionally reinforced AM composites, while the studies on micromechanics have been limited in scope. Therefore, a comprehensive multiscale bottom-up approach has been proposed in this thesis, including experimental and numerical analysis through multiple length scales.

The state-of-the-art in additive manufacturing has been presented in this chapter, which highlighted the characteristics of available AM technologies regarding the positive and negative aspects of a particular manufacturing method. Due to its simplicity, the FDM method has proven to be the most versatile approach. However significant deficiencies in AM polymer componets also confirmed that the introduction of fiber reinforcement is essential for this particular method. Therefore, various types of AM composites have been discussed, among which the continuous fiber reinforced polymers have been selected for further analysis due to their preferable mechanical properties. Having selected this material, distinctive methods of analysis have also been presented; these indicate the necessity for a multiscale protocol to account for the heterogeneity and orthotropy of the fiber reinforced composites. Focusing on the recent development of such analytical solutions, a review of micromechanical modelling techniques has been presented first. A comparison between the applicable models has been discussed and, due to its versatility, the FEA approach has been selected in this thesis. The macroscale modelling approach has also been presented in this chapter, and the application of continuum damage mechanics has been discussed accordingly. The phenomenological nature of stress-based damage models has been compared with the discrete concepts in synergistic damage models. This comparison led to a conclusion that, despite the numerical advantage, the synergistic damage models reacquire the crack density master curves, which are difficult to obtain experimentally using the available technology, hence the phenomenological models have been adopted instead. Based on this survey, the focus on the theoretical basics of the selected multiscale modelling techniques will be presented in the following chapter, starting with basic laminate mechanics, followed by the mathematical proofs of the micromechanical homogenisation of the representative volume elements, and concluding with a detailed summary of the Puck's failure theory within the framework of continuum damage mechanics.

3. THEORETICAL BACKGROUND

Based on the comprehensive review of the state-of-the-art in material behaviour modelling, a multiscale approach has been proposed in this thesis. The micromechanical analysis will provide specific insight into AM composite microstructural composition, upon which the RVE will be designed and numerically homogenized using FEA software. The acquired holistic homogenization results will be compared to experimental data and implemented in a user-defined CDM model where failure is identified using Puck failure criteria. The model will be calibrated according to the experimentally acquired data and validated on distinctive LSS cases. Henceforth, the theoretical concepts of constitutive and damage modelling will be summarized in this chapter, starting with the essential concepts in classical laminate theory (CLT), microstructural homogenization based on the representative volume element, and the proposed Puck failure theory in continuum damage mechanics.

3.1. Constitutive modelling of laminated structures

A constitutive model is a mathematical simplification of a complex material behaviour formulated in respect of physical concepts and experimental evidence. The constitutive behaviour of fiber reinforced composites is highly influenced by the distinctive constitutive behaviour of its constituents, hence it is often inspected, and modelled through multiple length scales. Therefore, this chapter will be focused on the theoretical background of constitutive modelling in laminated composites. The analytical solutions will be synthesized through linear elastic classical laminate theory, with highlighting of the proposed assumptions upon which the constitutive model of the laminate is built.

3.1.1. Classical laminate theory

Since composite laminates in engineering practice are often applied as thin-shelled structures like beams, plates and cylinders, where thickness is kept in an order of magnitude that is less than the others' dimensions, the fundamental assumption of in-plane stress state is valid [178,192]. Regarding the material orthotropy, the redefinition of a coordinate system within the lamina is also necessary. Following the conventional definition, the 1-2-3 coordinate system is often adopted, where 1- is for the direction in which the reinforcements are laid, 2- is for the

direction perpendicular to the reinforcement placement, while 3- is for the lamina stacking direction, as shown in Figure 3.1. The 1-2-3 axes are often referred as fiber, matrix and thickness direction, respectively, together forming the principal material coordinate system according to which all stresses and strains on a lamina level are computed [10,87,192].

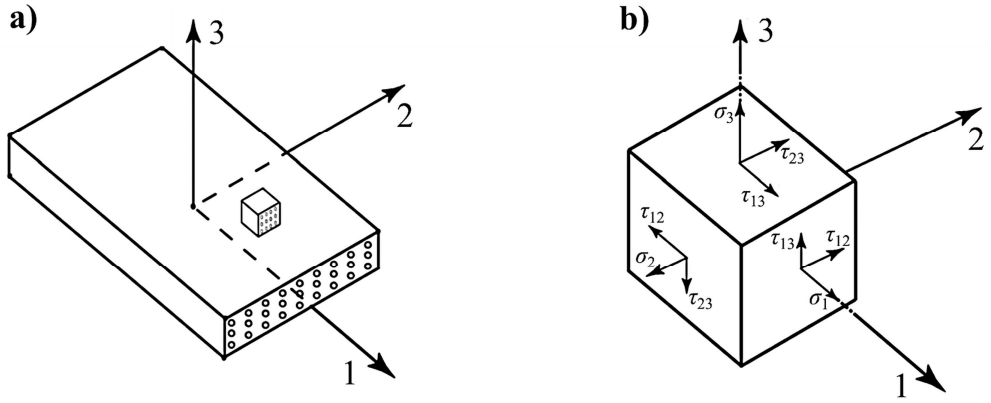

Figure 3.1 Coordinate system of a lamina and its homogenized RVE [192]

From the macro-mechanical point of view, the distinctive stresses and strains of the constituents are neglected, assuming the lamina as a homogenized continuum with anisotropic properties. Since the materials with distinctive properties in mutually perpendicular directions are referred as orthotropic, the layers within the laminate are also orthotropic [10,87,192]. The stresses on the infinitely small segment showed in Figure 3.1 are divided into distinctive normal stresses σ_1, σ_2, σ_3 and shear stresses τ_1, τ_2, τ_3. in connection with normal strains ε_1, ε_2, ε_3, and shear strains γ_{12}, γ_{23}, γ_{13}, respectively [10,87,192]. Following these assumptions, the constitutive matrix of the classical laminate theory is defined, where (E_{11}, E_{22}, G_{12}, ν_{12}, ν_{21}) are the adopted homogenized lamina properties, while the constitutive relations are assumed linear elastic, as shown in Eq. 3.1.

$$\{\varepsilon\} = [S]\{\sigma\} \tag{3.1}$$

According to the CLT formulation, $\{\sigma\}$ and $\{\varepsilon\}$ represent the 6×1 stress and strain tensor respectively, while $[S]$ is referred as the compliance matrix [10,87,192]. The expression can be expanded using the elastic constants, as shown in Eq. 3.2, where E_1, E_2, E_3 represent the stiffnesses in directions of the principal coordinate system 1-2-3, respectively; the ν_{ij} (i, j =1, 2, 3) represent the Poisson ratio values, G_{12}, G_{23} and G_{13} represent the values of shear moduli. Moreover, the tensor symmetricity $S_{ij} = S_{ji}$ is assumed, leading to $\frac{\nu_{12}}{E_1} = \frac{\nu_{21}}{E_2}$, as shown in Eq. 3.2.

$$\begin{Bmatrix} \varepsilon_1 \\ \varepsilon_2 \\ \varepsilon_3 \\ \gamma_{23} \\ \gamma_{13} \\ \gamma_{12} \end{Bmatrix} = \begin{bmatrix} 1/E_1 & -\nu_{21}/E2 & -\nu_{31}/E3 & 0 & 0 & 0 \\ -\nu_{12}/E_1 & 1/E_2 & -\nu_{32}/E_3 & 0 & 0 & 0 \\ -\nu_{13}/E_1 & -\nu_{23}/E_2 & 1/E_3 & 0 & 0 & 0 \\ 0 & 0 & 0 & 1/G_{23} & 0 & 0 \\ 0 & 0 & 0 & 0 & 1/G_{13} & 0 \\ 0 & 0 & 0 & 0 & 0 & 1/G_{12} \end{bmatrix} \begin{Bmatrix} \sigma_1 \\ \sigma_2 \\ \sigma_3 \\ \tau_{23} \\ \tau_{13} \\ \tau_{12} \end{Bmatrix} \tag{3.2}$$

Furthermore, the expression can be simplified as shown in Eq. 3.3.

$$\begin{Bmatrix} \varepsilon_1 \\ \varepsilon_2 \\ \varepsilon_3 \\ \gamma_{23} \\ \gamma_{13} \\ \gamma_{12} \end{Bmatrix} = \begin{bmatrix} S_{11} & S_{12} & S_{13} & 0 & 0 & 0 \\ S_{12} & S_{22} & S_{23} & 0 & 0 & 0 \\ S_{13} & S_{23} & S_{33} & 0 & 0 & 0 \\ 0 & 0 & 0 & S_{44} & 0 & 0 \\ 0 & 0 & 0 & 0 & S_{55} & 0 \\ 0 & 0 & 0 & 0 & 0 & S_{66} \end{bmatrix} \begin{Bmatrix} \sigma_1 \\ \sigma_2 \\ \sigma_3 \\ \tau_{23} \\ \tau_{13} \\ \tau_{12} \end{Bmatrix} \tag{3.3}$$

Furthermore, the stiffness matrix [C] is acquired by inverting the compliance matrix [S], upon which the expression shown in Eq. 3.4 is acquired.

$$\{\sigma\} = [C]\{\varepsilon\} \tag{3.4}$$

Since the compliance and stiffness tensors are symmetric [10,87,192], the expression is further simplified by assuming $C_{21} = C_{12}$, $C_{23} = C_{32}$, $C_{13} = C_{31}$, leading to the formulations presented in Eq. 3.5.- 3.11.

$$C_{11} = \frac{1}{S}\left(S_{22}S_{33} - S_{23}S_{23}\right) \tag{3.5}$$

$$C_{12} = \frac{1}{S}\left(S_{13}S_{23} - S_{12}S_{33}\right) \tag{3.6}$$

$$C_{22} = \frac{1}{S}\left(S_{33}S_{11} - S_{13}S_{13}\right) \tag{3.7}$$

$$C_{13} = \frac{1}{S}\left(S_{12}S_{23} - S_{13}S_{22}\right) \tag{3.8}$$

$$C_{44} = \frac{1}{S_{44}} \tag{3.9}$$

$$C_{44} = \frac{1}{S_{55}} \tag{3.10}$$

$$C_{44} = \frac{1}{S_{66}} \tag{3.11}$$

Since not all material constants within the compliance matrix are mutually independent it is necessary to introduce the reciprocity relations, as shown in Eq. 3.12, leaving nine independent constants for an orthotropic material [10,87,192].

$$\frac{\nu_{12}}{E_1}=\frac{\nu_{21}}{E_2};\quad \frac{\nu_{13}}{E_1}=\frac{\nu_{31}}{E_3};\quad \frac{\nu_{23}}{E_2}=\frac{\nu_{32}}{E_3} \tag{3.12}$$

3.1.2. Plane stress state

Assuming the plane stress state that is often attributed to the laminated structures due to the nature of their practical applications, the principal axes 1-2 are often defined within the lamina. Therefore the stress components σ_1, σ_2 and τ_{12} manifest within the lamina plane, while the perpendicular σ_3, τ_{23} i τ_{13} components can be ignored [10,87,192]. By adopting this assumption, the constitutive equation can be additionally simplified as shown in Eq. 3.13.

$$\begin{Bmatrix}\varepsilon_1\\ \varepsilon_2\\ \varepsilon_3\\ \gamma_{23}\\ \gamma_{13}\\ \gamma_{12}\end{Bmatrix}=\begin{bmatrix}S_{11} & S_{12} & S_{13} & 0 & 0 & 0\\ S_{12} & S_{22} & S_{23} & 0 & 0 & 0\\ S_{13} & S_{23} & S_{33} & 0 & 0 & 0\\ 0 & 0 & 0 & S_{44} & 0 & 0\\ 0 & 0 & 0 & 0 & S_{55} & 0\\ 0 & 0 & 0 & 0 & 0 & S_{66}\end{bmatrix}\begin{Bmatrix}\sigma_1\\ \sigma_2\\ 0\\ 0\\ 0\\ \tau_{12}\end{Bmatrix} \tag{3.13}$$

Furthermore, based on the plane stress assumption, the following expressions shown in Eq. 3.14 can also be adopted.

$$\gamma_{23}=0,\quad \gamma_{13}=0,\quad \varepsilon_3=S_{13}\sigma_1+S_{23}\sigma_2\neq 0 \tag{3.14}$$

Implementing the assumptions, a simplified constitutive relation for plane stress state can be adopted, as shown in Eq. 3.15.

$$\begin{Bmatrix}\varepsilon_1\\ \varepsilon_2\\ \gamma_{12}\end{Bmatrix}=\begin{bmatrix}S_{11} & S_{12} & 0\\ S_{12} & S_{22} & 0\\ 0 & 0 & S_{66}\end{bmatrix}\begin{Bmatrix}\sigma_1\\ \sigma_2\\ \tau_{12}\end{Bmatrix} \tag{3.15}$$

The reduced 3×3 compliance matrix, shown in Eq. 3.15, can be inverted to acquire the reduced stiffness matrix as shown in Eq. 3.16, where the matrix components are given by Eq. 3.17 to Eq. 3.20.

$$\begin{Bmatrix}\sigma_1\\ \sigma_2\\ \tau_{12}\end{Bmatrix}=\begin{bmatrix}Q_{11} & Q_{12} & 0\\ Q_{12} & Q_{22} & 0\\ 0 & 0 & Q_{66}\end{bmatrix}\begin{Bmatrix}\varepsilon_1\\ \varepsilon_2\\ \gamma_{12}\end{Bmatrix} \tag{3.16}$$

$$Q_{11}=\frac{S_{22}}{S_{11}S_{22}-S_{12}^2}=\frac{E_{11}^2}{(E_{11}+\nu_{12}E_{22})} \tag{3.17}$$

$$Q_{12}=\frac{S_{12}}{S_{11}S_{22}-S_{12}^2}=\frac{\nu_{12}E_{11}E_{22}}{(E_{11}-\nu_{12}^2E_{22})} \tag{3.18}$$

$$Q_{22}=\frac{S_{11}}{S_{11}S_{22}-S_{12}^2}=\frac{E_{11}E_{22}}{(E_{11}-\nu_{12}^2E_{22})} \tag{3.19}$$

$$Q_{66}=\frac{1}{S_{66}}=G_{12} \tag{3.20}$$

3.1.3. Laminate coordinate systems

To analyse the mechanical behaviour of a composite laminate, it is also necessary to study the contribution of each lamina. This is achieved by transforming the local 1-2-3 into global coordinate system *x-y-z*, while using standard stress-strain formulations adopted for the plane stress state [10,87,192]. Hence, if an infinitesimally small element within the 1-2-3 coordinate system is transformed to the global *x-y-z* coordinate system, its fiber direction will be closing at angle ϑ with the *x*-axis direction; the 1-2 plane will remain parallel with the *x-y* plane, and the 3-direction will remain equal to the *z* axis, as presented in Figure 3.2. The orientation angle ϑ is assumed positive if the fiber layup is arranged counter-clockwise or observed from the *x*-axis versus *y* axis direction, while negative otherwise [10,87,178,192].

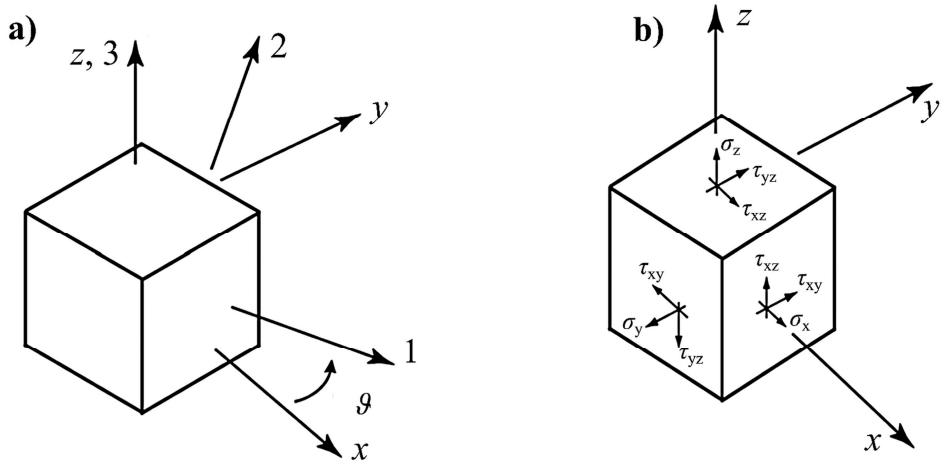

Figure 3.2 Coordinate systems of a lamina reinforced in an arbitrary direction [192]

The acquired stress and strain component can be defined as σ_x, σ_y, σ_z, τ_{yz}, τ_{xz}, τ_{xy}, and ε_x, ε_y, ε_z, γ_{yz}, γ_{xz}, γ_{xy} respectively; while applying the plane stress assumption the out-of-plane components σ_z, τ_{yz}, τ_{xz} could be reduced to zero, as shown in Eq. 3.21.

$$\begin{Bmatrix} \sigma_1 \\ \sigma_2 \\ \tau_{12} \end{Bmatrix} = \begin{bmatrix} m^2 & n^2 & 2mn \\ n^2 & m^2 & -2mn \\ -mn & mn & m^2-n^2 \end{bmatrix} \begin{Bmatrix} \sigma_x \\ \sigma_y \\ \tau_{xy} \end{Bmatrix} \tag{3.21}$$

With m=cos(θ) and n=sin(θ), and the expression can be simplified as shown in Eq. 3.22.

$$\begin{Bmatrix} \sigma_1 \\ \sigma_2 \\ \tau_{12} \end{Bmatrix} = [T] \begin{Bmatrix} \sigma_x \\ \sigma_y \\ \tau_{xy} \end{Bmatrix} \tag{3.22}$$

Where $[T]$ is the transformation matrix, with $[T]^{-1}$ being its inverted counterpart, as shown in Eq. 3.23:

$$[T] = \begin{bmatrix} m^2 & n^2 & 2mn \\ n^2 & m^2 & -2mn \\ -mn & mn & m^2-n^2 \end{bmatrix}; \qquad [T]^{-1} = \begin{bmatrix} m^2 & n^2 & -2mn \\ n^2 & m^2 & 2mn \\ mn & -mn & m^2-n^2 \end{bmatrix} \tag{3.23}$$

The inverted transformation matrix $[T]^{-1}$ is therefore adopted for conducting stress and strain component transformations, as shown in Eq. 3.24 and Eq. 3.25.

$$\begin{Bmatrix} \sigma_x \\ \sigma_y \\ \tau_{xy} \end{Bmatrix} = [T]^{-1} \begin{Bmatrix} \sigma_1 \\ \sigma_2 \\ \tau_{12} \end{Bmatrix} \tag{3.24}$$

$$\begin{Bmatrix} \varepsilon_1 \\ \varepsilon_2 \\ \frac{1}{2}\gamma_{12} \end{Bmatrix} = [T] \begin{Bmatrix} \varepsilon_x \\ \varepsilon_y \\ \frac{1}{2}\gamma_{xy} \end{Bmatrix}; \qquad \begin{Bmatrix} \varepsilon_x \\ \varepsilon_y \\ \frac{1}{2}\gamma_{xy} \end{Bmatrix} = [T]^{-1} \begin{Bmatrix} \varepsilon_1 \\ \varepsilon_2 \\ \frac{1}{2}\gamma_{12} \end{Bmatrix} \tag{3.25}$$

Accounting for the shear factor of ½, from the strain tensor in Eq. 3.25, the resulting stress and strain tensor expressions for plane stress assumption can be rewritten as shown in Eq. 3.26, respectively [192].

$$\begin{Bmatrix} \varepsilon_1 \\ \varepsilon_2 \\ \frac{1}{2}\gamma_{12} \end{Bmatrix} = \begin{bmatrix} S_{11} & S_{12} & 0 \\ S_{12} & S_{22} & 0 \\ 0 & 0 & \frac{1}{2}S_{66} \end{bmatrix} \begin{Bmatrix} \sigma_1 \\ \sigma_2 \\ \tau_{12} \end{Bmatrix}; \quad \begin{Bmatrix} \sigma_1 \\ \sigma_2 \\ \tau_{12} \end{Bmatrix} = \begin{bmatrix} Q_{11} & Q_{12} & 0 \\ Q_{12} & Q_{22} & 0 \\ 0 & 0 & 2Q_{66} \end{bmatrix} \begin{Bmatrix} \varepsilon_1 \\ \varepsilon_2 \\ \frac{1}{2}\gamma_{12} \end{Bmatrix} \tag{3.26}$$

Furthermore, the strain tensor equation Eq.3.27 is acquired by substituting Eq. 3.22 and the

first expression of Eq. 3.25 into the first expression in Eq. 3.26, and multiplying the third row by the factor of two where $\left[\overline{S}\right]$ stands for the reduced compliance matrix given by the Eq. 3.28 [192].

$$\begin{Bmatrix} \varepsilon_x \\ \varepsilon_y \\ \gamma_{xy} \end{Bmatrix} = \begin{bmatrix} \overline{S}_{11} & \overline{S}_{12} & \overline{S}_{16} \\ \overline{S}_{12} & \overline{S}_{22} & \overline{S}_{26} \\ \overline{S}_{16} & \overline{S}_{26} & \overline{S}_{66} \end{bmatrix} \begin{Bmatrix} \sigma_x \\ \sigma_y \\ \tau_{xy} \end{Bmatrix} \tag{3.27}$$

$$\left[\overline{S}\right] = \begin{bmatrix} \overline{S}_{11} & \overline{S}_{12} & \overline{S}_{16} \\ \overline{S}_{12} & \overline{S}_{22} & \overline{S}_{26} \\ \overline{S}_{16} & \overline{S}_{26} & \overline{S}_{66} \end{bmatrix} = \left[\overline{T}\right]^{-1} \begin{bmatrix} S_{11} & S_{12} & 0 \\ S_{12} & S_{22} & 0 \\ 0 & 0 & S_{66} \end{bmatrix} [T] \tag{3.28}$$

Similarly, the substitution of Eq. 3.22 and the first expression of Eq. 3.25 into the second expression of Eq. 3.26 while multiplying the third row by the factor of two, results in Eq. 3.29 where $\left[\overline{Q}\right]$ represents the reduced stiffness matrix given by the expression on Eq. 3.30 [192].

$$\begin{Bmatrix} \sigma_x \\ \sigma_y \\ \tau_{xy} \end{Bmatrix} = \begin{bmatrix} \overline{Q}_{11} & \overline{Q}_{12} & \overline{Q}_{16} \\ \overline{Q}_{12} & \overline{Q}_{22} & \overline{Q}_{26} \\ \overline{Q}_{16} & \overline{Q}_{26} & \overline{Q}_{66} \end{bmatrix} \begin{Bmatrix} \varepsilon_x \\ \varepsilon_y \\ \gamma_{xy} \end{Bmatrix} \tag{3.29}$$

$$\left[\overline{Q}\right] = \begin{bmatrix} \overline{Q}_{11} & \overline{Q}_{12} & \overline{Q}_{16} \\ \overline{Q}_{12} & \overline{Q}_{22} & \overline{Q}_{26} \\ \overline{Q}_{16} & \overline{Q}_{26} & \overline{Q}_{66} \end{bmatrix} \left[\overline{T}\right]^{-1} \begin{bmatrix} Q_{11} & Q_{12} & 0 \\ Q_{12} & Q_{22} & 0 \\ 0 & 0 & Q_{66} \end{bmatrix} [T] \tag{3.30}$$

The expressions in Eq. 3.25 and Eq. 3.27 describe the behaviour of fiber-reinforced composites in the state of plane stress when subjected to off-axis loads, with the consequent appearance of shear-extension coupling; in this case, normal stresses also cause shear strains, while shear stresses cause external strains [87,192]. As a result, the reciprocity relation between the reduced compliance and reduced stiffness tensors is conserved, as shown by expressions in Eq. 3.31.

$$\left[\overline{Q}\right] = \left[\overline{S}\right]^{-1}; \qquad \left[\overline{S}\right] = \left[\overline{Q}\right]^{-1} \tag{3.31}$$

Furthermore, the material properties acquired with respect to the 1-2-3 coordinate system of the lamina can be redefined according to the global *x-y-z* coordinate system directly from its definitions as shown on expressions from Eq. 3.32 to Eq. 3.36 [192].

$$E_{\mathrm{x}} = \frac{E_1}{m^4 + \left(\frac{E_1}{G_{12}} - 2\nu_{12}\right) n^2 m^2 + \frac{E_1}{E_2} n^4} \tag{3.32}$$

$$\nu_{\mathrm{xy}} = \frac{\nu_{12}\left(n^4 + m^4\right) - \left(1 + \frac{E_1}{E_2} - \frac{E_1}{G_{12}}\right) n^2 m^2}{m^4 + \left(\frac{E_1}{G_{12}} - 2\nu_{12}\right) n^2 m^2 + \frac{E_1}{E_2} n^2} \tag{3.33}$$

$$E_{\mathrm{y}} = \frac{E_2}{m^4 + \left(\frac{E_2}{G_{12}} - 2\nu_{21}\right) n^2 m^2 + \frac{E_2}{E_1} n^4} \tag{3.34}$$

$$\nu_{\mathrm{xy}} = \frac{\nu_{21}\left(n^4 + m^4\right) - \left(1 + \frac{E_2}{E_1} - \frac{E_2}{G_{12}}\right) n^2 m^2}{m^4 + \left(\frac{E_2}{G_{12}} - 2\nu_{21}\right) n^2 m^2 + \frac{E_2}{E_1} n^2} \tag{3.35}$$

$$G_{\mathrm{xy}} = \frac{G_{12}}{n^4 + m^4 + 2\left(\frac{2G_{12}}{E_1}\left(1 + 2\nu_{12}\right) + \frac{2G_{12}}{E_2} 1\right) n^2 m^2} \tag{3.36}$$

Additional parameters also need to be acquired for the in-plane behaviour analysis of fiber-reinforced composites. Besides the Poisson ratio, acquired as the relation between the transversal and longitudinal strains, it is also necessary to define the coefficient of mutual influence of the first and second kind, as shown in Eq. 3.37 and Eq. 3.38 respectively, where the first expression in both equations is valid for $\sigma_{\mathrm{x}} \neq 0$, $\sigma_{\mathrm{y}} = 0$, and $\sigma_{\mathrm{z}} = 0$, while the second expression is supported for, $\sigma_{\mathrm{x}} = 0$, $\sigma_{\mathrm{y}} \neq 0$, and $\sigma_{\mathrm{z}} = 0$ [192].

$$\eta_{\mathrm{x,xy}} = \frac{\varepsilon_{\mathrm{x}}}{\gamma_{\mathrm{xy}}}; \qquad \eta_{\mathrm{y,xy}} = \frac{\varepsilon_{\mathrm{y}}}{\gamma_{\mathrm{xy}}}; \tag{3.37}$$

$$\eta_{\mathrm{xy,x}} = \frac{\gamma_{\mathrm{xy}}}{\varepsilon_{\mathrm{x}}} \qquad \eta_{\mathrm{xy,y}} = \frac{\gamma_{\mathrm{xy}}}{\varepsilon_{\mathrm{y}}} \tag{3.38}$$

These coefficients can be rewritten in terms of compliance tensor components as shown in Eq. 3.39 and Eq. 3.40 [192], simplifying the computational process.

$$\eta_{\mathrm{xy,x}} = \frac{\overline{S}_{16}}{\overline{S}_{11}}; \qquad \eta_{\mathrm{xy,x}} = \frac{\overline{S}_{26}}{\overline{S}_{22}} \tag{3.39}$$

$$\eta_{\mathrm{x,xy}} = \frac{\overline{S}_{16}}{\overline{S}_{11}}; \qquad \eta_{\mathrm{y,xy}} = \frac{\overline{S}_{26}}{\overline{S}_{22}} \tag{3.40}$$

3.1.4. Geometrical characteristics of the composite laminate

Following the previous theoretical summary on the mechanical properties of a lamina, a generic laminate is usually manufactured as a layered structure composed of N layers generating a finite laminate thickness equal to H, as a sum of all the lamina thicknesses h. Since the generic laminate definition assumes equal lamina thicknesses, the thickness of the k^{th} layer is often referred as h_k [87,192]. The origin of the laminate coordinate system is usually placed in its geometric midplane, either within a particular layer or at the interface between the two middle layers. By convention, the z axis is referred as positive from $-H/2$ to $+H/2$, with the first layer having the most negative value; the laminate is built until the most positive N^{th} layer is reached [87,192]. An arbitrary layer position is therefore defined as layer k bounded by its interfaces z_{k-1} and z_k, starting from the first layer with z_0 and z_1, until the final layer with z_{N-1} and z_N is reached, as shown in Figure 3.3 a) [87,192].

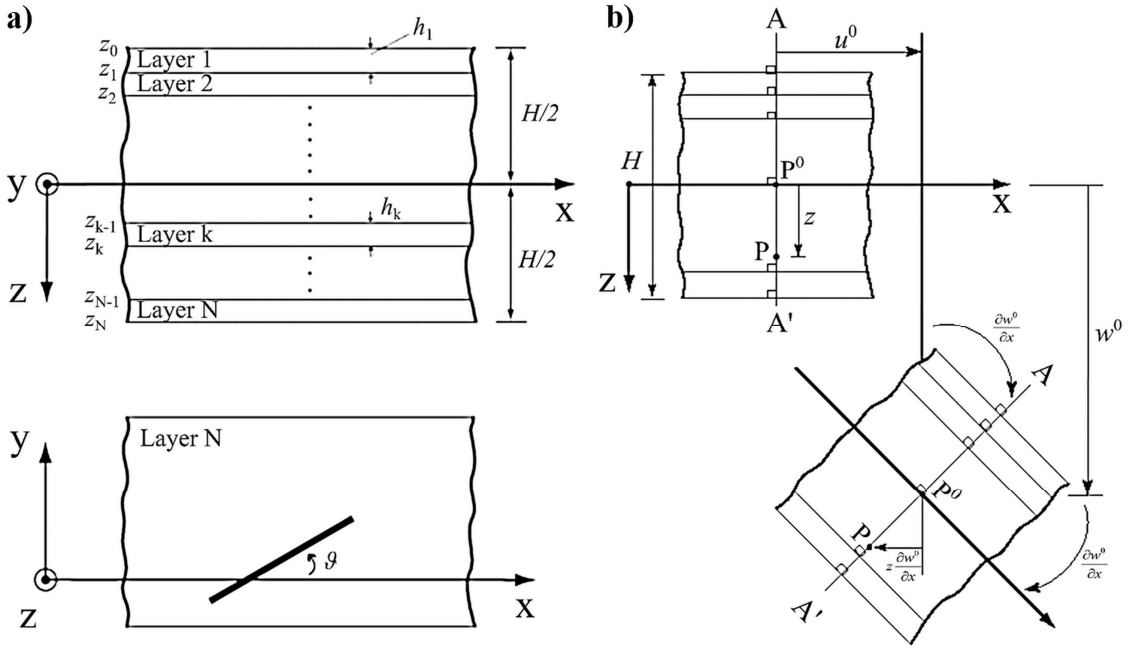

Figure 3.3 a) Laminate cross-section [192], b) Laminate in rotation [192]

Furthermore, the deformation of laminate x-z cross-section can be analysed by measuring the displacement of the point P placed at an arbitrary distance z from the point P^0 on a reference plane forming a $\overline{AA'}$ distance on which both points are situated, while the superscript value "0" represents the kinematics applied on the point P^0. The displacement in the x and y directions is defined with u^0 and w^0 respectively. The rotation of the reference surface about y axis as $\partial w^0/\partial x$, is also valid for the $\overline{AA'}$ distance due to the Kirchhoff hypothesis of perpendicularity, assuming $\partial w^0/\partial x < 1$ [192].

Based on this assumption, the sines and tangents values of these angles can be replaced with the exact values of rotations, while the cosines are equal to one. This approximation causes the translation of P^0 by the value of $z = \partial w^0/\partial x$ due to rotation, as shown in Figure 3.3 b) [192]. Therefore, the axial translation of the point $P\,(x,y,z)$ is given by the expressions in Eq. 3.41, Eq. 3.42, Eq. 3.43, respectively.

$$u(x,y,z) = u^0(x,y) - z\frac{\partial w^0(x,y)}{\partial x} \tag{3.41}$$

$$v(x,y,z) = v^0(x,y) - z\frac{\partial w^0(x,y)}{\partial y} \tag{3.42}$$

$$w(x,y,z) = w^0(x,y) \tag{3.43}$$

According to the Kirchhoff hypothesis, strains within the laminate can also be computed based on the acquired displacements, as shown in Eq. 3.44 to Eq.3.49 [192],

$$\varepsilon_{\mathrm{x}}(x,y,z) \equiv \frac{\partial u(x,y,z)}{\partial x} = \varepsilon_{\mathrm{x}}^0(x,y) - zk_{\mathrm{x}}^0(x,y) \tag{3.44}$$

$$\varepsilon_{\mathrm{y}}(x,y,z) \equiv \frac{\partial v(x,y,z)}{\partial y} = \varepsilon_{\mathrm{y}}^0(x,y) - zk_{\mathrm{y}}^0(x,y) \tag{3.45}$$

$$\varepsilon_{\mathrm{z}}(x,y,z) \equiv \frac{\partial w(x,y,z)}{\partial z} = \frac{\partial w^0(x,y,z)}{\partial z} = 0 \tag{3.46}$$

$$\gamma_{\mathrm{yz}}(x,y,z) \equiv \frac{\partial w(x,y,z)}{\partial y} + \frac{\partial v(x,y,z)}{\partial z} = \frac{\partial w^0(x,y)}{\partial y} - \frac{\partial w^0(x,y)}{\partial y} = 0 \tag{3.47}$$

$$\gamma_{\mathrm{xz}}(x,y,z) \equiv \frac{\partial w(x,y,z)}{\partial x} + \frac{\partial u(x,y,z)}{\partial z} = \frac{\partial w^0(x,y)}{\partial x} - \frac{\partial w^0(x,y)}{\partial x} = 0 \tag{3.48}$$

$$\gamma_{\mathrm{xy}}(x,y,z) \equiv \frac{\partial v(x,y,z)}{\partial x} + \frac{\partial u(x,y,z)}{\partial y} = \gamma_{\mathrm{xy}}^0 + zk_{\mathrm{xy}}^0 \tag{3.49}$$

where specific variables are introduced as abbreviations of the expressions, as shown in Eq. 3.50 to Eq. 3.56 [192], where $\varepsilon_{\mathrm{x}}^0$ is referred to as the extensional strain of the reference surface in the x direction, k_{x}^0 as the curvature of the reference surface in the x direction, $\varepsilon_{\mathrm{y}}^0$ as the reference surface extensional strain in the y direction, k_{y}^0 as the reference surface curvature in the y direction, $\varepsilon_{\mathrm{xy}}^0$ as the reference surface in-plane shear strain, and k_{xy}^0 as reference surface twisting curvature [192].

$$\varepsilon_{\mathrm{x}}^{0}\left(x,y\right)=\frac{\partial u^{0}\left(x,y\right)}{\partial x};\tag{3.50}$$

$$k_{\mathrm{x}}^{0}\left(x,y\right)=\frac{\partial^{2} w^{0}\left(x,y\right)}{\partial x^{2}}\tag{3.51}$$

$$\varepsilon_{\mathrm{y}}^{0}\left(x,y\right)=\frac{\partial v^{0}\left(x,y\right)}{\partial y}\tag{3.52}$$

$$\varepsilon_{\mathrm{y}}^{0}\left(x,y\right)=\frac{\partial v^{0}\left(x,y\right)}{\partial y}\tag{3.53}$$

$$k_{\mathrm{y}}^{0}\left(x,y\right)=\frac{\partial^{2} w^{0}\left(x,y\right)}{\partial y^{2}}\tag{3.54}$$

$$\gamma_{\mathrm{xy}}^{0}\left(x,y\right)=\frac{\partial v^{0}\left(x,y\right)}{\partial x}+\frac{\partial u^{0}\left(x,y\right)}{\partial y}\tag{3.55}$$

$$k_{\mathrm{xy}}^{0}\left(x,y\right)=-2\frac{\partial^{2} w^{0}\left(x,y\right)}{\partial x\partial y}\tag{3.56}$$

Furthermore, according to the plane stress state assumption, the strains and curvatures of the reference surface are used to calculate the stress-strain relations, as shown in Eq. 3.57 [192].

$$\begin{Bmatrix}\sigma_{\mathrm{x}}\\ \sigma_{\mathrm{y}}\\ \tau_{\mathrm{xy}}\end{Bmatrix}=\begin{bmatrix}\bar{Q}_{11} & \bar{Q}_{12} & \bar{Q}_{16}\\ \bar{Q}_{12} & \bar{Q}_{22} & \bar{Q}_{26}\\ \bar{Q}_{16} & \bar{Q}_{26} & \bar{Q}_{66}\end{bmatrix}\begin{Bmatrix}\varepsilon_{\mathrm{x}}^{0}+zk_{\mathrm{x}}^{0}\\ \varepsilon_{\mathrm{y}}^{0}+zk_{\mathrm{y}}^{0}\\ \gamma_{\mathrm{xy}}^{0}+zk_{\mathrm{xy}}^{0}\end{Bmatrix}\tag{3.57}$$

Consequently, resulting forces and moments are calculated based on the adopted stresses, as shown in expressions from Eq. 3.58 to Eq. 3.63 [192].

$$N_{\mathrm{x}}=\int_{-H/2}^{H/2}\sigma_{\mathrm{x}}dz\tag{3.58}$$

$$N_{\mathrm{y}}=\int_{-H/2}^{H/2}\sigma_{\mathrm{y}}dz\tag{3.59}$$

$$N_{\mathrm{xy}}=\int_{-H/2}^{H/2}\tau_{\mathrm{xy}}dz\tag{3.60}$$

$$M_{\mathrm{x}}=\int_{-H/2}^{H/2}\sigma_{\mathrm{x}}zdz\tag{3.61}$$

$$M_{\mathrm{y}}=\int_{-H/2}^{H/2}\sigma_{\mathrm{y}}zdz\tag{3.62}$$

$$M_{\mathrm{xy}}=\int_{-H/2}^{H/2}\tau_{\mathrm{xy}}zdz\tag{3.63}$$

Similarly, knowing the laminate stiffness matrix and the applied forces N_x, N_y i N_{xy} and moments M_x, M_y i M_{xy} shown on Figure 3.4, both cross-thickness and referent surface strains can be computed according to the strains and curvatures of the reference surface based on Eq. 3.64 and Eq. 3.65 respectively [192].

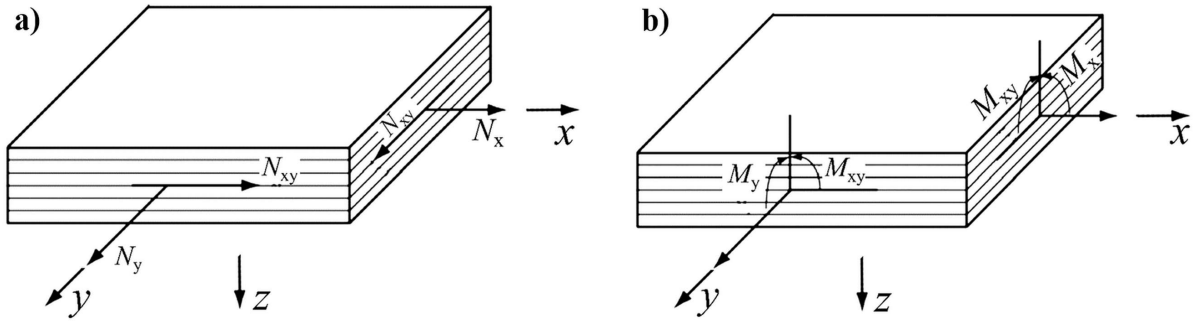

Figure 3.4 a) Forces on laminate [192], b) Moments on laminate [192]

$$\begin{Bmatrix} N_x \\ N_y \\ N_{xy} \end{Bmatrix} = \begin{bmatrix} A_{11} & A_{12} & A_{16} \\ A_{12} & A_{22} & A_{26} \\ A_{16} & A_{26} & A_{66} \end{bmatrix} \begin{Bmatrix} \varepsilon_x^0 \\ \varepsilon_y^0 \\ \gamma_{xy}^0 \end{Bmatrix} + \begin{bmatrix} B_{11} & B_{12} & B_{16} \\ B_{12} & B_{22} & B_{26} \\ B_{16} & B_{26} & B_{66} \end{bmatrix} \begin{Bmatrix} \kappa_x^0 \\ \kappa_y^0 \\ \kappa_{xy}^0 \end{Bmatrix} \tag{3.64}$$

$$\begin{Bmatrix} M_x \\ M_y \\ M_{xy} \end{Bmatrix} = \begin{bmatrix} B_{11} & B_{12} & B_{16} \\ B_{12} & B_{22} & B_{26} \\ B_{16} & B_{26} & B_{66} \end{bmatrix} \begin{Bmatrix} \varepsilon_x^0 \\ \varepsilon_y^0 \\ \gamma_{xy}^0 \end{Bmatrix} + \begin{bmatrix} D_{11} & D_{12} & D_{16} \\ D_{12} & D_{22} & D_{26} \\ D_{16} & D_{26} & D_{66} \end{bmatrix} \begin{Bmatrix} \kappa_x^0 \\ \kappa_y^0 \\ \kappa_{xy}^0 \end{Bmatrix} \tag{3.65}$$

The stiffness matrix components A_{ij}, B_{ij}, D_{ij} (i, j = 1,2,6) shown in Eq. 3.64 i 3.65 are calculated according to the expressions given in Eq. 3.66, Eq. 3.67, and Eq. 3.68 respectively.

$$A_{ij} = \sum_{k=1}^{N} \bar{Q}_{ij_k} \left(z_k - z_{k-1} \right) \tag{3.66}$$

$$B_{ij} = \frac{1}{2} \sum_{k=1}^{N} \bar{Q}_{ij_k} \left(z_k^2 - z_{k-1}^2 \right) \tag{3.67}$$

$$D_{ij} = \frac{1}{3} \sum_{k=1}^{N} \bar{Q}_{ij_k} \left(z_k^3 - z_{k-1}^3 \right) \tag{3.68}$$

To calculate the laminate constitutive response, the adopted stiffness constituents are merged into a 6×6 laminate stiffness matrix, as shown in Eq. 3.69, while its inverted expression shown in Eq. 3.70 provides the laminate compliance matrix [10,87,192].

$$\begin{Bmatrix} N_{xx} \\ N_{yy} \\ N_{xy} \\ M_{xx} \\ M_{yy} \\ M_{xy} \end{Bmatrix} = \begin{bmatrix} A_{11} & A_{12} & A_{16} & B_{11} & B_{12} & B_{16} \\ A_{12} & A_{22} & A_{26} & B_{12} & B_{22} & B_{26} \\ A_{16} & A_{26} & A_{66} & B_{16} & B_{26} & B_{66} \\ B_{11} & B_{12} & B_{16} & D_{11} & D_{12} & D_{16} \\ B_{12} & B_{22} & B_{26} & D_{12} & D_{22} & D_{26} \\ B_{16} & B_{26} & B_{66} & D_{16} & D_{26} & D_{66} \end{bmatrix} \begin{Bmatrix} \varepsilon_{xx} \\ \varepsilon_{yy} \\ \varepsilon_{xy} \\ k_{xx} \\ k_{yy} \\ k_{xy} \end{Bmatrix} \tag{3.69}$$

$$\begin{bmatrix} \varepsilon_{xx} \\ \varepsilon_{yy} \\ \varepsilon_{xy} \\ k_{xx} \\ k_{yy} \\ k_{xy} \end{bmatrix} = \begin{bmatrix} a_{11} & a_{12} & a_{16} & b_{11} & b_{12} & b_{16} \\ a_{12} & a_{22} & a_{26} & b_{12} & b_{22} & b_{26} \\ a_{16} & a_{26} & a_{66} & b_{16} & b_{26} & b_{66} \\ b_{11} & b_{12} & b_{16} & d_{11} & d_{12} & d_{16} \\ b_{12} & b_{22} & b_{26} & d_{12} & d_{22} & d_{26} \\ b_{16} & b_{26} & b_{66} & d_{16} & d_{26} & d_{66} \end{bmatrix} \cdot \begin{bmatrix} N_{xx} \\ N_{yy} \\ N_{xy} \\ M_{xx} \\ M_{yy} \\ M_{xy} \end{bmatrix} \tag{3.70}$$

3.1.5. Stacking sequence effects

According to the CLT, a laminate is considered symmetric when for each distinctive layer a counterpart with equal geometrical and mechanical properties exists at an equal distance on the opposite side of the laminate's reference surface [10,87,192]. From the mechanical perspective, the laminate symmetricity causes the stiffness components B_{ij} to be ignored, hence the laminate stiffness matrix is reduced to A_{ij} and D_{ij} only, as shown in Eq. 3.71, 3.72 and 3.73 [10,87,192].

$$\begin{Bmatrix} N_x \\ N_y \\ N_{xy} \end{Bmatrix} = \begin{bmatrix} A_{11} & A_{12} & A_{16} \\ A_{12} & A_{22} & A_{26} \\ A_{16} & A_{26} & A_{66} \end{bmatrix} \begin{Bmatrix} \varepsilon_x^0 \\ \varepsilon_y^0 \\ \gamma_{xy}^0 \end{Bmatrix} \tag{3.71}$$

$$B_{ij} = 0 \tag{3.72}$$

$$\begin{Bmatrix} M_x \\ M_y \\ M_{xy} \end{Bmatrix} = \begin{bmatrix} D_{11} & D_{12} & D_{16} \\ D_{12} & D_{22} & D_{26} \\ D_{16} & D_{26} & D_{66} \end{bmatrix} \begin{Bmatrix} \kappa_x^0 \\ \kappa_y^0 \\ \kappa_{xy}^0 \end{Bmatrix} \tag{3.73}$$

Furthermore, the laminate is considered balanced if for every distinctive layer a counterpart with equal geometrical and mechanical properties, but an opposite fiber orientation, exists at any distance on the opposite side of the laminate's reference surface [10,87,192]. This consequently ignores the influence of both A_{16} and A_{16} components. The laminate is therefore considered symmetric and balanced if both conditions are present, which breaks down the ABD matrix to a more simplified constitutive response, as defined with expressions Eq. 3.74, Eq. 3.75, Eq. 3.76 [87,192].

$$\begin{Bmatrix} N_x \\ N_y \end{Bmatrix} = \begin{bmatrix} A_{11} & A_{12} \\ A_{12} & A_{22} \end{bmatrix} \begin{Bmatrix} \varepsilon_x^0 \\ \varepsilon_y^0 \end{Bmatrix} \tag{3.74}$$

$$N_{xy} = A_{66}\gamma_{xy}^0 \tag{3.75}$$

$$\begin{Bmatrix} M_x \\ M_y \\ M_{xy} \end{Bmatrix} = \begin{bmatrix} D_{11} & D_{12} & D_{16} \\ D_{12} & D_{22} & D_{26} \\ D_{16} & D_{26} & D_{66} \end{bmatrix} \begin{Bmatrix} \kappa_x^0 \\ \kappa_y^0 \\ \kappa_{xy}^0 \end{Bmatrix} \tag{3.76}$$

Another frequently adopted LSS is in the cross-ply laminates where fiber orientation is alternated between 0° and 90° at each subsequent layer, leading to a configuration where the stiffness components A_{16}, A_{26}, B_{16}, B_{26}, D_{16} i D_{26} are ignored [87,192]. The layer stacking sequence has a direct influence on the laminate's stiffness matrix, affecting the constitutive response significantly.

3.1.6. Laminate effective properties

In the engineering application of composite laminates, it is often necessary to analyse the laminates' properties in reference to the global coordinate system. Such properties are referred as effective material properties which include [192]:

- Effective elastic modulus in *x* axis direction $\bar{E}_x$
- Effective elastic modulus in *y* axis direction $\bar{E}_y$
- Effective shear modulus in *x*-*y* plane $\bar{G}_{xy}$
- Effective Poisson's ratios $\bar{\nu}_{xy}$ and $\bar{\nu}_{yx}$

The effective mechanical properties are usually defined by considering the in-plane loading of a symmetric and balanced, or a cross-ply laminate. These LSS cases are also considered in the expressions for average stress calculations, as shown in Eq. 3.77, Eq. 3.78, and Eq. 3.79 [192].

$$\bar{\sigma}_x = \frac{1}{H}\int_{-H/2}^{H/2} \sigma_x dz \tag{3.77}$$

$$\bar{\sigma}_y = \frac{1}{H}\int_{-H/2}^{H/2} \sigma_y dz \tag{3.78}$$

$$\bar{\tau}_{xy} = \frac{1}{H}\int_{-H/2}^{H/2} \tau_{xy} dz \tag{3.79}$$

Furthermore, the expressions proposed in Eq. 3.77, Eq. 3.78, and Eq. 3.79 are comparable with the average stress values acquired through principal loads over zero-width laminate thickness, as shown Eq. 3.80, Eq. 3.81, and Eq. 3.82 [192].

$$\bar{\sigma}_{\mathrm{x}} = \frac{1}{H} N_{\mathrm{x}} \tag{3.80}$$

$$\bar{\sigma}_{\mathrm{y}} = \frac{1}{H} N_{\mathrm{y}} \tag{3.81}$$

$$\bar{\tau}_{\mathrm{xy}} = \frac{1}{H} N_{\mathrm{xy}} \tag{3.82}$$

By solving the Eq. 3.80, Eq. 3.81, and Eq. 3.82 for N_{x}, N_{y}, and N_{xy}, and substituting the results into Eq. 3.74, and Eq. 3.75, the expression in Eq. 3.83 is acquired. In this expression, the 3×3 matrix represents the stiffness matrix of a symmetric and balanced laminate, based on which the effective material properties can be extracted according to the expressions from Eq. 3.84 to Eq. 3.89 [192].

$$\begin{Bmatrix} \varepsilon_{\mathrm{x}}^{0} \\ \varepsilon_{\mathrm{y}}^{0} \\ \gamma_{\mathrm{xy}}^{0} \end{Bmatrix} = \begin{bmatrix} a_{11}H & a_{12}H & 0 \\ a_{12}H & a_{22}H & 0 \\ 0 & 0 & a_{66}H \end{bmatrix} \begin{Bmatrix} \bar{\sigma}_{\mathrm{x}} \\ \bar{\sigma}_{\mathrm{y}} \\ \bar{\tau}_{\mathrm{xx}} \end{Bmatrix} \tag{3.83}$$

$$\bar{E}_{\mathrm{x}} = \frac{1}{a_{11}H} = \frac{A_{11}A_{22} - A_{12}^{2}}{A_{22}H} \tag{3.84}$$

$$\bar{E}_{\mathrm{y}} = \frac{1}{a_{22}H} = \frac{A_{11}A_{22} - A_{12}^{2}}{A_{11}H} \tag{3.85}$$

$$\bar{G}_{\mathrm{xy}} = \frac{1}{a_{66}H} = \frac{A_{66}}{H} \tag{3.86}$$

$$\bar{\nu}_{\mathrm{xy}} = -\frac{a_{12}}{a_{11}} = \frac{A_{12}}{A_{22}} \tag{3.87}$$

$$\bar{\nu}_{\mathrm{yx}} = -\frac{a_{12}}{a_{22}} = \frac{A_{12}}{A_{11}} \tag{3.88}$$

$$\frac{\bar{\nu}_{\mathrm{xy}}}{\bar{E}_{\mathrm{x}}} = \frac{\bar{\nu}_{\mathrm{yx}}}{\bar{E}_{\mathrm{y}}} \tag{3.89}$$

All things considered, the CLT is a comprehensive tool for the accurate calculation of composite laminate material properties under the assumptions of plane stress and linear elastic response. Moreover, most damage and failure theories are developed as extensions of the capabilities of the CLT. Additionally, the initial assumptions are also a limiting factor in CLT application, especially when linear behaviour is compromised. Analogous to CLT, the first-order shear deformation theory (FSDT) also supports the assumptions of in-plane cross-section and ignores the transverse normal deformation. It accounts for the transverse shear deformability

by introducing an additional rotational degree of freedom based on the application of constant shear deformation, which induces interlaminar and discontinuous shear stresses through the laminate thickness [48]. In contrast, the higher-order shear deformation theory (HSDT) abandons the assumption of the in-plane cross section by introducing additional degrees of freedom to represent the distribution of in-plane displacements through the laminate's thickness. Therefore, a parabolic distribution of shear strains through the laminate's thickness has been proposed in [56,179], leading to a parabolic layer-wise distribution of shear stresses [48]. The ignoring of the interlaminar strains is addressed in theories which include transverse normal deformation. Such approaches are still based on HSDT, but also consider a holistic 3D constitutive law. They assume a quadratic displacement distribution through the laminate's thickness, leading to a linear strain distribution [48,108,109]. All things considered, the discussed constitutive models either ignore or simplify the through-thickness behaviour in laminated composites, hence their application is restricted to the analysis of global laminate response, while shear predictions can only be acquired in post-processing [30,48,110,140,169,193].

3.2. Micromechanical homogenization

The increasing need for fuel economy encourages the development of lightweight designs through topology optimization. This leads to the necessity for high performance engineering materials. Among the solutions, the adoption of heterogenic materials has been proven promising for tailoring the necessary material properties according to specific industrial demands. They are widely used, from cementitious materials and fiber reinforced laminates to nanocomposites and metallic foams. The applications of heterogenic materials have been increasing even more with the ready availability of additive manufacturing, where material heterogeneity is also a consequence of the manufacturing process. Since tailoring the properties for these novel materials often results from trial and error instead of an optimization process, virtual material testing is crucial. Therefore, computational homogenization theories have been developed that calculate the macroscopic properties based on the microscopic properties of the material's constituents. This avoids the necessity for an explicit definition of heterogeneity, and simplifies the numerical evaluations of heterogenic materials in engineering structures. Within this framework, the macroscopic/effective properties of solid structures are expressed by material parameters involved in the relations between stress and strain tensors [82]. The acquired relations are then adopted as local constitutive laws for structural calculations assuming homogeneity of the

studied material [82]. This satisfies the condition of statistical uniformity. To comply with these requirements, the studied domain volume has to represent the material constitution. It must be large enough to represent the constituent's heterogeneity, yet small enough in comparison to the targeted component in industrial application, hence the RVE size has to be appropriately determined. Moreover, it is also necessary to ensure independent relations between the averaged variables and the RVE position, while assuming the ergodicity of all statistical information contained in a single RVE. Therefore, the theoretical background of the proposed approach will be presented in this section. The basic assumptions of the mechanics in heterogenic media will be considered, focusing on the representation of strain and stress localization problems and their appropriate boundary conditions. Furthermore, the fundamentals of periodic boundary conditions will be investigated, focusing on the numerical procedure for their imposition in linear elasticity problems following the guidelines presented in [82] and [199].

3.2.1. Localization Problem for Elasticity

The basic concept of a representative volume element can be derived from a generic heterogenous domain $\Omega \subset \mathbb{R}^D$ containing N phases, as shown in Figure 3.5, where space dimensions are denoted as $D = 2$ and $D = 3$, while domain and phase boundaries are denoted as $\partial\Omega$ and Γ, respectively [199].

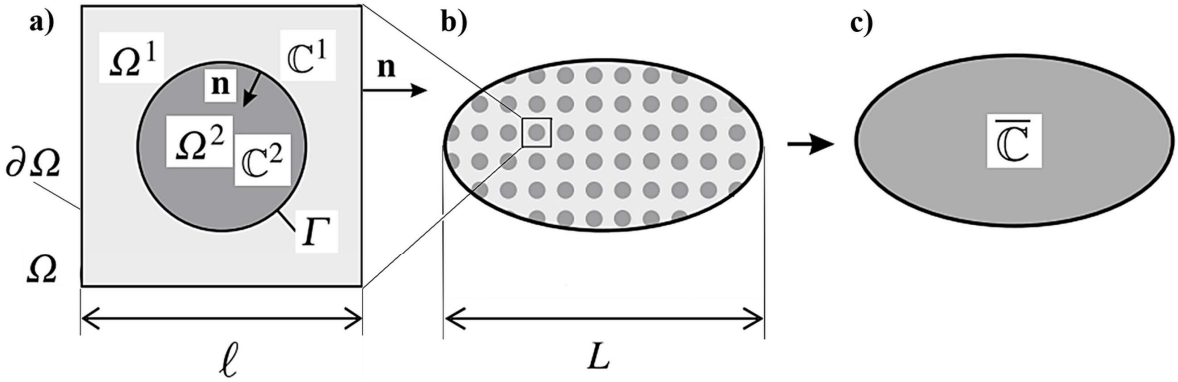

Figure 3.5 a) RVE of the heterogenic structure under consideration, b) Heterogenic domain, c) Equivalent homogenized domain; after [199]

Within this framework, the fourth-order elasticity tensor $\mathbb{C}^i$ is assumed constant in each considered material phase i. An ideal interface between the constituents is adopted which leads to continuous displacement values and traction stresses $\boldsymbol{\sigma}\mathbf{n}$ across the interface [199]. For the case of linear elasticity, the effective elastic tensor $\mathbb{C}$ of the equivalent homogeneous structure can be expressed as shown in Eq. 3.90 [199].

$$\mathbb{C}(\mathbf{x}) = \sum_{\mathrm{i}=1}^{\mathrm{N}} \chi^{\mathrm{i}}(\mathbf{x})\mathbb{C}^{\mathrm{i}} \tag{3.90}$$

The expression shown in 3.91 represents the first localization problem based on the assumption that the RVE is subjected to a homogeneous strain field $\bar{\varepsilon}$ [82,125,199].

$$\nabla \cdot \boldsymbol{\sigma}[\mathbf{u}(\mathbf{x})] = 0 \; \forall \mathbf{x} \, \epsilon \, \Omega \tag{3.91}$$

Where:

$$\boldsymbol{\sigma}[\mathbf{u}(\mathbf{x})] = \mathbb{C}(\mathbf{x}) : \boldsymbol{\varepsilon}[\mathbf{u}(\mathbf{x})] \tag{3.92}$$

$$\boldsymbol{\varepsilon}[\mathbf{u}(\mathbf{x})] = \frac{1}{2}[\nabla \mathbf{u}(\mathbf{x}) + \nabla^{\mathrm{T}}\mathbf{u}(\mathbf{x})] \tag{3.93}$$

$$\langle \boldsymbol{\varepsilon} \rangle = \bar{\boldsymbol{\varepsilon}} \tag{3.94}$$

While an alternative localization problem, as shown in Eq. 3.95, is based on the assumption that that the RVE is subjected to a homogeneous stress field $\bar{\sigma}$ [125,199]:

$$\nabla \cdot \boldsymbol{\sigma}[\mathbf{u}(\mathbf{x})] = 0 \; \forall \mathbf{x} \, \epsilon \, \Omega \tag{3.95}$$

Where:

$$\boldsymbol{\sigma}[\mathbf{u}(\mathbf{x})] = \mathbb{C}(\mathbf{x}) : \boldsymbol{\varepsilon}[\mathbf{u}(\mathbf{x})] \tag{3.96}$$

$$\langle \boldsymbol{\sigma} \rangle = \bar{\boldsymbol{\sigma}} \tag{3.97}$$

Furthermore, the strain condition presented in Eq. 3.94 is satisfied when the first localization problem is solved by enforcing the appropriate boundary conditions, assuming that the constant macroscopic strain field $\bar{\boldsymbol{\varepsilon}}$ and the local microscopic fluctuation $\tilde{\boldsymbol{\varepsilon}}$ are superpositioned into local strain field $\boldsymbol{\varepsilon}$, as shown in Eq. 3.98, leading to Eq. 3.99 after averaging [199].

$$\boldsymbol{\varepsilon}(\mathbf{x}) = \bar{\boldsymbol{\varepsilon}} + \tilde{\boldsymbol{\varepsilon}}(\mathbf{x}) \tag{3.98}$$

$$\begin{gathered} \langle \boldsymbol{\varepsilon}(\mathbf{x}) \rangle = \bar{\boldsymbol{\varepsilon}} + \langle \tilde{\boldsymbol{\varepsilon}}(\mathbf{x}) \rangle = \bar{\boldsymbol{\varepsilon}} + \frac{1}{V}\int_{\Omega} \tilde{\boldsymbol{\varepsilon}}(\mathbf{x}) d\Omega \\ \langle \boldsymbol{\varepsilon}(\mathbf{x}) \rangle = \bar{\boldsymbol{\varepsilon}} + \frac{1}{2V}\int_{\Omega} \{\nabla[\tilde{\mathbf{u}}(\mathbf{x})] + \nabla^{\mathrm{T}}[\tilde{\mathbf{u}}(\mathbf{x})]\} d\Omega \end{gathered} \tag{3.99}$$

In the Eq. 3.99, the tensor $\tilde{\mathbf{u}}$ represents the fluctuating displacement, given by Eq. 3.100, while the average value for the local strain field is acquired by applying the divergence theorem, as shown in Eq. 3.101 [199].

$$\tilde{\mathbf{u}} = \mathbf{u}(\mathbf{x}) - \bar{\boldsymbol{\varepsilon}}\mathbf{x} \tag{3.100}$$

$$\langle \boldsymbol{\varepsilon}(\mathbf{x}) \rangle = \bar{\boldsymbol{\varepsilon}} + \frac{1}{2V}\int_{\partial\Omega} [\tilde{\mathbf{u}}(\mathbf{x}) \otimes \mathbf{n} + \mathbf{n} \otimes \tilde{\mathbf{n}}(\mathbf{x})] d\Gamma \tag{3.101}$$

According to the homogeneous strain definition shown in Eq. 3.91 to 3.94, the condition $\langle \boldsymbol{\varepsilon} \rangle = \bar{\boldsymbol{\varepsilon}}$ is satisfied if the value of the integral in Eq. 3.101 is equal to zero, which leads to $\tilde{\mathbf{u}}(\mathbf{x})$

being equal to zero on the domain boundary $\partial\Omega$, while being periodic on the domain Ω. Integration of the expression in Eq. 3.99 results in "*kinematically uniform*" or "*periodic*" boundary conditions, referred to as KUBC or PBC, shown in Eq. 3.102 and Eq. 3.103 respectively [82,199].

$$\mathbf{u}(\mathbf{x}) = \bar{\boldsymbol{\varepsilon}}\mathbf{x} \; \forall \; \mathbf{x} \epsilon \; \partial\Omega \tag{3.102}$$

$$\mathbf{u}(\mathbf{x}) = \bar{\boldsymbol{\varepsilon}}\mathbf{x} + \tilde{\mathbf{u}}(\mathbf{x}) \; \forall \; \mathbf{x} \epsilon \; \partial\Omega \tag{3.103}$$

In KUBC the displacement $\mathbf{u}(\mathbf{x})$ is imposed at a distinctive point $\mathbf{x} \; \epsilon \; \partial\Omega$, while in PBC it is given over the domain boundary $\partial\Omega$. The fluctuation $\tilde{\mathbf{u}}(\mathbf{x})$ is periodic, taking the same values of two homologous points on the opposite faces of the domain parallelepiped Ω [199].
Moreover, the traction vector $\boldsymbol{\sigma}\mathbf{n}$ is antiperiodic. According to the macroscopic stress approach presented in Eq.3.98 to Eq.3.100, the statistically uniform boundary conditions (SUBC) are satisfied [82]. The traction vector is prescribed at the domain boundary, as shown in Eq. 3.104 [199].

$$\boldsymbol{\sigma}\mathbf{n} = \bar{\boldsymbol{\sigma}}\mathbf{x} \; \forall \; \mathbf{x} \epsilon \; \partial\Omega \tag{3.102}$$

3.2.2. Averaged strain and stress approach

When a simple case of two-phase composite RVE is analysed, the displacement fields in the first Ω^1 and the second domain Ω^2 are referred to as u^1 and u^2 respectively. In this case, the spatial average of the strain can be expressed as Eq. 3.103. which, using the divergence theorem, leads to Eq. 3.104 [199].

$$\frac{1}{V}\int_{\Omega} \varepsilon_{\mathrm{ij}} d\Omega = \frac{1}{2V}\int_{\Omega} \left(u_{\mathrm{i,j}} + u_{\mathrm{j,i}}\right) d\Gamma \tag{3.103}$$

$$\frac{1}{2V}\int_{\partial\Omega} \left(u_{\mathrm{i}}^{1} n_{\mathrm{j}} + u_{\mathrm{j}}^{1} n_{\mathrm{i}}\right) d\Gamma + \frac{1}{2V}\int_{\Gamma} \left\{\left[\left[u_{\mathrm{i}}\right]\right] n_{\mathrm{j}} + \left[\left[u_{\mathrm{j}}\right]\right] n_{\mathrm{i}}\right\} d\Gamma \tag{3.104}$$

Using the kinematic uniform boundary conditions (KUBC) presented in in Eq. 3.102 leads to the expression in Eq. 3.105, and applying the divergence theorem in Eq. 3.106, results in the final expression presented in Eq. 3.107, which is for the perfect interface reduced to Eq. 3.108 [82,199].

$$\frac{1}{V}\int_{\Omega} \varepsilon_{\mathrm{ij}} d\Omega = \frac{1}{2V}\int_{\partial\Omega} \left(\bar{\varepsilon}_{\mathrm{ik}} x_{\mathrm{k}} n_{\mathrm{j}} + \bar{\varepsilon}_{\mathrm{jk}} x_{\mathrm{k}} n_{\mathrm{j}}\right) d\Gamma + \frac{1}{2V}\int_{\Gamma} \left\{\left[\left[u_{\mathrm{i}}\right]\right] n_{\mathrm{j}} + \left[\left[u_{\mathrm{j}}\right]\right] n_{\mathrm{i}}\right\} d\Gamma \tag{3.105}$$

$$\frac{1}{V}\int_{\partial\Omega} \bar{\varepsilon}_{\mathrm{ik}} x_{\mathrm{k}} n_{\mathrm{j}} d\Gamma = \frac{1}{V}\int_{\Omega} \bar{\varepsilon}_{\mathrm{ik}} \frac{\partial x_{\mathrm{k}}}{\partial x_{\mathrm{j}}} d\Omega = \frac{1}{V}\int_{\Omega} \bar{\varepsilon}_{\mathrm{ik}} \delta_{kj} d\Omega = \frac{1}{V}\int_{\Omega} \bar{\varepsilon}_{\mathrm{ij}} d\Omega = \bar{\varepsilon}_{\mathrm{ij}} \tag{3.106}$$

$$\begin{aligned}\bar{\boldsymbol{\varepsilon}} &= \frac{1}{V}\int_{\Omega} \boldsymbol{\varepsilon} d\Omega - \frac{1}{2V}\int_{\Gamma} \{[[\mathbf{u}]]\otimes\mathbf{n} + \mathbf{n}\otimes[[\mathbf{u}]]\}\, d\Gamma \\ &= \frac{1}{2V}\int_{\partial\Omega} (\mathbf{u}\otimes\mathbf{n} + \mathbf{n}\otimes\mathbf{u})\, d\Gamma - \frac{1}{2V}\int_{\Gamma} \{[[\mathbf{u}]]\otimes\mathbf{n} + \mathbf{n}\otimes[[\mathbf{u}]]\} d\Gamma\end{aligned} \tag{3.107}$$

$$\bar{\boldsymbol{\varepsilon}} = \frac{1}{V}\int_{\Omega} \boldsymbol{\varepsilon} d\Omega = \frac{1}{2V}\int_{\partial\Omega} (\mathbf{u}\otimes\mathbf{n} + \mathbf{n}\otimes\mathbf{u})\, d\Gamma \tag{3.108}$$

Additionally, in cases when the presence of voids leads to an undefined strain in the second domain, the expression in Eq. 3.108 is valid. For the cases of cohesive relation between normal traction and displacement, the correction in Eq. 3.109 is applied, where *K* is referred as the interface stiffness tensor, resulting in Eq. 3.110 [199].

$$[[u_{\mathrm{i}}]] = K^{\mathrm{I}}_{\mathrm{ik}}\sigma_{\mathrm{kp}}n_{\mathrm{p}} \tag{3.109}$$

$$\bar{\varepsilon}_{\mathrm{ij}} = \frac{1}{V}\int_{\Omega} \varepsilon_{\mathrm{ij}} d\Omega = \frac{1}{2V}\int_{\Gamma} \left(K^{\mathrm{I}}_{\mathrm{ik}}\sigma_{\mathrm{kp}}n_{\mathrm{p}}n_{\mathrm{j}} + K^{\mathrm{I}}_{\mathrm{jk}}\sigma_{\mathrm{kp}}n_{\mathrm{p}}n_{\mathrm{i}}\right) d\Gamma \tag{3.110}$$

The averaging theorem from the stress perspective can be determined based on the homogenous strain field expression for $\sigma_{ij} = 0$, resulting in Eq. 3.111.

$$\frac{\partial}{\partial x_{\mathrm{j}}}(\sigma_{\mathrm{ij}}x_{\mathrm{k}}) = \sigma_{\mathrm{ij,j}}x_{\mathrm{k}} + \sigma_{\mathrm{ij}}\delta_{\mathrm{kj}} = \sigma_{\mathrm{ik}} \tag{3.111}$$

Implementing the spatial average and the divergence theorem, the expression can be rewritten as Eq. 3.112. Moreover, by adopting $\sigma^1$and σ^2 for the stress tensors in domains Ω^1 and Ω^2 respectively, the expression presented in Eq. 3.113 is acquired [199].

$$\frac{1}{V}\int_{\Omega} \sigma_{\mathrm{ij}} d\Omega = \frac{1}{V}\int_{\Omega} \frac{\partial}{\partial x_{\mathrm{j}}}(\sigma_{\mathrm{ij}}x_{\mathrm{k}})\, d\Omega = \frac{1}{V}\int_{\partial\Omega} \frac{\partial}{\partial x_{\mathrm{j}}}\sigma_{\mathrm{ij}}n_{\mathrm{j}}x_{\mathrm{k}} d\Gamma \tag{3.112}$$

$$\begin{aligned}\frac{1}{V}\int_{\Omega} \sigma_{\mathrm{ik}} d\Omega &= \frac{1}{V}\int_{\Omega^1} \sigma^1_{\mathrm{ik}} d\Omega + \frac{1}{V}\int_{\Omega^2} \sigma^2_{\mathrm{ik}} d\Omega \\ &= \frac{1}{V}\int_{\partial\Omega} \sigma^1_{\mathrm{ij}}n_{\mathrm{j}}x_{\mathrm{k}} d\Gamma + \frac{1}{V}\int_{\Gamma} \sigma^1_{\mathrm{ij}}n_{\mathrm{j}}x_{\mathrm{k}} d\Gamma - \frac{1}{V}\int_{\Gamma} \sigma^2_{\mathrm{ij}}n_{\mathrm{j}}x_{\mathrm{k}} d\Gamma\end{aligned} \tag{3.113}$$

By applying the statically uniform boundary conditions (SUBC), Eq. 3.114 is obtained, leading to the expressions presented in Eq. 3.115 and Eq. 3.116. For perfect interfaces and continuous values of normal traction across Γ, the expression is reduced to Eq. 3.117 [199].

$$\frac{1}{V}\int_{\partial\Omega} \sigma^1_{\mathrm{ij}}n_{\mathrm{j}}x_{\mathrm{k}} d\Gamma = \frac{1}{V}\int_{\partial\Omega} \bar{\sigma}^1_{\mathrm{ij}}n_{\mathrm{j}}x_{\mathrm{k}} d\Gamma = \frac{1}{V}\int_{\Omega} \left(\bar{\sigma}^1_{\mathrm{ij}}x_{\mathrm{k}}\right)_{,\mathrm{j}} d\Omega = \bar{\sigma}_{\mathrm{ik}} \tag{3.114}$$

$$\bar{\boldsymbol{\sigma}} = \frac{1}{V}\int_{\partial\Omega} \boldsymbol{\sigma} d\Omega - \frac{1}{V}\int_{\Gamma} [[\boldsymbol{\sigma}\mathbf{n}]]\otimes\mathbf{x} d\Gamma \tag{3.115}$$

$$\bar{\boldsymbol{\sigma}} = \frac{1}{V}\int_{\partial\Omega} \boldsymbol{\sigma}\mathbf{n}\otimes\mathbf{x}d\Gamma - \frac{1}{V}\int_{\Gamma} \left[[\boldsymbol{\sigma}\mathbf{n}]\right]\otimes\mathbf{x}d\Gamma \tag{3.116}$$

$$\bar{\boldsymbol{\sigma}} = \frac{1}{V}\int_{\partial\Omega} \boldsymbol{\sigma}d\Omega = -\frac{1}{V}\int_{\partial\Omega} \boldsymbol{\sigma}\mathbf{n}\otimes\mathbf{x}d\Gamma \tag{3.117}$$

Similar to the strain theorem, the perfectly rigid inclusions lead to undefined stress within the inclusion domain, but they do not undermine the validity of Eq. 3.117.

For both approaches, the equivalence between microscopic and macroscopic energy can be expressed by Hill-Mandel auxiliary axiom Eq. 3.118. The validation of the axiom, assuming both linear-elastic response and the idealistic constituent's interfaces, is given in the expression Eq. 3.119. by multiplying the Eq. 3.90 with the displacement vector **u** and integrating over the domain Ω [125,199].

$$\langle\boldsymbol{\sigma}(\mathbf{x}):\boldsymbol{\varepsilon}(\mathbf{x})\rangle = \bar{\boldsymbol{\sigma}}:\bar{\boldsymbol{\varepsilon}} \tag{3.118}$$

$$\int_{\Omega} \sigma_{\mathrm{ij,j}}u_{\mathrm{i}}d\Omega = 0 \tag{3.119}$$

The expression in Eq. 3.119 can be reframed, as shown in Eq. 3.120, which leads to Eq. 3.121 after implementing the divergence theorem [199].

$$\frac{1}{V}\int_{\Omega} \sigma_{\mathrm{ij,j}}u_{\mathrm{i}}d\Omega = \frac{1}{V}\int_{\Omega} \left(\sigma_{\mathrm{ij}}u_{\mathrm{i}}\right)_{,\mathrm{j}}d\Omega - \frac{1}{V}\int_{\Omega} \sigma_{\mathrm{ij,j}}u_{\mathrm{i,j}}d\Omega = 0 \tag{3.120}$$

$$\frac{1}{V}\int_{\partial\Omega} \sigma_{\mathrm{ij,j}}u_{\mathrm{i}}n_{\mathrm{j}}d\Gamma - \frac{1}{V}\int_{\Omega} \sigma_{\mathrm{ij}}\varepsilon_{\mathrm{ij}}d\Omega = 0 \tag{3.121}$$

Applying the KUBC boundary conditions, the final formulation Eq. 3.122, and the proof of the Hill–Mandel axiom are acquired [125,199].

$$\begin{aligned}\frac{1}{V}\int_{\Omega} \sigma_{\mathrm{ij,j}}u_{\mathrm{i}}n_{\mathrm{j}}d\Gamma &= \frac{1}{V}\int_{\Omega} \sigma_{\mathrm{ij}}\bar{\varepsilon}_{\mathrm{ik}}x_{\mathrm{k}}n_{\mathrm{j}}d\Gamma = \frac{\bar{\varepsilon}_{\mathrm{ik}}}{V}\int_{\Omega} \left(\sigma_{\mathrm{ij}}u_{\mathrm{k}}\right)_{,\mathrm{j}}d\Omega \\ &= \frac{\bar{\varepsilon}_{\mathrm{ik}}}{V}\int_{\Omega} \left(\sigma_{\mathrm{ij,j}}x_{\mathrm{k}} + \sigma_{\mathrm{ij}}\delta_{\mathrm{kj}}\right)d\Omega = \frac{\bar{\varepsilon}_{ik}}{V}\int_{\Omega} \sigma_{\mathrm{ik}}d\Omega = \bar{\varepsilon}_{\mathrm{ik}}\bar{\sigma}_{\mathrm{ik}}\end{aligned} \tag{3.122}$$

3.2.3. Effective tensor of elasticity

Confirming the linearity of the first localization problem enables its solution superposition by linear combination of six distinctive components of a 3D stress tensor, as shown in Eq. 3.123 [125,199].

$$\mathbf{u}(\mathbf{x}) = \mathbf{u}^{(11)}(\mathbf{x})\bar{\varepsilon}_{11} + \mathbf{u}^{(22)}(\mathbf{x})\bar{\varepsilon}_{22} + \mathbf{u}^{(33)}(\mathbf{x})\bar{\varepsilon}_{33} \tag{3.123}$$

$$+2\mathbf{u}^{(12)}(\mathbf{x})\bar{\varepsilon}_{12} + 2\mathbf{u}^{(13)}(\mathbf{x})\bar{\varepsilon}_{13} + 2\mathbf{u}^{(23)}(\mathbf{x})\bar{\varepsilon}_{23}$$

From the strain perspective, the first localization problem solution can be denoted by $\mathbf{u}^{(ij)}(\mathbf{x})$, where $\bar{\varepsilon}_{ij}$ represents the component of the strain $\bar{\boldsymbol{\varepsilon}}$ applied on the macro scale, as shown in Eq. 3.124, with $\mathbf{e}_i$ being the unitary basis vectors [125,199].

$$\bar{\boldsymbol{\varepsilon}} = \frac{1}{2}\left(\mathbf{e}_i \otimes \mathbf{e}_j + \mathbf{e}_j \otimes \mathbf{e}_i\right) \tag{3.124}$$

Each of the vectors $\mathbf{u}^{(11)}$, $\mathbf{u}^{(22)}$, $\mathbf{u}^{(33)}$ and $\mathbf{u}^{(12)}$, $\mathbf{u}^{(23)}$, $\mathbf{u}^{(23)}$ is acquired by solving the first localization problem for a distinctive value of $\bar{\boldsymbol{\varepsilon}}$, shown in Eq. (3.125), leading to the expression in Eq. 3.127 based on the relation defined in Eq.3.126 [199].

$$\begin{gathered}\bar{\boldsymbol{\varepsilon}} = \begin{bmatrix}1 & 0 & 0\\ 0 & 0 & 0\\ 0 & 0 & 0\end{bmatrix}, \bar{\boldsymbol{\varepsilon}} = \begin{bmatrix}0 & 0 & 0\\ 0 & 1 & 0\\ 0 & 0 & 0\end{bmatrix}, \bar{\boldsymbol{\varepsilon}} = \begin{bmatrix}0 & 0 & 0\\ 0 & 0 & 0\\ 0 & 0 & 1\end{bmatrix},\\ \bar{\boldsymbol{\varepsilon}} = \begin{bmatrix}0 & 0.5 & 0\\ 0.5 & 0 & 0\\ 0 & 0 & 0\end{bmatrix}, \bar{\boldsymbol{\varepsilon}} = \begin{bmatrix}0 & 0 & 0.5\\ 0 & 0 & 0\\ 0.5 & 0 & 0\end{bmatrix}, \bar{\boldsymbol{\varepsilon}} = \begin{bmatrix}0 & 0 & 0\\ 0 & 0 & 0.5\\ 0 & 0.5 & 0\end{bmatrix}\end{gathered} \tag{3.125}$$

$$\boldsymbol{\varepsilon}^{ij}(\mathbf{x}) = \boldsymbol{\varepsilon}\left(\mathbf{u}^{ij}\mathbf{x}\right) \tag{3.126}$$

$$\begin{aligned}\boldsymbol{\varepsilon}(\mathbf{x}) = {} & \boldsymbol{\varepsilon}^{11}(\mathbf{x})\bar{\boldsymbol{\varepsilon}}_{11} + \boldsymbol{\varepsilon}^{22}(\mathbf{x})\bar{\boldsymbol{\varepsilon}}_{22} + \boldsymbol{\varepsilon}^{33}(\mathbf{x})\bar{\boldsymbol{\varepsilon}}_{33}\\ & +2\boldsymbol{\varepsilon}^{12}(\mathbf{x})\bar{\boldsymbol{\varepsilon}}_{12} + 2\boldsymbol{\varepsilon}^{13}(\mathbf{x})\bar{\boldsymbol{\varepsilon}}_{13} + 2\boldsymbol{\varepsilon}^{23}(\mathbf{x})\bar{\boldsymbol{\varepsilon}}_{23}\end{aligned} \tag{3.127}$$

The expression in Eq. 3.127 can be abbreviated, as shown in Eq. 3.128, where the resulting fourth-order localization tensor relating micro- and macro-strains are expressed as $A_{ijkl}(\mathbf{x}) = \varepsilon_{ij}^{kl}(\mathbf{x})$ [199].

$$\boldsymbol{\varepsilon}(\mathbf{x}) = \mathbb{A}(\mathbf{x}) : \bar{\boldsymbol{\varepsilon}}\ \forall \mathbf{x}\ \epsilon\Omega \tag{3.128}$$

Applying Hooke's law, the Eq. 3.129 is acquired. By considering the space averaging, the macroscopic constitutive relationship is acquired, as shown in Eq. 3.130 [199].

$$\sigma_{pq}(\mathbf{x}) = C_{pqij}(\mathbf{x})A_{ijkl}(\mathbf{x})\bar{\varepsilon}_{kl} \tag{3.129}$$

$$\bar{\boldsymbol{\sigma}} = \bar{\mathbb{C}}^{\mathrm{KUBC/PBC}} : \bar{\boldsymbol{\varepsilon}} \tag{3.130}$$

The superscript notations "KUBC/PBC" are consistent with the adopted boundary conditions, denoting the elasticity tensor as $\bar{\mathbb{C}}^{\mathrm{KUBC}}$ or $\bar{\mathbb{C}}^{\mathrm{PBC}}$ respectively, while the expression remains unaffected. The alternative definition of the effective elasticity tenor is acquired by using the Hill-Mandel axiom on micro- and macro-mechanical energy equivalence, leading to the expression Eq. 3.131 [199].

$$\bar{\mathbb{C}}^{SUBC/PBC} = \langle \mathbb{A}^{\mathrm{T}}(\mathbf{x}) : \mathbb{C}(\mathbf{x}) : \mathbb{A}(\mathbf{x}) \rangle \tag{3.131}$$

Within the framework of computing the first localization based on the stress approach, the solution can be expanded as the linear combination of the macroscopic stress components, as shown in Eq. 3.132 [199].

$$\boldsymbol{\sigma}(\mathbf{x}) = \boldsymbol{\sigma}^{(11)}(\mathbf{x})\overline{\sigma}_{11} + \boldsymbol{\sigma}^{(22)}(\mathbf{x})\overline{\sigma}_{22} + \boldsymbol{\sigma}^{(33)}(\mathbf{x})\overline{\sigma}_{33} + \boldsymbol{\sigma}^{(12)}(\mathbf{x})\overline{\sigma}_{12} + \boldsymbol{\sigma}^{(13)}(\mathbf{x})\overline{\sigma}_{13} + \boldsymbol{\sigma}^{(23)}(\mathbf{x})\overline{\sigma}_{23} \tag{3.132}$$

The first localization problem solution can be denoted by $\boldsymbol{\sigma}^{(\mathrm{kl})}(\mathbf{x})$. Each of the vectors $\boldsymbol{\sigma}^{(11)}$, $\boldsymbol{\sigma}^{(22)}$, $\boldsymbol{\sigma}^{(33)}$ and $\boldsymbol{\sigma}^{(12)}$, $\boldsymbol{\sigma}^{(23)}$, $\boldsymbol{\sigma}^{(23)}$ is acquired by solving the first localization problem for the distinctive value of $\overline{\boldsymbol{\sigma}}$, as shown in Eq. (3.133). This leads to the expression in Eq. 3.134, where stress localization tensor $B_{\mathrm{ijkl}}(\mathbf{x})$ relates the macroscopic to microscopic stress [199].

$$\begin{gathered}\overline{\boldsymbol{\sigma}} = \begin{bmatrix}1 & 0 & 0\\ 0 & 0 & 0\\ 0 & 0 & 0\end{bmatrix}, \overline{\boldsymbol{\sigma}} = \begin{bmatrix}0 & 0 & 0\\ 0 & 1 & 0\\ 0 & 0 & 0\end{bmatrix}, \overline{\boldsymbol{\sigma}} = \begin{bmatrix}0 & 0 & 0\\ 0 & 0 & 0\\ 0 & 0 & 1\end{bmatrix},\\ \overline{\boldsymbol{\sigma}} = \begin{bmatrix}0 & 1 & 0\\ 1 & 0 & 0\\ 0 & 0 & 0\end{bmatrix}, \overline{\boldsymbol{\sigma}} = \begin{bmatrix}0 & 0 & 1\\ 0 & 0 & 0\\ 1 & 0 & 0\end{bmatrix}, \overline{\boldsymbol{\sigma}} = \begin{bmatrix}0 & 0 & 0\\ 0 & 0 & 1\\ 0 & 1 & 0\end{bmatrix}\end{gathered} \tag{3.133}$$

$$\sigma_{\mathrm{ij}}(\mathbf{x}) = \sigma_{\mathrm{ij}}^{(\mathrm{kl})}(\mathbf{x})\overline{\sigma}_{\mathrm{kl}} = B_{\mathrm{ijkl}}(\mathbf{x})\overline{\sigma}_{\mathrm{kl}} \tag{3.134}$$

Furthermore, by multiplying the expression from Eq. 3.130 with the compliance matrix $\mathbb{C}^{-1}(\mathbf{x})$, the expression shown in Eq. 3.135 is acquired. This gives the macroscopic constitutive law Eq. 3.136, after taking the spatial average over the domain Ω and applying the boundary conditions for the stress case approach $\overline{\mathbb{C}}^{\mathrm{SUBC}} = \langle \mathbb{C}^{-1}(\mathbf{x}) : \mathbb{B}(\mathbf{x}) \rangle$ [82,199].

$$\boldsymbol{\varepsilon}(\mathbf{x}) = \mathbb{C}^{-1}(\mathbf{x}) : \mathbb{B}(\mathbf{x}) : \overline{\boldsymbol{\sigma}} \tag{3.135}$$

$$\overline{\boldsymbol{\sigma}} = \overline{\mathbb{C}}^{\mathrm{SUBC}} : \overline{\boldsymbol{\varepsilon}} \tag{3.136}$$

The alternative boundary condition definition is acquired using the Hill-Mandel axiom [125], from Eq. 3.137.

$$\overline{\mathbb{C}}^{\mathrm{SUBC}} = \langle \mathbb{B}^{\mathrm{T}}(\mathbf{x}) : \mathbb{C}^{-1}(\mathbf{x}) : \mathbb{B}(\mathbf{x}) \rangle^{-1} \tag{3.137}$$

However, the authors in [125] confirmed that the effective properties acquired through the stress approach depend on the applied boundary condition, resulting in $\overline{\mathbb{C}}^{\mathrm{SUBC}} \leq \overline{\mathbb{C}}^{\mathrm{PBC}} \leq \overline{\mathbb{C}}^{\mathrm{KUBC}}$. This is caused by the positive eigenvalues acquired as $\overline{\mathbb{C}}^{\mathrm{PBC}} - \overline{\mathbb{C}}^{\mathrm{SUBC}}$ and $\overline{\mathbb{C}}^{\mathrm{KUBC}} - \overline{\mathbb{C}}^{\mathrm{PBC}}$, and not by the $\overline{\mathbb{C}}$ components. Therefore, if the domain Ω is an RVE, the effective elasticity tensor is unaffected $\overline{\mathbb{C}}^{\mathrm{SUBC}} = \overline{\mathbb{C}}^{\mathrm{PBC}} = \overline{\mathbb{C}}^{\mathrm{KUBC}}$ [199].

3.2.4. In-plane transverse effective properties

To compute the effective normal transverse and shear properties using the FEA procedure, a

practical approach according to [199] is to assume the FRP is reinforced in the *z* axis direction, hence the in-plane properties are analysed in the *x*-*y* plane, while the out-of-plane properties along the *z* axis. Considering the strain approach, the displacement solution in normal transverse in-plane case can be acquired as shown in Eq. 3.138, where $\mathbf{u}^{(ij)}(\mathbf{x})$ represents the FEA solution of the first localization problem for the macroscopic strain $\bar{\varepsilon}_{ij}$, applied through PBC or KUBC on the external nodes of the studied RVE mesh [199].

$$\mathbf{u}(\mathbf{x}) = \mathbf{u}^{(11)}(\mathbf{x})\bar{\varepsilon}_{11} + \mathbf{u}^{(22)}(\mathbf{x})\bar{\varepsilon}_{22} + \mathbf{u}^{(12)}(\mathbf{x})\bar{\varepsilon}_{12} \tag{3.138}$$

An example of three elementary problems in a 3-node plane element is presented in Figure 3.6, where each node displacement is defined as u and v with a corresponding node index 1, 2 or 3 respectively.

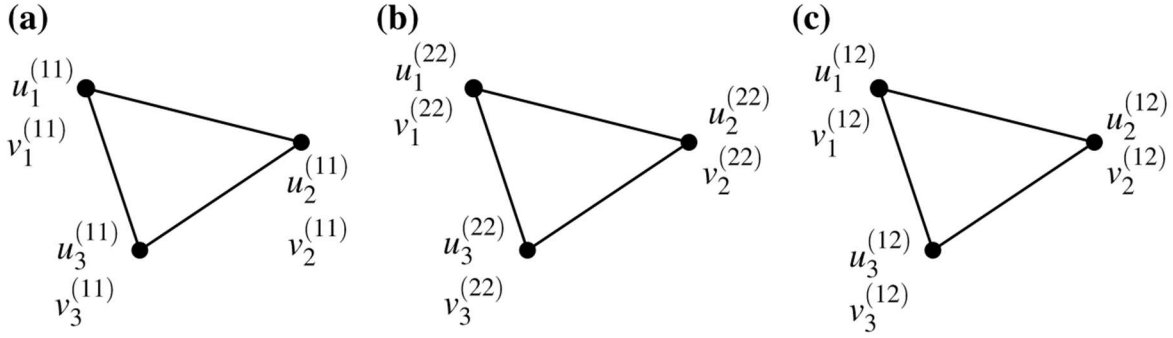

Figure 3.6 Illustrations of three elementary problems in a plane 3-node element [199]: a) $\bar{\boldsymbol{\varepsilon}} = \bar{\varepsilon}_{11}\boldsymbol{e}_1 \otimes \boldsymbol{e}_1$, b) $\bar{\boldsymbol{\varepsilon}} = \bar{\varepsilon}_{22}\boldsymbol{e}_2 \otimes \boldsymbol{e}_2$, c) $\bar{\boldsymbol{\varepsilon}} = \frac{1}{2}\bar{\varepsilon}_{12}(\boldsymbol{e}_1 \otimes \boldsymbol{e}_2 + \boldsymbol{e}_2 \otimes \boldsymbol{e}_1)$

Furthermore, the nodal solution for each of the elementary problems can be defined as a row within the combined matrix, resulting in the expression shown in Eq. 3.139 [199].

$$\mathbf{U}^{e} = \begin{bmatrix} u_1^{(11)} & u_1^{(22)} & u_1^{(12)} \\ v_1^{(11)} & v_1^{(22)} & v_1^{(12)} \\ u_2^{(11)} & u_2^{(22)} & u_2^{(12)} \\ v_2^{(11)} & v_2^{(22)} & v_2^{(12)} \\ u_3^{(11)} & u_3^{(22)} & u_3^{(12)} \\ v_3^{(11)} & v_3^{(22)} & v_3^{(12)} \end{bmatrix} \tag{3.139}$$

Furthermore, the vector for 2D plane strain is defined for each element according to Eq. 3.140 [199].

$$[\varepsilon(\mathbf{x})] = \begin{bmatrix} \varepsilon_{11}^{(11)} & \varepsilon_{11}^{(22)} & \varepsilon_{11}^{(12)} \\ \varepsilon_{22}^{(11)} & \varepsilon_{22}^{(22)} & \varepsilon_{22}^{(12)} \\ 2\varepsilon_{12}^{(11)} & 2\varepsilon_{12}^{(22)} & 2\varepsilon_{12}^{(12)} \end{bmatrix} \cdot \begin{bmatrix} \bar{\varepsilon}_{11} \\ \bar{\varepsilon}_{22} \\ 2\bar{\varepsilon}_{12} \end{bmatrix} \tag{3.140}$$

The expression can be rewritten to represent the localization tensor $\varepsilon_{ij}^{kl}(\mathbf{x})$ as $A_{ijkl}(\mathbf{x})$, where

the relation $\mathbf{A}(\mathbf{x}) = \mathbf{B}(\mathbf{x})\mathbf{U}^{\mathrm{e}}$ is valid, therefore the expression in Eq. 3.141 is acquired [199].

$$[\boldsymbol{\varepsilon}(\mathbf{x})] = \mathbf{B}(\mathbf{x})\mathbf{U}^{\mathrm{e}} \cdot \begin{bmatrix} \bar{\varepsilon}_{11} \\ \bar{\varepsilon}_{22} \\ 2\bar{\varepsilon}_{12} \end{bmatrix} \tag{3.141}$$

The Eq. 3.142 is acquired by applying the matrix form of the Hooke's law for the plane strain case, which leads to the spatial averaged expression shown in Eq. 3.143 [199].

$$[\boldsymbol{\sigma}(\mathbf{x})] = \mathbf{C}(\mathbf{x})\mathbf{B}(\mathbf{x})\mathbf{U}^{\mathrm{e}}[\bar{\boldsymbol{\varepsilon}}] \tag{3.142}$$

$$[\boldsymbol{\sigma}(\mathbf{x})] = \left(\frac{1}{V}\int_{\Omega} \mathbf{C}(\mathbf{x})\mathbf{B}(\mathbf{x})\mathbf{U}^{\mathrm{e}}\, d\Omega\right)[\bar{\boldsymbol{\varepsilon}}] \tag{3.143}$$

The two expressions for the effective elasticity tensor $\mathbf{C}^{\mathrm{KUBC/PBC}}$ in the plane strain case are presented in Eq. 3.144, and Eq. 3.145 respectively, where the KUBC/PBC index describes the prescribed boundary condition and $\mathbf{C}^{\mathrm{e}}$ is the stiffness related to the element "*e"* [199].

$$\bar{\mathbf{C}}^{\mathrm{KUBC/PBC}} = \frac{1}{V}\int_{\Omega} \mathbf{C}(\mathbf{x})\mathbf{B}(\mathbf{x})\mathbf{U}^{\mathrm{e}}\, d\Omega \tag{3.144}$$

$$\bar{\mathbf{C}}^{\mathrm{KUBC/PBC}} = \frac{1}{V}\int_{\Omega} [\mathbf{U}^{\mathrm{e}}]^{\mathrm{T}}\mathbf{B}^{\mathrm{T}}(\mathbf{x})\mathbf{C}(\mathbf{x})\mathbf{B}(\mathbf{x})\mathbf{U}^{\mathrm{e}}\, d\Omega \tag{3.145}$$

In the case of a three-node element, the expression can be reduced to Eq. 3.146 [199].

$$\bar{\mathbf{C}}^{\mathrm{KUBC/PBC}} = \frac{1}{\sum_{\mathbf{e}} A^{\mathrm{e}}}\sum_{\mathbf{e}} \mathbf{C}^{\mathrm{e}}\mathbf{B}(\mathbf{x})\mathbf{U}^{\mathrm{e}}\mathbf{A}^{\mathrm{e}} \tag{3.146}$$

Considering the stress approach, the solution of the first localization problem can be rewritten based on the superposition principle [125], leading to the expression shown in Eq. 3.147, where $\mathbf{u}^{(\mathrm{ij})}(\mathbf{x})$ represents the FEA solution of the first localization problem for the macroscopic stress component $\bar{\sigma}_{\mathrm{ij}}$, applied through the SUBC of the domain boundary $\partial\Omega$ [199].

$$\mathbf{u}(\mathbf{x}) = \mathbf{u}^{(11)}(\mathbf{x})\bar{\sigma}_{11} + \mathbf{u}^{(22)}(\mathbf{x})\bar{\sigma}_{22} + \mathbf{u}^{(12)}(\mathbf{x})\bar{\sigma}_{12} \tag{3.147}$$

Furthermore, for each of the elements the expression presented in Eq. 3.148 is acquired. Eq. 3.149 is acquired after applying the spatial average over the domain Ω, based on which the elasticity matrix is defined in Eq. 3.150 [199].

$$[\boldsymbol{\varepsilon}(\mathbf{x})] = \left[\boldsymbol{\varepsilon}^{(11)}(\mathbf{x})\right]\bar{\sigma}_{11} + \left[\boldsymbol{\varepsilon}^{(22)}(\mathbf{x})\right]\bar{\sigma}_{22} + \left[\boldsymbol{\varepsilon}^{(12)}(\mathbf{x})\right]\bar{\sigma}_{12} = \mathbf{B}(\mathbf{x})\mathbf{U}^{\mathrm{e}}[\bar{\sigma}] \tag{3.148}$$

$$[\bar{\boldsymbol{\varepsilon}}] = \left(\frac{1}{V}\int_{\Omega} \mathbf{B}(\mathbf{x})\mathbf{U}^{\mathrm{e}} d\Omega\right)[\bar{\sigma}] \tag{3.149}$$

$$\bar{\mathbf{C}}^{SUBC} = \left(\frac{1}{V}\int_{\Omega} \mathbf{B}(\mathbf{x})\mathbf{U}^{\mathrm{e}} d\Omega\right)^{-\mathbf{1}} \tag{3.150}$$

If a three-node element is considered, the above expression can be simplified as shown in Eq.

3.151, [199].

$$\bar{\mathbf{C}}^{SUBC} = \left(\frac{1}{\sum_{\mathrm{e}} V^{\mathrm{e}}} \sum_{\mathrm{e}} \mathbf{B}(\mathbf{x}) \mathbf{U}^{\mathrm{e}} \mathbf{A}^{\mathrm{e}} \right)^{-1} \tag{3.151}$$

3.2.5. Out-of-plane effective properties

Based on the previously studied concept of FRP composite reinforced in the *z* axis direction, the out-of-plane analysis along *z* axis requires the 33-component to be accounted for. By introducing the relation between the micro- and macro- strains as $\varepsilon_{33} = \bar{\varepsilon}_{33}$, the vectors for strain and stress are formulated as shown in Eq. 3.152, while the elastic tensor is extended to a 4×4 matrix as shown in Eq. 3.153 [199].

$$[\boldsymbol{\varepsilon}(\mathbf{x})] = \begin{bmatrix} \varepsilon_{11}(\mathbf{x}) \\ \varepsilon_{22}(\mathbf{x}) \\ 2\varepsilon_{12}(\mathbf{x}) \\ \varepsilon_{33}(\mathbf{x}) = \bar{\varepsilon}_{33} \end{bmatrix}, \qquad [\boldsymbol{\sigma}(\mathbf{x})] = \begin{bmatrix} \sigma_{11}(\mathbf{x}) \\ \sigma_{22}(\mathbf{x}) \\ \sigma_{12}(\mathbf{x}) \\ \sigma_{33}(\mathbf{x}) \end{bmatrix} \tag{3.152}$$

$$\mathbf{C} = \begin{bmatrix} C_{1111} C_{1122} C_{1112} C_{1133} \\ C_{1122} C_{2222} C_{2212} C_{2233} \\ C_{1112} C_{2212} C_{1212} C_{1233} \\ C_{1133} C_{2233} C_{1233} C_{3333} \end{bmatrix} \tag{3.153}$$

Due to the constant value of the component ε_{33}, the strain vector of the RVE can be defined according to the Eq. 3.154 [199].

$$[\boldsymbol{\varepsilon}(\mathbf{x})] = \begin{bmatrix} \varepsilon_{11}(\mathbf{x}) \\ \varepsilon_{22}(\mathbf{x}) \\ 2\varepsilon_{12}(\mathbf{x}) \\ 0 \end{bmatrix} + \begin{bmatrix} 0 \\ 0 \\ 0 \\ \bar{\varepsilon}_{33} \end{bmatrix} = [\boldsymbol{\varepsilon}^{\mathbf{0}}(\mathbf{x})] + \bar{\varepsilon}_{33} \begin{bmatrix} 0 \\ 0 \\ 0 \\ 1 \end{bmatrix} \tag{3.154}$$

Furthermore, the modified matrix of the shape function derivatives is introduced according to Eq. 3.155, where $\mathbf{B}^0(\mathbf{x})$ is defined as Eq. 3.156 [199].

$$[\boldsymbol{\varepsilon}^0(\mathbf{x})] = \mathbf{B}^{\mathbf{0}}(\mathbf{x}) \mathbf{u}^{\mathrm{e}}, \qquad [\delta\boldsymbol{\varepsilon}^0(\mathbf{x})] = \mathbf{B}^{\mathbf{0}}(\mathbf{x}) \delta\mathbf{u}^{\mathrm{e}} \tag{3.155}$$

$$\mathbf{B}^{\mathbf{0}}(\mathbf{x}) = \begin{bmatrix} \frac{\partial N_1}{\partial x} & 0 & \frac{\partial N_2}{\partial x} & 0 & \frac{\partial N_3}{\partial x} & 0 \\ 0 & \frac{\partial N_1}{\partial y} & 0 & \frac{\partial N_2}{\partial y} & 0 & \frac{\partial N_3}{\partial y} \\ \frac{\partial N_1}{\partial y} & \frac{\partial N_1}{\partial x} & \frac{\partial N_2}{\partial y} & \frac{\partial N_2}{\partial x} & \frac{\partial N_3}{\partial y} & \frac{\partial N_3}{\partial x} \\ 0 & 0 & 0 & 0 & 0 & 0 \end{bmatrix} \tag{3.156}$$

The expressions in Eq.3.152 and Eq. 3.153 can be rewritten in a weak form as explained in

[199], Chapter 2.2 *Linear Elasticity*. The introduction of the boundary condition leads to the expression Eq. 3.157 where the body forces $\mathbf{f}$ and traction $\mathbf{F}^*$ are ignored [199].

$$\int_{\Omega} [\boldsymbol{\varepsilon}^0(\delta\mathbf{u})]^{\mathrm{T}}\mathbf{C}(\mathbf{x})\left[\varepsilon^0(\mathbf{u}) + \bar{\varepsilon}_{33}\begin{bmatrix}0\\0\\0\\1\end{bmatrix}\right]d\Omega = 0 \tag{3.157}$$

Furthermore, the implementation of FEA discretization enables the expression to be reformulated as Eq. 3.158. After the introduction of boundary conditions and the adoption of expressions presented in Eq. 3.159 and Eq. 3.160, the equation can be reformulated as a linear system as shown in Eq. 3.161 [199].

$$\int_{\Omega} [\mathbf{B^0}(\mathbf{x})\delta\mathbf{u}^{\mathrm{e}}]^{\mathrm{T}}\mathbf{C}(\mathbf{x})[\mathbf{B^0}(\mathbf{x})\mathbf{u}^{\mathrm{e}}]d\Omega = -\bar{\varepsilon}_{33}\int_{\Omega} [\mathbf{B^0}(\mathbf{x})\delta\mathbf{u}^{\mathrm{e}}]^{\mathrm{T}}\mathbf{C}(\mathbf{x})\begin{bmatrix}0\\0\\0\\1\end{bmatrix}d\Omega \tag{3.158}$$

$$\mathbf{K} = \int_{\Omega} [\mathbf{B^0}(\mathbf{x})]^{\mathrm{T}}\mathbf{C}(\mathbf{x})\,\mathbf{B^0}(\mathbf{x})d\Omega \tag{3.159}$$

$$\mathbf{F} = -\int_{\Omega} [\mathbf{B^0}(\mathbf{x})]^{\mathrm{T}}\mathbf{C}(\mathbf{x})\begin{bmatrix}0\\0\\0\\1\end{bmatrix}d\Omega \tag{3.160}$$

$$\mathbf{K}\mathbf{u} = \bar{\varepsilon}_{33}\mathbf{F} \tag{3.161}$$

Using the Eq. 3.160, the first localization problem can be solved for $\bar{\varepsilon}_{33} = 1$, with all the other strain components being equal to zero, acquiring $\mathbf{u}^{33}$ [199]. Furthermore, the matrix of the nodal unknowns is defined for each of the elements within the FE mesh; the four elementary problems are formulated as shown in Eq. 3.162 [199].

$$\mathbf{U}^e = \begin{bmatrix} u_1^{(11)} & u_1^{(22)} & u_1^{(12)} & u_1^{(33)} \\ v_1^{(11)} & v_1^{(22)} & v_1^{(12)} & v_1^{(33)} \\ u_2^{(11)} & u_2^{(22)} & u_2^{(12)} & u_2^{(33)} \\ v_2^{(11)} & v_2^{(22)} & v_2^{(12)} & v_2^{(33)} \\ u_3^{(11)} & u_3^{(22)} & u_3^{(12)} & u_3^{(33)} \\ v_3^{(11)} & v_3^{(22)} & v_3^{(12)} & v_3^{(33)} \end{bmatrix} \tag{3.162}$$

The strain vector in each element can be expressed as Eq. 3.165, assuming that both $[\bar{\boldsymbol{\varepsilon}}]$ and the relation between $[\bar{\boldsymbol{\varepsilon}}]$ and $\bar{\varepsilon}_{33}$ are acquired according to Eq. 3.164 and assembled into the strain vector expression, as presented in Eq. 3.163 [199].

$$[\boldsymbol{\varepsilon}(\mathbf{x})] = \mathbf{B^0}(\mathbf{x})\mathbf{U}^{\mathrm{e}}[\bar{\boldsymbol{\varepsilon}}] \tag{3.163}$$

$$[\bar{\boldsymbol{\varepsilon}}] = \begin{bmatrix} \bar{\varepsilon}_{11} \\ \bar{\varepsilon}_{22} \\ 2\bar{\varepsilon}_{12} \\ \bar{\varepsilon}_{33} \end{bmatrix}, \quad \begin{bmatrix} 0 \\ 0 \\ 0 \\ 1 \end{bmatrix} \bar{\varepsilon}_{33} = \begin{bmatrix} 0 & 0 & 0 & 0 \\ 0 & 0 & 0 & 0 \\ 0 & 0 & 0 & 0 \\ 0 & 0 & 0 & 1 \end{bmatrix} [\bar{\boldsymbol{\varepsilon}}] \tag{3.164}$$

$$[\boldsymbol{\varepsilon}(\mathbf{x})] = [\boldsymbol{\varepsilon}^0(\mathbf{x})] + \begin{bmatrix} 0 & 0 & 0 & 0 \\ 0 & 0 & 0 & 0 \\ 0 & 0 & 0 & 0 \\ 0 & 0 & 0 & 1 \end{bmatrix} [\bar{\boldsymbol{\varepsilon}}] = \left[\mathbf{B}^{\mathbf{0}}(\mathbf{x}) \mathbf{U}^{\mathrm{e}} + \begin{bmatrix} 0 \\ 0 \\ 0 \\ 1 \end{bmatrix} \right] [\bar{\boldsymbol{\varepsilon}}] \tag{3.165}$$

The acquired expression can be abbreviated according to Eq. 3.166, from which the elastic tensor with the addition of $\bar{C}_{33}$ component can be expressed as Eq. 3.167 [199]:

$$[\bar{\boldsymbol{\sigma}}] = \bar{\mathbf{C}} [\bar{\boldsymbol{\varepsilon}}] \tag{3.166}$$

$$\bar{\mathbf{C}}^{KUBC} = \frac{1}{V} \int_{\Omega} \mathbf{C}(\mathbf{x}) \left[\mathbf{B}^{\mathbf{0}}(\mathbf{x}) \mathbf{U}^{\mathrm{e}} + \begin{bmatrix} 0 \\ 0 \\ 0 \\ 1 \end{bmatrix} \right] d\Omega \tag{3.167}$$

3.2.6. Periodic Boundary Conditions

One of the methods of prescribing the PBCs on the unit cell is by using Lagrange multipliers. For a 2D case of linear elasticity, the corresponding expressions Eq. 3.168 and Eq. 3.169 can be formulated by considering the node pairs (α and β) located on the opposite faces of the unit cell [199].

$$u_{\mathrm{i}}(\mathbf{x}^{\alpha}) = \bar{\varepsilon}_{\mathrm{ij}} x_{\mathrm{j}}^{\alpha} + \tilde{u}_{\mathrm{i}}(\mathbf{x}^{\alpha}) \tag{3.168}$$

$$u_{\mathrm{i}}(\mathbf{x}^{\beta}) = \bar{\varepsilon}_{\mathrm{ij}} x_{\mathrm{j}}^{\beta} + \tilde{u}_{\mathrm{i}}(\mathbf{x}^{\beta}) \tag{3.169}$$

Since the periodic boundary conditions, presented in Eq. 3.103, define the equality of displacements at the domain boundary, Eq. 3.170 and Eq. 3.103 can be reformulated as Eq. 3.171 [199].

$$\tilde{u}_{\mathrm{i}}(\mathbf{x}^{\alpha}) = \tilde{u}_{\mathrm{i}}(\mathbf{x}^{\beta}) \tag{3.170}$$

$$u_{\mathrm{i}}(\mathbf{x}^{\alpha}) - u_{\mathrm{i}}(\mathbf{x}^{\beta}) = \bar{\varepsilon}_{\mathrm{ij}} \left(x_{\mathrm{j}}^{\alpha} - x_{\mathrm{j}}^{\beta} \right) \tag{3.171}$$

Furthermore, discretization is achieved by prescribing the constraints equations using the Lagrange multiplier method, as shown in Eq. 3.172 [199].

$$C_{\mathrm{i}}^{\alpha\beta} = u_{\mathrm{i}}^{\alpha} - u_{\mathrm{i}}^{\beta} - \bar{\varepsilon}_{\mathrm{ij}} \left(x_{\mathrm{j}}^{\alpha} - x_{\mathrm{j}}^{\beta} \right) = R^{\alpha\beta} = 0 \tag{3.172}$$

In the equation, the notations α and β indicate the node couples located on the opposite side of the unit cell [199], as illustrated in Figure 3.7.

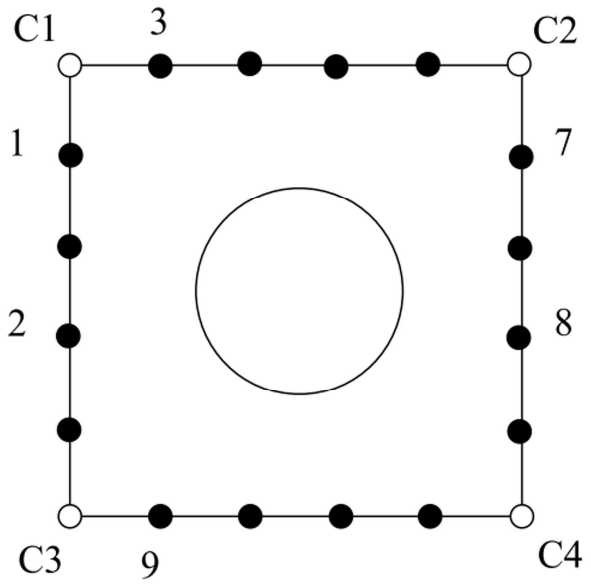

Figure 3.7 Example of node pairs in PBC, [199]

Each nodal couple is prescribed with two constraint equations formulated as Eq. 3.173, where matrix **P** relates the coupled nodes indices $\{1,7\},\{2,8\},\{3,9\}$, ... to the whole set of i-node indices [199].

$$C_{\mathrm{i}}^{\alpha\beta} = P_{\mathrm{ij}} u_{\mathrm{j}} - R_{\mathrm{i}}^{\alpha\beta} = 0 \tag{3.173}$$

Furthermore, the constraint minimization can be formulated according to the Eq. 3.174, where $\mathbf{u}$ represents the global vector of displacement unknowns, and n_{c} is the number of constraint equations [199].

$$\inf_{\substack{\mathbf{u} \\ C_{\mathrm{i}}=0, \mathrm{i}=1,\ldots,n_{\mathrm{c}}}} \frac{1}{2}\mathbf{u}^{\mathrm{T}} \cdot \mathbf{K}\mathbf{u} \tag{3.174}$$

If a Lagrange multiplier $\boldsymbol{\Lambda}$ associated with the periodic constraints is introduced, the equation is reformulated as Eq. 3.175. This leads to a saddle-point problem for the unconstrained minimization Eq. 3.176, with the stationary of $\mathcal{L}$ acquired according to Eq. 3.177, where $D_{\delta\mathbf{u}}$ and $D_{\delta\boldsymbol{\Lambda}}$ stand for Gateaux directional derivative [199].

$$\mathcal{L} = \frac{1}{2}\mathbf{u}^{\mathrm{T}} \cdot \boldsymbol{\Lambda} \cdot (\mathbf{P}\mathbf{u} - \mathbf{R}) \tag{3.175}$$

$$\{\mathbf{u}, \boldsymbol{\Lambda}\} = \inf_{\mathbf{u}} \sup_{\boldsymbol{\lambda}} \mathcal{L} \tag{3.176}$$

$$\begin{cases} D_{\delta\mathbf{u}}\mathcal{L} = 0 \\ D_{\delta\boldsymbol{\Lambda}}\mathcal{L} = 0 \end{cases} \tag{3.177}$$

The expression presented in Eq. 3.178 is obtained when the stationary of $\mathcal{L}$ is acquired, but before the Dirichlet boundary conditions are introduced [199], where **K** represents the elasticity matrix after discretization.

$$\begin{cases} \delta\mathbf{u} \cdot \mathbf{K}\mathbf{u} + \mathbf{\Lambda} \cdot \mathbf{P}\delta\mathbf{u} = \mathbf{0} \\ \delta\mathbf{\Lambda} \cdot \mathbf{P}\mathbf{u} = \delta\mathbf{\Lambda} \cdot \mathbf{R} \end{cases} \tag{3.178}$$

Utilizing the random nature of $\delta\mathbf{u}$ and $\delta\mathbf{\Lambda}$, the acquired set of equations can be reformulated as a linear system, as shown in Eq. 3.179 [199].

$$\begin{bmatrix} \mathbf{K} & \mathbf{P}^{\mathrm{T}} \\ \mathbf{P} & 0 \end{bmatrix} \begin{bmatrix} \mathbf{u} \\ \mathbf{\Lambda} \end{bmatrix} = \begin{bmatrix} 0 \\ \mathbf{R} \end{bmatrix} \tag{3.179}$$

Considering the illustration presented in Figure 3.7, the unknowns can be assumed to be ordered in a vector form, as shown in Eq. 3.180, where u^{i}, and v^{i} represent the displacements as point "*i"* in *x* and *y* directions, respectively [199].

$$\mathbf{q} = [u^1 \;\; v^1 \;\; u^2 \;\; v^2 \;\; u^3 \;\; v^3 \;\; u^4 \;\; v^4 \;\; u^5 \;\; v^5 \;\; u^6 \;\; v^6 \;\; u^7 \;\; v^7 \;\; u^8 \;\; v^8 \;\; u^9 \;\; v^9] \tag{3.180}$$

Therefore, the components in each line of **P** matrix acquire values of "-1", "0", or "1", where the degrees of freedom associated with the node couples in the global vector of unknowns are represented as i^{th} and j^{th} rows, which acquire values "1" and "-1" respectively for each of matrix lines [199]. Consequently, if a simple case of two node couples, for example $\{1,7\}$ and $\{3,9\}$, is considered, the **P** matrix can be formulated as Eq. 3.181, with the vector **R** as Eq. 3.182.

$$\mathbf{P} = \begin{bmatrix} 1 & 0 & 0 & 0 & 0 & 0 & 0 & 0 & 0 & 0 & 0 & 0 & -1 & 0 & 0 & 0 & 0 & 0 \\ 0 & 1 & 0 & 0 & 0 & 0 & 0 & 0 & 0 & 0 & 0 & 0 & 0 & -1 & 0 & 0 & 0 & 0 \\ 0 & 0 & 0 & 0 & 1 & 0 & 0 & 0 & 0 & 0 & 0 & 0 & 0 & 0 & 0 & 0 & -1 & 0 \\ 0 & 0 & 0 & 0 & 0 & 1 & 0 & 0 & 0 & 0 & 0 & 0 & 0 & 0 & 0 & 0 & 0 & -1 \end{bmatrix} \tag{3.181}$$

$$\mathbf{R} = \begin{bmatrix} \bar{\varepsilon}_{11}(x^1 - x^7) + \bar{\varepsilon}_{12}(y^1 - y^7) \\ \bar{\varepsilon}_{21}(x^1 - x^7) + \bar{\varepsilon}_{22}(y^1 - y^7) \\ \bar{\varepsilon}_{11}(x^3 - x^9) + \bar{\varepsilon}_{12}(y^3 - y^9) \\ \bar{\varepsilon}_{21}(x^3 - x^9) + \bar{\varepsilon}_{22}(y^3 - y^9) \end{bmatrix} \tag{3.182}$$

Additionally, it is also necessary to sort and include the corner nodes into their associated pairs. However, if all the associated pairs of corner nodes are included into the minimization equation 3.174, the resulting system becomes over-constrained [199]. Therefore, it is recommended to reduce the number of corner node couples. In a 2D case presented in Figure 3.7 it leads to: $\{C1, C2\}$, $\{C1, C3\}$, $\{C2, C3\}$ [199]. Even so, to avoid the possibility of poor system conditioning, due to the potential order equality between the **P** and **K** caused by the unitary terms in **P**, the system in Eq. 3.179 is reformulated as 3.183, where α_{norm} is a normalization parameter acquired according to Eq. 3.184 [199].

$$\begin{bmatrix} \mathbf{K} & \alpha_{\mathrm{norm}}\mathbf{P}^{\mathrm{T}} \\ \alpha_{\mathrm{norm}}\mathbf{P} & 0 \end{bmatrix} \begin{bmatrix} \mathbf{T} \\ \mathbf{\Lambda} \end{bmatrix} = \begin{bmatrix} 0 \\ \alpha_{\mathrm{norm}}\mathbf{R} \end{bmatrix} \tag{3.183}$$

$$\alpha_{\mathrm{norm}} = \max_{\mathrm{i,j}} \{K_{\mathrm{ij}}\} \tag{3.184}$$

The mathematical foundation of heterogenic material homogenization has been summarized

according to [199] and presented in this subsection. Positive and negative effects of the process are highlighted. According to the authors' guidelines [141,143,199], a homogenization procedure with periodic domain boundaries and strains applied through Dirichlet's boundary has been adopted in this thesis. These assumptions have been implemented in the FEA framework with the addition of cohesive contact interfaces between the constituents.

3.3. Puck's failure theory

Fracture in fiber-reinforced polymer composites typically occurs suddenly without major plastic strains. This brittle failure can be observed on the lamina scale; the fracture mechanisms initiate at the microscale and progress over laminar to interlaminar delamination, leading to the final macroscale fracture. Hence, a fracture hypothesis predicting multiple fracture states based on the few known parameters is necessary [48]. Due to the orthotropic nature of the FRP lamina, fracture theories tend to treat the fiber and matrix fractures with different criteria based on theoretical assumptions and measurable experimental data [156]. Hence, this section will be dedicated to the theoretical fundamentals of Puck's stress-based fracture theory, beginning with a brief introduction to failure hypothesis, while also addressing the distinctions between the fiber and inter-fiber criteria, and elaborating the fracture plane definition. In conclusion, the application and validation of Puck's theory will be addressed.

3.3.1. Failure theory fundamentals

In order to determine if an arbitrary applied load leads to lamina failure, the resulting stress is checked against the adopted hypotheses which encompass all the possible states of fracture. These hypotheses, also referred to as fracture criteria, give the statements on multiple fracture states based on a small number of experimentally determinable states referred to as basic strengths or basic strains, depending on which the failure theory is based. Analyzing the UD FRP composites, four distinctive basic strengths, based on the loads applied longitudinally ($\parallel$) and perpendicularly ($\perp$) to the fiber direction in tension (t) and compression (c), could be extracted as $R_{\parallel}^{\mathrm{t}}$, $R_{\perp}^{\mathrm{t}}$, $R_{\parallel}^{\mathrm{c}}$, and $R_{\perp}^{\mathrm{c}}$, while two more are acquired based on the applied in-plane and out-of-plane shear loads as $R_{\perp\parallel}$ and $R_{\perp\perp}$, respectively [48]. Therefore, a fracture criterion defines a closed surface within the six-dimensional stress space ($\sigma_1, \sigma_2, \sigma_3, \tau_{12}, \tau_{13}, \tau_{23}$), and should contain all the experimentally acquired basic stresses, while predicting the other stress

combinations with reasonable accuracy [48]. Considering these requirements, a fracture criterion is fundamentally hypothetical, hence it could be based on pure mathematical surface definition, or on physical foundations of fracture mechanics, and consequently validated or disproven by further experimental investigations. Regarding the analysis of fiber-reinforced composites, Puck's theory is the first among the physically-based fracture theories to have advantages over mathematically-based that are being confirmed through multiple studies [48,49,92,183]. The visualization of fracture criteria for plane stress load cases is presented in Figure 3.8, where a) shows the global stress-based criteria proposed by Tsai-Hill and Tsai-Wu in the $(\sigma_1, \sigma_2, \tau_{12})$ stress space, while b) shows the result of an action plane-related criteria proposed by Puck. This consists of two sub-surfaces defining the fiber and the inter-fiber fracture criteria, represented as end faces and the lateral surface, respectively [48]. This division is the key feature of Puck's fracture theory since it enables a distinctive response to the significant mechanical differences between both fracture types [48,190].

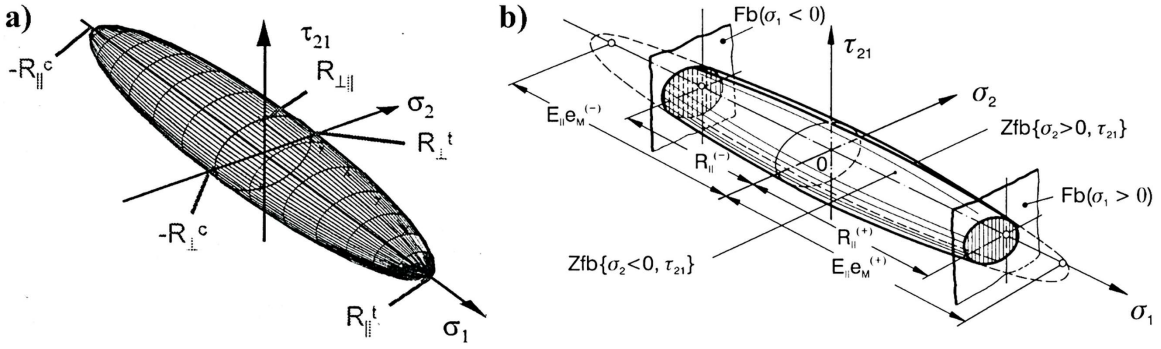

Figure 3.8 Facture criteria visualization: a) Tsai-Hill, Tsai-Wu global stress-based fracture criteria, b) Puck's action plane-related criteria [48]

3.3.2. Fiber fracture criteria

According to the material behaviour mechanics, the fiber fracture is caused by stressing $\sigma_{\parallel}$ parallel to the fiber direction, hence for in-plane stress state $(\sigma_1, \sigma_2, \tau_{12})$ the maximum stress formulation is valid [97,190]. Therefore, a physically based hypothesis (3.100) has been proposed in [155,193], postulating that fiber fracture under multiaxial stresses in unidirectional lamina occurs when stress parallel to the fiber direction is equal or greater than the stress necessary to achieve fracture under uniaxial stress σ_1, as shown in Eq. 3.85. and Eq. 3.86.

$$\frac{\sigma_1}{R_{\parallel}^{\mathrm{t}}} = 1 \quad \text{if: } \sigma_1 > 0 \tag{3.85}$$

$$\frac{\sigma_1}{-R_{\parallel}^{\mathrm{c}}} = 1 \quad \text{if: } \sigma_1 < 0 \tag{3.86}$$

In these expressions, σ_1 is the tensile stress, while the material tensile and compressive strengths are referred as $R_{\parallel}^{\mathrm{t}}$ and $-R_{\parallel}^{\mathrm{c}}$ respectively, depending on the nature of the applied load. Consequently, if σ_1 reaches the material strength, the failure criterion is fulfilled [97]. These failure conditions are reformulated to a fracture criterion by expressing the variable of stress exposure $f_{\mathrm{E,FF}}$, as shown in Eq. 3.87 and Eq. 3.88, resulting in the formulation for preliminary analyses [97,190].

$$f_{\mathrm{E,FF}} = \frac{\sigma_1}{R_{\parallel}^{\mathrm{t}}} \quad \text{if: } \sigma_1 > 0 \tag{3.87}$$

$$f_{\mathrm{E,FF}} = \frac{\sigma_1}{-R_{\parallel}^{\mathrm{c}}} \quad \text{if: } \sigma_1 < 0 \tag{3.88}$$

However, a more accurate analysis is required to account for the secondary increase of micro-mechanical strain ε_1 in fiber direction due to the influence of uniaxial stresses σ_2, and σ_3 [97]. Moreover, the stress within the matrix is not homogenously distributed, leading to local extrema and effectively larger stress values than σ_2 or σ_3 on a lamina level. Analogous to a model with serially connected springs, a transversely stressed thin UD lamina experiences a load transfer through the matrix or fiber material alone. Consequently, the stress σ_2 is equal in both the fiber and the matrix material, while the micro-mechanical strain differs due to the variant material stiffness. Since the interface load is carried by the fibers alone, a biaxial strain is generated near the fiber/matrix interface. This additional effect is accounted for by the stress magnification factor $m_{\sigma,\mathrm{f}}$, adopting the proposed values as 1.1 and 1.3 for carbon and glass reinforced polymers respectively; its distinction originates from the difference in the transverse Young's modulus of the fiber [155]. All things considered, a more sophisticated fiber fracture (FF) hypothesis had been proposed in [155,159,160]. According to this hypothesis, if a UD lamina is subjected to combined stresses, the fiber fracture (FF) will occur when the value of stress $\sigma_{1\mathrm{f}}$ equals the stress in fibers achieved through the applied uniaxial tensile $\sigma_{1\mathrm{t}}$, or compressive $\sigma_{1\mathrm{c}}$ stress, respectively [97,190]. The initial step is the calculation of the strain of the fibers $\varepsilon_{1\mathrm{f}}$, caused by the combined stresses σ_1,σ_2, σ_3, is shown in Eq. 3.189.

$$\varepsilon_{1\mathrm{f}} = \frac{\sigma_{1\mathrm{f}}}{E_{\parallel\mathrm{f}}} - \frac{\nu_{\parallel\perp\mathrm{f}}}{E_{\perp\mathrm{f}}} \cdot m_{\sigma\mathrm{f}} \cdot (\sigma_2 + \sigma_3) \tag{3.189}$$

Assuming $\nu_{\parallel\perp\mathrm{f}}/E_{\perp\mathrm{f}} = \nu_{\parallel\perp\mathrm{f}}/E_{\parallel\mathrm{f}}$ and $\varepsilon_{1\mathrm{f}} = \varepsilon_1$, the stress equation can be rewritten as shown in Eq. 3.190.

$$\sigma_{1\mathrm{f}} = E_{\parallel\mathrm{f}} \cdot \varepsilon_1 + \nu_{\parallel\perp\mathrm{f}} \cdot m_{\sigma\mathrm{f}} \cdot (\sigma_2 + \sigma_3) \tag{3.190}$$

Furthermore, if the strain ε_1 and the stress $\sigma_{1\mathrm{f}}$ are replaced with the elastic law and the fracture

resistance $R_{\parallel}$ of the UD-lamina respectively, the expression can be reformulated as shown in Eq. 3.191 and Eq. 3.192, where $\varepsilon_{\parallel}$ is the fracture strain from the uniaxial $\sigma_1$of both fiber and UD lamina.

$$\varepsilon_1 = \frac{\sigma_1}{E_{\parallel}} - \frac{\nu_{\parallel\perp}}{E_{\parallel}} \cdot (\sigma_2 + \sigma_3) \tag{3.191}$$

$$R_{\parallel \mathrm{f}} = E_{\parallel \mathrm{f}} \cdot \varepsilon_{\parallel}; \quad R_{\parallel} = E_{\parallel} \cdot \varepsilon_{\parallel} \tag{3.192}$$

The acquired expressions lead to the development of fiber-fracture criteria for the UD lamina, as shown in Eq. 3.193, where $R_{\parallel}^{t}$ and $-R_{\parallel}^{c}$ are implemented for tensile and compressive cases respectively.

$$\frac{1}{\pm R_{\parallel}^{\mathrm{t,c}}}\left[\sigma_1 - \left(\nu_{\parallel\perp} - \nu_{\parallel\perp \mathrm{f}} \cdot m_{\sigma \mathrm{f}} \frac{E_{\parallel}}{E_{\parallel \mathrm{f}}}\right)(\sigma_2 + \sigma_3)\right] = 1 \tag{3.193}$$

The acquired homogenous fracture criteria can be rewritten to formulate a stress exposure expression $f_{\mathrm{E,FF}}$, as presented in Eq. 3.194 [97,190].

$$f_{\mathrm{E,FF}} = \frac{1}{\pm R_{\parallel}^{\mathrm{t,c}}}\left[\sigma_1 - \left(\nu_{\parallel\perp} - \nu_{\parallel\perp \mathrm{f}} \cdot m_{\sigma \mathrm{f}} \frac{E_{\parallel}}{E_{\parallel \mathrm{f}}}\right)(\sigma_2 + \sigma_3)\right] \tag{3.194}$$

In the above equation, $\nu_{\parallel\perp}$ and $\nu_{\parallel\perp \mathrm{f}}$ are referred to as Poisson's ratios of UD lamina and fiber respectively. Similarly, the longitudinal moduli for UD lamina and fiber are defined as $E_{\parallel}$ and $E_{\parallel \mathrm{f}}$ respectively, while the stress magnification factor is given by $m_{\sigma \mathrm{f}}$. The influence of shear stress on fiber fracture in compressive cases has been discussed in [152,175], concluding that the shear stressing reduces compressive strength of the UD lamina. Additional research has been conducted in [158], confirming that shear stress causes the reduction in fracture strength due to microstructural damage after a critical threshold is reached. No further influences of fiber fracture are considered in the maximum stress criteria. However, in the inter-fiber fracture (IFF) hypothesis, the influence of the adjacent lamina on the FF is accounted for, leading to a more complex process of failure analysis [97,190].

3.3.3. Inter-fiber fracture criteria

The fracture limits of transverse and shear stress (σ_2, τ_{21}) combinations shown in Figure 3.9, were studied in [43].

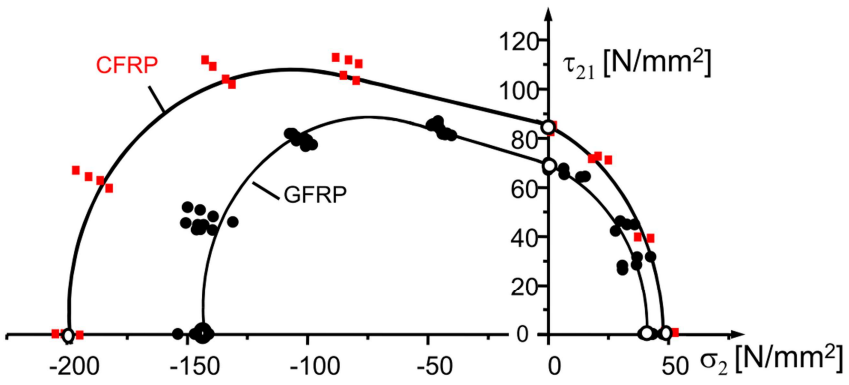

Figure 3.9 Simultaneous fracture limits of transverse and shear stress (σ_2, τ_{21}) [97]

The simultaneous interaction between stresses σ_2^t and τ_{21} has been experimentally proven by observing the failures occurring before $\sigma_2^t = R_\perp^t$ or $\tau_{21} = R_{\perp\parallel}$ is reached respectively [97]. Moreover, the compressive stress has a beneficial effect on shear-fracture strength, hence a higher limit of shear stress could be reached if a shear-loaded component is simultaneously subjected to an additional moderate amount of compressive stress. It was also observed that when stress ratio $|\sigma_2^c/\tau_{21}|$ in a component under simultaneous compressive transverse and shear loads reaches a certain value, the fracture occurs under a fracture angle θ_{fp} that is different than zero. If the ratio $|\sigma_2^c/\tau_{21}|$ is increased, the fracture angle grows until the value of $\pm 54°$ is reached in the case of pure transverse compression [97,190]. As shown in Figure 3.10, the failure envelope consists of three distinctive failure modes and, due to its unsymmetrical shape, can't be modelled using the global failure criteria.

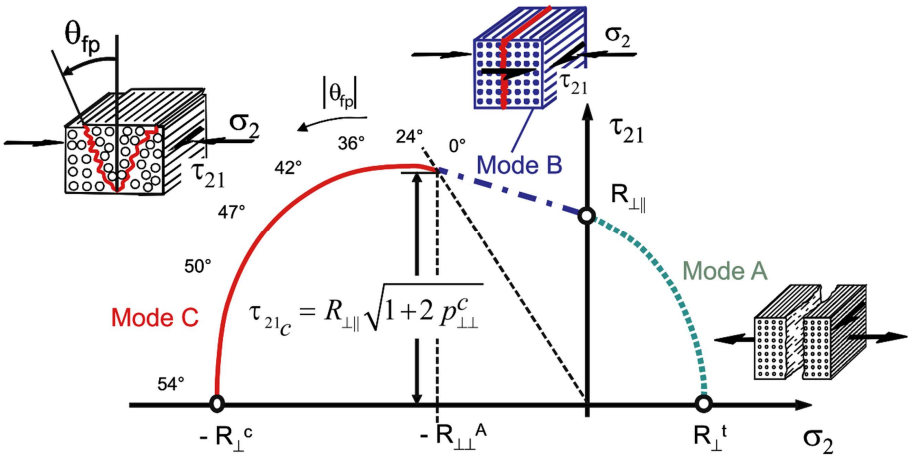

Figure 3.10 Fracture envelope for combined loads [97]

Therefore, a more applicable fracture hypothesis based on the stresses acting on the action plane, instead of being based on the lamina stresses ($\sigma_2, \sigma_3, \tau_{23}, \tau_{31}, \tau_{21}$), has been proposed in [97,190]. The different types of failure observed under the combined loading can be described

by three distinctive IFF-fracture modes, referred to as A, B, and C respectively. Mode A describes the fracture caused by transverse tensile stressing $\sigma_{\perp}^{\mathrm{t}}$, or by longitudinal shear stressing $\tau_{\perp\parallel}$ alone or in combination [97,190]. For in-plane stress case, such failure is characterized by cracks running in the thickness direction, hence in the action plane containing both σ_2 and τ_{21}, as shown in Figure 3.10. In this case, the tensile stressing causes the fracture surface separation, leading to the macroscopic degradation of the transverse elastic and the shear modulus referred to as E_{T} and $G_{\perp\parallel}$ respectively [97,190]. Mode B defines a fracture occurring on the action plane of the external shear stress τ_{21} caused by shear stressing $\tau_{\perp\parallel}$, and simultaneously applied normal compressive stressing $\sigma_{\perp}^{\mathrm{c}}$. The presence of compressive stress prevents the crack opening process, hence the impact on the stiffness degradation is reduced in comparison with the Mode A [97]. This mode of failure is achieved if the ratio between the compressive stress at fracture and the transverse compressive strength $|\sigma_{\perp}^{\mathrm{c}}/R_{\perp}^{\mathrm{c}}|$ is smaller than 0.4 [97]. By exceeding the value of $|\sigma_{\perp}^{\mathrm{c}}/R_{\perp}^{\mathrm{c}}|$ ratio, the fracture is not generated in the τ_{21} plane anymore, leading to a fracture angle $\theta_{\mathrm{fp}} \neq 0°$, which increases until the threshold value of $\pm 54°$ is reached for the case of pure compression. This implies the risk of delamination between the failed and the adjected layers [97,190]. Furthermore, an additional mode A* may occur for the cases of 3D stress state, where a combination of $\sigma_{\perp}^{\mathrm{t}}$, $\tau_{\perp\perp}$, and $\tau_{\perp\parallel}$ is acting on the fracture plane [97,190].

3.3.4. Puck's fracture hypotheses

Due to the brittle behaviour of FRP composites, the adoption of yielding hypothesis often encountered in global strength criteria such as Von Misses or Tasi-Wu does not consider the material behaviour appropriately. Therefore, the authors [97] propose that failure analysis for brittle materials should be based on the Coulomb and Mohr hypothesis, which determines the fracture limit of a material by the stress on the fracture plane. With a reasonable understanding of the brittle fracture in FRP composites, a physically-based fracture hypothesis has been proposed by Puck; it considers normal σ_{n}, and shear stresses τ_{nt} and τ_{n1} or their combination $\tau_{\mathrm{n}\psi}$, acting on a mutual action plane parallel to the fiber direction within the UD lamina [97,190]. The first hypothesis states that stresses σ_{n} and $\tau_{\mathrm{n}\psi}$, acting on the fracture plane parallel to the fiber direction, cause the inter-fiber fracture [97]. In the second hypothesis, Puck postulates that tensile stress promotes the fracture alone, $\tau_{\mathrm{n}\psi} = 0$, or by acting with shear stress $\tau_{\mathrm{n}\psi}$ simultaneously. But the increase of the compressive normal stress impedes the fracture development by enhancing the shear fracture resistance [97,190]. Furthermore, based on the experimentally

observed fractures developed in the principal stress action plane under the stresses equal to the induced transverse shear stressing $\tau_{\perp\perp}$, a law has been formulated for the case of combined stresses $\sigma_2, \sigma_3, \tau_{23}$ or $\sigma_{\mathrm{II}}, \sigma_{\mathrm{III}}$, respectively [97,190]. Therefore, if the UD-lamina is subjected only to $\sigma_2, \sigma_3, \tau_{23}$ stresses, the tensile fracture will occur based on the highest normal stress σ_{n} and the compressively reduced shear stress τ_{nt}, depending on the ratio between the applied stresses $\sigma_2, \sigma_3, \tau_{23}$ [97]. It has to be emphasized that the additional rule to Puck's IFF hypothesis is valid for $R_{\perp}^{\mathrm{c}}/R_{\perp}^{\mathrm{t}} < 2$, which is often encountered in thermoset and thermoplastic composites, while in cases where this criterion is not fulfilled, the stressing $\tau_{\perp\perp}$ would manifest a mixed mode fracture of combined $\sigma_{\perp}^{\mathrm{t}}$ and $\tau_{\perp\perp}$ stressing [97]. To calibrate the stress-based fracture criterion of UD composites, it is necessary to acquire the values of maximal sustainable stresses under uniaxial tensile, compressive, and pure shear load, $R_{\parallel}^{\mathrm{t}},\ R_{\parallel}^{\mathrm{c}}, R_{\perp}^{\mathrm{t}}, R_{\perp}^{\mathrm{c}}, R_{\perp\perp}, R_{\perp\parallel}$. These material properties are also referred as basic strengths and correspond to $\sigma_{\parallel}, \sigma_{\perp}, \tau_{\perp\perp}, \tau_{\perp\parallel}$ stressing, as shown in Figure 3.11 respectively. Each property should be acquired experimentally in the absence of any other type of stressing, regardless of the type of the occurred failure [97,190].

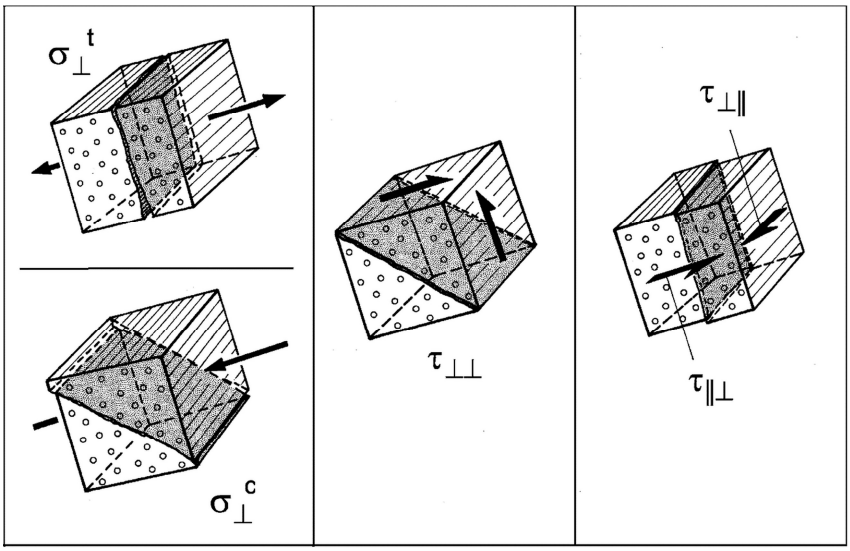

Figure 3.11 Representations of the UD lamina stressings and the corresponding IFF fracture planes [97]

Since Puck's IFF criteria are formulated using the stresses $(\sigma_{\mathrm{n}}, \tau_{\mathrm{nt}}, \tau_{\mathrm{n1}})$ present in the action plane, instead of the coordinate system (x_1, x_2, x_3), the basic strength values need to be corrected accordingly, leading to the reformulation of the IFF condition, as shown in Eq. 3.195 and 3.196.

$$F\left(\sigma_1, \sigma_2, \sigma_3, \tau_{23}, \tau_{31}, \tau_{21}, R_{\parallel}^{\mathrm{t}}, R_{\parallel}^{\mathrm{c}}, R_{\perp}^{\mathrm{t}}, R_{\perp}^{\mathrm{c}}, R_{\perp\perp}, R_{\perp\parallel}\right) = 1 \tag{3.195}$$

$$F\left[\sigma_{\mathrm{n}}\left(\theta_{\mathrm{fp}}\right), \tau_{\mathrm{nt}}\left(\theta_{\mathrm{fp}}\right), \tau_{\mathrm{n1}}\left(\theta_{\mathrm{fp}}\right), R_{\perp}^{\mathrm{A\,t}}, R_{\perp\perp}^{\mathrm{A}}, R_{\perp\parallel}^{\mathrm{A}}\right] = 1 \tag{3.196}$$

The variables $\sigma_{\mathrm{n}}(\theta), \tau_{\mathrm{nt}}(\theta)$, and $\tau_{\mathrm{n1}}(\theta)$, described by the "n" in the stress index, stand for the stresses which usually act simultaneously on the same action plane, as shown on Figure 3.12. Fulfilling the condition of the inclination $\theta = \theta_{\mathrm{fp}}$, the action plane becomes the fracture plane due to the highest calculated risk of fracture [97,190].

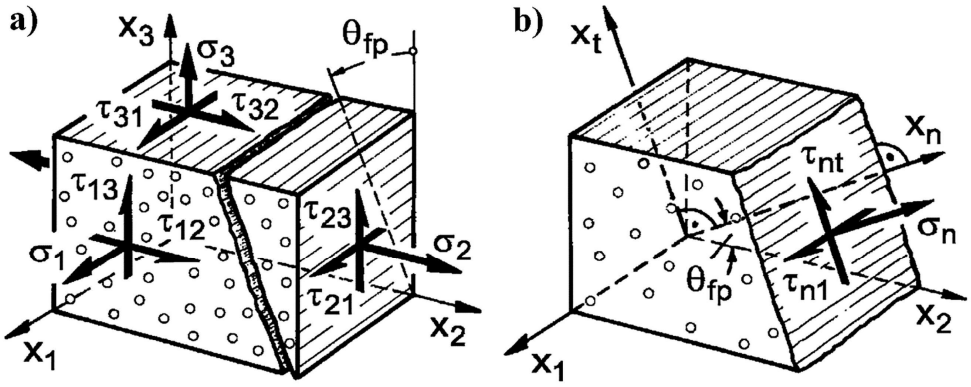

Figure 3.12 a) Stresses on UD-lamina, b) Stresses on IFF-fracture plane parallel to the fibers, [97]

Moreover, such criteria can only be calibrated using uniaxial and pure shear experimental tests where the isolated stressing such as $\sigma_{\perp}, \tau_{\perp\perp}, \tau_{\perp\parallel}$ can be applied. Therefore, each of the fracture resistances of the action plane R^A is defined as an action plane's resistance to fracture as a consequence of single stressing $\sigma_{\perp}, \tau_{\perp\perp}$, or $\tau_{\perp\parallel}$ [97,190]. While some R^A remain equal to basic strengths, it is necessary to identify the relevant stressing that provokes the fracture on its action plane, and not on just any action plane. The remaining fracture resistances $R_{\perp}^{\mathrm{A\,t}}, R_{\perp\perp}^{\mathrm{A}}$, and $R_{\perp\parallel}^{\mathrm{A}}$ can be distinctively defined as action plane fracture resistances due to transverse tensile stressing $\sigma_{\perp}^{\mathrm{t}}$, transverse shear stressing $\tau_{\perp\perp}$, and longitudinal shear stressing $\tau_{\perp\parallel}$ respectively. In processing data it is essential that $R_{\perp}^{\mathrm{A\,t}}$ is equal to $R_{\perp}^{\mathrm{t}}$ for a UD material in normal temperature and humidity, the $R_{\perp\perp}^{\mathrm{A}}$ is not equal to $R_{\perp\perp}$, with the $R_{\perp\parallel}^{\mathrm{A}}$ and $R_{\perp\parallel}$ remaining equal [97,190].

3.3.5. Action plane IFF criteria formulation

Based on the Puck hypothesis, the action plane related to IFF criteria is formulated with stresses $\sigma_{\mathrm{n}}(\theta), \tau_{\mathrm{nt}}(\theta), \tau_{\mathrm{n1}}(\theta)$ calculated based on $\sigma_2, \sigma_3, \tau_{23}, \tau_{31}, \tau_{21}$, and contingent on their action plane angle θ [97,190]. When stresses within the UD lamina pass the fracture limit the IFF is triggered on the action plane $\theta = \theta_{\mathrm{fp}}$, after the stresses $\sigma_{\mathrm{n}}(\theta), \tau_{\mathrm{nt}}(\theta), \tau_{\mathrm{n1}}(\theta)$ reach the fracture limit [97,190]. The risk of fracture is acquired by computing the stress exposure $f_{\mathrm{E}}(\theta)$ on the action plane, based on which the maximal value of the fracture plane is defined, as shown in Eq. 3.197.

$$f_{\mathrm{E}}(\theta) = [f_{\mathrm{E}}(\theta)]_{\max} = f_{\mathrm{E}}|_{\theta=\theta_{\mathrm{fp}}} \tag{3.197}$$

Moreover, by multiplying the stresses by a stretch factor $f_{\mathrm{Smin}} = 1/[f_{\mathrm{E}}(\theta)]_{\max}$ the IFF will manifest on the fracture surface only [97,190]. For an arbitrary stress state, the fracture plane is acquired through numerical iteration by calculating the $f_{\mathrm{E}}(\theta)$ for action planes in the range from $-90° < \theta < 90°$ with a 1° step, as shown in Figure 3.13, while the action plane with the highest stress exposure is adopted as the fracture plane [97].

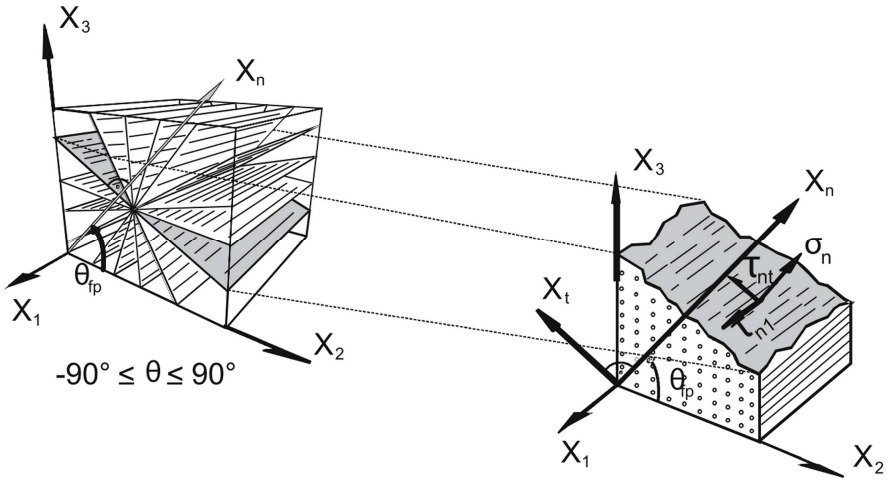

Figure 3.13 Illustration of the fracture plane iteration procedure [97]

3.3.6. IFF condition in tension

The fracture condition for tensile stress σ_{n} is based on the experimentally acquired longitudinal section of the master fracture body (MFB) characterized by $\tau_{\mathrm{nt}} = 0$ and $\psi = 90°$, where the angle ψ can be expressed according to the Eq. 3.198.

$$\psi = \tan^{-1}\left(\frac{\tau_{\mathrm{n1}}(\theta)}{\tau_{\mathrm{nt}}(\theta)}\right) \tag{3.198}$$

Since the fracture occurs on the action plane common to both σ_2 and τ_{21}, the values of $\sigma_{\mathrm{n}}(\theta_{\mathrm{fp}})$ and $\tau_{\mathrm{n1}}(\theta_{\mathrm{fp}})$ are equal to σ_2 and τ_{21} respectively. For the region of tensile stress on the fracture plane, the fracture curve is fitted using an elliptical function with a negative inclination at $\sigma_{\mathrm{n}} = 0$, $\tau_{\mathrm{n1}} = R_{\perp\parallel}$, which perpendicularly intersects the σ_{n} axis at $\sigma_{\mathrm{n}} = R_{\perp}^{t}$, $\tau_{\mathrm{n1}} = 0$ [97,190]. With that in mind, similar curves are applied to the other longitudinal sections.

According to Puck's hypothesis, the resultant shear stress $\tau_{\mathrm{n}\psi}(\theta)$ based on $\tau_{\mathrm{n1}}(\theta)$ and $\tau_{\mathrm{nt}}(\theta)$ is calculated as shown in Eq. 3.199. The fracture resistance of the action plane against it is defined as $R_{\perp\psi}^{\mathrm{A}}$, while the formulation of the fracture condition is based on an elliptical

equation, as presented in Eq. 3.200. For simplicity, the shear and normal stresses are abbreviated from this point forward as $\tau_{n\psi}(\theta) = \tau_{n\psi}$, and $\sigma_n(\theta) = \sigma_n$, respectively [97]. The identification of the fracture angle will be explained separately.

$$\tau_{n\psi}(\theta) = \sqrt{\tau_{nt}^2(\theta) + \tau_{n1}^2(\theta)} \tag{3.199}$$

$$\left(\frac{\tau_{n\psi}}{R_{\perp\psi}^{A}}\right)^2 + c_1 \cdot \frac{\sigma_n}{R_{\perp}^{At}} + c_2 \cdot \frac{\sigma_n^2}{\left(R_{\perp}^{At}\right)^2} = 1; \quad \text{if: } \sigma_n > 0 \tag{3.200}$$

The constants c_1 and c_2 are determined from the boundary conditions fulfilling the expression $\sigma_n = R_{\perp}^{At}$ for $\tau_{n\psi} = 0$, leading to the sum of c_1 and c_2 being equal to one. The fracture curve acquires the value of $R_{\perp\psi}^{A}$ at the intersection with the $\tau_{n\psi}$ axis, while the inclination is computed according to the expression in Eq. 3.201.

$$(-p_{\perp\psi}^{t}) = \left(\frac{\partial \tau_{n\psi}}{\partial \sigma_n}\right)_{\sigma_n=0} \tag{3. 201}$$

Acquiring the implicit differentiation of Eq. 3.200 for $\sigma_n = 0$ and $\tau_{n\psi} = R_{\perp\psi}^{A}$, the expression shown in Eq. 3.202 is acquired, leading to a refined version of the IFF condition for $\sigma_n \geq 0$ in Eq. 3.203.

$$\frac{2}{R_{\perp}^{At}} \cdot \left(\frac{\partial \tau_{n\psi}}{\partial \sigma_n}\right)_{\sigma_n=0} + \frac{c_1}{R_{\perp}^{At}} = 0 \tag{3.202}$$

$$\left(\frac{\tau_{n\psi}}{R_{\perp\psi}^{A}}\right)^2 + 2 \cdot \frac{p_{\perp\psi}^{t} \cdot \sigma_n}{R_{\perp}^{At}} + \left(1 - 2 \cdot \frac{p_{\perp\psi}^{t} \cdot R_{\perp}^{At}}{R_{\perp\psi}^{At}}\right) \cdot \frac{\sigma_n^2}{\left(R_{\perp}^{At}\right)} = 1 \tag{3.203}$$

3.3.7. IFF condition in compression

Based on both the Mohr hypothesis and the observed experimental data, up to the stress magnitude of $|\sigma_2^c| \approx 0.4 R_{\perp}^{c}$, Puck proposed a parabolic formulation for the fracture condition under compressive stress, as shown in Eq. 3.204, where the inclination for $\sigma_n = 0$ is acquired as shown in Eq. 3.205.

$$\left(\frac{\tau_{n\psi}}{R_{\perp\psi}^{A}}\right)^2 + c \cdot \sigma_n = 1; \quad \text{if: } \sigma_n < 0 \tag{3.204}$$

$$(-p_{\perp\psi}^{c}) = \left(\frac{\partial \tau_{n\psi}}{\partial \sigma_n}\right)_{\sigma_n=0} \tag{3.205}$$

Consistent with the case of tension, the differentiation of Eq. 3.200 for $\sigma_n = 0$ and $\tau_{n\psi} = 0$,

returns the Eq. 3.206, which eventually leads to the fracture condition for compression on the fracture plan, as shown in Eq. 3.207.

$$c = 2 \cdot \frac{p_{\perp\psi}^{\mathrm{c}}}{R_{\perp\psi}^{\mathrm{At}}} \tag{3.206}$$

$$\left(\frac{\tau_{\mathrm{n}\psi}}{R_{\perp\psi}^{\mathrm{A}}}\right)^2 + 2 \cdot \frac{p_{\perp\psi}^{\mathrm{c}}}{R_{\perp\psi}^{\mathrm{At}}} \cdot \sigma_{\mathrm{n}} = 1 \tag{3.207}$$

Furthermore, the unknown values for fracture resistance $R_{\perp\psi}^{\mathrm{A}}$ and the inclination parameters $p_{\perp\psi}^{\mathrm{t}}$ and $p_{\perp\psi}^{\mathrm{c}}$used in tensile and compressive cases need to be acquired separately. The fracture resistance $R_{\perp\psi}^{\mathrm{A}}$ can be visualized as the distance from the $\sigma_{\mathrm{n}} = 0$ point to the MFB surface origin depending on the value of angle ψ, defined in Eq. 3.198, which characterizes the longitudinal section. In the case of angle ψ being equal to zero, the shear stress on the action plane $\tau_{\mathrm{n}\psi}$ is equal to τ_{nt}, and τ_{n1} is ignored, leading to the fracture resistance being equal to $R_{\perp\perp}^{\mathrm{A}}$. On the other hand, if ψ reaches 90°, shear stress on the action plane is equal to τ_{n1}, while $\tau_{\mathrm{n}t}$ is equal to zero, hence the fracture resistance is equal to $R_{\perp\parallel}^{\mathrm{A}}$ [97]. Since the difference between the fracture resistances is significant yet still small enough, the adopted elliptical approach for the intermediate values of $R_{\perp\psi}^{\mathrm{A}}$ is valid, as shown in Eq. 3.208, where the additional index "0" states the stresses are taken at $\sigma_{\mathrm{n}} = 0$ [97].

$$\left(\frac{\tau_{\mathrm{n}\psi_0}}{R_{\perp\psi}^{\mathrm{A}}}\right)^2 = \left(\frac{\tau_{\mathrm{nt}_0}}{R_{\perp\perp}^{\mathrm{A}}}\right)^2 + \left(\frac{\tau_{\mathrm{n1}_0}}{R_{\perp\parallel}^{\mathrm{A}}}\right)^2 = 1 \tag{3.208}$$

Moreover, if the additional correlations $\tau_{\mathrm{nt}_0} = \tau_{\mathrm{n}\psi_0}\cos(\psi)$ and $\tau_{\mathrm{n1}_0} = \tau_{\mathrm{n}\psi_0}\sin(\psi)$ are added to the elliptical equation Eq. 3.208, the following expression Eq. 3.209 is acquired.

$$\left(\frac{1}{R_{\perp\psi}^{\mathrm{A}}}\right)^2 = \left(\frac{\cos(\psi)}{R_{\perp\perp}^{\mathrm{A}}}\right)^2 + \left(\frac{\sin(\psi)}{R_{\perp\parallel}^{\mathrm{A}}}\right)^2 = 1 \tag{3.209}$$

Additionally, since the normal stress σ_{n} doesn't influence the value of angle ψ, the following expressions shown in Eq. 3.210, and Eq. 3. 211 can be adopted for all the values of σ_{n}. This leads to a general term, shown in Eq. 3. 212, which defines the transverse section $\sigma_{\mathrm{n}} = 0$, with an infinite number of longitudinal sections $\psi = \mathrm{constant}$ [97].

$$\cos(\psi) = \frac{\tau_{\mathrm{nt}}}{\tau_{\mathrm{n}\psi}} \tag{3.110}$$

$$\sin(\psi) = \frac{\tau_{\mathrm{n1}}}{\tau_{\mathrm{n}\psi}} \tag{3.111}$$

$$\left(\frac{\tau_{\mathrm{n}\psi}}{R^{\mathrm{A}}_{\perp\psi}}\right)^2 = \left(\frac{\tau_{\mathrm{nt}}}{R^{\mathrm{A}}_{\perp\perp}}\right)^2 + \left(\frac{\tau_{\mathrm{n1}}}{R^{\mathrm{A}}_{\perp\parallel}}\right)^2 \tag{3.112}$$

However, in the case of pure transverse compression when $\tau_{\mathrm{n}t} = \tau_{\mathrm{n1}} = 0$, and $\sigma_{\mathrm{n}} < 0$, the fracture condition is not defined, and the value of the $p^{\mathrm{t}}_{\perp\psi}/R^{\mathrm{A}}_{\perp\psi}$ coefficient is insignificant. Instead, on the plane of pure compression the fracture develops on another action plane [97].

3.3.8. Fracture plane and inclination parameters

As previously described, the fracture plane is acquired based on the maximal local stress exposure $f_{\mathrm{E}}(\theta_{\mathrm{fp}})$ with θ in range from -90° to 90°. Since the action planes without stress return the value of a stress exposure f_{E} equal to zero and the stretch factor f_{S} equal to "∞", numerical approach in fracture-plane identification favors the former to avoid the numerical inconsistencies [97]. Therefore, the stresses $\sigma_{\mathrm{n}}(\theta)$ and $\tau_{\mathrm{n}\psi}(\theta)$ need to be divided with $f_{\mathrm{E}}(\theta)$ to generate a fracture in the action plane on angle θ, and so fulfil the fracture conditions. Since the fracture conditions presented in Eq. 3.203 and Eq. 3.207 are quadratic equations, their explicit solutions for $f_{\mathrm{E}}(\theta)$ are homogeneous of the first order. The values grow linearly with the increase in stress, directly indicating the risk of fracture [97]. Therefore, the IFF stress exposure in tensile and compressive conditions can be expressed according to Eq. 3.213, and Eq. 3.214 respectively, while implementing the expressions from Eq. 3.215 to 3.218, as derived in [97].

$$f_{\mathrm{E}}(\theta) = \sqrt{\left[\left(\frac{1}{R^{\mathrm{t}}_{\perp}} - \frac{p^{\mathrm{t}}_{\perp\psi}}{p^{\mathrm{A}}_{\perp\psi}}\right)\cdot\sigma_{\mathrm{n}}(\theta)\right]^2 + \left(\frac{\tau_{\mathrm{nt}}(\theta)}{R^{\mathrm{A}}_{\perp\perp}}\right)^2\left(\frac{\tau_{\mathrm{n1}}(\theta)}{R^{\mathrm{A}}_{\perp\parallel}}\right)^2} + \frac{p^{\mathrm{t}}_{\perp\psi}}{p^{\mathrm{A}}_{\perp\psi}}\cdot\sigma_{\mathrm{n}}(\theta) \tag{3.213}$$

$$f_{\mathrm{E}}(\theta) = \sqrt{\left(\frac{\tau_{\mathrm{nt}}(\theta)}{R^{\mathrm{A}}_{\perp\perp}}\right)^2 + \left(\frac{\tau_{\mathrm{n1}}(\theta)}{R^{\mathrm{A}}_{\perp\parallel}}\right)^2 + \left(\frac{p^{\mathrm{c}}_{\perp\psi}}{p^{\mathrm{A}}_{\perp\psi}}\cdot\frac{p^{\mathrm{c}}_{\perp\psi}}{p^{\mathrm{A}}_{\perp\psi}}\sigma_{\mathrm{n}}(\theta)\right)^2} + \frac{p^{\mathrm{c}}_{\perp\psi}}{p^{\mathrm{A}}_{\perp\psi}}\cdot\sigma_{\mathrm{n}}(\theta) \tag{3.214}$$

$$\frac{p^{\mathrm{t,c}}_{\perp\psi}}{p^{\mathrm{A}}_{\perp\psi}} = \frac{p^{\mathrm{A}}_{\perp\perp}}{R^{\mathrm{A}}_{\perp\perp}}\cos^2(\psi) + \frac{p^{\mathrm{t,c}}_{\perp\parallel}}{R^{\mathrm{A}}_{\perp\parallel}}\sin^2(\psi) \tag{3.215}$$

$$R^{\mathrm{A}}_{\perp\perp} = \frac{R^{\mathrm{c}}_{\perp}}{2\cdot(1+p^{\mathrm{c}}_{\perp\perp})} \tag{3.216}$$

$$\cos^2(\psi) = \frac{\tau^2_{\mathrm{nt}}}{\tau^2_{\mathrm{nt}} + \tau^2_{\mathrm{n1}}} \tag{3.217}$$

$$\sin^2(\psi) = \frac{\tau^2_{\mathrm{n1}}}{\tau^2_{\mathrm{nt}} + \tau^2_{\mathrm{n1}}} = 1 - \cos^2(\psi) \tag{3.218}$$

Furthermore, since the fracture angle θ_{fp} is equal to zero in both transverse tensile and compressive cases, the inclination parameters $p^{t}_{\perp\parallel}$ and $p^{c}_{\perp\parallel}$ at $\psi = 90°$ can be derived from the fracture curve, while adopting the normal σ_n and shear τ_{n1} stress values on the fracture plane as σ_2 and τ_{21} respectively. The fracture curve is calibrated to fit the experimental data, while the best results are acquired when the values of the inclination parameters are adopted within the range from 0.25 to 0.35 while keeping the $p^{t}_{\perp\parallel}$ value slightly higher [157]. In contrast, the fracture curve data can't be determined when the value of normal stress is close to zero, hence the inclination parameters $p^{t}_{\perp\perp}$ and $p^{c}_{\perp\perp}$ at $\psi = 0°$ can't be experimentally validated [97]; neither their acquisition from transverse fracture tests, nor the equality with the tensile parameters can be supported [97]. Hence, the recommended inclination parameters for an arbitrary FRP material has been proposed in [157], and presented in Table 3.1.

Table 3.1 Proposed inclination parameters

	$p^{t}_{\perp\parallel}$	$p^{c}_{\perp\parallel}$	$p^{t}_{\perp\perp}$	$p^{c}_{\perp\perp}$
GFRP/Epoxy	0.3	0.25	0.2 – 0.25	0.2 – 0.25
CFRP/Epoxy	0.35	0.3	0.25 – 0.30	0.25 – 0.30

The proposed values presented in Table 3.1 are based $R^{c}_{\perp}/R^{t}_{\perp}$ ratio which for CFRP and GFRP holds $R^{c}_{\perp}/R^{t}_{\perp} \geq 3$ and $R^{c}_{\perp}/R^{t}_{\perp} \geq 2.8$ respectively. These proposed values are reported for composites with a thermosetting matrix [97], while approximate values have also been acquired for thermoplastic PEEK and PA12 matrix composites [97]. Considering the theoretical background, Puck's FF and IFF criteria are applicable to most FRPs, therefore the presented theory can be applied to the analysis of additively manufactured fiber-reinforced thermoplastic materials. Since the theory is not readily available in commercial FEA software, a user-defined material model has to be prepared using a Fortran script. Therefore, the code will be prepared according to the guidelines presented in [8,48,92,93,98], executed in Abaqus FEA software, and experimentally validated for tensile and shear cases. The tensile and shear lamina properties will be identified experimentally, while the compressive and fracture properties and parameters will be adopted from the literature.

In this chapter the Classical laminate theory, with basic assumptions for the in-plane stress state, has been summarized. The multiscale nature of the laminate geometry has been revised, focusing on local and global coordinate systems, stacking sequence effects, and the assembly

of the laminate stiffness matrix for calculating the effective load-bearing capabilities of an arbitrary reinforced laminate.

Following the concept of multiscale analysis, the theoretical background of the micromechanical homogenization has also been presented in this chapter. The localization problem for elasticity, and the theoretical validation of a representative volume element have been discussed using stress- and strain-based approaches. The calculations of in-plane and out-of-plane effective properties have been derived for three types of elementary problems regarding the longitudinal, transversal, and shear loads introduced on a three-node element respectively. This was followed by a theoretical summary on boundary conditions, based on which an example for imposing periodic boundary conditions on a simple mesh has been presented and adopted for further analysis. Following the presented concepts of unified periodic homogenisation, the representative volume elements have been designed in the Abaqus CAE environment; periodic boundary conditions have been imposed by linking the nodal degrees of freedom using linear constraints equations, while introducing the loads as displacements through Dirichlet boundary conditions. Cohesive fiber/matrix contacts have also been adopted and prepared for calibration according to the experimental results.

Furthermore, the theoretical basis of continuum damage mechanics and Puck's fracture theory have been presented in the last part of this section. The key distinctions between fiber and inter-fiber failure criteria have been discussed, and solutions for tensile and compressive cases of fiber fracture have been derived for both cases respectively. Despite the simplicity of the fiber criterion, the Puck's inter-fiber fracture criterion is based on Coulomb and Mohr action-plane hypothesis. That resulted in a more complex definition and the necessity for iterative identification of the fracture plane, in accordance with the brittle fracture in FRP composites. This had a negative impact on the calculation efforts. Following the presented theory and the available models in the literature, the Puck's theory was implemented in Abaqus using a UMAT subroutine. The model was tested on readily available data showing consistent results, and therefore it was adopted for further analyses.

The theoretical concepts for micro- and macro-mechanical approaches were summarized in this section. The models were prepared for implementation in the Abaqus CAE environment and tested on readily available data. However, due to the distinctive manufacturing process leading to material inconsistencies, the properties of additively manufactured materials are often inferior to those of their conventionally manufactured counterparts. Therefore, an experi-

mental campaign including microstructural analysis, and macroscale destructive test is proposed. Three distinctive experimental protocols will be conducted: microscopic constituents' inspections, lamina properties acquisition through longitudinal and transverse tensile and shear tests, concluding with damage monitoring in multidirectionally reinforced laminates. The microstructural images will be analysed using machine learning algorithms, statistically evaluated, based on which the representative volume elements will be modelled, homogenized, and experimentally validated for longitudinal and transverse tensile, and shear cases. The results will be implemented in the continuum damage model, the model parameters will be calibrated and validated by comparison with multidirectionally reinforced laminates and similar readily available damage models.

4. EXPERIMENTAL PROCEDURES

The presented theoretical concepts of the laminate mechanics, micromechanical homogenization, and Puck's fracture theory have been derived for application in Abaqus CAE environment. The models have been tested on readily available data will be prepared for calibration and experimental validation. In this section, a multiscale experimental approach will be presented. The section will be divided into two distinctive subsections, featuring experimental protocols and results respectively. Firstly, a microscopic inspection using SEM imaging will be proposed to identify the microscale geometrical properties of the studied composites. Upon the microscopic evaluation, carbon-reinforced composite will be adopted for the procedure of lamina properties identification according to ASTM D3039 and ASTM D3518, followed by the inspection of multidirectionally reinforced composite, designed in accordance with ASTM D5766, with LSS enforcing multiaxial stress states [28,162]. The results of the conducted experimental protocols will be presented in subsection 4.2, starting with the image analysis using machine-learning algorithms and statistical evaluation of the acquired data, followed by the calculation of UD and shear lamina properties and concluded with critical discussion on the behaviour of multidirectionally reinforced CFRP composites by evaluation of the off-axis influence on the overall laminate behaviour. This section will cover in detail the methods and models used in this thesis, along with a comprehensive overview of the developed experimental setups[1].

4.1. Specimen design and test protocols

This subsection synthesizes the multiscale experimental protocol starting with sample preparation for the microscopic inspection and SEM parameter calibration, followed by UD specimen preparation, testing and full-field strain monitoring, while concluding with the preparation, and experimental study of multidirectionally reinforced composites.

[1] Part of the work described in this section was published by the author of the thesis and his collaborators in two peer-reviewed scientific papers ([59] and [60]), which were produced and published as part of the obligations foreseen in the curriculum of the doctoral study of the Faculty of Engineering of the University of Rijeka, Croatia, hence this section is based, partly directly derived and cited from this work.

4.1.1. Samples for microscopic inspection

In order to inspect the heterogenic structure of the AM composites, a microscale approach based on SEM imaging has been proposed based on three cases of composite laminates reinforced with carbon (C), glass (G), and aramid (K) fiber respectively. The specimens have been modelled as 25×25 mm square laminates and manufactured using an industrial grade 3D printer Markforged-X7 utilizing the FFF approach. The thickness of the specimens was adjusted to attain an equal number of layers within a cross-ply $[0/90_2/0/90_2]_s$ configuration for each of the studied cases, as shown in Figure 4.1.

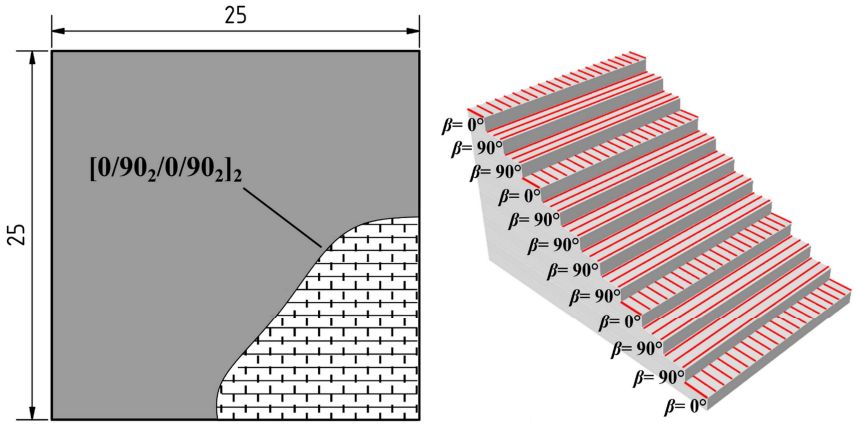

Figure 4.1 Geometry and LSS of the cross-ply specimens for microscopic analysis

The specimens were cut with a sectioning machine into distinctive *x*-*y*, *x*-*z*, and *y*-*z* cross-sections, where the printing direction was assumed as the *x* axis, perpendicular to the printing direction as *y* axis, leaving the thickness direction as the *z* axis. Each of the extracted cross-section was embedded in polymer resin, and ground using multiple grades of granulation then polished with 3μm suspension using an automatic polishing machine STRUERS-LABOPOL. The prepared specimens were scanned using the FEI-QUANTA-250-FEG microscope utilizing the Low-vacuum Secondary Electron (LFD) and the Solid-state Diode Backscatter Electron (BSED) detectors, adopting configurations presented in Table 4.1.

Table 4.1 SEM configuration

Accelerating voltage, kV	Pressure, Pa	Distance, mm	Spot	Magnification
20.00	100	9.1 – 10.5	4.0	100× – 1600×

After comparing the captured images, a better surface morphology representation was achieved when LFD detectors were used, Figure 4.2, a) and c), while BSED presented a better contrast in chemical composition based on density, therefore displaying heavier materials in lighter shades of grey, Figure 4.2, b) and d).

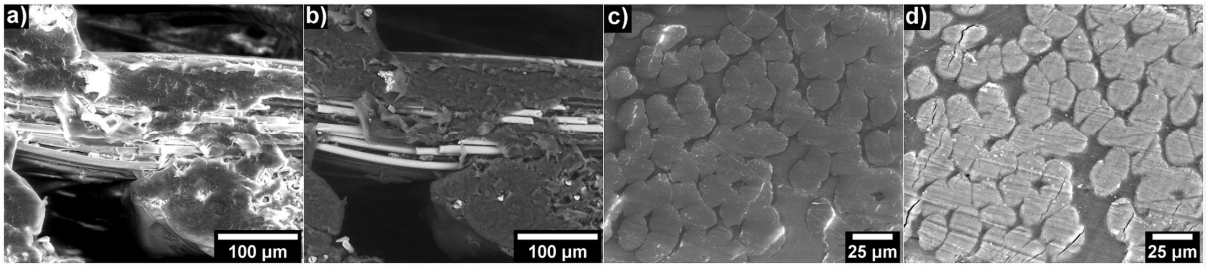

Figure 4.2 a) Fiber side-view acquired using LFD detector, b) Fiber side-view acquired using BSED detector, c) Fiber cross-sections acquired using LFD detector, d) Fiber cross-sections acquired using BSED detector

Therefore, both detectors were utilized in image acquisition, adopting LFD for accurate measurements, while BSED was used for further image analysis. The microscopic constituent's properties (including fiber diameter and misalignment, layer height, and material deposition width) were evaluated using an open-source image analysis software Image-J (FIJI) [174], based on ten randomly selected images within each of the cross-sections presented in Figure 4.3.

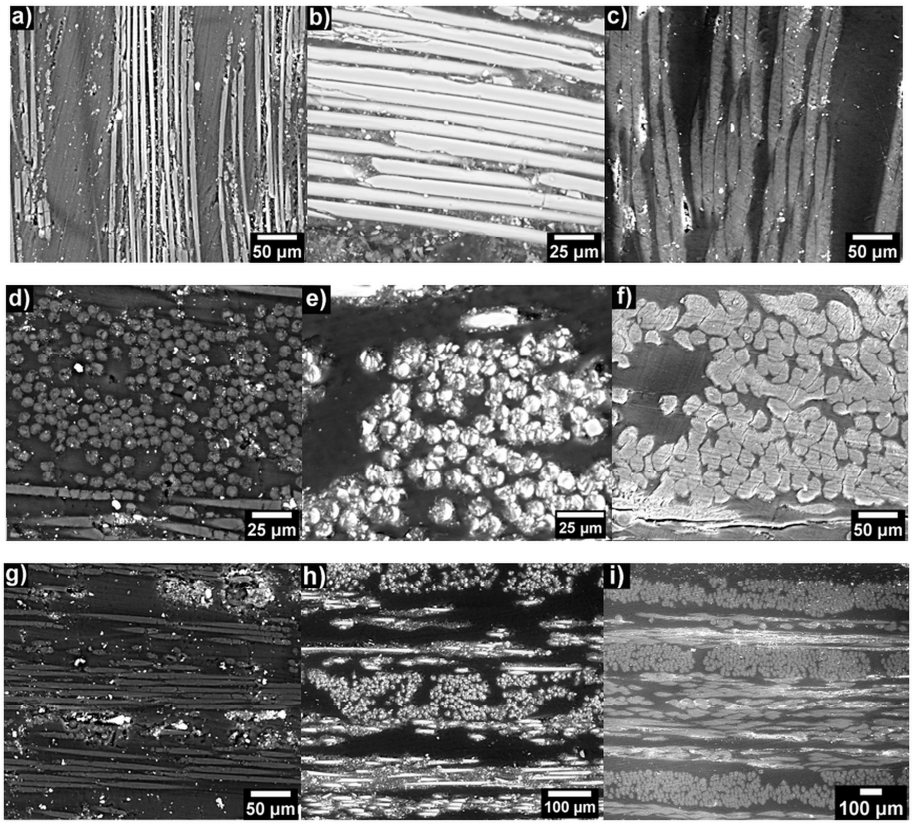

Figure 4.3 Cross-section images for carbon, glass, and aramid fiber reinforced sample respectively: a) C-x-y section, b) G-x-y section, c) K-x-y section, d) C-y-z section, e) G-y-z section, f) K-y-z section g) C-x-z section, h) G-x-z section, i) K-x-z section

Most of the measurements were conducted through multiple magnifications (200×, 400×, 800×, and 1600×) and their corresponding image sizes (1500×1380µm, 747×688µm,

375×345μm, and 186×171μm) respectively. The fiber diameters and misalignments were acquired from *y-z* and *x-y* cross-sections images respectively, with magnification in the range from 800× to 1600× times. The measurements were statistically analysed, and the results were presented in subsection 4.2.

4.1.2. Unidirectional and shear CFRP composite specimens

Having the microscale properties evaluated for the designated numerical homogenization protocol, the corresponding lamina longitudinal, transverse and in-plane shear properties also had to be acquired for validation. Therefore, adopting carbon fiber as the reinforcement, three distinctive sets of specimens (UD-0, UD-90, and SH-45) were designed according to ASTM-D3039 [204] and ASTM-D3518 [203], as shown in Figure 4.4 a) – c), then manufactured using a Markforged-X7 3D, while the adopted LSS-es shown in Figure 4.4 d) – f), were achieved by configuring the raster paths in the slicer software, where the usage of polymeric contour edges was also disabled.

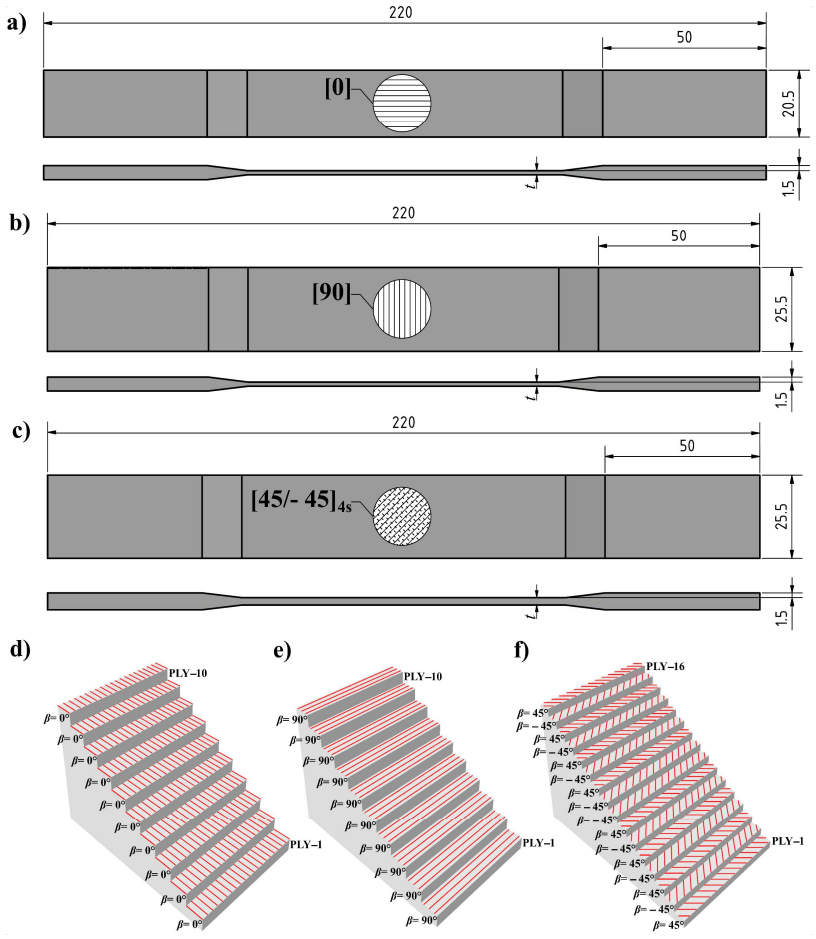

Figure 4.4 Unidirectional and shear specimens: a) UD-0 geometry, b) UD-90 geometry, c) SH-45 geometry, d) UD-0 LSS, e) UD-90 LSS, f) SH-45 LSS

The issue of stress concentration within the gripping area was also addressed by introducing the reinforcing tabs during the AM process while implementing a fiber striping reinforcement technique to achieve a steady rise of thickness in the gripping region and reduce the manufacturing costs. Since the AM tab bonding resulted in the necessity for a support material, a support jig has been implemented instead. Width and thickness have been measured across multiple sections within the gauge length for each of the produced specimens using a digital micrometer. These statistics have been calculated and summarized in the Table 4.2. Comparing the measurements with the CAE dimensions, discrepancies reaching up to 21%. have been detected. Nevertheless, removing both the excess support structure and the polymer top coating returned more consistent results.

Table 4.2 Dimensions of UD and SH specimens

Spec.	LSS	Length, mm	Width, mm			Thickness, mm				
			CAE	Measured	Error, %	CAE	Measured	Error, %	Top and support removed	Error, %
UD-0	[0]	220	20.5	19.993 ± 0.058	2.5	1.25	1.54 ± 0.001	18.8	1.29 ± 0.001	3.1
UD-90	[90]	220	25.5	26.903 ± 0.154	2.6	1.25	1.58 ± 0.017	20.9	1.33 ± 0.017	1.7
SH-45	$[45/-45]_{4s}$	220	25.5	27.250 ± 0.017	3.9	2.25	2.55 ± 0.010	11.8	2.30 ± 0.017	2.2

With their geometrical properties evaluated, the specimens have been prepared for DIC measurement by applying a stochastically random high contrast pattern on the specimens' surface according to the GOM documentation and guidelines presented in [18]. The first coating consisted of a polymer primer which was sprayed over by a thin matte white coating, followed by a matte black speckled pattern after drying. The surface quality has been evaluated within GOM Aramis software, as shown in Figure 4.5, which was also used in image processing and measurements. The images have been acquired using a GOM Aramis 5M (GigE) adjustable base 800 system with 35mm lenses, resulting in image resolution of 2448×2050 pixels. The cameras have been positioned at 560 mm from the specimen, with the distance between the cameras equal to 265 mm, closing the angle of 26°. The sensor calibration has been achieved using software-guided protocol at 22.5°C resulting in average deviation of 0.048 pixels in a measuring volume of 130×110×90 mm.

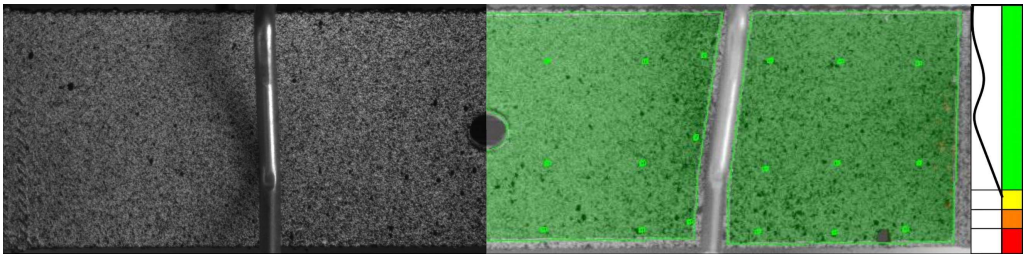

Figure 4.5 Applied raster and surface quality evaluation using GOM Aramis software

With full-field strain data acquired, two virtual extensometers have been adopted to extract the strain data within gauge length in the longitudinal and the transverse directions respectively. Furthermore, the real-time data from the load cell has been acquired using an auxiliary input to the DIC system from the tensile machine controller. The load-voltage calibration has been conducted at a lower force up to 250N in a preliminary test protocol. The experiments have been conducted using an Instron servo-hydraulic testing system under quasistatic conditions at the speed of 0.01 mm/s. The strains were measured using both the DIC and the contact extensometer as separate systems, as shown in Figure 4.6.

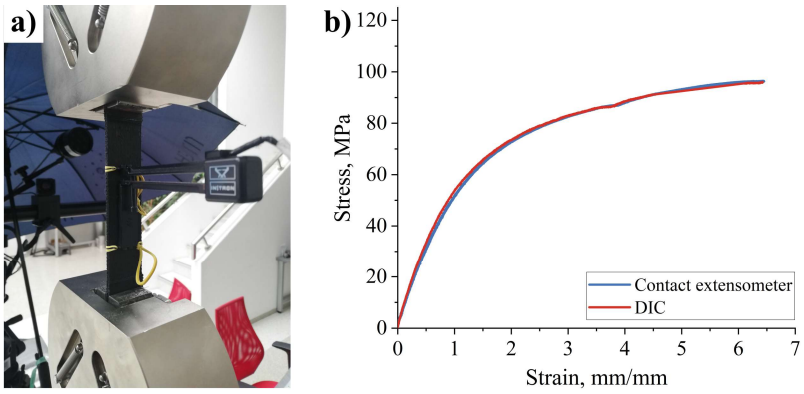

Figure 4.6 a) Specimen during the experiment, b) Measurement method comparison for specimen SH45

To address the anticipated material behaviour for each of the studied cases, the test protocols had to be designed accordingly. Since the UD-0 case represents a unidirectionally reinforced laminate loaded in the direction of the fiber reinforcements [204], the anticipated failure mode is brittle and instantaneous. Therefore, to capture the damage initiation, the experiment had been additionally monitored using a high frame rate thermal camera due to the slow frame rate of the available DIC system. Both monitoring methods confirmed a fiber tow failure outside the gauge length, followed by a rapid failure cascade which developed into a long splitting failure within the gauge mid-region (SGM) [204], as shown in Figure 4.7 a) - d).

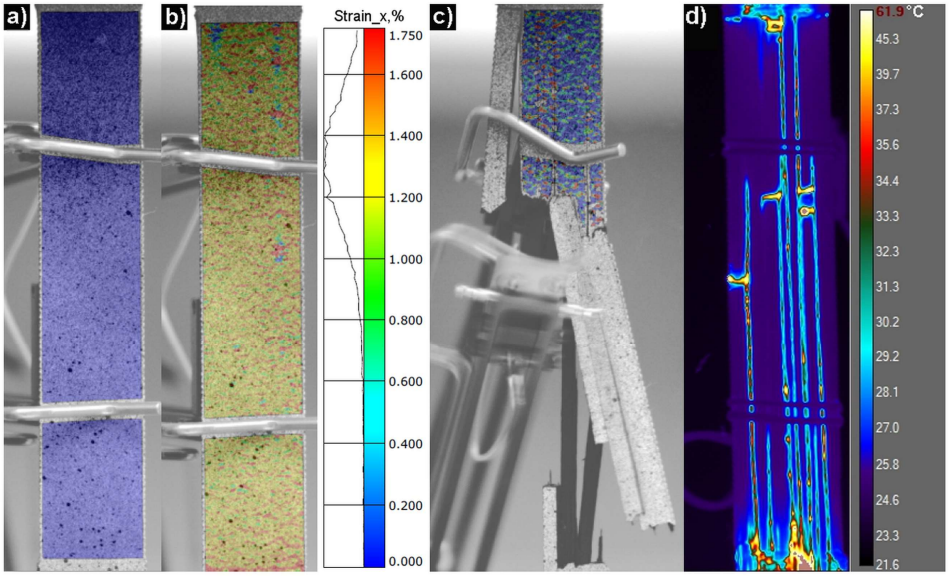

Figure 4.7 UD-0 full-field strain measurements: a) Initial, b) Pre-failure, c) Failure, d) Thermal imaging of an additional specimen

In contrast, the UD-90 case, shown in shown in Figure 4.8, represents transversely reinforced laminate loaded perpendicularly to the direction of the fiber reinforcements. Therefore, ASTM-D3039 [204] refers to this case for the determination of the transverse tensile properties in the laminate based on the uniaxial tensile test results.

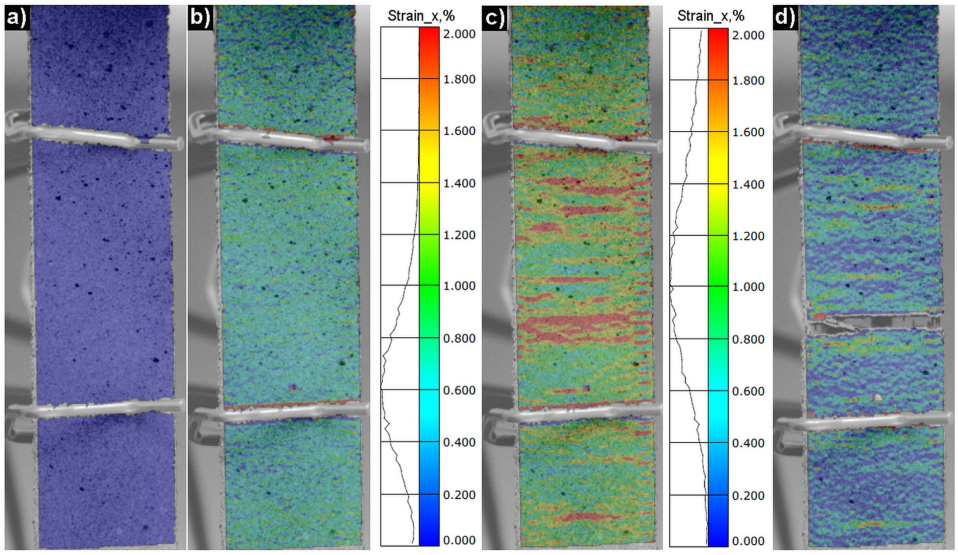

Figure 4.8 UD-90 full-field strain measurements: a) Initial, b) Yield point, c) Pre-failure, d) Failure

The transverse tensile behaviour of FRPs is highly influenced by the matrix response, and is often assumed to be equal to the matrix behaviour. However, the implementation of full-field strain measurements confirms the assumed inter-raster cohesive contact influence on the overall elastic-plastic response, supporting the FFF approach influence for significantly lower yield

and ultimate tensile stress in comparison with the injection-molded counterparts. While this behaviour could be easily modelled using plasticity, the UD-90 case behaviour is more influenced by the cohesive interfaces, leading to multiple local yielding zones divided by the material deposition width, as shown in Figure 4.8.

In addition, the SH-45 specimens, shown in Figure 4.9, represent a specific case where the LSS is tailored to enforce a multiaxial stress state in uniaxial tension. To that end, the specimens are prepared according to ASTM-D3039 [204], and ASTM-D3518 [203] guidelines, with LSS equal to $[45/-45]_{4s}$. That resolves the uniaxially introduced loads into the in-plane shear stress state. The anticipated ductile failure in SH-45 cases is followed by the fiber rearrangement phenomenon reaching up to 25% strain at failure. Since these large strains are uncommon in composite laminates, the ASTM-D3518 standard [203] recommends truncating the experimental results at 5% of shear strain if the failure doesn't occur before that.

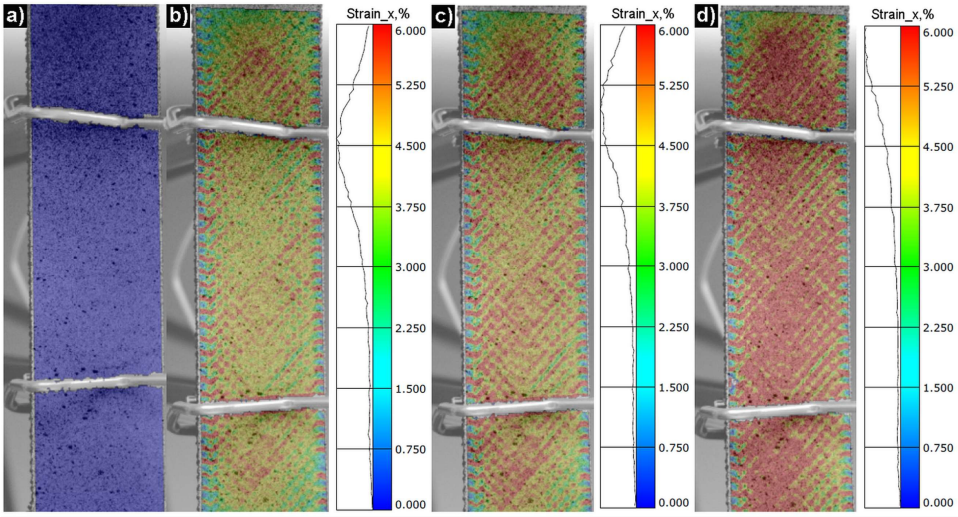

Figure 4.9 SH-45 full-field strain measurements: a) Initial, b) 5% shear strain, c) 5% axial strain, d) Termination

Figure 4.9 also shows local inter-raster yielding zones divided by the material deposition width, reinforcing the assumption of a major cohesive influence on overall AM CFRP composite behaviour. Therefore, this assumption will be considered in the numerical representation of the RVE behaviour.

4.1.3. Multidirectional CFRP composite specimens

Since fiber reinforced composites are seldom used as unidirectional, studying the behaviour of multidirectionally reinforced CFRP composites is essential. Therefore, to inspect the damage initiation and propagation in engineering applications, an experimental investigation of LSS-

induced multiaxial stress states in AM CFRP composites has been proposed according to [28,162]. Therefore, three distinctive open-hole (OH) specimen designs have been adopted according to the ASTM D5766 guidelines, with an internal architecture equal to $[0/90_2/0/90_2]_S$, $[0/45_2/0/-45_2]_S$, and $[0/60_2/0/-60_2]_S$. These internal architectures resulted in coefficients of biaxiality λ_{12} equal to 0, 1.61, and 0.57 respectively. The specimens have been designed and additively manufactured using the same parameters as the UD cases, while the hole within the gauge length was drilled subsequently. The geometrical characteristics of the manufactured specimens have been evaluated in the same way as the UD cases and reported in Table 4.3. In comparison to the CAE data, Table 4.3 shows the measured dimensions varied from 1.65% to 2.96% in width and from 12.59% to 16%. in thickness. Since OH specimens were also manufactured with end-tabs in the same way as the UD cases, more consistent measurements with an error from 0.11% to 4.55% were achieved by removing the support and top polymer layers. Eventually, a ratio between the width and the hole diameter was also calculated for each of the OH cases and reported in Table 4.3, showing consistency with the ASTM D5766 guidelines.

Table 4.3 Dimensions of OH specimens

LSS	Width			Width/ Φ_{HOLE}	Thickness				
	CAE, mm	Measured, mm	Error, %		CAE, mm	Measured, mm	Error, %	Top and support removed, mm	Error, %
$[0/90_2/0/90_2]_S$	26.2	26.99 ± 0.064	2.96	6.67	1.75	2.02 ± 0.045	12.59	1.752 ± 0.045	0.11
$[0/45_2/0/-45_2]_S$	26.2	26.64 ± 0.017	1.65	6.66	1.75	2.02 ± 0.025	13.51	1.77 ± 0.025	1.32
$[0/60_2/0/-60_2]_S$	26.2	26.67± 0.015	1.75	6.67	1.75	2.08 ± 0.025	16.00	1.833 ± 0.025	4.55

As in UD cases, the specimen preparation has been conducted according to the GOM documentation and guidelines presented in [18]. The stochastic pattern has also been applied using primer and white/black contrast, evaluated in the GOM-Aramis software, and tested quasistatically in tension using the same machine as in the UD cases. In these experiments, the full-field strain measurements were focused on the gauge-length area where the stress concentration effects were most significant. The full field strain output was divided into *x* and *y* direction strains, as shown in Figure 4.10 - 4.10 respectively, capturing the strains at damage initiation and before final failure. Ultimately, DIC imaging also captured the final failure, confirming the fracture direction consistency with the off-axis fiber orientation, as presented in Figure 4.10 d) - 4.10 d).

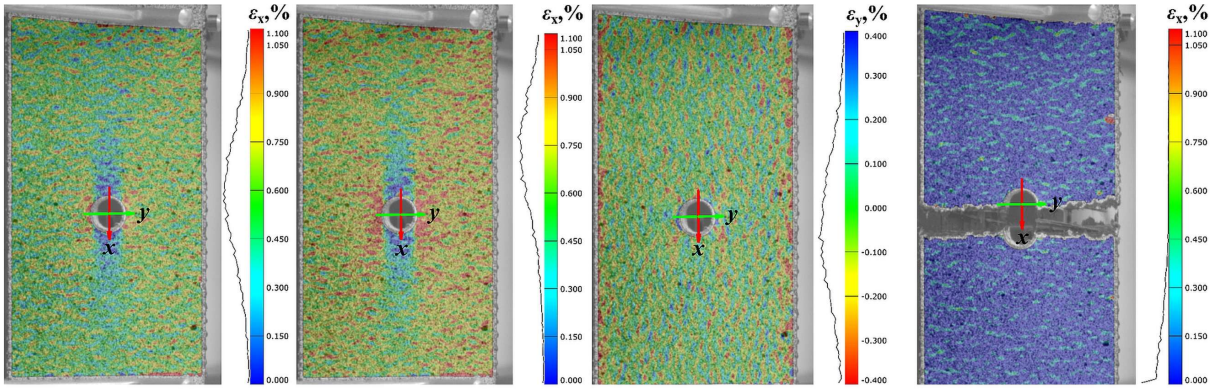

Figure 4.10 DIC results of OH-90 specimen: a) Longitudinal strains at damage initiation, b) Longitudinal pre-failure strains, c) Transverse pre-failure strains, d) Failure

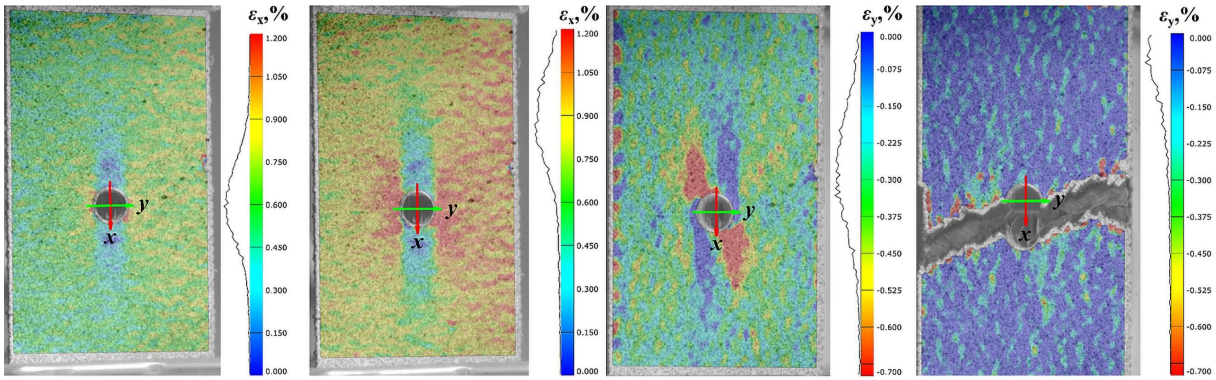

Figure 4.11 DIC results of OH-60 specimen: a) First localization, b) Longitudinal pre-failure strains, c) Transverse pre-failure strains, d) Failure

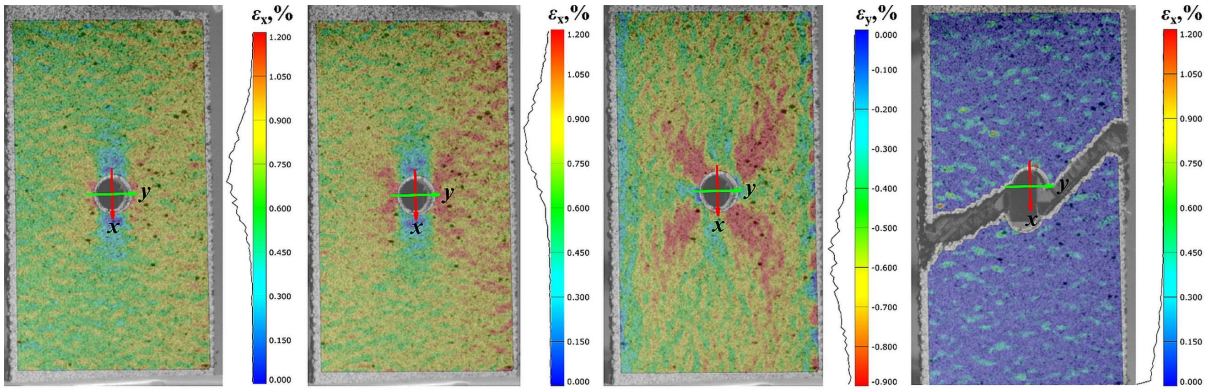

Figure 4.12 DIC results of OH-45 specimen: a) Longitudinal strains at damage initiation, b) Longitudinal pre-failure strains, c) Transverse pre-failure strains, d) Failure

The acquired experimental results were analysed according to the ASTM D5766 guidelines, and reported in subsection 4.2, covering biaxiality ratio, tensile modulus, tensile strength, and the strain at failure for each tested case. The influence of the off-axis layers on the overall laminate response for each of the studied cases was also discussed. In this subsection, a multiscale experimental procedure has been presented, starting with SEM imaging and the inspec-

tion of the constituents, followed by the destructive testing of unidirectional and shear specimens, and concluding with damage monitoring using DIC. Each step in the procedure is briefly explained, focusing on the technical aspects of conducting these experiments, while the acquired results are presented in subsection 4.2.

4.2. Experimental results

This subsection is dedicated to the presentation of the acquired experimental results through multiscale analysis, starting with the application of machine-learning algorithms in microscopic image analysis and the statistical evaluation of the acquired data, followed by the experimental evaluations of composite lamina properties and the behaviour of multidirectionally reinforced AM composites.

4.2.1. Microstructural evaluations

The geometrical values of the constituents for each of the test cases, presented in Section 4.1.1, have been measured based on the microstructural images from each cross-section. The images have been recalibrated and analysed using the open-source software FIJI, acquiring a statistically significant number of measurements for fiber diameter and misalignment, material deposition width, and layer height. The values are statistically analysed and summarized in Figure 4.13.

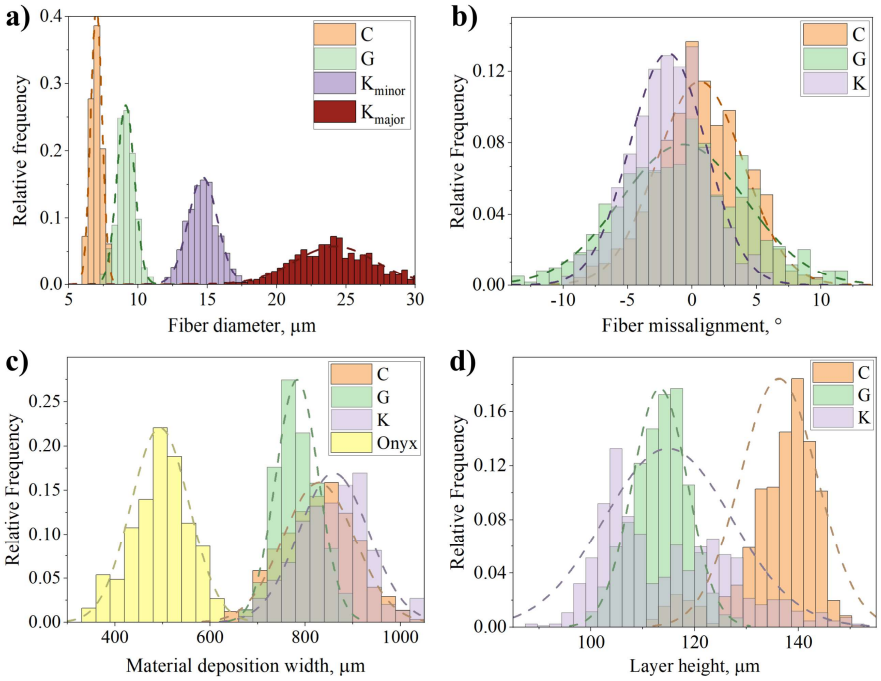

Figure 4.13 Measured data histogram compared with normal distribution: a) Fiber diameter, um; b) Fiber misalignment, °; c) Raster width, µm, d) Layer height

As shown in the graphical representation, the fiber diameters, alignments, and material deposition widths follow a normal data distribution, with the Anderson-Darling values in the range from 0.052 to 0.390, and are therefore acceptable for parametric ANOVA. However, fitting the measured layer heights with normal distribution results in an Anderson-Darling value lower than 0.005, thus a non-parametric statistical approach must be assumed instead. The acquired statistics have also been analysed using the Games-Howell pairwise comparison and the simultaneous tests for differences of means, and summarized in Table 4.4 and Table 4.5, confirming the statistical distinction between the fiber diameters, and significant dissimilarities in fiber misalignment. The comparison between glass and aramid layer height yielded a Mann-Whitney significance of 0.878, confirming the data reported by the material manufacturer.

Table 4.4 Fiber diameter and alignment statistics

	Fiber diameter				Fiber misalignment		
Material	Carbon	Glass	Aramid $_{min/maj}$	Material	Carbon	Glass	Aramid
Mean, μm	7.00 ± 0.41	9.11 ± 0.64	14.68/24.22 ±1.06/1.5	Mean, °	0.61 ± 3.37	-0.68 ± 4.88	-1.87 ± 2.96
Median, μm	7.00	9.12	14.67/24.05	Median, °	0.55	-0.52	-1.84
Skewness	0.171	-0.032	0.085	Skewness	-0.113	0.046	-0.057
Kurtosis	-0.449	-0.111	-0.375	Kurtosis	-0.170	-0.258	-0.105
Count	523	993	1177/402	Count	800	596	800
p^{AD} value	0.111	0.117	0.100	p^{AD} value	0.109	0.390	0.112

Table 4.5 Material deposition width and layer height statistics

	Deposition width				Layer height		
Material	Carbon	Glass	Aramid	Material	Carbon	Glass	Aramid
Mean, μm	829.32 ± 75.65	783.61 ± 45.55	859.83 ± 73.79	Mean, μm	138.22 ± 5.11	113.75 ± 5.40	114.86 ± 12.36
Median, μm	826.50	779.27	864.55	Median, μm	138.79	114.32	112.51
Skewness	0.025	0.207	-0.016	Skewness	-0.225	-0.226	0.607
Kurtosis	-0.406	-0.312	-0.214	Kurtosis	-0.361	-0.108	-0.326
Count	590	356	299	Count	829	400	837
p^{AD} value	0.089	0.052	0.141	p^{AD} value	<0.005	<0.005	<0.005

The measurements of fiber diameters have been conducted on *y-z* cross-sections, summarized in Figure 4.13 a), and compared to the data acquired through pyrolytic and digestive chemical procedures in Table 4.6, showing consistent results for diameter values of carbon and glass fibers. Additionally, both the minor and major diameters of the assumed ellipsoidal cross-section shape of aramid fibers were measured, showing significant deviation for both values in comparison with the available data.

Table 4.6 Fiber diameter comparison

	Fiber diameter, d_f, μm		
Material	Carbon	Glass	Aramid*
SEM	7.0 ± 0.40	9.1 ± 0.60	14.7 ± 1.05 (24.22 ± 1.5)*
Pyrolysis, [146]	7.2 ± 0.30	9.1 ± 0.30	11.7 ± 0.3
Digestion, [146]	7.0 ± 0.20	10.6 ± 0.70	/

* Minor and major diameter of the assumed elliptical cross-section

Moreover, due to the problematic definition of the reference axis, as well as the identification of the exact printing direction based on 2D SEM images, the value of fiber misalignment was adopted as the deviation between the mean and median value from the raw data summary presented in Figure 4.13. Despite the similar deposition width for CFRP and KFRP samples, Figure 4.13 c) shows a distinctive difference for the deposition width in GFRP samples, which should be investigated in further studies. Furthermore, the summary presented in Figure 4.13 d) also highlights the most probable layer height values in both CFRP and GFRP samples, while the representation of data for KFRP is scattered in the range from 100 to 130 μm. Since the material deposition is influenced by its thermal and adhesive properties, the influence of aramid fibers on material cooling and deposition should also be studied for a better understanding of both deposition width and layer height discrepancies, as presented in Figure 4.13 c) and Figure 4.13 d) respectively. Although most of the constituent's measurements can be acquired from the SEM images directly, see Figure 4.14 a), the identification of the volume fraction of the constituents requires further image processing based on thresholding and segmentation. However, despite BSED providing an enhanced image contrast, the ununiform image background led to a high standard deviation during thresholding, making the approach inapplicable. Therefore, by using the "*Trainable WEKA segmentation*" machine-learning algorithms available in FIJI, the constituents were distinguished by the pixel colour, and the images were segmented into four areas of interest including fiber, matrix, debris, voids and cracks. The segmentation process has been retrained several times to achieve the necessary refinement, resulting in the probability maps shown in Figure 4.14 b), c) and d). These were additionally processed using threshold methods to acquire the constituents' ratios. Since fragments from grinding and polishing were filling some of the initially present voids, the debris fraction has been included in the void fraction and reported as a single variable. The calculated constituents' ratios have also been compared to the measurements in Markforged filament acquired through pyrolysis, matrix digestion and TGA provided in the literature [146].

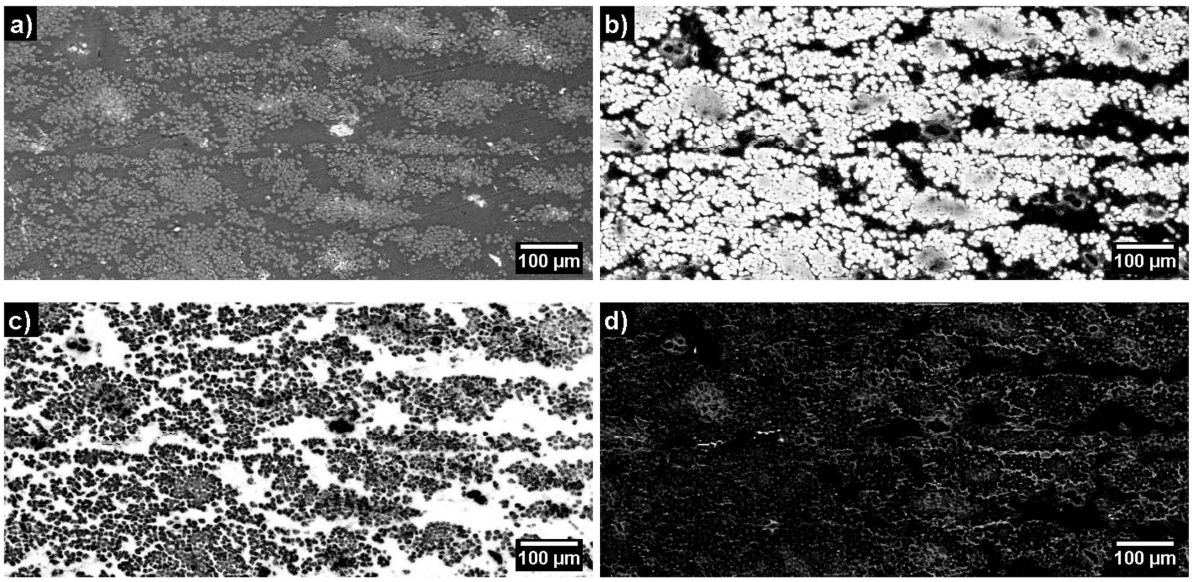

Figure 4.14 Processing image example: a) SEM image of CFRP cross-section, b) Fiber fraction probability map, c) Matrix fraction probability map, d) Voids cracks and debris fraction probability map

The comparison has been summarized in Table 4.7, showing 35%, 31%, and 37% variance between the fiber volume fraction in filaments and the samples for carbon, glass, and aramid cases respectively. The contradictions grow even more significant in localized inspections. The authors [146] selected, analysed and reported few isolated zones with denser fiber placement, while measurements on multiple randomly selected 100×100 µm fiber rich areas within each layer of each cross-section were considered in this study. Consequently, such areas of measurement caused a higher matrix presence in each of the analysed cases, while isolating the fiber dense agglomerations according to [146] led to the fiber fractions reaching 0.9 for KFRP case.

Table 4.7 Constituent volume fraction comparison

Volume fraction	Carbon reinforced sample	Carbon filament, [146]	Glass Reinforced sample	Glass filament, [146]	Aramid reinforced sample	Aramid filament, [146]
Fiber	0.536 ± 0.026	0.34 ± 0.002 0.36 ± 0.004	0.508 ± 0.043	0.32 ± 0.002 0.38 ± 0.002	0.621 ± 0.048	0.38 ± 0.03 0.40 ± 0.004
Matrix	0.41 ± 0.02	0.66 ± 0.002 0.64 ± 0.004	0.492 ± 0.011	0.68 ± 0.002 0.62 ± 0.002	0.357 ± 0.011	0.62 ± 0.03 0.60 ± 0.004
Fiber local*	0.568 ± 0.028	0.90	0.539 ± 0.012	0.68	0.869 ± 0.026	0.55
Fiber local**	0.243 ± 0.012	0.1	0.222 ± 0.005	0.32	0.45 ± 0.013	0.45
Void	0.04 ± 0.002	/	0.0767 ± 0.002	/	0.003 ± 0.0001	/

* Fiber local fraction measured within a layer in fiber rich zones; Area [100×100µm]

** Fiber local fraction measured within a layer in matrix rich zones; Area [100×100µm]

4.2.2. Lamina properties acquisition

Due to the necessity for experimental evaluation of the CFRP lamina properties, a study of unidirectional and shear behaviour was conducted. Three sets of test specimens reinforced with continuous carbon fibers were designed and additively manufactured using Markforged-X7 3D printer. Two of the sets (UD-0 and UD-90) were designed according to the ASTM-D3039 guidelines [204] as unidirectionally reinforced laminates to allow the examination of longitudinal and transversal tensile behaviour. In contrast, the third set was designed according to ASTM-D3518 [203] as multidirectionally reinforced laminate (SH-45) in order to study the LSS induced in-plane shear behaviour. The acquired experimental results have been analysed and presented in Figure 4.15, with the values for strength and stiffness in UD cases determined according to the ASTM D3093 guidelines. The calculation of shear strength, marked as red "×"sign in Figure 4.15 c), has been calculated according to the ASTM D3518 [203] as the intersection between the shear stress-shear strain (τ-γ) curve and the 0.2% offset of the shear modulus G_{12}.

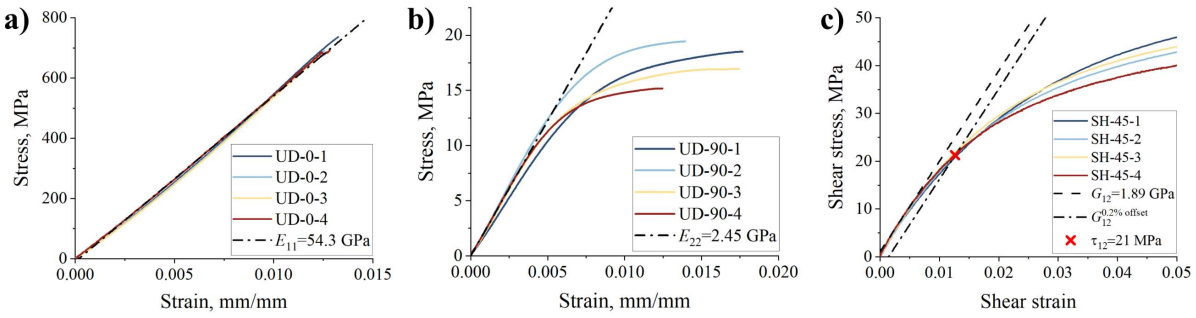

Figure 4.15 Experimental results: a) UD-0, b) UD-90, c) SH-45

The acquired experimental results were compared with the data obtained from the literature and summarized in Table 4.8, highlighting the significant discrepancies in comparison to [117] and [146].

Table 4.8 Comparison between the experimental results

Material	E_{11}, GPa	σ_1, MPa	E_{22}, GPa	σ_2, MPa	G_{12}, GPa	τ_{12}, MPa	Composite	Ref.
HM-CF-UD	175	1000	8	40	5	60	C/Epoxy	[148]
STD-CF-UD	135	1500	10	50	5	70	C/Epoxy	[148]
TorayCetex®TC910/CF	100	1900	/	/	/	/	C/PA-6	[206]
TorayCARBOSTAMP®UD	115	2200	/	/	2.5	123	C/PA-6	[206]
	60	800	/	/	/	/		[117]
CFRP-AM	69.4	905	3.5	17.9	1.9	43.4*	C/PA-6-3T	[146]
	57.35	700	2.34	18.1	1.89	43.21*		**

* Shear stress at 5% shear strain

**Experimentally acquired data

An additional comparison with conventionally manufactured UD composites using either thermoplastic or thermoset matrices has also been included in Table 4.8. However, despite the advantages of an industrial-grade 3D printer, the conventionally manufactured UD composites exceeded their AM counterparts by 45-68% for longitudinal elastic modulus and 16-68% in ultimate tensile strength. The distinction is also observed perpendicular to the fiber direction, reaching a 65-72% difference in transverse elastic modulus, with a 36-50% lower ultimate transversal strength. Similar conclusions were drawn for shear cases with a 54% difference for shear modulus and a 58-64% difference for shear strength.

An experimental study was conducted on three distinctive sets of carbon-fiber-reinforced specimens designed according to ASTM-D3039 and ASTM-D3515, additively manufactured using a Markforged-X7 3D printer, and tested while utilizing DIC measurement. The full-field strain monitoring confirmed local inter-raster debonding zones typical for failure in AM components. These debondings were detected as local high strain zones in UD-90 and SH-45 cases, corresponding to the material deposition paths while being absent from the UD-0 cases. The acquired experimental results have been analysed and summarized, then compared with both the equivalent AM and the conventionally manufactured composite laminates from the literature. The comparison with the equivalent AM studies shows consistent results, while severely diverging from the data acquired for the conventionally manufactured counterparts. Since the implementation of unidirectional composites is limited in practical applications, further study focused on the behaviour of multidirectionally reinforced laminates.

4.2.3. Damage monitoring in multidirectional CFRP composites

The behaviour of multidirectionally reinforced AM composites was studied in three distinctive cases of open-hole specimens manufactured and tested according to the ASTM D5766 standard. The specimens were designed with alternating longitudinal axial and double supporting off-axis layers $[0/\beta_2/0/\beta_2]_S$, following the guidelines from [28,162] to achieve a steady damage growth and in-plane biaxial stress state during uniaxial test conditions enforced by the LSS equivalent to $[0/90_2/0/90_2]_S$, $[0/45_2/0/\text{-}45_2]_S$, and $[0/60_2/0/\text{-}60_2]_S$. The experimental results have been summarized in Table 4.9, presenting the biaxiality ratio, tensile modulus, tensile strength, and strain at failure for each of the tested cases.

Table 4.9 Experimental results

Specimen	Layer stacking sequence	Biaxiality ratio, λ_{12}	Tensile modulus, GPa	Tensile strength, MPa	Strain at failure, %
OH90-1	$[0/90_2/0/90_2]_S$	0	19.523	156.4	0.80
OH90-2			20.061	166.6	0.83
OH90-3			18.451	144.1	0.78
OH90-4			19.816	160.0	0.86
OH60-1	$[0/60_2/0/-60_2]_S$	0.57	19.672	181.24	0.9
OH60-2			19.377	199.15	1.1
OH60-3			19.014	187.14	1.0
OH60-4			19.400	186.38	0.97
OH45-1	$[0/45_2/0/-45_2]_S$	1.61	21.552	216.25	1.0
OH45-2			22.060	213.75	1.0
OH45-3			22.846	211.9	0.9
OH45-4			22.006	187.37	0.0089

According to the synthesis reported in Table 4.9, the elastic modulus for the OH-90 case can be adopted between 18.4 GPa and 20.06 GPa, the tensile strength from 144.1 MPa to 166.6 MPa, and the strain at failure within the range of 0.78 % and 0.83 %. Similar values of the elastic moduli in range from 19.014 GPa to 19.672 GPa were also identified for the OH-60 cases, where the ultimate tensile strength and strain reached higher values of 154.76 MPa to 199.15 MPa and 0.86 % and 1.1 % respectively. As predicted, the highest values of the elastic moduli between 21.552 GPa and 22.846 GPa and the tensile strength between 187.37 MPa and 216.25MPa have been found in the OH-45 case, where the ultimate strains fell between 0.86 % and 1.1 % and did not diverge from the results acquired in the OH-60 case. The post-failure images and the acquired load-strain responses are presented in Figure 4.16 – 4.16 for each of the tested case. Comparing the acquired results with the estimates based on UD lamina data only, the influence of the supporting layers' orientation on both strength and stiffness values was observed. The case of OH-90, which did not demonstrate any characteristic biaxial behaviour, was analysed first. The study confirmed the negligible influence of perpendicularly oriented supporting layers, which consequently led to the anticipated failure mode with cracks growing perpendicular to the load direction, as shown in Figure 4.16.

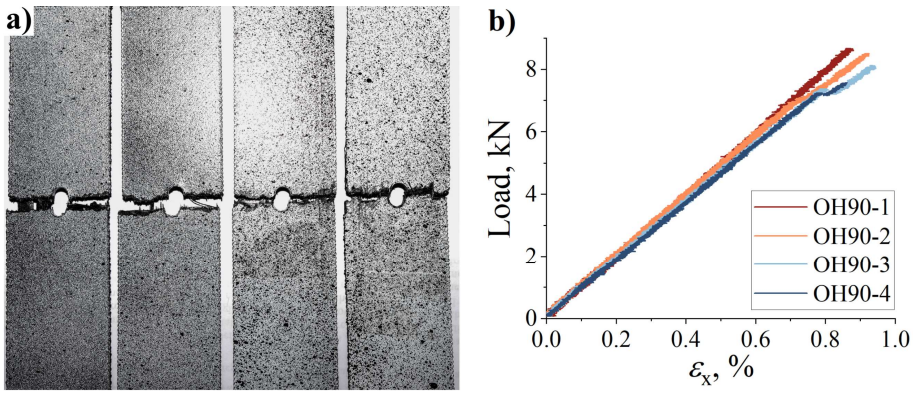

Figure 4.16 a) Failed OH-90 specimens, b) Load-strain diagram

The behaviour of OH-60 specimens is also highly influenced by the presence of UD-0 layers. Since in this case the off-axis layers carry a larger proportion of the axial load, an average increase of 6.2% and 7% has been measured for the ultimate strength and strain values, in comparison with the OH-90 case. Additionally, the damage growth in OH-60 cases shows an increased dependence on the orientation of the supporting layers, leading to an equivalent crack inclination, as shown in Figure 4.17.

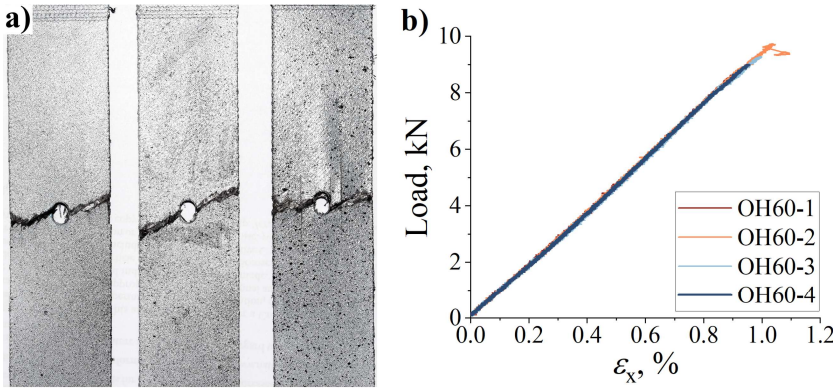

Figure 4.17 a) Failed OH-60 specimens, b) Load-strain diagram

In contrast, the supporting layers in OH-45 cases carry a larger percentage of the axial load, which, in comparison with the OH-90 case, leads to an increase in the average values of ultimate strength and strain by 18% and 3.8% respectively. Furthermore, the damage progression follows the direction of the supporting layers' orientation as in the OH-60 case, leading to an anticipated failure mode, as shown in Figure 4.18.

Overall, the experimental investigations have shown a reasonable degree of scatter and results consistent with the available data in the literature. In microstructural evaluation, significant distinctions have been detected for the fiber fractions of unidirectionally reinforced layers in comparison with the published data for the single filament. This was followed by even larger discrepancies after analysing fiber or matrix dominant local distributions.

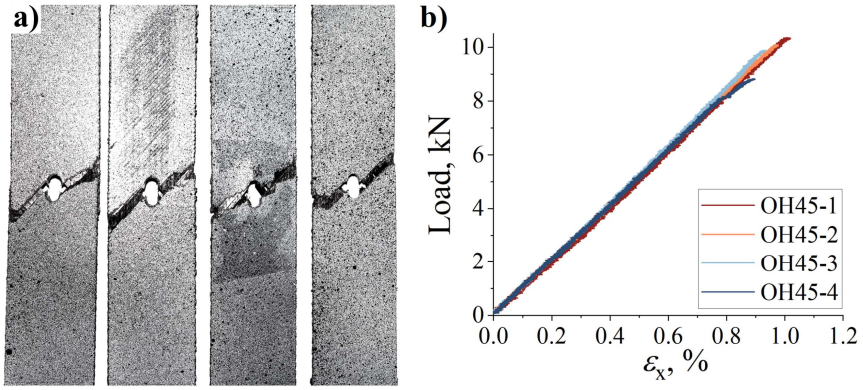

Figure 4.18 a) Failed OH-45 specimens, b) Load-strain diagram

Furthermore, the UD and shear tests yielded results consistent with the available dataset, while some deviations have been detected when comparing the ultimate tensile strength in UD0 cases. Since the experimental studies of additively manufactured multidirectionally reinforced open-hole specimens with LSS induced multiaxial in-plane stress state are not available in the literature for comparison, the conducted experiments have only been validated with small data scatter and crack growth following the estimated path guided by the supporting layers.

The initial part of this section has been intended for presentation of the proposed multiscale experimental procedure, including the design and manufacturing features during the processes, to summarize the acquired results in the micro-, meso- and macro-level. The microstructural inspection was presented first, describing the procedures in SEM image acquisition. The guidelines for the design and preparation of tensile and shear specimens were presented subsequently, focusing on the description of the DIC system application. This was followed by the summary on LSS configuration in multidirectionally reinforced laminates, and the damage monitoring using full field strain measurements. The results have been presented in the second subsection, following the sequence of the conducted experimental procedures. The results of the statistical evaluations have been summarized in this subsection, enabling the comparison of the microstructural data with relevant sources. Furthermore, the results of tensile and shear test were also analysed, and results were consistent with the data from the literature. The section ends with the presentation of the results acquired for multidirectionally reinforced laminates with open-hole stress concentrators, highlighting the influence of the supporting layers on the overall load-bearing capacity of the tested cases. Based on these experimental results, an appropriate micromechanical and a continuum damage model will be determined, calibrated, and validated as presented in the following section.

5. MATERIAL MODELLING

In order to demonstrate the material behaviour simulation through multiple length scales, this section[2] is divided into two subsections: micromechanical modelling and macromechanical damage analysis. The analysis presented in the first subsection is based on strain-controlled numerical homogenization of a heterogenic material system, while the second subsection is focused on the damage modelling in multidirectional reinforced laminates based on unidirectional inputs using Fortran-Abaqus subroutines.

5.1. Micromechanical modelling

While the behaviour of unidirectional reinforced AM CFRP composites has been comprehensively studied, it has rarely been supported by a micromechanical analysis. Therefore, a strain-controlled numerical homogenization of a heterogenic material system has been proposed to acquire the material properties in tensile and shear loading conditions. The representative volume element has been designed based on the results from the microscopic analyses for carbon, glass, and aramid fiber-reinforced composites respectively. Additionally, the carbon-fiber-reinforced RVE has been calibrated according to the results from the tensile and shear experiments, assuming the cohesive nature instead of an ideal bond for the fiber/matrix interface. The same assumption has been applied on other types of RVEs, confirming the validity of cohesive interphase implementation to account for bonding defects in AM materials.

5.1.1. RVE design

For the purpose of unifying the various constitutive models within a single homogenized response, a representative element was modelled according to the data from the statistically evaluated material's microstructure. The basic RVE conventions have been adopted according to [8,32,40,133,141,143], with the assumption of hexahedral fiber arrangement. The RVE size was kept small enough to save on computational time, while the RVEs included more than one

[2] Part of the work described in this section was published by the author of the thesis and his collaborators in two peer-reviewed scientific papers [59] and [60], which were produced and published as part of the obligations foreseen in the curriculum of the doctoral study of the Faculty of Engineering of the University of Rijeka, Croatia, hence this section is based, partly directly derived and cited from this work.

fiber for more accurate results in yielding and plasticity [5,141]. To comply with these requirements, and to respect the measured ratio of fibers for each of the studied cases, the length of the RVEs' equilateral base was defined as double the value of the inter-fiber distance in a hexagonal arrangement. A cubic RVE designed according to these assumptions included one fiber in the centre and four fiber quarters placed along the RVE edges in the longitudinal direction. The implementation of such an arrangement enables the fibers to geometrically complete each other upon virtual assembly, ensuring geometrical, material, and mesh periodicity, while enforcing periodic boundary conditions. Therefore, to determine the necessary RVE size, the inter-fiber length was varied for each of the studied composites, returning the calculated volume fractions as shown in Figure 5.1.

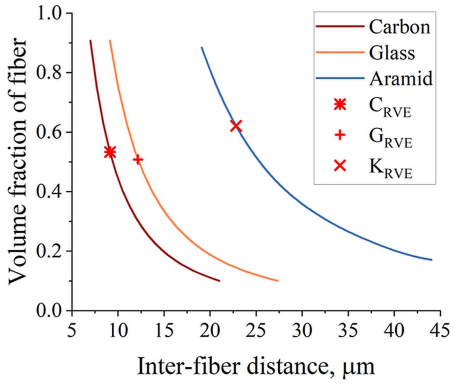

Figure 5.1 Calculated relation between the inter-fiber distance and the volume fraction for carbon, glass, and aramid-fiber-reinforced UD composite, respectively

Respecting the measured fiber fraction and following the results from Figure 5.1, the inter-fiber distance was determined for each of the studied cases, and presented in Table 5.1.

Table 5.1 RVE size determination

Fiber Material	Fiber diameter, μm	Fiber fraction	RVE size			Inter-fiber distance	Fiber diameter / RVE length
			L, μm	*W*, μm	*H*, μm	μm	
Carbon	7.00	0.533	9.13	9.13	15.81	9.13	0.767
Glass	9.11	0.508	12.17	12.17	21.08	12.17	0.748
Aramid	14.68*/24.22**	0.621	22.81	22.81	39.51	22.82	0.64*/1.06**

Inter-fiber distance is expressed as a distance between fiber cross-section origins
* Minor diameter of the assumed elliptical cross-section
** Major diameter of the assumed elliptical cross-section

As shown in Figure 5.2, the resulting RVE models have been designed in the Abaqus CAE environment as equi-lateral base hexahedrons with fibers arranged in the *x* axis direction. Following the guidelines presented in [143] the fibers were modelled as parts of the original domain, while preserving the internal boundaries. Since the SEM inspections of *x*-*y* and *x*-*z* cross-sections revealed fiber/matrix bonding deficiencies, voids and inter-fiber cracks, the influence

of these defects on mechanical behaviour was anticipated. These defects caused discrepancies between the experimental and numerical results. These have therefore been compensated for by introducing zero-thickness cohesive interphases modelled as mesh offset from fiber internal boundaries, as shown in Figure 5.2 d). Following the guidelines presented in [133], similar interphases have also been introduced as fiber-breaking planes on edge fibers in order to simulate the pulled and broken fibers as opposed to the ideally bonded central fiber.

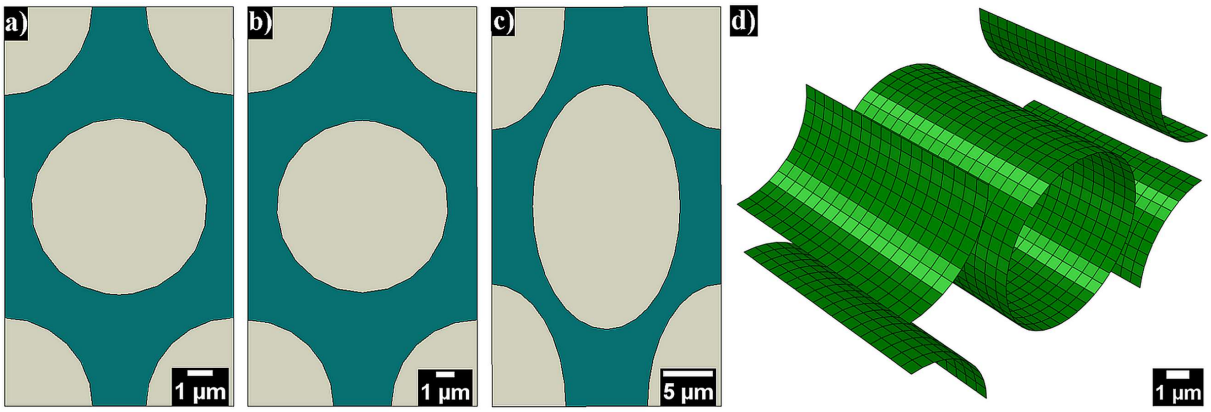

Figure 5.2 RVE models: a) C-RVE ($V_{\mathrm{ff}} = 0.533$); b) G-RVE ($V_{\mathrm{ff}} = 0.508$); c) K-RVE ($V_{\mathrm{ff}} = 0.621$), d) Cohesive interface

5.1.2. Material model of the constituents

After achieving geometrical consistency with the microstructural measurements, the RVE-s were updated with the appropriate constituents' material models in order to represent the composite material behaviour more accurately. Due to the absence of data on the exact filament composition, the mechanical characteristics of the fibers, given in Table 5.2, were adapted from [146]. Additionally, the fiber elastic moduli were modified to account for the measured fiber misalignment.

Table 5.2. Fiber material properties acquired through pyrolytic analysis [146]

Type of fiber	ρ, g/cm^3	E_f, GPa	σ_f, GPa
Carbon fiber	0.74 ± 0.05	191 ± 6	2.6 ± 0.2
Aramid fiber	1.60 ± 0.10	117 ± 7	1.1 ± 0.4
Glass fiber	1.59 ± 0.12	80 ± 3	2.4 ± 0.5

ρ = linear density; E_f = elastic modulus; σ_f = tensile strength

Based on DSC thermographic analysis conducted in [146], and the comparison of its thermal behaviour to that of the injection-molded counterparts [191], the matrix material used in Mark-forged carbon fiber composites was identified as amorphic polyamide PA6-3-T, while the properties of fiber reinforcements were also adopted from [146]. The same process has also been adopted for other filaments, identifying the PA6 as matrix in glass and aramid fiber reinforced

composites. Since the linear-elastic law is not applicable for modelling of the matrix behaviour at the microlevel, the experimental data for the elastic-plastic and Ramberg-Osgood plasticity models have been adopted based on experimental data for injection-moulded PA6-3T at the temperature of 20°C [191]. The Ramberg Osgood coefficients have been calculated by fitting the Eq. 5.1 to experimental data while minimizing the error using the least square method.

$$\varepsilon = \frac{\sigma}{E} + \alpha \left(\frac{\sigma}{\sigma_0} \right)^{n-1} \tag{5.1}$$

Based on the expression presented in Eq. (5.1), a Fortran script has been developed to calculate the stress values σ_i for an arbitrary strain value ε_i, while minimizing the errors in Eq. 5.2 using the Newton-Raphson method, where σ_i is the approximation of the stress value, σ_y is the yield strength, and E is modulus of elasticity. The Newton-Raphson algorithm is repeated until the accuracy of 10^{-8} has been acquired.

$$\sigma_{i+1} = \sigma_i - \frac{f(\sigma_i)}{f'(\sigma_i)} = \sigma_i - \frac{\frac{\sigma_i}{E} + \alpha \cdot \frac{\sigma_i}{E} \cdot \left(\frac{\sigma_i}{\sigma_y} \right)^{(n-1)} - \varepsilon}{\left(\alpha \cdot n \cdot \sigma_i^{\,n-1} \right) \cdot \left(\sigma_y^{(n-2\cdot(n-1)-1)} \right) + 1} \tag{5.2}$$

The resulting parameters and the calculated stress-strain relations have been compared with the experimental data [191], and presented in Figure 5.3 for both PA-6 and PA-6-3T with yield strengths of 20MPa and 30 MPa respectively.

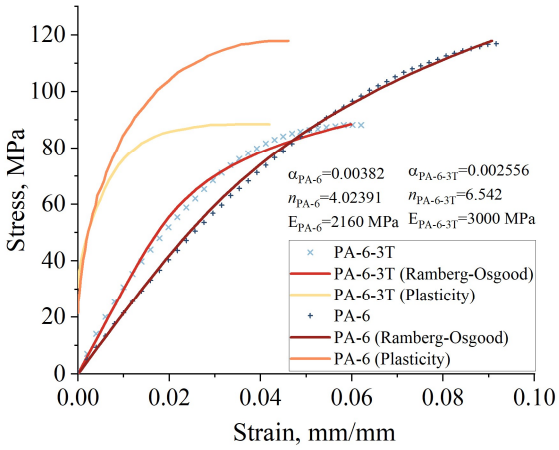

Figure 5.3 Experimental data [191], Ramberg-Osgood model, and plasticity data for polyamides PA-6-3T and PA-6

5.1.3. Homogenization

The numerical homogenization of the RVE model has been conducted following the guidelines presented in [141] and [143]. The process initiates with RVE boundary nodes being sorted

into surfaces, edges, and corners respectively. Analysing the node coordinates on the RVE boundary, each node is paired with its matching node from the opposite side of the RVE model based on the required mapping accuracy. Subsequently, these nodes are appended within the same set in the same order, then the sets are linearly constrained to link the degrees of freedom (DOF) of the associated pairs. Therefore, this process synthesizes the boundary conversion to single node sets with matching node and location labels to previously associated sets. The linking is achieved through linear constraint equations and compensation for the rigid body motions based on DOF-s and reference points (RF) [143]. Since the calculation for each of the material properties requires specific loads and constraints enforced through boundary conditions, the homogenization is performed through multiple stages, where each of the properties is analysed separately. Therefore, following the guidelines presented in [143], the homogenized mechanical properties can be calculated as shown in Eq. 5.3 and Eq. 5.4.

$$E_{11}=\frac{\sigma_1}{\varepsilon_1}=\frac{\frac{\sum_{i=0}^{N}F_i}{(h\cdot w)}}{\frac{\Delta l}{l}};\qquad E_{22}=\frac{\sigma_2}{\varepsilon_2}=\frac{\frac{\sum_{i=0}^{N}F_i}{(w\cdot l)}}{\frac{\Delta h}{h}};\qquad E_{33}=\frac{\sigma_3}{\varepsilon_3}=\frac{\frac{\sum_{i=0}^{N}F_i}{(h\cdot l)}}{\frac{\Delta w}{w}} \tag{5.3}$$

$$G_{12}=\frac{\tau_{12}}{\gamma_{12}}=\frac{\frac{\sum_{i=0}^{N}F_i^{12}}{(l\cdot w)}}{\frac{\Delta l}{h}+\frac{\Delta h}{l}};\qquad G_{13}=\frac{\tau_{13}}{\gamma_{13}}=\frac{\frac{\sum_{i=0}^{N}F_i^{13}}{(l\cdot h)}}{\frac{\Delta l}{w}+\frac{\Delta w}{l}};\qquad G_{23}=\frac{\tau_{23}}{\gamma_{23}}=\frac{\frac{\sum_{i=0}^{N}F_i^{23}}{(l\cdot h)}}{\frac{\Delta h}{w}+\frac{\Delta w}{h}} \tag{5.4}$$

In these expressions, the number of nodes on the surface is defined by N, while the RVE lengths in x, y and z axis directions are represented by l, w, and h, respectively. The homogenized properties acquired through Eq. 5.3 and Eq. 5.4 are accurate only for small strains or in cases where linear elastic behaviour of the constituents is assumed. In cases with constituents' nonlinearity or high strain values, damage and plasticity models should be considered for brittle and ductile constituents [133,141].

The meshing procedure has been conducted in the Abaqus CAE environment with tetrahedral C3D6 elements, using the sweeping algorithm as suggested in [141,143]. The mesh sensitivity analysis has been initially conducted on single fiber RVE, confirming that if the required periodic mapping accuracy is achieved, the mesh size has no significant influence on the homogenization results for low strains [5,133,143]. According to these results, and following the

methodology presented in [33], three multi-fiber RVEs with cohesive fiber/matrix interfaces have been designed, adopting 54588, 56952 and 51934 elements for carbon, glass, and aramid reinforced composite respectively. To account for the cohesive effects, a nonlinear analysis has been carried out in the Abaqus CAE environment through a time-period of 100s with an initial increment size of 0.1 within the interval from 0.001 to 1.0. The study has been conducted for each of the cases in order to acquire the homogenized tensile and shear properties. However, only carbon fiber composites have been experimentally validated. The homogenized parameters for glass- and aramid-fiber-reinforced composites have only been proposed in this phase of research.

5.1.4. Calibration and validation

Analyzing the initial RVE homogenization assuming the ideal fiber/matrix interface, significant discrepancies in comparison with the experimentally acquired data have been observed. This is assumed to be caused by fiber/matrix cohesion weaknesses and material deposition bonding manifested as matrix rich contact-zones and inter-fiber voids on the microscale, which was observed using SEM. It was also confirmed on the macroscale as localized high strains using DIC and thermal imaging. Based on these observations, a weaker cohesive contact has been assumed for the fiber/matrix contact and embedded into the homogenization procedure as a cohesive zone interphase to account for the constituents debonding. However, the cohesive contact between the deposited filaments has been ignored due to the absence of clear contact distinctions in microstructural observations. Given that the properties of the cohesive interface have not been acquired experimentally, the cohesive zone model (CZM) has been adopted for a similar thermoplastic/fiber interface [170], and calibrated according to the experimentally acquired CFRP response, as shown in Table 5.3. The effects of cracked and pulled fibres have also been accounted for by longitudinally fracturing half of the embedded fibers and introducing cohesive contacts on the breaking planes to simulate the fiber damage due to low bonding. These CZM parameters have also been calibrated according to the experimental results.

Table 5.3 Adopted CZM properties used in the analysis

	Parameter	C/PA6-3T	G/PA6	K/PA6	C_{axial}	G_{axial}	K_{axial}
Traction	E/E_{nn}	$4 \cdot 10^5$	$7 \cdot 10^5$	$3 \cdot 10^5$	$1.9 \cdot 10^5$	$0.7 \cdot 10^5$	$1.17 \cdot 10^5$
	G_1/E_{ss}	$1.05 \cdot 10^5$		$0.65 \cdot 10^5$			
	G_2/E_{tt}						
Quads damage nominal stress	Normal-only mode	10	12	15	520	480	220
	First direction	11	5	7			

	Second direction	
Damage evolution	Type	Energy
	Softening	Linear
	Degradation	Maximum
Mix mode behaviour	BK	0.63
Mode mix ratio fracture energy	Normal mode	0.949
	Shear mode 1st dir.	1.35
	Shear mode 2nd dir.	1.35

Experimental and numerical results for longitudinal, transverse and shear behaviour in carbon-fiber-reinforced cases have been compared and presented in Figure 5.4 a), b), and c) respectively. The comparison of the results for longitudinally loaded composites, shown in Figure 5.4 a), validates the effects caused by cracked and pulled fibres, and it is consistent with the experimental results. Therefore, further studies should concentrate on experimentally acquiring fiber-pullout data. As anticipated for the transverse tests in FRPs [8], significant discrepancies in the plastic region surpassing 0.6% strain have been observed in experimental results and presented in Figure 5.4 b). Even so, the implementation of the ideal fiber/matrix bond diverged significantly from the already scattered experimental data, thus a weaker cohesive interface has been necessary in this case. Furthermore, by observing in-plane shear response, presented in Figure 5.4 c), little scatter between the experimental results could be found before reaching the shear strength. The shear strength was determined according to ASTM D3518 [203], as the intersection between the shear stress-shear strain (τ-γ) curve and the 0.2% offset of the shear modulus G_{12}. At higher values of shear strain the interlaminar effects on the laminate behaviour grow significantly, hence divergence of RVE predictions from the experimentally acquired data is expected. However, by introducing a weaker fiber/matrix cohesive interphase, the RVE results are consistent with the experimental results up to 3% of shear strain, while the deviation shifts approaching 5% of shear strain.

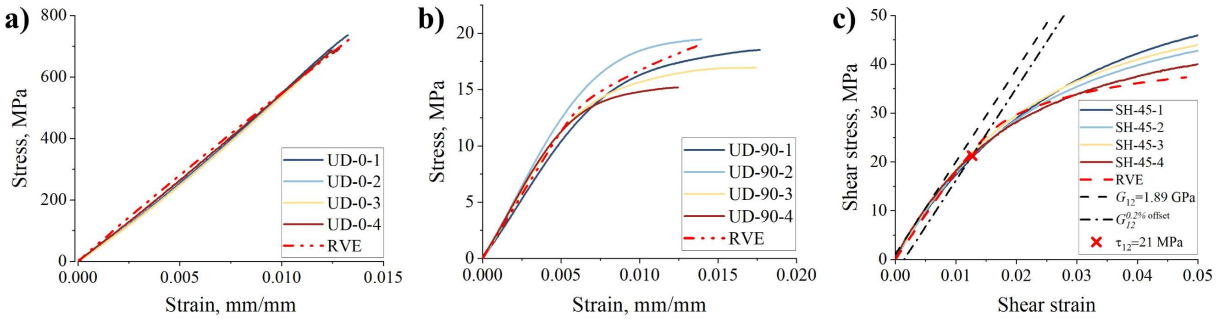

Figure 5.4 Comparison between RVE and experimental results for CF specimens: a) UD-0, b) UD-90, c) SH-45

All things considered, the proposed cohesive interface has also been adopted in glass and aramid reinforced RVEs. However, without experimental comparison, the CZM properties for transverse and shear have been calibrated according to carbon fiber composite and the experimental results of the conventionally manufactured counterparts [84]. For these cases, only the proof of the concept is proposed, emphasizing the necessity for further experimental studies. The comparison between RVE responses of the studied carbon (C_{RVE}), Glass (G_{RVE}), and Aramid (K_{RVE}) cases has been given in Figure 5.5 a), b), and c), showing longitudinal, transverse and in-plane shear behaviour respectively.

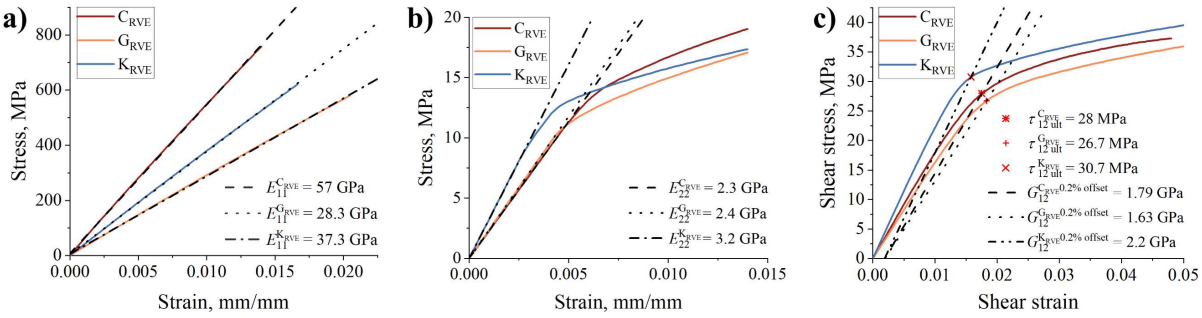

Figure 5.5 RVE result comparison: a) Longitudinal uniaxial, b) Transverse uniaxial, c) In-plane shear

The difference in longitudinal response between the studied cases is consistent with the mechanical properties of the embedded fibres, and the response follows the trends of the available data. However, lacking the experimental data, the transverse and in-plane shear response of glass and aramid reinforced RVEs is calibrated according to CFRP response, keeping the strength relations analogous to the conventionally manufactured composite counterparts, hence the necessity for proper experimental validation is again emphasized. A summary of the experimental and numerical results for each of the studied cases has also been presented in Table 5.4. where a comparison with similar AM and conventionally manufactured composites has also been conducted, correlating fiber content, stiffnesses, and strengths.

Table 5.4 Composite material properties comparison

Material	V_{ff}	E_{11}, GPa	σ_1, MPa	E_{22}, GPa	σ_2, MPa	G_{12}, GPa	τ_{12}, MPa	Composite	Ref
HM-CF-UD	0.60	175	1000	8	40	5	60	Carbon//Epoxy	[148]
STD-CF-UD	0.60	135	1500	10	50	5	70	Carbon//Epoxy	[148]
Toray Cetex® TC910/CF	0.60	100	1900	/	/	/	/	Carbon//PA-6	[206]
Toray CARBOSTAMP®UD	0.50	115	2200	/	/	2.5	123	Carbon//PA-6	[206]

CFRP - AM	/ 0.53 0.53	60 54.3 55	800 700 750	/ 2.34 2.4	/ 18.1 16.65	/ 1.89 1.83	/ 21 23.3	Carbon/PA-6-3T	[117] * **
E-Glass-UD	0.60	40	1000	8	30	4	40	Glass /Epoxy	[148]
Toray Cetex® TC910/GF	0.60	30	900	/	/	/	/	Glass /PA-6	[206]
GFRP - AM	/ 0.51	21 22.4	590 314	/ 2.17	/ 17.25	/ 1.8	/ 18.7	Glass/PA-6	[117] **
Kevlar-UD	0.60	75	1300	6	30	2	60	Kevlar/Epoxy	[148]
KFRP - AM	/ 0.60	27 39.8	610 525	/ 1.83	/ 15.9	/ 1.7	/ 20.0	Kevlar/PA-6	[117] **

* Experimental results: uniaxial ASTM-D3039; shear ASTM-D3518

** Homogenized RVE results utilizing CZM at fiber/matrix interphase: indices (1) and (2) at 1.4% strain, (12) at 0.2% shear modulus offset according to ASTM-D3518

According to the summary presented in Table 5.4, the RVE results for carbon-fiber-reinforced composites are consistent with the available data, while glass and aramid-fiber-reinforced RVEs follow the transversal and in-plane shear trends observed in conventionally manufactured composites. However, the longitudinal RVE case for aramid-fiber-reinforced RVE overpredicts the composite modulus by 12.8 GPa in comparison to the available data. Further research on the micromechanical response is necessary. Despite these inconsistencies, the RVE calculations can still be used as guidelines in preliminary design due to the absence of other readily available data. In the research of novel material compositions, the presented protocol can be replicated for conducting virtual experiments with similar fiber/matrix systems. In addition, a comparison between the AM and similar conventionally manufactured thermoset and thermoplastic UD composites is presented in Table 5.4. While the experimentally acquired strength and stiffness for AM composites differ from the manufacturers' data by only 5% and 12.5% respectively, the conventionally manufactured composites manifest 45-68% higher stiffness and 16-68% higher ultimate tensile strength values in comparison, despite the AM counterparts being produced using an industrial grade 3D printer. Furthermore, the measured transverse modulus of the AM carbon-fiber-reinforced composite is 65-72% lower in comparison to its conventionally manufactured counterpart, followed by a 36-50% lower value for its ultimate tensile strength in the transverse direction. Similar distinctions can be observed in the shear case, where the AM carbon-fiber-reinforced composite reaches 54% lower value for the shear modulus, followed by 58-64% lower value for the shear strength. Analogous results can also be acquired by comparing the G_{RVE} and K_{RVE} results with their conventionally manufactured counterparts. The presented study leads to a conclusion that AM technology still struggles to deliver components with the necessary mechanical properties. However, by analysing the UD experimental data, the influence of the additive manufacturing method on material properties can be determined.

5.2. Macro-scale damage and failure analysis

Based on the conducted numerical and experimental analyses, the unidirectional and shear lamina properties have been determined. However, as composites are seldom used as unidirectional in engineering applications, this subsection is focused on the behaviour of multidirectionally reinforced AM composite laminates, their constitutive relations, and modelling of damage initiation and propagation based on Puck's failure theory within CDM framework.

5.2.1. Damage modelling

Since the micromechanical response of fiber-reinforced polymer composites is influenced by the interactions between the constituents on the microlevel, and the layers on the mesolevel, the modelling strategies for their behaviour often include multiple length scales. While the microscale analysis is based on the microstructural inspections of the constituents, and focuses on modelling their interactions which are difficult to acquire experimentally [133,135], the mesoscale analysis is based on lamina orthotropy, and is usually acquired through standardized destructive tests. To analyse the macromechanical behaviour of the multidirectionally reinforced composite laminates based on experimentally and numerically acquired lamina properties, a progressive damage analysis protocol has been proposed based on [28,29,164]. Following these guidelines, the steady damage progression was realized by adopting a specific LSS $[0/\beta_2/0/\beta_2]_S$ including alternating laminas reinforced in the loading direction (UD-0), and the double off-axis laminas (UD-β). Furthermore, this LSS configuration also constrains the off-axis laminas between the UD-0 ones, which leads to a linear elastic laminate behaviour within 1.3% of longitudinal axial strain, which UD-0 can withstand, hence the implementation of linear elastic transversely orthotropic constitutive model is valid [190]. To comply with the CDM framework, each lamina has been assumed as an homogeneous orthotropic continuum, relating the strength criteria to the lamina itself as the homogenized calculation element [48]. A distinction between the fiber fracture (FF) and the inter-fiber fracture (IFF) is enforced in order to ensure the physical representation of the strength criteria. Based on the comprehensive studies presented in [98,156,190], the distinctive criteria for fiber fracture f_{FF} in tension (t) and compression (c) have been adopted. Based on the initial comparison between calculated and experimentally acquired data, the AM inherited susceptibility to shear damage caused by weaker interlaminar cohesion was accounted for in the tensile fracture criteria, hence the shear stress influence has been added to the original expression, as shown in Eq. 5.5.

$$f_{\mathrm{E_{FF}}} = \frac{1}{\pm R_{\|\mathrm{f}}^{\mathrm{t,c}}}\left[\sigma_{11} - \left(\nu_{\|\perp} - \nu_{\perp\|\mathrm{f}} \cdot m_{\sigma\mathrm{f}} \frac{E_{\|}}{E_{\|\mathrm{f}}}\right)\left(\sigma_{22}+\sigma_{33}\right) + m_{\tau\mathrm{f}}\sqrt{\left(\tau_{12}+\tau_{13}\right)^2}\right] \tag{5.5}$$

To distinguish between tension and compression the ultimate strength variable $\pm R_{\|\mathrm{f}}^{\mathrm{t,c}}$ presented in Eq. 5.5. is differentiated between tensile $+R_{\|\mathrm{f}}^{\mathrm{t}}$ and compressive $-R_{\|\mathrm{f}}^{\mathrm{c}}$ values. Furthermore, the effective stress in fiber direction is calculated as a relation between fiber and lamina load-bearing capabilities, as shown in Eq. 5.6. The coefficient ξ has also been introduced for more accurate calibration.

$$+R_{\|\mathrm{f}}^{\mathrm{t}} = \xi \cdot R_{\|\mathrm{UD}}^{\mathrm{t}} \cdot \left(\frac{E_{\|\mathrm{f}}}{E_{\|}}\right) \tag{5.6}$$

Additionally, the inter-fiber fracture criteria have been adopted according to the study presented in [48] for tensile and compressive cases, as shown in Eq. 5.7 and Eq. 5.8 respectively.

$$f_{\mathrm{E_{IFF}}}(\theta) = \sqrt{\left[\left(\frac{1}{R_{\perp}^{\mathrm{At}}} - \frac{p_{\perp\psi}^{\mathrm{t}}}{p_{\perp\psi}^{\mathrm{A}}}\right)\sigma_n(\theta)\right]^2 + \left(\frac{\tau_{\mathrm{nt}}(\theta)}{R_{\perp\perp}^{\mathrm{A}}}\right)^2 + \left(\frac{\tau_{\mathrm{n1}}(\theta)}{R_{\perp\|}^{\mathrm{A}}}\right)^2} + \frac{p_{\perp\psi}^{\mathrm{t}}}{p_{\perp\psi}^{\mathrm{A}}}\sigma_n(\theta) \tag{5.7}$$

$$f_{\mathrm{E_{IFF}}}(\theta) = \sqrt{\left(\frac{p_{\perp\psi}^{\mathrm{c}}}{p_{\perp\psi}^{\mathrm{A}}}\sigma_n(\theta)\right)^2 + \left(\frac{\tau_{\mathrm{nt}}(\theta)}{R_{\perp\perp}^{\mathrm{A}}}\right)^2 + \left(\frac{\tau_{\mathrm{n1}}(\theta)}{R_{\perp\|}^{\mathrm{A}}}\right)^2} + \frac{p_{\perp\psi}^{\mathrm{c}}}{p_{\perp\psi}^{\mathrm{A}}}\sigma_n(\theta) \tag{5.8}$$

In these expressions, variables $R_{\perp}^{\mathrm{A}}$ and $R_{\perp\|}^{\mathrm{A}}$ represent the tensile strength perpendicular to fiber direction and to the in-plane shear strength respectively. The $R_{\perp\perp}^{\mathrm{A}}$ represents the fracture resistance to transverse shear stressing and is calculated according to Eq. 5.9. Furthermore, the ratio $p_{\perp\psi}^{\mathrm{t,c}}/p_{\perp\psi}^{\mathrm{t,c}}$ is acquired according to Eq. 5.10, where ψ signifies the resultant shear direction within the fracture plane [48], as shown in Eq. 5.11.

$$R_{\perp\perp}^{\mathrm{A}} = \frac{R_{\perp}^{\mathrm{c}}}{2\left(1+p_{\perp\perp}^{\mathrm{c}}\right)} \tag{5.9}$$

$$\frac{p_{\perp\psi}^{\mathrm{t,c}}}{p_{\perp\psi}^{\mathrm{A}}} = \frac{p_{\perp\perp}^{\mathrm{t,c}}}{p_{\perp\perp}^{\mathrm{A}}}\cos^2(\psi) + \frac{p_{\perp\|}^{\mathrm{t,c}}}{p_{\perp\|}^{\mathrm{A}}}\sin^2(\psi) \tag{5.10}$$

$$\cos^2(\psi) = \frac{\tau_{\mathrm{nt}}^2}{\tau_{\mathrm{nt}}^2 + \tau_{\mathrm{n1}}^2} \tag{5.11}$$

Additionally, both inert-fiber fracture conditions are dependent on the fracture plane inclination θ, which is calculated based on the inclination parameters proposed in [48,190]. According to the summary on Puck failure criteria presented in [98,156,190], the fracture plane orientation is determined by calculating the inter-fiber fracture stress exposure in each of the potential planes within -90° to 90° interval with the 1° increment. The plane generating the maximal

value of stress exposure is adopted as the fracture plane. If the stress exposure reaches a threshold value equal to 1, a failure on the fracture plane within the continuum is assumed and the damage variable is set to 0.99, reducing the material properties within the damaged element. This damage is therefore represented using a smeared crack approach, showing areas of material stiffness degradation in contrast to discrete local material discontinuities. The material property degradation laws have been adopted from [98,156,190] and the stiffness deterioration is calculated according to Eq. 5.12 - 5.15. In order to increase the significance of shear stresses, two additional parameters κ_{DEG} and n_{DEG} have been introduced, modifying the expressions in Eq. 5.14 and 5.15 and leading to a nonlinear degradation law.

$$E_1 = (1 - D_{\mathrm{fc}})(1 - D_{\mathrm{ft}})E_1^{\mathrm{initial}} \tag{5.12}$$

$$E_2 = (1 - D_{\mathrm{ft}})(1 - D_{\mathrm{mt}})E_2^{\mathrm{initial}} \tag{5.13}$$

$$G_{12} = (1 - D_{\mathrm{ft}})(1 - D_{\mathrm{mc}} \cdot \kappa_{\mathrm{DEG}})^{n_{\mathrm{DEG}}} \cdot G_{12}^{\mathrm{initial}} + 0.05 \cdot G_{12}^{\mathrm{initial}} \cdot D_{\mathrm{mt}} \tag{5.14}$$

$$G_{23} = (1 - D_{\mathrm{ft}})(1 - D_{\mathrm{mc}} \cdot \kappa_{\mathrm{DEG}})^{n_{\mathrm{DEG}}} \cdot G_{23}^{\mathrm{initial}} + 0.05 \cdot G_{23}^{\mathrm{initial}} \cdot D_{\mathrm{mt}} \tag{5.15}$$

Within these degradation laws, the distinction between compressive and tensile damage is shown by subscripted indices (c) and (t), while (f) and (m) stand for fiber and matrix respectively. Since the stress exposure depends only on the post-failure load redistribution, this approach returns unrealistically smooth degradation [157].

5.2.2. Finite Element Analysis setup

Since the range of the readily available damage models for FRP materials in commercial FEA software is limited, it is often necessary to implement a user-defined material model to account for specific material behaviour. Therefore commercial FEM software, such as Abaqus and Ansys, has the ability to implement such models as customized subroutines [8]. However, none of the present models have been developed for additively manufactured composites [40,92]. Therefore, a progressive damage model based on Puck-Schurmann failure criteria [156] has been prepared for the Simulia-Abaqus FEA environment as a Fortran subroutine (UMAT), following the guidelines presented in [98,190] and modified according to [48], while the software and compiler connections has been achieved according to [8]. The required input properties have been summarized in Table 5.5, including stiffnesses, stresses and Poisson ratios. Each of these values is treated as average between the experimentally acquired data, RVE output and available data from the literature [117,118,146]. Furthermore, the stress exposure coefficient is adopted from [98], and fracture plane parameters are accepted according to the guidelines in [190].

Table 5.5 Adopted lamina properties

	Value	Unit	Description	Ref.
E_1	58675	MPa	Homogenized lamina modulus of elasticity in direction (1)	*, [117]
E_2	2340	MPa	Homogenized lamina modulus of elasticity in direction (2)	*
G_{12}	1890	MPa	Homogenized lamina shear modulus in 12 plane	*
v_{12}	0.30	/	Poisson ratio in 12 plane	*
v_{23}	0.28	/	Poisson ratio in 23 plane	[146]
$E_{\parallel f}$	191000	MPa	Longitudinal fiber modulus	[146]
$v_{\perp\parallel f}$	0.2	/	The Poisson ratio of fiber	[84]
σ^t_1	750	MPa	Tensile strength in the fiber direction	*, [117]
σ^c_1	426.70	MPa	Compressive strength in the fiber direction	[84]
σ^t_2	14.10	MPa	Tensile strength perpendicular to the fiber direction	*
σ^c_2	66	MPa	Compressive strength perpendicular to the fiber direction	[84]
τ_{12}	21	MPa	In-plane shear strength	*
$p^t_{\perp\parallel}$	0.35		Fracture plane inclination parameter in tension	[48]
$p^c_{\perp\parallel}$	0.3		Fracture plane inclination parameter in compression	[48]
$p^{t,c}_{\perp\perp}$	0.25-0.3		Fracture plane inclination parameter in shear	[48]
$m_{\sigma f}$	1.1		Stress magnification factor	[48]

* Values acquired experimentally

Following the ASTM D3039 guidelines, which were also adopted in specimen manufacturing, numerical twins have been designed in the Abaqus CAE environment as 220 mm long, 26.2 mm wide, and 1.75 mm thick rectangular plates with 50 mm gauge length, and a 4 mm diameter hole in its centre, as shown in Figure 5.6, while the layer thickness of 145.85μm has been adopted based on the microstructural results.

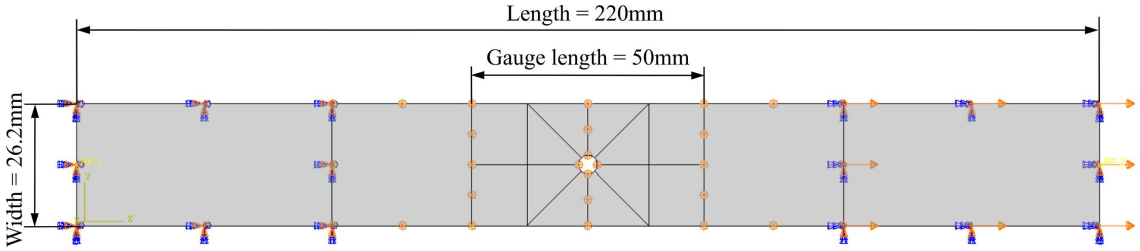

Figure 5.6 Specimen top-view outline

Since the laminate is loaded unidirectionally in tension, and its thickness is significantly lower than both its length and width by at least an order of magnitude, the stresses developed in the thickness direction can be ignored, hence conventional shell elements (S4R) can be

adopted. Therefore, three cases of 12-layered specimens, as shown in Figure 5.7, were designed in the Abaqus CAE environment using a "*Composite Layup"* approach adopting the LSS-es proposed in [28,29,164] as $[0/45_2/0/\text{-}45_2]_S$, $[0/90_2/0/90_2]_S$ and $[0/60_2/0/\text{-}60_2]_S$ respectively.

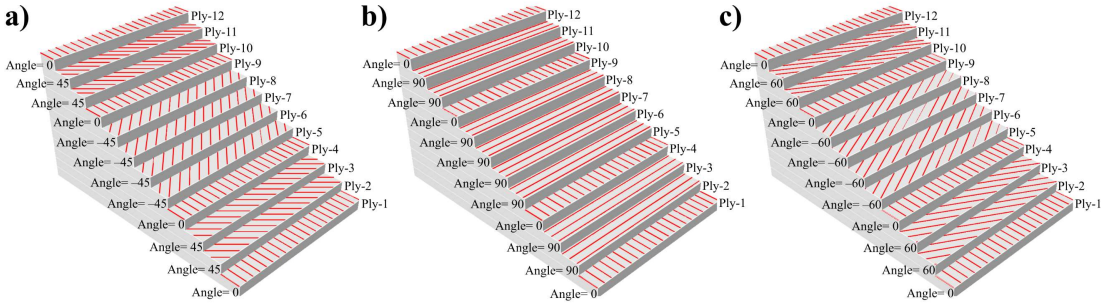

Figure 5.7 Proposed LSS cases: a) $[0/45_2/0/\text{-}45_2]_S$, b) $[0/90_2/0/90_2]_S$, c) $[0/60_2/0/\text{-}60_2]_S$

However, since laminates contain constrained stacks of equally oriented off-axis layers which are susceptible to damage initiation, a correction of the in-situ effects must be accounted for [29]. Following the guidelines given in [10], the transverse strength σ^t_2 and in-plane shear strength τ_{12} corrections for both thin and thick laminas have been presented in Eq. 5.16 - 5.19, while the fracture parameter values G_{IC} and G_{IIC} are adopted from [84].

$$F_{2t}^{IS-thin} = \sqrt{\frac{8G_{IC}}{\pi t_k \Lambda_{22}^0}} \tag{5.16}$$

$$F_{6}^{IS-thin} = \sqrt{\frac{8G_{IIC}}{\pi t_k \Lambda_{44}^0}} \tag{5.17}$$

$$F_{2t}^{IS-thick} = \sqrt{\frac{2G_{IC}}{\pi a_0 \Lambda_{22}^0}} \tag{5.18}$$

$$F_{6}^{IS-thick} = \sqrt{\frac{2G_{IIC}}{\pi a_0 \Lambda_{44}^0}} \tag{5.19}$$

In expressions Eq. 5.16 - 5.19, t_k indicates the value of lamina thickness, where the values of Λ_{22}^0 and Λ_{44}^0 are acquired in relation to the material orthotropic properties, as shown in Eq. 5.20 and Eq. 5.21.

$$\Lambda_{22}^0 = 2\left(\frac{1}{E_2} - \frac{\nu_{12}^2}{E_1}\right) \tag{5.20}$$

$$\Lambda_{44}^0 = \frac{1}{G_{12}} \tag{5.21}$$

Since the stacks of equally oriented laminas behave like a single thick lamina, allowing the formation of larger cracks, the parameter a_0 is calculated as t_k multiplied by the number of equally oriented laminas within the stack constrained between two adjacent layer interfaces.

The modified material properties accounting for the in-situ effects are summarized in Table 5.6.

Table 5.6 In-situ lamina properties

Layer	Variable	Value	Unit	Description
2, 3, 10, 11	$\sigma_2^{\mathrm{t\,IS}}$	143.2	MPa	In-situ tensile strength perpendicular to the fiber direction
	τ_{12}^{IS}	162	MPa	In-situ in-plane shear strength
4, 9	$\sigma_2^{\mathrm{t\,IS}}$	202.5	MPa	In-situ tensile strength perpendicular to the fiber direction
	τ_{12}^{IS}	230.1	MPa	In-situ in-plane shear strength
5-8	$\sigma_2^{\mathrm{t\,IS}}$	101.25	MPa	In-situ tensile strength perpendicular to the fiber direction
	τ_{12}^{IS}	114.53	MPa	In-situ in-plane shear strength

The implemented UMAT subroutine has been set to append the FEA result for each ply and to categorize the damage variables into (1-4) solution dependent variables (SDV), achieving a distinction between fiber and inter-fiber damage for tensile and compressive conditions separately. Subsequently, if one of the SDVs (1-4) reaches the value of 1.0, it triggers a degradation law according to the adopted damage criteria and is appended to the SDV (6-9) matrix. The list with the description for each SDV is presented in Table 5.7.

Table 5.7 Solution dependent variables

Variable	Description
SDV1	fiber failure under tensile loads in the range [0 - 1]
SDV2	fiber failure under compressive loads in the range [0 - 1]
SDV3	inter-fiber failure under tensile loads in the range [0 - 1]
SDV4	inter-fiber failure under compressive loads in the range [0 - 1]
SDV5	element fracture plane angle to thickness direction in the range [-90° to 90°]
SDV6	element failure for fiber failure in tension
SDV7	element failure for fiber failure in compression
SDV8	element failure for inter-fiber failure in tension
SDV9	element failure for inter-fiber failure in compression
SDV10	total damage in the material not depending on the failure mode

5.2.3. Mesh sensitivity analysis

The accuracy of FEA is significantly influenced by the type and the size of the finite elements, as well as the mesh quality. Therefore, by reducing the element size, the mesh density increases, which tends also to increase the result accuracy. However, the number of finite elements is proportional to the number of equations which need to be numerically solved, hence an increase in mesh density reacquires more computational effort, so a mesh sensitivity analysis is performed in order to find a balance between the requirements. Since the shell elements have been adopted according to the mechanics of the thin laminates, the mesh sensitivity has been performed by a gradual variation of the element size within the interval from 0.25 to 1.75 mm as

shown in Figure 5.8. While both coarse and fine meshes returned an equivalent response in the linear elastic region, the scatter between the calculated ultimate strengths was more consistent for higher mesh densities, as presented in Figure 5.8 a), achieving superior accuracy.

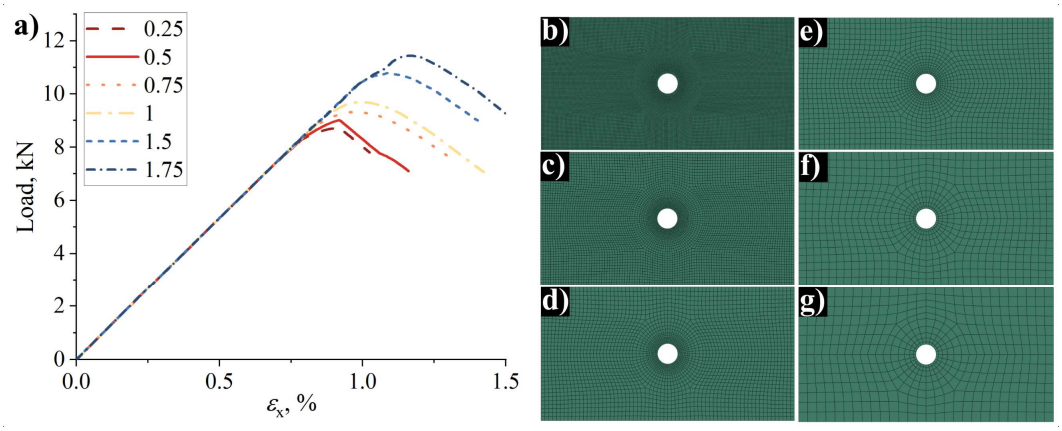

Figure 5.8. a) Load-strain diagram for tested meshes: b) Element size 0.25 mm, c) Element size 0.5 mm, d) Element size 0.75 mm, e) Element size 1.0 mm, f) Element size 1.5 mm, g) Element size 1.75 mm

Due to a small difference in accuracy with just a fraction of the computational effort, the element size of 0.5 mm has been adopted for each of the studied cases, leading to a final model with 17723 linear quadrilateral elements, 8219 of which are within the gauge region.

5.2.4. Damage model calibration and validation

Along with material properties, the damage model also required additional parameters, most of which were initially adopted from [98], which led to an overestimation of laminates' bearing capability. In order to acquire more accurate results, the model parameters have been calibrated according to the experimentally acquired data for OH-45 case and validated on OH-60 and OH-90 cases. The calibration has been carried out using the response-surface algorithms based on central composite design of experiments (DoE), analysing the interaction between four continuous factors, including shear stress multiplier $m_{\tau f}$, effective fiber strength coefficient ξ, and the moduli degradation parameters κ_{DEG} and n_{DEG}. The optimized parameter values have been obtained by targeting the minimal deviation between numerically and experimentally acquired loads at failure. According to this criterion, the response-surface algorithms returned a fit with the R-square value of 96.41%, while for better visualization the results have been presented in Figure 5.9 as six 2D plots, each having two of the factors constrained.

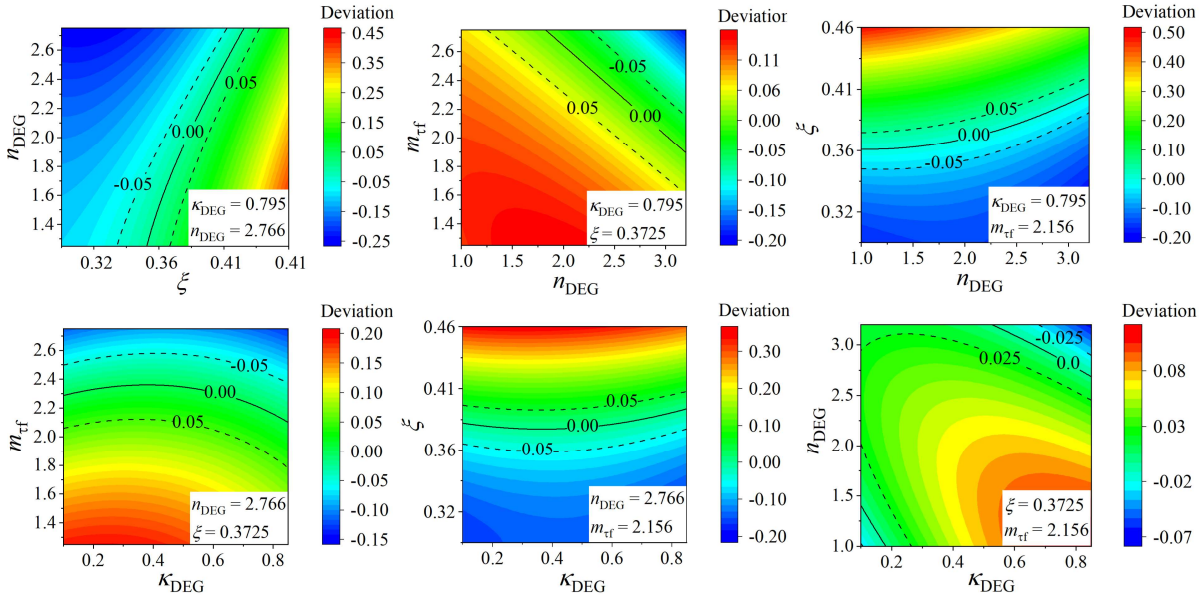

Figure 5.9 Response-surface solutions

The constrained factors were adopted by solving the response-surface equation from the optimization results. The solution was acquired using the MS excel solver to minimize the error between the numerical and experimental results in the OH-45 case, and shown in Table 5.8.

Table 5.8 Response-surface results

	Value	Description
κ_{DEG}	0.795	Shear degradation coefficient
n_{DEG}	2.773	Shear degradation exponent
ξ	0.372	Effective fiber strength coefficient
$m_{\tau f}$	2.156	Shear stress multiplier

By conducting the parametric analysis, the most significant effect on accuracy have been found for the effective fiber strength coefficient ξ, which is also consistent with the discrepancies observed between ideal and cohesive fiber/matrix bonds in microstructural analysis. Furthermore, the shear stress multiplier $m_{\tau f}$ has been identified as the second in significance, yet it is essential for minimizing the overprediction of load-bearing capabilities in OH-45 case. The moduli degradation parameters κ_{DEG} and n_{DEG} influenced the results up to 10%. In addition, the response-surface for κ_{DEG} and n_{DEG} revealed two distinctive intervals in which the parameters can be adopted for a minimized error. The first interval is regarded as the linear degradation where n_{DEG} equals one and the error is minimized by adopting the κ_{DEG} value as 0.2, while the second interval is nonlinear where n_{DEG} can be acquired in the range from 2.5 to 3.5, and κ_{DEG} from 0.5 to 0.9 respectively. With experimental results acquired and the numerical model calibrated, the application could be evaluated on other AM CFRP cases. The model was initially tested without the response-surface results, returning a significant overestimation in laminate

bearing capability. By adopting the acquired parameters, the results were consistent for each of the tested cases, based on load-strain behaviour. Furthermore, by analysing the experimental and numerical results of the OH cases, the linear-elastic laminate response dependence on UD-0 layers reinforced in the load direction has been determined, while the influence of the supporting layers' orientations on both damage progression and laminate's ultimate load-bearing capabilities has also been established.

The initial analysis was conducted on the OH-90 case, where the absence of biaxial behaviour in supporting layers returned an insignificant influence on both damage progression and laminate's ultimate strength. The analysis also confirmed that crack growth direction follows the supporting layers' orientation in both numerical and experimental analysis, as shown in Figure 5.10 a), and Figure 5.10 c) respectively. The numerical analysis returned a rather conservative estimate of load-bearing capability in comparison with the experimentally acquired data Figure 5.10 b).

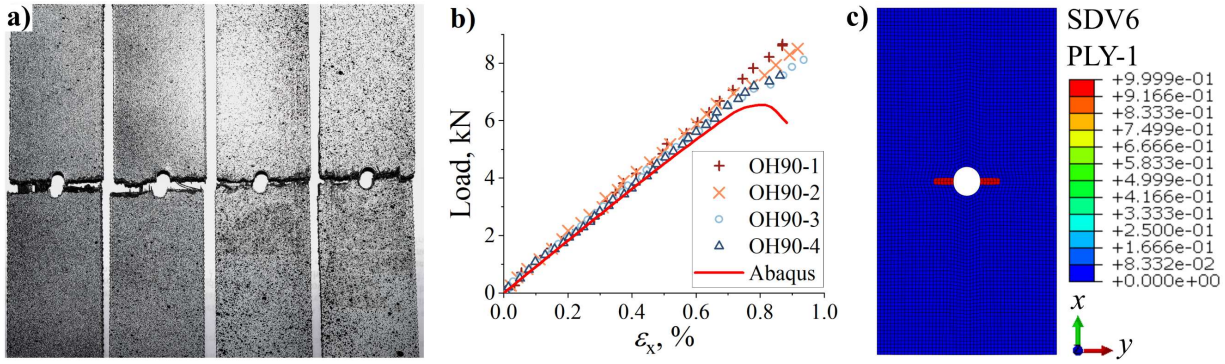

Figure 5.10. a) Failed OH90 specimens, b) Load-strain diagram, c) Fiber failure in tension at maximal load value

Similar to the OH-90 case, the UD-0 layers also have a dominant influence on the behaviour of OH-60 specimens. However, the orientation of these supporting layers enables the axial load-bearing function of the embedded fibers, increasing the average strength and strain by 7%, and 6.2% respectively. The evaluation of experimental results, given in Figure 5.11 a), shows how crack direction should follow the orientation of the supporting layers. However, the results of the numerical model, presented on Figure 5.11 c), do not capture the fracture behaviour accurately. They return the crack growth perpendicular to the load direction at maximal load. Despite this discrepancy, the comparison between numerical and experimental results, presented in Figure 5.11 b), is mainly consistent, while conservatively estimating the ultimate load-bearing capabilities of the OH-60 laminate.

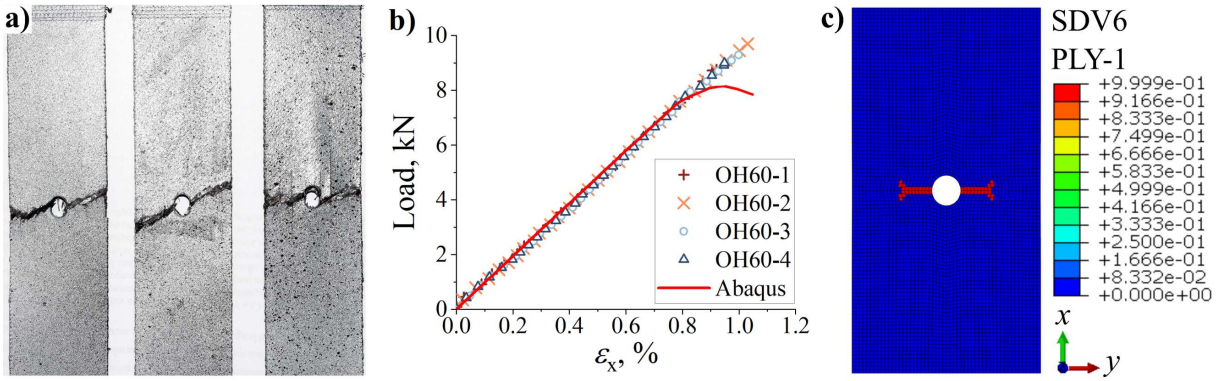

Figure 5.11. a) Failed OH60 specimens, b) Load-strain diagram, c) Fiber failure in tension at maximal load value

In contrast to the previous cases, the supporting layers in OH-45 carry a more significant amount of the axial loads, manifesting a greater in-plane biaxiality ratio. In comparison with the OH-90 case, the OH-45 reaches 18% higher limits for the ultimate strength, followed by a 3.8% increased ultimate strain at failure. Analogous to OH-60 cases, the damage in OH-45 specimens follows the orientation of the supporting layers, as shown experimentally in Figure 5.12 a), and is accurately captured by the damage model, as shown in Figure 5.12 c). The consistency between the experimental and numerical results is presented in Figure 5.12 b).

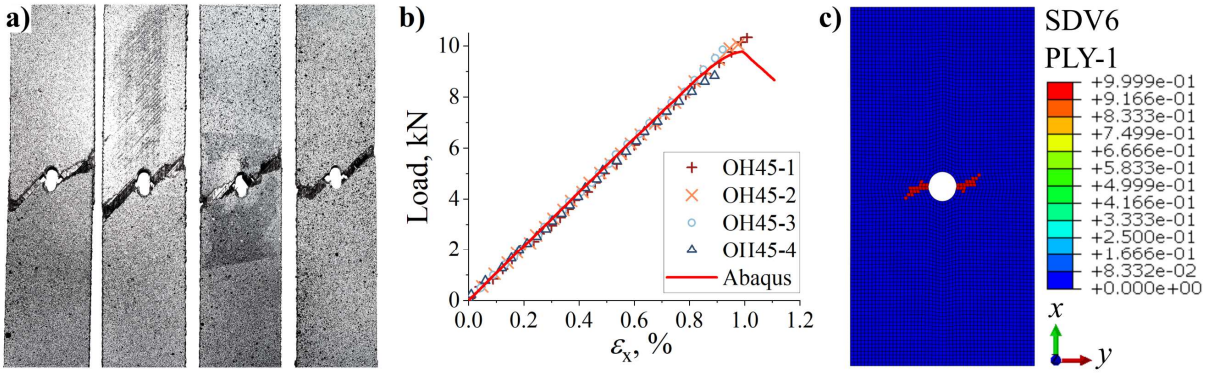

Figure 5.12.a) Failed OH45 specimens, b) Load-strain diagram, c) Fiber failure in tension at maximal load value

Considering the lack of comparable research in the literature, the results have been evaluated according to similar existing damage models, as reported in Table 5.9. According to the comparison, a damage model based on Hashin failure criteria exhibits a load-bearing overprediction in the range from 2.93% in OH-90, 18.73% in OH-60, and 30.67% in OH-45 cases. There is an underestimation of 6.20% in the OH-90 case, but an overestimation of 3.67% and 28.65% in the OH-60 and OH-45 cases respectively for a damage model based on Puck's failure criteria, adopted from [98] and modified to account for lower longitudinal strength in AM UD CFRP-s. To increase the compliance with the experimental investigation, Puck's fiber failure criteria have been modified to include shear stresses, which account for the influence of the intralaminar

weaknesses on the behaviour of AM composites. Consequently, the proposed model underestimates the ultimate strength in the OH-90 and OH-60 cases by 13.75% and 8.34% respectively, followed by 0.08% underestimation in the OH-45 case, according to which it has also been calibrated.

Table 5.9. Damage model comparison

	Load at failure, kN			Error, %		
Model	OH90	OH60	OH45	OH90	OH60	OH45
Hashin	7.81	10.88	12.79	2.93	18.73	30.67
Puck*	7.12	9.50	12.59	-6.20	3.67	28.65
Puck**	6.55	8.40	9.78	-13.75	-8.34	-0.08
Experiment	7.59	9.16	9.79	/	/	/
*	Based on [98] with calibrated effective fiber strength					
**	Proposed in the current work					

As the proposed model estimates the load-bearing capability of the studied laminates most accurately, while the underestimation error is shifted in the safe zone, its application describing the damage behaviour of AM CFRP composite laminates can be considered. However, as the introduction of fiber failure criteria modification to include shear stresses led to the increase in model accuracy for each of the studied cases, the proposed model does not accurately represent the failure at the complete loss of bearing capability. This is especially evident in the OH90 and OH60 cases, as presented in Figure 5.13, and therefore an appropriate damage evolution law should be investigated in further research.

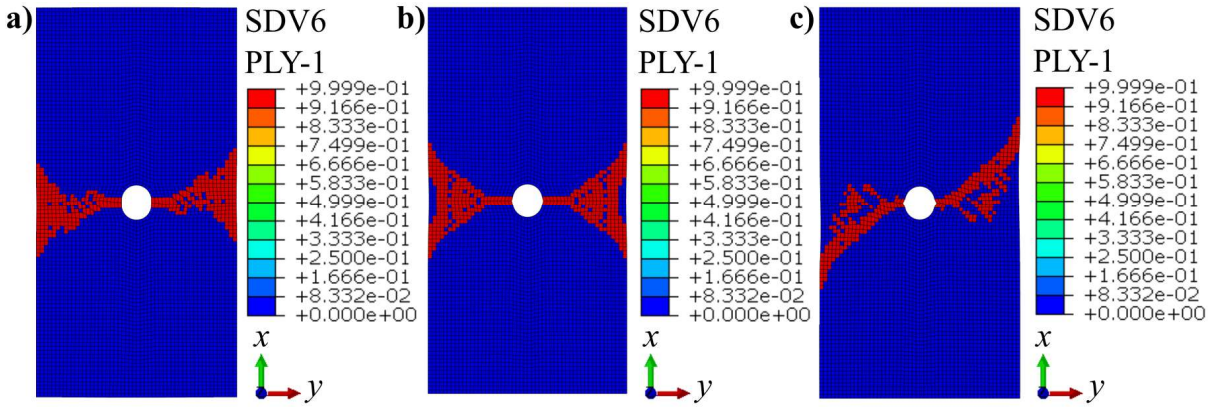

Figure 5.13. Fiber failure at complete loss of bearing capability: a) OH90, b) OH60, c) OH45

The procedure of material modelling through multiple length scales has been shown in this section. The development of RVE models has been described, presenting the methods used in geometrical modelling based on constituents' statistics. The RVEs were updated with the readily available constituents' properties, and the fiber/matrix contacts were realized using cohesive interfaces. In order to simulate the deformation of the environment around an RVE, the periodic

boundary conditions have been imposed by linking the nodal degrees of freedom using linear constraints equations, while the loads on the RVE have been introduced as displacements through Dirichlet boundary conditions. Numerical homogenization has been conducted and the results have been compared with the experimentally acquired data for UD-0, UD-90, and SH-45 specimens subjected to tensile and in-plane shear loads respectively. The cohesive zone model parameters were calibrated according to the experimentally acquired material response, with consistent results between the numerical calculations and experimental data for each of the tested cases.

The identified lamina properties were updated with additional data from the literature and adopted in the continuum damage model based on Puck's failure theory in order to analyse the behaviour of multidirectionally reinforced laminates. Despite being validated using readily available data obtained for similar composites, the model did not return consistent results with the experimentally acquired data. Since the most significant discrepancies were found in cases subjected to shear loads, the shear stress was included in fiber fracture criterion. Additionally, a nonlinear shear degradation laws has been adopted instead of the linear model in order to account for the material susceptibility to shear damage. The modified model has shown results consistent with the experimentally acquired data, especially for the OH-45 case, but it underestimates the ultimate strength in the OH-90 and OH-60 cases. In comparison with the unmodified Puck model and also the Hashin model readily available in Abaqus, the proposed model estimates the load-bearing capability of the studied laminates most accurately, while the underestimation is moved to the safe zone. However, as the modification led to the increase in model accuracy, the proposed model does not accurately represent the failure at the complete loss of bearing capability

6. RESULTS AND DISCUSSION

A comprehensive description of additive manufacturing and its role in the bottom-up approach to composite material design has been presented in the initial part of this thesis. Novel methods of design and manufacturing have been debated, following the latest trends in engineering applications. The basic principles of additive manufacturing technology have been presented, focusing mainly on fused filament fabrication and its compatibility with various polymeric matrix materials. Its capability to embed particulate and continuous reinforcements necessary for achieving multifunctional and lightweight designs encountered in aeronautic, automotive, and space industries wearable technologies, medical applications has also been presented. The necessity for accurate identification of the material properties, material constitutive relations and damage initiation, propagation and failure mechanisms has been discussed in order to define the potential of the specific strength and tailoring of multifunctional capabilities in AM CFRP composite structures. Additionally, the difficulty of delivering reliable components for engineering applications, using additive manufacturing in comparison to conventional manufacturing methods, has been observed in multiple studies throughout the literature, hence further research fields of both manufacturing and damage mechanics has been proposed.

Following these findings, a multiscale modelling approach has been proposed in this thesis as a scientific contribution. Initially, the microstructural inspections upon which micromechanical homogenization with cohesive constituent interfaces has been carried out and experimentally validated in longitudinal, transversal and shear test cases. Furthermore, a continuum damage mechanics based on Puck's fracture theory has been proposed for failure analysis in multidirectionally reinforced composite laminates and implemented in Abaqus as a user-defined material model (UMAT) subroutine written in Fortran. Failure criteria modification has been proposed for a better description of shear damage in AM composites, followed by the experimental calibration of the model parameters on specimens with LSS induced in-plane multiaxial stress state. Following the main aims for the scientific contribution, the presented work has been organized in sections, each dedicated to a specific part of the research. Therefore, a comprehensive review of the state-of-the-art in additive manufacturing has been presented in the following section, briefly describing the early developments of AM technology, basic AM principles, and the currently available technologies, while mainly focusing on the FDM manufacturing method and its compatibility with particulate, short and continuous fiber reinforcements. Furthermore,

a review of the applicable modelling methods has also been presented within this section, describing the available micromechanical, mesomechanical and macromechanical models, highlighting the assumptions, issues and result significance related to each of the modelling approaches.

Based on the conducted review, a multiscale approach using numerical RVE homogenization and continuum damage modelling with Puck's failure criteria has been adopted in this thesis. The theoretical background for each step of the adopted approach has been given in the following section. The initial part presents the concept of classical laminate theory, summarizing the essential assumptions, and presenting the basics of laminate mechanics. Furthermore, the concept of microstructural homogenization in heterogenic materials has also been reviewed within this section, presenting the mathematical formulation for strength- and strain-based RVE schemes. Critical assumptions in the homogenization approach have been discussed, followed by an example for each boundary condition's implementation and its limitations. Subsequently, the section concludes with a comprehensive summary of the Puck-Schurmann failure theory, where basic assumptions for the proposed fiber and matrix fracture criteria are also discussed. The fundamental action plane theory and its role within Puck's fracture hypothesis has been presented, followed by the classification of inter-fiber fracture criteria in tension and compression. Finally, the presented theory has been adopted for failure analysis in AM composites and implemented in the Abaqus CAE environment as a user-defined material model (UMAT) subroutine prepared in Fortran.

A summary of the conducted experimental studies has been divided between experimental procedures and the acquired results for each of the length-scales and presented in the fourth section. Specimen design and manufacturing methods have been discussed for microstructural, lamina, and laminate cases, where cross-ply LSS-es have been adopted for microscopic inspections of carbon, glass, and aramid reinforced composites. Rectangular specimens were adopted according to ASTM D3039 and ASTM D3518 for UD and shear cases of continuous fiber reinforced composites. The multidirectional laminates have been designed with circular stress concentrators according to ASTM D5766, while adopting the LSS-es of $[0/90_2/0/90_2]_S$, $[0/45_2/0/-45_2]_S$, and $[0/60_2/0/-60_2]_S$, which transform the uniaxial loads into in-plane biaxial stress states in ratios equal to 0, 1.61, and 0.57 respectively. This enables a multiaxial experimental evaluation with uniaxial tensile tests. The section also includes the preparation of cross-ply samples for the microscopic inspection of longitudinal and transversal cross-sections. The results have been reported for multiple magnifications in the range from 200× to 1600×, with

the corresponding image sizes from 1500×1380μm to 186×171μm respectively, using LFD for better measurement accuracy, and BSED for better compatibility with image analysis tools. Furthermore, the geometrical comparison between the CAE and the measurement of AM unidirectional, shear, and OH specimens has also been reported in this section, where the expected repeatability issues of the adopted AM technology have been confirmed and elaborated. Therefore, to detect the effects of these local inconsistencies, full-field strain measurement using DIC technology has been proposed. The measured surfaces have been prepared using high contract stochastically random patterns, while the achieved surface quality has been evaluated with GOM-Aramis software. The 2448×2050-pixel images have been captured using a GOM Aramis 5M (GigE) adjustable base 800 system with 35 mm lenses positioned at 560 mm from the specimen, with the distance between the cameras equal to 265 mm, closing the angle of 26°. Uniaxial tensile tests have been conducted using an Instron servo-hydraulic testing system under quasistatic conditions at the speed of 0.01 mm/s, reporting and comparing the measurements acquired using both DIC and the contact extensometer.

The experimental results were divided according to the length scales, starting with the trainable WEKA segmentation algorithms and the resultant probability maps, upon which the microscale constituent ratio was evaluated. These segmented images have been statistically analysed for each case of embedded reinforcement, reporting the fiber diameter, misalignment, material deposition width, and layer height, consistent with the data in the relevant literature. The results of the microscopic analysis have been summarized and adopted in the RVE development. The experimental evaluation of lamina mechanical properties has also been covered within this section, describing the specimen LSS design and measurement techniques. Longitudinal and transversal tensile properties have been acquired based on the UD-0 and UD-90 specimen uniaxial behaviour, while the LSS-induced shear behaviour has been studied and reported for SH-45 cases. All three test cases have been compared with the readily available data in the literature, showing consistent results after comparing them with other AM composites, while showing significant deviation from the behaviour of the conventionally manufactured counterparts. In this comparison, the conventionally manufactured UD composites exceeded their AM counterparts by 45-68% for longitudinal elastic modulus and by 16-68% in ultimate tensile strength. Stiffness reduction, up to 65-72%, with a 36-50% lower ultimate transversal strength, has been acquired in the transverse direction. Similar conclusions have also been drawn for shear behaviour, reaching 54% difference in shear modulus and a 58-64% difference in shear strength.

The experimental results of multidirectionally reinforced AM CFRP-s have been presented in the final part of this section, focusing on the damage initiation and propagation in three cases of open-hole specimens with specific LSS-induced in-plane biaxial stress states in uniaxial load conditions. The experimental results have been acquired for both specimen surfaces, using a contact extensometer and DIC system respectively, showing consistent results. Subsequently, these results have been summarized, comparing biaxiality ratio, tensile modulus, tensile strength, and strain at failure for each of the tested OH cases, while the load-bearing distinctions have also been critically discussed. Lacking readily available comparable data from the literature, the OH-90 case has been adopted as a reference against which the remaining cases have been compared. Without exhibiting any biaxial behaviour, the OH-90 specimens achieved longitudinal stiffness between 18.4 GPa and 20.06 GPa, and a tensile strength between 144.1 and 166.6 MPa, while the specimen failure occurred at 0.78% and 0.83 % of the longitudinal strain. Similar values of the elastic moduli, in the range from 19.014 GPa to 19.672 GPa, have been acquired for the OH-60 cases, with higher values of tensile strength and strain between 154.76 MPa to 199.15 MPa and 0.86 % and 1.1 % respectively. The highest stiffness values were recorded between 21.552 GPa and 22.846 GPa, with tensile strength measurements recorded between 187.37 MPa and 216.25 MPa in the OH-45 case. The strains at failure were in a range from 0.86 % to 1.1% and did not diverge from the OH-60 case significantly. Subsequently, the influence of the supporting layers' orientation on both strength and stiffness values has been compared, confirming the negligible influence of perpendicularly oriented supporting layers in the OH-90 case, leading to transversal damage growth. Similar behaviour has also been observed in the OH-60 case, where off-axis layers carried a larger proportion of the axial load, leading to an increase of strength and strain values up to 6.2% and 7% respectively, and damage growth followed the orientation of supporting layers. The increased load-bearing capability of the supporting layers enhanced both strength and strain at failure by 18% and 3.8% respectively. Damage propagation in the direction of the supporting layers' orientation led to an equivalent failure mode.

Based on the comprehensive state-of-the-art review and the presented multiscale experimental results, a numerical representation including each of the test cases was adopted. To represent a unified response of multiple micromechanical constitutive models found within each of the cases of heterogenic materials, a numerical homogenization based on statistical evaluation of microscopic inspection has also been adopted. Distinctive RVE models of carbon, glass and aramid-fiber-reinforced composites have been designed in the Abaqus CAE environment.

Respecting the measured constituents' ratio for each of the studied cases, a hexagonal fiber arrangement within an equilateral base cubic RVE has been adopted, assuming one fiber in the centre and four fiber quarters placed along the RVE edges in the longitudinal direction, thus enabling the fibers to geometrically complete one another, achieving both geometrical and material periodicity. This was essential for generating a periodic FE mesh, and consequently for adopting the periodic boundary conditions. Subsequently, the necessary RVE size for achieving the measured fiber fraction was iteratively determined for each of the studied cases, leading to three distinctive RVE sizes. After achieving geometrical compatibility with the microscopic measurements, the appropriate material models of the embedded constituents were implemented within each of the RVE-s, while cohesive contacts were introduced as fiber/matrix interfaces to represent the AM composite material behaviour more accurately. The constituents' material models have been adopted from the literature, while the CZM has been calibrated according to the experimentally acquired response of carbon-fiber-reinforced composite, achieving consistency between the numerical and experimental results for longitudinal transverse and in-plane shear behaviour. However, lacking the readily available experimental data for the glass and aramid fiber-reinforced counterparts, the transverse and in-plane shear responses were calibrated according to carbon fiber-reinforced specimens, while keeping the strength relations comparable to the traditionally manufactured composites. This confirms the necessity for additional experimental validation. All things considered, the numerical microscale homogenization approach based on RVE models designed according to microscopic imaging returned adequate results in comparison to the macroscale experimental studies, validating the initial hypothesis, and confirming the necessity for further experimental studies on constituents' interface behaviour. Proving the consistency between the experimental analyses and numerical RVE simulations of unidirectional and shear behaviour, the orthotropic lamina properties were determined and adopted in macroscale modelling of the multidirectionally reinforced laminates.

Analysing the experimental observations of the material behaviour, the assumption of the orthotropic continuum was validated, and the CDM framework utilizing Puck's failure criteria was adopted. The model was written in Fortran and implemented in the Abaqus CAE environment as a user-defined material model subroutine. Numerical twins have been designed in the Abaqus CAE environment for each of the OH cases and analysed using this UMAT subroutine. In comparison with the experimental results, the original model overpredicted the material's response, especially in the OH-45 case where significant values of shear stresses occurred. In order to compensate for the AM material susceptibility to shear damage, the shear stresses were

introduced into the fiber fracture criteria, while the shear modulus degradation due to damage was nonlinearly modified. The model parameters were calibrated using the response-surface algorithms of the central composite design of experiments (DOE), analysing the interactions between four continuous factors, including: shear stress multiplier $m_{\tau f}$, effective fiber strength coefficient ξ, and the moduli degradation parameters κ_{DEG} and n_{DEG}. Subsequently, the response-surface equation was optimized for minimal deviation between numerically and experimentally acquired results for the OH-45 case, reaching an R-square value of 96.41%. Finally, the model accuracy was evaluated on the three OH cases and compared with the Puck model which uses the original parameters and also with the Hashin damage model readily available in Abaqus. Analysing the results, an overprediction of 2.93% in OH-90, 18.73% in OH-60, and 30.67% in OH-45 was observed in the Hashin case. Observing the result from the damage model based on Puck's failure criteria, adopted from the literature and modified to account for lower longitudinal strength in AM UD CFRP-s, an underestimation of 6.20% in the OH-90 case, and an overestimation of 3.67% and 28.65% in the OH-60 and OH-45 cases has been recorded respectively. After introducing shear strength in fiber failure criteria, the proposed model underestimated the load-bearing capabilities in OH-90 and OH-60 cases by 13.75% and 8.34% respectively, followed by an underestimation of 0.08% in the OH-45 case. According to the presented comparison, the proposed model returns the most accurate results without dangerous overpredictions of the material properties, therefore its application in damage modelling of AM CFRP composite laminates should be considered

7. CONCLUSION

Recognizing the growth of AM technology and its significance to modern manufacturing, the main motivation of this study was to identify the behaviour of AM materials applicable in engineering practice. Based on the conducted state-of-the-art, the additive manufacturing of polymers was identified as the most cost-effective among the readily available AM methods, with FDM confirmed as most versatile due to the material compatibility, availability, and manufacturing scalability. However, as deficiencies in polymer components manufactured using FDM are common, the load-bearing capabilities of these materials are consequently lower in comparison with their conventionally manufactured counterparts. Therefore, various methods of reinforcing the basic polymer matrix have been considered in a comprehensive literature review, concluding that AM methods implementing continuous fiber composites are the most suitable for engineering application.

While multiple studies confirmed the specific load-bearing capability of AM CFRP composites, their behaviour is still not determined by constitutive models, and the damage resistance to both uniaxial and multi-axial loads remains unknown. In order to identify the material behaviour and to expand its potential industrial application, a better understanding of constitutive relations, damage initiation, propagation, and failure mechanisms was necessary. As the microstructural deficiencies within the AM materials have been identified on various length-scales, this work was focused on multiscale analysis of AM composites by developing a representative volume element of unidirectionally reinforced composites in order to update the lamina properties in a continuum damage model.

In this work, comparison of the applicable micromechanical models was conducted and the numerical homogenization using FEA proved to be most suitable for identifying the micromechanical response in AM composites. Thus, a representative volume element had to be developed based on the material microstructure. Therefore, a microscopic analysis was conducted on three types of AM composites identifying the fiber size, volume ratio, and misalignment, layer height, and material deposition width for carbon, glass, and aramid fiber-reinforced composites respectively; this also showed inter-fiber cracks, voids, and bonding inconsistencies. Representative volume elements were developed for each of the studied cases and updated with the readily available data on the constituents' behaviours. Because they are seldom available in the literature, these findings provide an opportunity for further material research, and subsequent

development of novel micromechanical modes, hence contributing to advancements in additive manufacturing technology. However, to account for the material inconsistencies in matrix/fiber interactions, the cohesive contact has been adopted as the most suitable option. In this thesis, the case of carbon fiber-reinforced composites was selected for further analysis: standardized test specimens were designed, and the lamina properties were identified in unidirectional tensile and shear tests, according to which the RVE models were calibrated and validated. The study proved that this protocol can be adopted for the identification of lamina properties in similar AM materials. However, the results may be inconsistent if the fiber/matrix interface properties are not acquired experimentally. Therefore, an experimental campaign focused on the identification of the fiber/matrix contact is proposed for further study.

Since fiber-reinforced composites are rarely applied as unidirectional, the need to model the behaviour of multidirectionally reinforced laminates has proven to be essential. Since commercial FEA software includes a limited selection of readily available damage models applicable to fiber reinforced composites, the model had to be specifically prepared. Based on the conducted literature review, continuum damage mechanics was adopted in this study and the damage modelling was based on Puck's failure theory. Following the available cases in the literature, the damage model was prepared as a Fortran UMAT subroutine and implemented in the Abaqus CAE environment, then validated with readily available data. The experimentally acquired data on lamina behaviour was subsequently used as the model input, while the missing data were updated based on the conducted literature survey. In order to validate the proposed model, an experimental campaign focusing on multidirectionally reinforced composites subjected to LSS induced in-plane biaxial stresses was proposed. Three cases of specimens were designed and additively manufactured, circular stress concentrators were introduced in the mid-gauge length, and the specimens' surfaces were prepared for monitoring using digital image correlation. Since the adopted LSS-es caused three specific ratios of in-plane biaxiality, which is seldom investigated in the literature, the results were published to provide a deeper insight into the multiaxial behavior of additively manufactured composites. Digital counterparts were also designed and analyzed using the proposed model, then compared with the experimentally acquired results. However, the inconsistencies arisen from the comparison led to the introduction of certain modifications to the failure criteria. Since the experimental study confirmed the significant susceptibility of AM composites to shear damage, the shear stresses were introduced to the fiber failure criterion, while the shear effect on the moduli degradation was nonlinearly enhanced. The parameters were calibrated and validated experimentally, showing consistency

with the OH-45 case, but underestimating the ultimate strength in the OH-90 and OH-60 cases to some extent. In comparison with the unmodified Puck and the Hashin model, the implementation of the proposed model provided the most accurate estimation of the load-bearing capability, while avoiding the overestimations present in the compared models. However, as the modification led to the increase in model accuracy, the proposed model does not accurately represent the failure at the complete loss of bearing capability. These comparisons provide guidelines for the safer application of unidirectionally and multidirectionally reinforced AM composites and improve the prospects of modelling their behavior and avoiding damage of components in engineering applications

In this work, the behavior of AM materials was investigated in multiple length scales and some assumptions had to be adopted; subsequent work to improve these sections is proposed in future research. In further microscale studies, the experimental investigations will be conducted on constituents' contact zones to acquire a more accurate microstructural response. To avoid most of the geometrical assumptions, the microscopic investigation will be conducted using μCT and the 3D imaging will be imported into FEA to produce a genuine RVE model. Furthermore, fracture toughness, interlaminar delamination, and intralaminar cohesive weaknesses will be experimentally evaluated in static and cyclic conditions in order to be integrated into the proposed damage model. This application of the model will then be extended for fatigue damage analysis based on the strength and stiffness degradations determined from the unified cyclic response of unidirectional and shear composite specimens. The modelling will also be re-evaluated by comparing the continuum with the phase-field approach, and further evaluated through multiple length scales in order to enable the safe implementation of the AM composites in the functional design of lightweight components in the transport industries, in wearable technologies, and in medical and aerospace applications

List of References

[1] J. Aboudi, S.M. Arnold, B.A. Bednarcyk, Micromechanics of Composite Materials: A Generalized Multiscale Analysis Approach, 2013.

[2] D.F. Adams, D.R. Doner, Longitudinal Shear Loading of a Unidirectional Composite, J. Compos. Mater. 1 (1967) 4.

[3] D.F. Adams, D.R. Doner, D.R. Doner, Transverse Normal Loading of a Unidirectional Composite, J. Compos. Mater. 1 (1967) 152–164.

[4] K. Agarwal, S.K. Kuchipudi, B. Girard, M. Houser, Mechanical properties of fiber reinforced polymer composites: A comparative study of conventional and additive manufacturing methods, J. Compos. Mater. 52 (2018) 3173–3181.

[5] A.I. Akpoyomare, M.I. Okereke, M.S. Bingley, Virtual testing of composites: Imposing periodic boundary conditions on general finite element meshes, Compos. Struct. 160 (2017) 983–994.

[6] A.V. Azarov, M.V. Golubev, F.K. Antonov, WO 2018/190750 (A1)– Print head for additive manufacturing of articles, 2018.

[7] A.V. Azarov, V.V. Vasiliev, A.F. Razin, V.A. Salov, WO 2017/188861 (A1) - Composite reinforcing thread, prepreg, tape for 3D printing and installation for preparing same, 2017.

[8] E.J. Barbero, Finite element analysis of composite materials using Abaqus, CRC Press, Taylor & Francis Group, LCC, 2013.

[9] E.J. Barbero, Finite element analysis of composite materials ® using ansys, 2nd ed., CRC Press LCC, 2014.

[10] E.J. Barbero, Introduction to Composite Materials Design, 3rd ed., CRC, New York, 2017.

[11] E.J. Barbero, D.H. Cortes, A mechanistic model for transverse damage initiation, evolution, and stiffness reduction in laminated composites, Compos. Part B. 41 (2010) 124–132.

[12] E.J. Barbero, G. Sgambitterra, A. Adumitroaie, X. Martinez, A discrete constitutive model for transverse and shear damage of symmetric laminates with arbitrary stacking sequence, Compos. Struct. 93 (2011) 1021–1030.

[13] J.C. Barbero, Thermal-Fatigue and Thermo-Mechanical Equivalence for Transverse Cracking Evolution in Laminated Composites, West Virginia University, 2018.

[14] Y. Benveniste, A new approach to the application of Mori-Tanaka's theory in composite materials, Mech. Mater. 6 (1987) 147–157.

[15] S. Berretta, K. Evans, O. Ghita, Additive manufacture of PEEK cranial implants: Manufacturing considerations versus accuracy and mechanical performance, Mater. Des. 139 (2018) 141–152.

[16] J.G. Berryman, B. Laboratories, Long-wavelength propagation in composite elastic media I. Spherical inclusions, J. Acoust. Soc. Am. 68 (1980) 1809–1819.

[17] P. Bettini, G. Alitta, G. Sala, L. Di Landro, Fused Deposition Technique for Continuous Fiber Reinforced Thermoplastic, J. Mater. Eng. Perform. 26 (2017) 843–848.

[18] R. Blenkinsopp, E. Al., A method for Calibrating a Digital Image Correlation System for Full-Field Strain Measurements during Large Deformations, Appl. Sci. 2828 (2019) 9(14).

[19] L.G. Blok, M.L. Longana, H. Yu, B.K.S. Woods, An investigation into 3D printing of fibre reinforced thermoplastic composites, Addit. Manuf. 22 (2018) 176–186.

[20] B. Budiansky, On the elastic moduli of some heterogeneous materials, J. Mech. Phys. Solids. 13 (1965) 1–5.

[21] P.P. Camanho, S.R. Hallett, Numerical Modelling of Failure in Advanced Composite Materials, 2015.

[22] P.P. Camanho, P. Maimi, A continuum damage model for composite laminates : Part I – Constitutive model, Mech. Mater. 39 (2007) 897–908.

[23] P.P. Camanho, P. Maimi, A continuum damage model for composite laminates : Part II – Computational implementation and validation, Mech. Mater. 39 (2007) 909–919.

[24] M.A. Caminero, J.M. Chacón, I. García-Moreno, J.M. Reverte, Interlaminar bonding performance of 3D printed continuous fibre reinforced thermoplastic composites using fused deposition modelling, Polym. Test. 68 (2018) 415–423.

[25] M.A. Caminero, J.M. Chacón, I. García-Moreno, G.P. Rodríguez, Impact damage resistance of 3D printed continuous fibre reinforced thermoplastic composites using fused deposition modelling, Compos. Part B Eng. 148 (2018) 93–103.

[26] J.T. Cantrell, S. Rohde, D. Damiani, R. Gurnani, L. DiSandro, J. Anton, A. Young, A. Jerez, D. Steinbach, C. Kroese, P.G. Ifju, Experimental characterization of the mechanical properties of 3D-printed ABS and polycarbonate parts, Rapid Prototyp. J. 23 (2017) 811–824.

[27] P.A. Carraro, L. Maragoni, M. Quaresimin, Prediction of the crack density evolution in multidirectional laminates under fatigue loadings, Compos. Sci. Technol. 145 (2017) 24–39.

[28] P.A. Carraro, M. Quaresimin, A stiffness degradation model for cracked multidirectional laminates with cracks in multiple layers, Int. J. SOLIDS Struct. 58 (2014) 34–51.

[29] P.A. Carraro, M. Quaresimin, Fatigue damage and stiffness evolution in composite laminates: A damage-based framework, Procedia Eng. 213 (2018) 17–24.

[30] E. Carrera, An assessment of mixed and classical theories on global and local response of multilayered orthotropic plates, Compos. Struct. 50 (2000) 183–198.

[31] G. Catalanotti, P.P. Camanho, A.T. Marques, Three-dimensional failure criteria for fiber-reinforced laminates, Compos. Struct. 95 (2013) 63–79.

[32] C.R. Cater, Multiscale modeling of composite laminates with free edge effects, Michigan State University, 2015.

[33] R.C. Cater, Multiscale modeling of composite laminates with free edge effects, Michigan State University, 2015.

[34] J.L. Chaboche, Continuum Damage Mechanics: Part I — General Concepts, J. Appl. Mech. 55 (1988) 59–64.

[35] J.L. Chaboche, Continuu Damage Mechanics: Part II — Damage Growth, Crack Initiation, and Crack Growth, J. Appl. Mech. 55 (1988) 65–72.

[36] J.L. Chaboche, Development of Continuum Damage Mechanics for Elastic Solids

Sustaining Anisotropic and Unilateral Damage, Int. J. Damage Mech. 2 (1993) 311–329.
[37] J.L. Chaboche, Continuum Damage Mechanics, Anisotropy and Damage Deactivation for Brittle Materials Like Concrete and Ceramic Composites, Int. J. Damage Mech. 4 (1995) 5–22.
[38] T. Chen, G.J. Dvorak, Mori-Tanaka Estimates of the Overall Elastic Moduli of Certain, J. Appl. Mech. 59 (1992) 539–546.
[39] G.-H.D.-H.S.-H. Choi, Exchange of CAD Part Models Based on the Macro-Parametric Approach, Int. J. CAD/CAM. 2 (2002) 13–21.
[40] N.T. Chowdhury, N.K. Balasubramani, G.M. Pearce, C. Tao, A multiscale modelling procedure for predicting failure in composite textiles using an enhancement approach, Eng. Fail. Anal. 102 (2019) 148–159.
[41] D.H. Cortes, E.J. Barbero, Stiffness reduction and fracture evolution of oblique matrix cracks in composite laminates, Ann. Solid Struct. Mech. 1 (2010) 29–40.
[42] S.S. Crump, APPARATUS AND METHOD FOR CREATING THREE-DIMENSIONAL OBJECTS, 5121329, 1992.
[43] R.G. Cuntze, Evaluation of multiaxial test data of UD-laminae by so-called " fracture-type strength criteria " and by supporting probabilistic means, in: Proc. ICCM–11, 1997: pp. 273–289.
[44] R.G. Cuntze, A. Freund, The predictive capability of failure mode concept-based strength criteria for multidirectional laminates, Compos. Sci. Technol. 64 (2004) 343–377.
[45] D. Dapaah, A. Bahmani, J. Montesano, T.L. Willett, A continuum damage mechanics model of the microdamage process zone during cortical bone fracture, Mater. Today Proc. 7 (2019) 402–409.
[46] C.G. Dávila, P.P. Camanho, C.A. Rose, Failure criteria for FRP laminates, J. Compos. Mater. 39 (2005) 323–345.
[47] L.J. Deng, Y.L. Wu, X.H. He, K.N. Xie, L. Xie, Y. Deng, Simvastatin delivery on PEEK for bioactivity and osteogenesis enhancements, J. Biomater. Sci. Polym. Ed. 29 (2018) 2237–2251.
[48] H.M. Deuschle, 3D Failure Analysis of UD Fibre Reinforced Composites: Puck's Theory within FEA, Universitat Stuttgart, 2010.
[49] H.M. Deuschle, B.-H. Kröplin, Finite element implementation of Puck's failure theory for fibre-reinforced composites under three-dimensional stress, J. Compos. Mater. 46 (2012) 2486–2513.
[50] V. Den Eindmck, Berechnung der elastischen Konstanten des Vielkristalls aus den Konstanten des Einkristalls, Zeitschrift Ffir Phys. 151 (1958) 504–518.
[51] I. Ferreira, M. Machado, F. Alves, A. Torres Marques, A review on fibre reinforced composite printing via FFF, Rapid Prototyp. J. 25 (2019) 972–988.
[52] A. Fischer, S. Rommel, T. Bauernhansl, New Fiber Matrix Process with 3D Fiber Printer – A Strategic In-process Integration of Endless Fibers Using Fused Deposition Modeling (FDM), in: IFIP Int. Fed. Inf. Process., 2013: pp. 167–175.
[53] S.-Y. Fu, B. Lauke, Y.-W. Mai, Science and Engineering of Short Fibre-Reinforced Polymer Composites, 2nd ed., Woodhead Publishing, 2019.

[54] S. Fu, X. Hu, C. Yue, A new model for the transverse modulus of unidirectional fiber composites, J. Mater. Sci. 33 (1998) 4953–4960.

[55] A. Gebhardt, Additive Manufacturing 3D Printing for Prototyping and Manufacturing, 2016.

[56] Y.M. Ghugal, R.P. Shimp, A Review of Refined Shear Deformation Theories of Isotropic and Anisotropic Laminated Plates, J. Reinf. Plast. Compos. 21 (2002) 775–795.

[57] I. Gibson, D.W. Rosen, B. Stucker, Additive Manufacturing Technologies, Springer, New York, 2015.

[58] E. Giner, A. Vercher, M. Marco, C. Arango, Estimation of the reinforcement factor n for calculating the transverse stiffness E 2 with the Halpin – Tsai equations using the finite element method, Compos. Struct. 124 (2015) 402–408.

[59] M. Gljušćić, M. Franulović, D. Lanc, A. Žerovnik, Representative volume element for microscale analysis of additively manufactured composites, Addit. Manuf. 56 (2022) 102902.

[60] M. Gljušćić, M. Franulović, B. Žužek, A. Žerovnik, Experimental validation of progressive damage modeling in additively manufactured continuous fiber composites, Compos. Struct. 295 (2022) 115869.

[61] G.D. Goh, V. Dikshit, A.P. Nagalingam, G.L. Goh, S. Agarwala, S.L. Sing, J. Wei, W.Y. Yeong, Characterization of mechanical properties and fracture mode of additively manufactured carbon fiber and glass fiber reinforced thermoplastics, Mater. Des. (2017).

[62] E. V González, P. Maimí, P.P. Camanho, A. Turon, J.A. Mayugo, Simulation of drop-weight impact and compression after impact tests on composite laminates, Compos. Struct. 94 (2012) 3364–3378.

[63] J.P. Greene, Engineering Plastics, in: J.P. Greene (Ed.), Automot. Plast. Compos., William Andrew Publishing, 2021: pp. 107–125.

[64] F. Guo-dong, L. Jun, W. Bao-lai, Progressive damage and nonlinear analysis of 3D four-directional braided composites under unidirectional tension, Compos. Struct. 89 (2009) 126–133.

[65] Q. Guo, W. Yao, W. Li, N. Gupta, Constitutive models for the structural analysis of composite materials for the finite element analysis: A particular review of recent practices, Compos. Struct. (2020) 113267.

[66] J.C. Halpin, Effects of Environmental Factors on Composite Materials, 1969.

[67] J.C. Halpin, Primer on Composite Materials Analysis, 2nd ed., Taylor & Francis Group, LLC, 1992.

[68] M. Hardiman, T.J. Vaughan, C.T. McCarthy, A review of key developments and pertinent issues in nanoindentation testing of fibre reinforced plastic microstructures, Compos. Struct. 180 (2017) 782–798.

[69] R.J. Hart, E.G. Patton, O. Sapunkov, E.G. Patton, O. Sapunkov, Characterization of Continuous Fiber-Reinforced Composite Materials Manufactured Via Fused Filament Fabrication, Detroit, 2018.

[70] Z. Hashin, Analysis of cracked laminates: a variational approach, Mech. Mater. 4 (1985) 121–136.

[71] Z. Hashin, S. Shtrikman, On some variational principles in anisotropic and

nonhomogeneous elasticity, J. Mech. Phys. Solids. 10 (1962).

[72] Z. Hashin, S. Shtrikman, A variational approach to the theory of the elastic behaviour of multiphase materials, J. Mech. Phys. Solids. 11 (1963).

[73] Q. He, Z. Man, L. Chang, L. Ye, On structure-mechanical and tribological property relationships of additive manufactured continuous carbon fiber/polymer composites, Elsevier Inc., 2020.

[74] M. Herráez Matesanz, Computational Micromechanics Models for Damage and Fracture of Fiber-Reinforced Polymers, (2018) 240.

[75] R.L. Hewitt, M.C. De Malherbe, An Approximation for the Longitudinal Shear Modulus of Continuous Fibre Composites, J. Compos. Mater. 4 (1970) 280–282.

[76] R. Hill, Theory of mechanical properties of fibre-strengthened materials-III. Self-consistent model, J. Mech. Phys. Solids. 13 (1965) 189–198.

[77] T. Hofstätter, I.W. Gutmann, T. Koch, D.B. Pedersen, G. Tosello, G. Heinz, H.N. Hansen, Distribution and orientation of carbon fibers in polylactic acid parts produced by fused deposition modeling, in: Proc. - ASPE/Euspen 2016 Summer Top. Meet. Dimens. Accuracy Surf. Finish Addit. Manuf., 2016: pp. 44–49.

[78] D.A. Hopkins, Thermoviscoplastic Nonlinear Constitutive Relationships for Structural Analysis of High Temperature Metal Matrix Composites, 1988.

[79] Z. Hou, X. Tian, J. Zhang, D. Li, 3D printed continuous fibre reinforced composite corrugated structure, Compos. Struct. 184 (2018) 1005–1010.

[80] Q. Hu, Y. Duan, H. Zhang, D. Liu, B. Yan, F. Peng, Manufacturing and 3D printing of continuous carbon fiber prepreg filament, J. Mater. Sci. 53 (2018) 1887–1898.

[81] T. Huang, Y. Gong, A multiscale analysis for predicting the elastic properties of 3D woven composites containing void defects, Compos. Struct. 185 (2018) 401–410.

[82] C. Huet, Application of variational concepts to size effects in elastic heterogeneous bodies, J. Mech. Phys. Solids. 38 (1990) 813–841.

[83] E. Hull, W. Grove, M. Zhang, X. Song, Z.J. Pei, Effects of Process Variables on Extrusion of Carbon Fiber Reinforced Abs, in: Proc. ASME 2015 Int. Manuf. Sci. Eng. Conf. MSEC2015, 2015: pp. 1–9.

[84] M. Iragi, C. Pascual-González, A. Esnaola, C.S. Lopes, L. Aretxabaleta, Ply and interlaminar behaviours of 3D printed continuous carbon fibre-reinforced thermoplastic laminates; effects of processing conditions and microstructure, Addit. Manuf. 30 (2019) 1–12.

[85] E. Jacquet, F. Trivaudey, D. Varchon, Calculation of the transverse modulus of a unidirectional composite material and of the modulus of an aggregate . Application of the rule of mixtures, Compos. Sci. Technol. 60 (2000) 345–350.

[86] M.N. Jahangir, K.M.M. Billah, Y. Lin, D.A. Roberson, R.B. Wicker, D. Espalin, Reinforcement of material extrusion 3D printed polycarbonate using continuous carbon fi ber, Addit. Manuf. 28 (2019) 354–364.

[87] Jean-Marie Berthelot, Composite Materials Mechanical Behavior and Structural Analysis, Springer-Verlag Berlin Heidelberg GmbH, Berlin, 1999.

[88] J. Justo, L. Távara, Garcia-Guzman, F. París, Characterization of 3D printed long fibre reinforced composites, Compos. Struct. 185 (2018) 537–548.

[89] L. Kachanov, Mechanics of Elastic Stability: Introduction to Continuum Damage, Kluwer Academic Publishers, 1986.

[90] A. Kalkal, S. Kumar, P. Kumar, R. Pradhan, M. Willander, G. Packirisamy, S. Kumar, B.D. Malhotra, Recent advances in 3D printing technologies for wearable (bio)sensors, Addit. Manuf. 46 (2021) 102088.

[91] T. Kermavnar, A. Shannon, L.W. O'Sullivan, The application of additive manufacturing / 3D printing in ergonomic aspects of product design: A systematic review, Appl. Ergon. 97 (2021).

[92] A.I. Khan, Progressive failure analysis of laminated composite structures, Virginia State University in, 2015.

[93] A.I. Khan, S. Venkataraman, I. Miller, Predicting fatigue damage of composites using strength degradation and cumulative damage model, J. Compos. Sci. 2 (2018).

[94] V. Kishore, X. Chen, C. Ajinjeru, A.A. Hassen, J. Lindahl, J. Failla, V. Kunc, C. Duty, Additive manufacturing of high performance semicrystalline thermoplastics and their composites, in: 26th Annu. Int. Solid Free. Fabr. Symp., 2016: pp. 906–915.

[95] F. Van Der Klift, 3D Printed Unidirectional Carbon Fibre Reinforced Poly- mers for Aerospace Applications, Open J. Compos. Mater. 06 (2016) 18–27.

[96] F. Van Der Klift, Y. Koga, A. Todoroki, M. Ueda, Y. Hirano, R. Matsuzaki, 3D Printing of Continuous Carbon Fibre Reinforced Thermo-Plastic (CFRTP) Tensile Test Specimens, Open J. Compos. Mater. 6 (2016) 18–27.

[97] M. Knops, Analysis of Failure in Fiber Polymer Laminates: The Theory of Alfred Puck, Springer, 2008.

[98] K. Kodagali, Progressive Failure Analysis of composite Materials using the Puck Failure Criteria, 2017.

[99] I. Lapczyk, J. Hurtado, Progressive Damage Modeling In Fiber-Reinforced Materials, (2006).

[100] C. Lee, J. Kim, S. Kim, D. Ryu, J. Lee, Initial and progressive failure analyses for composite laminates using Puck failure criterion and damage-coupled finite element method, Compos. Struct. 121 (2015) 406–419.

[101] J. Li, C. Huang, T. Ma, X. Huang, W. Li, M. Liu, Numerical investigation of composite laminate subjected to combined loadings with blast and fragments, Compos. Struct. 214 (2019) 335–347.

[102] N. Li, Y. Li, S. Liu, Rapid prototyping of continuous carbon fiber reinforced polylactic acid composites by 3D printing, J. Mater. Process. Tech. 238 (2016) 218–225.

[103] P. Li, Q. Wang, S. Shi, Differential scheme for the effective elastic properties of nano-particle composites with interface effect, Comput. Mater. Sci. 50 (2011) 3230–3237.

[104] G. Liao, Z. Li, Y. Cheng, D. Xu, D. Zhu, S. Jiang, J. Guo, X. Chen, G. Xu, Y. Zhu, Properties of oriented carbon fiber/polyamide 12 composite parts fabricated by fused deposition modeling, Mater. Des. 139 (2018) 283–292.

[105] G.R. Liu, A step-by-step method of rule-of-mixture of fiber- and particle-reinforced composite materials, Compos. Struct. 40 (1998) 313–322.

[106] H. Liu, B.G. Falzon, S. Li, W. Tan, J. Liu, H. Chai, Compressive failure of woven fabric reinforced thermoplastic composites with an open-hole : An experimental and numerical

study, Compos. Struct. 213 (2019) 108–117.
[107] J. Llorca, C. González, J. Segurado, R. Seltzer, F. Sket, M. Rodríguez, S. Sádaba, R. Muñoz, L.P. Canal, Multiscale Modeling of Composite Materials : a Roadmap Towards Virtual Testing, Adv. Mater. 23 (2011) 5130–5147.
[108] K.H. Lo, R.M. Christensen, E.M. Wu, A High-Order Theory of Plate Deformation - Part 1: Homogeneous Plates, J. Appl. Mech. (1977) 663–668.
[109] K.H. Lo, R.M. Christensen, E.M. Wu, A High-Order Theory of Plate Deformation - Part 2: Laminated Plates, (1977) 669–676.
[110] K.H. Lo, R.M. Christensen, E.M. Wu, Stress solution determination for high order plate theory, Int. J. Solids Struct. 14 (1978) 655–662.
[111] M.L. Longana, H. Yu, An investigation into 3D printing of fibre reinforced thermoplastic composites, Additive. 22 (2018) 176–186.
[112] C.S. Lopes, Z. Gurdal, P.P. Camanho, B.F. Tatting, Progressive Failure Analysis of Tow-Placed , Variable-Stiffness Composite Panels, in: 48th AIAA/ASME/ASCE/AHS/ASC Struct. Struct. Dyn. Mater. Conf., 2007.
[113] Y. Ma, M. Ueda, T. Yokozeki, T. Sugahara, Y. Yang, H. Hamada, A comparative study of the mechanical properties and failure behavior of carbon fiber/epoxy and carbon fiber/polyamide 6 unidirectional composites, Compos. Struct. 160 (2017) 89–99.
[114] C.G. Mahajan, D. Cormier, 3D Printing of Carbon Fiber Composites With Preferentially Aligned Fibers, Mater. Sci. Eng. (2015).
[115] P. Maimí, P.P. Camanho, J.A. Mayugo, C.G. Dávila, A Thermodynamically Consistent Damage Model for Advanced Composites. NASA/TM-2006-214282, Nasa Tm. (2006) 47.
[116] P. Maimi, J.A. Mayugo, P.P. Camanho, A Three-dimensional Damage Model for Transversely Isotropic Composite Laminates, J. Compos. Mater. 42 (2008) 2717–2745.
[117] MarkForged, Material Datasheet Composites, (2018).
[118] Markforged Ltd., Markforged, (n.d.).
[119] A. Matzenmiller, J. Lubliner, R.L. Taylor, A constitutive model for anisotropic damage in fiber-composites, Mech. Mater. 20 (1995) 125–152.
[120] C. McCarthy, T. Vaughan, Micromechanical failure analysis of advanced composite materials, Elsevier Ltd., 2015.
[121] R. Mclaughlin, A study of the differential scheme for composite materials, Inl I. Engng Sci. 15 (1977) 237–244.
[122] G.W. Melenka, B.K.O. Cheung, J.S. Schofield, M.R. Dawson, J.P. Carey, Evaluation and prediction of the tensile properties of continuous fiber-reinforced 3D printed structures, Compos. Struct. 153 (2016) 866–875.
[123] A.R. Melro, P.P. Camanho, F.M.A. Pires, S.T. Pinho, Numerical simulation of the non-linear deformation of 5-harness satin weaves, Comput. Mater. Sci. 61 (2012) 116–126.
[124] C. Methods, A. Mech, X. Zhang, D.J.O. Brien, S. Ghosh, ScienceDirect Parametrically homogenized continuum damage mechanics (PHCDM) models for composites from micromechanical analysis, Comput. Methods Appl. Mech. Eng. 346 (2019) 456–485.
[125] J.C. Michel, H. Moulinec, P. Suquet, Effective properties of composite materials with periodic microstructure: a computational approach, 7825 (1999).

[126] M. Miguel, M. Leite, A.M.R. Ribeiro, A.M. Deus, L. Reis, M.F. Vaz, Failure of polymer coated nylon parts produced by additive manufacturing, Eng. Fail. Anal. 101 (2019) 485–492.

[127] L. Mishnaevsky, G. Dai, Hybrid carbon/glass fiber composites: Micromechanical analysis of structure-damage resistance relationships, Comput. Mater. Sci. 81 (2014) 630–640.

[128] N. Mohan, P. Senthil, S. Vinodh, N. Jayanth, A review on composite materials and process parameters optimisation for the fused deposition modelling process, Virtual Phys. Prototyp. 12 (2017) 47–59.

[129] K.I. Mori, T. Maeno, Y. Nakagawa, Dieless forming of carbon fibre reinforced plastic parts using 3D printer, Procedia Eng. 81 (2014) 1595–1600.

[130] T. Mori, K. Tanaka, Average stress in matrix and average elastic energy of materials with misfitting inclusions, Acta Metall. 21 (1973) 571–574.

[131] A.N. Morris, An Examination of the Mori-Tanaka Effective Medium Approximation for Multiphase Composites, Trans. ASME. 56 (2014) 83–88.

[132] J.I. Múgica, C.S. Lopes, F. Naya, M. Herráez, V. Martínez, C. González, Multiscale modelling of thermoplastic woven fabric composites: From micromechanics to mesomechanics, Compos. Struct. 228 (2019) 111340.

[133] J.I. Múgica, C.S. Lopes, F. Naya, M. Herráez, V. Martínez, C. González, Multiscale modelling of thermoplastic woven fabric composites: From micromechanics to mesomechanics, Compos. Struct. 228 (2019) 111340.

[134] S. Murakami, Mechanical Modeling of Material Damage, Trans. ASME. 55 (1988).

[135] M. Naghdinasab, A. Farrokhabadi, H. Madadi, A numerical method to evaluate the material properties degradation in composite RVEs due to fiber-matrix debonding and induced matrix cracking, Finite Elem. Anal. Des. 146 (2018) 84–95.

[136] Y. Nakagawa, K. ichiro Mori, T. Maeno, 3D printing of carbon fibre-reinforced plastic parts, Int. J. Adv. Manuf. Technol. 91 (2017) 2811–2817.

[137] T.D. Ngo, A. Kashani, G. Imbalzano, K.T.Q. Nguyen, D. Hui, Additive manufacturing (3D printing): A review of materials , methods , applications and challenges, Compos. Part B. 143 (2018) 172–196.

[138] M. Nikzad, S.H. Masood, I. Sbarski, Thermo-mechanical properties of a highly filled polymeric composites for Fused Deposition Modeling, Mater. Des. 32 (2011) 3448–3456.

[139] F. Ning, W. Cong, J. Qiu, J. Wei, S. Wang, Additive manufacturing of carbon fiber reinforced thermoplastic composites using fused deposition modeling, Compos. Part B Eng. 80 (2015) 369–378.

[140] A.K. Noor, W.S. Burton, Assessment of computational models for multilayered composite shells, Appl. Mech. Rev. 43 (1990) 67–97.

[141] M. Okereke, S. Keates, Finite Element Applications: A Practical Guide to the FEM Process, Springer International Publishing, 2018.

[142] M.I. Okereke, A.I. Akpoyomare, A virtual framework for prediction of full-field elastic response of unidirectional composites, Comput. Mater. Sci. 70 (2013) 82–99.

[143] S.L. Omairey, P.D. Dunning, S. Sriramula, Development of an ABAQUS plugin tool for

periodic RVE homogenisation, Eng. Comput. 35 (2019) 567–577.
[144] C. Oztan, R. Karkkainen, M. Fittipaldi, M. Lane, L. Roberson, G. Nygren, E. Celik, Microstructure and mechanical properties of three dimensional-printed continuous fiber composites, J. Compos. Mater. 53 (2018) 271–280.
[145] M. Palizvan, M. Tahaye Abadi, M.H. Sadr, Micromechanical damage behavior of fiber-reinforced composites under transverse loading including fiber-matrix debonding and matrix cracks, Int. J. Fract. 226 (2020) 145–160.
[146] C. Pascual-González, M. Iragi, A. Fernández, J.P. Fernández-Blázquez, L. Aretxabaleta, C.S. Lopes, An approach to analyse the factors behind the micromechanical response of 3D-printed composites, Compos. Part B Eng. 186 (2020) 1–9.
[147] W. Patterson, A. Force, The Halpin-Tsai Equations: A Review, Polym. Eng. Sci. 16 (1976).
[148] Performance-composites Ltd., Performance composites, Mech. Prop. Carbon Fiber Compos. Mater. (2009).
[149] D.C. Pham, X. Cui, X. Ren, J. Lua, A discrete crack informed 3D continuum damage model and its application for delamination migration in composite laminates, Compos. Part B Eng. 165 (2019) 554–562.
[150] H.A. Pierson, E. Celik, A. Abbott, H. De Jarnette, L.S. Gutierrez, K. Johnson, H. Koerner, J.W. Baur, Mechanical Properties of Printed Epoxy-Carbon Fiber Composites, Exp. Mech. 59 (2019) 843–857.
[151] S.T. Pinho, Modelling failure of laminated composites using physically-based failure models, University of London, 2005.
[152] S.T. Pinho, L. Iannucci, P. Robinson, Physically-based failure models and criteria for laminated fibre-reinforced composites with emphasis on fibre kinking: Part I: Development, Compos. Part A. 37 (2006) 63–73.
[153] S.T. Pinho, P. Robinson, L. Iannucci, Fracture toughness of the tensile and compressive fibre failure modes in laminated composites, Compos. Sci. Technol. 66 (2006) 2069–2079.
[154] H. Prüß, T. Vietor, Design for Fiber-Reinforced Additive Manufacturing, J. Mech. Des. Trans. ASME. 137 (2015) 1–7.
[155] A. Puck, Calculating the strength of glass fiber/plastic laminates under combined load, Ger. Plast. 55 (1969) 18.
[156] A. Puck, H.M. Deuschle, Progress in the Puck Failure Theory for Fibre Reinforced Composites : Analytical solutions for 3D-stress, 2013.
[157] A. Puck, J. Kopp, M. Knops, Guidelines for the determination of the parameters in Puck ' s action plane strength criterion, Compos. Sci. Technol. 62 (2002) 371–378.
[158] A. Puck, M. Mannigel, Physically based non-linear stress-strain relations for the inter-fibre fracture analysis of FRP laminates, Compos. Sci. Technol. 67 (2007) 1955–1964.
[159] A. Puck, H. Schürmann, Failure analysis of FRP laminates by means of physically based phenomenological models*, Compos. Sci. Technol. 58 (1996) 1045–1069.
[160] A. Puck, H. Schürmann, Failure analysis of FRP laminates by means of physically based phenomenological models, Compos. Sci. Technol. 62 (2002) 1633–1662.
[161] Z. Quan, J. Suhr, J. Yu, X. Qin, C. Cotton, Printing direction dependence of mechanical

behavior of additively manufactured 3D preforms and composites, Compos. Struct. (2017).
[162] M. Quaresimin, A damage-based approach for the fatigue design of composite structures, IOP Conf. Ser. Mater. Sci. Eng. 139 (2016).
[163] M. Quaresimin, P.A. Carraro, L.P. Mikkelsen, N. Lucato, L. Vivian, P. Brøndsted, B.F. Sørensen, J. Varna, R. Talreja, Composites : Part B Damage evolution under cyclic multiaxial stress state : A comparative analysis between glass / epoxy laminates and tubes, Compos. PART B. 61 (2014) 282–290.
[164] M. Quaresimin, P.A. Carraro, L.P. Mikkelsen, N. Lucato, L. Vivian, P. Brøndsted, B.F. Sørensen, J. Varna, R. Talreja, Damage evolution under cyclic multiaxial stress state: A comparative analysis between glass/epoxy laminates and tubes, Compos. Part B Eng. 61 (2014) 282–290.
[165] Y.N. Rabotnov, Creep problems in structural members, 1969.
[166] B. Raju, S.R. Hiremath, D. Roy Mahapatra, A review of micromechanics based models for effective elastic properties of reinforced polymer matrix composites, Compos. Struct. 204 (2018) 607–619.
[167] S. Rangisetty, L.D. Peel, The effect of infill patterns and annealing on mechanical properties of additively manufactured thermoplastic composites, in: ASME 2017 Conf. Smart Mater. Adapt. Struct. Intell. Syst. SMASIS 2017, 2017: pp. 1–12.
[168] J.-L. Rebiere, D. Gamby, A decomposition of the strain energy release rate associated with the initiation of transverse cracking , longitudinal cracking and delamination in cross-ply laminates, Compos. Struct. 84 (2008) 186–197.
[169] J.N. Reddy, D.H. Bobbins, Theories and computational models for composite laminates, Appl. Mech. Rev. 47 (1994) 147–169.
[170] J.R. Reeder, 3D Mixed-Mode Delamination Fracture Criteria–An Experimentalist's Perspective, Damage Compos. (2006) 1–18.
[171] M. Rinaldi, M. Ferrara, L. Pigliaru, C. Allegranza, F. Nanni, Additive manufacturing of polyether ether ketone-based composites for space application: a mini-review, CEAS Sp. J. (2021) 1–16.
[172] M. Salavatian, L.V. Smith, An investigation of matrix damage in composite laminates using continuum damage mechanics, Compos. Struct. 131 (2015) 565–573.
[173] M.J. Sauer, Evaluation of the Mechanical Properties of 3D Printed Carbon Fiber Composites, (2018) 1–151.
[174] J. Schindelin, I. Arganda-Carreras, E. Frise, V. Kaynig, M. Longair, T. Pietzsch, S. Preibisch, C. Rueden, S. Saalfeld, B. Schmid, J.Y. Tinevez, D.J. White, V. Hartenstein, K. Eliceiri, P. Tomancak, A. Cardona, Fiji: An open-source platform for biological-image analysis, Nat. Methods. 9 (2012) 676–682.
[175] H. Schürmann, Konstruieren mit Faser-Kunststoff- Verbunden, Springer, Berlin, 2007.
[176] V. Shanmugam, O. Das, K. Babu, U. Marimuthu, A. Veerasimman, D.J. Johnson, R.E. Neisiany, M.S. Hedenqvist, S. Ramakrishna, F. Berto, Fatigue behaviour of FDM-3D printed polymers, polymeric composites and architected cellular materials, Int. J. Fatigue. 143 (2021) 1–15.
[177] M.L. Shofner, K. Lozano, F.J. Rodrı, Nanofiber-Reinforced Polymers Prepared by Fused

Deposition Modeling, J. Appl. Polym. Sci. 89 (2002) 3081–3090.
[178] I. Smojver, Mehanika kompozitnih materijala, (2006) 65 p.
[179] K.P. Soldatos, A refined laminated plate and shell theory with applications, J. Sound Vib. 144 (1991) 109–129.
[180] M. Somireddy, A. Czekanski, C.V. Singh, Development of constitutive material model of 3D printed structure via FDM, Mater. Today Commun. 15 (2018) 143–152.
[181] M. Somireddy, C. V. Singh, A. Czekanski, Mechanical behaviour of 3D printed composite parts with short carbon fiber reinforcements, Eng. Fail. Anal. 107 (2020) 1650–6307.
[182] A.A. Stepashkin, D.I. Chukov, F.S. Senatov, A.I. Salimon, A.M. Korsunsky, S.D. Kaloshkin, 3D-printed PEEK-Carbon Fiber (CF) composites: Structure and thermal properties, Compos. Sci. Technol. 164 (2018) 319–326.
[183] L. Takacs, L. Kovacs, T. Olajos, Numerical tool with mean-stress correction for fatigue life estimation of composite plates, Eng. Fail. Anal. 111 (2020).
[184] H.L. Tekinalp, V. Kunc, G.M. Velez-Garcia, C.E. Duty, L.J. Love, A.K. Naskar, C.A. Blue, S. Ozcan, Highly oriented carbon fiber-polymer composites via additive manufacturing, Compos. Sci. Technol. 105 (2014) 144–150.
[185] W. Tian, L. Qi, C. Su, J. Liang, J. Zhou, Numerical evaluation on mechanical properties of short-fiber-reinforced metal matrix composites : Two-step mean-field homogenization procedure, Compos. Struct. 139 (2016) 96–103.
[186] X. Tian, T. Liu, Q. Wang, A. Dilmurat, D. Li, G. Ziegmann, Recycling and remanufacturing of 3D printed continuous carbon fiber reinforced PLA composites, J. Clean. Prod. 142 (2017) 1609–1618.
[187] S.W. Tsai, E.M. Wu, Theory of Strength for Anisotropic Materials, 5 (1971).
[188] T.H.J. Vaneker, Material Extrusion of Continuous Fiber Reinforced Plastics Using Commingled Yarn, in: 1st Cirp Conf. Compos. Mater. Parts Manuf. Cirp-Ccmpm2017, The Author(s), 2017: pp. 317–322.
[189] J. Varna, R. Joffe, R. Talreja, A synergistic damage-mechanics analysis of transverse cracking [±Θ/90_4]s laminates, Compos. Sci. Technol. 61 (2001) 657–665.
[190] VDI-Richtlinien, Development of FRP components (fibre-reinforced plastics) Analysis, 2006.
[191] VDI/VDE, Werkstoffe der Feinwerktechnik; Polyamid-Formstoffe unverstärkt, Blatt 1 (1978) 24.
[192] G.Z. Voyiadjis, P.I. Kattan, Mechanics of composite materials with MATLAB, 2005.
[193] J.M. Whitney, The Effect of Transverse Shear Deformation on the Bending of Laminated Plates, J. Compos. Mater. 3 (1969) 534–547.
[194] T.T. Wu, The effect of inclusion shape on the elastic moduli of a two-phase material, Int. J. Solids Struct. 2 (1966) 1–8.
[195] C. Yang, X. Tian, T. Liu, Y. Cao, D. Li, 3D printing for continuous fiber reinforced thermoplastic composites: Mechanism and performance, Rapid Prototyp. J. 23 (2017) 209–215.
[196] X. Yao, C. Luan, D. Zhang, L. Lan, J. Fu, Evaluation of carbon fiber-embedded 3D printed structures for strengthening and structural-health monitoring, Mater. Des. 114

(2017) 424–432.
[197] W. Ye, G. Lin, W. Wu, P. Geng, X. Hu, Z. Gao, J. Zhao, Separated 3D printing of continuous carbon fiber reinforced thermoplastic polyimide, Compos. Part A. (2019).
[198] T. Yokozeki, T. Aoki, Stress analysis of symmetric laminates with obliquely-crossed matrix cracks, Adv. Compos. Mater. (2012) 37–41.
[199] J. Yvonnet, Computational Homogenization of Heterogeneous Materials with Finite Elements, Springer, 2019.
[200] C. Zhang, E.A. Duodu, J. Gu, Finite element modeling of damage development in cross-ply composite laminates subjected to low velocity impact, Compos. Struct. (2017).
[201] W. Zhang, C. Cotton, J. Sun, D. Heider, B. Gu, B. Sun, T.W. Chou, Interfacial bonding strength of short carbon fiber/acrylonitrile-butadiene-styrene composites fabricated by fused deposition modeling, Compos. Part B Eng. 137 (2018) 51–59.
[202] W. Zhong, F. Li, Z. Zhang, L. Song, Z. Li, Short fiber reinforced composites for fused deposition modeling, Mater. Sci. Eng. A. 301 (2001) 125–130.
[203] ASTM D3518/D3518M – 18 Standard Test Method for In-Plane Shear Response of Polymer Matrix Composite Materials by Tensile Test of a +/-45° Laminate, (2001) 1–7.
[204] ASTM D 3039/D 3039M – 00 Standard Test Method for Tensile Properties of Polymer Matrix Composite Materials, 15 (2002).
[205] ASTM F2792 − 12a: Standard Terminology for Additive Manufacturing Technologies, 2012.
[206] 900gpa, Compos. Mater. Database. (2021).

Articles relevant to this thesis recently published by the author:

- M. Gljušćić, M. Franulović, D. Lanc, A. Žerovnik, Representative volume element for microscale analysis of additively manufactured composites, Addit. Manuf. 56 (2022) 102902.
- M. Gljušćić, M. Franulović, B. Žužek, A. Žerovnik, Experimental validation of progressive damage modeling in additively manufactured continuous fiber composites, Compos. Struct. 295 (2022) 115869.
- M. Gljušćić, M. Franulović, D. Lanc, and Ž. Božić, Application of digital image correlation in behavior modelling of AM CFRTP composites, *Eng. Fail. Anal.*, 136 (2022) 106–133.

List of Symbols

Latinic Symbols

Variable	Definition
E_{ij}	Lamina Young modulus; i,j=1,2,3; i=j
G_{ij}	Lamina shear modulus; i,j=1,2,3; i≠j
$[S]$	Compliance matrix
$[C]$	Stiffness matrix
S_{ij}	Compliance matrix component; i,j=1,2,3
C_{ij}	Stiffness matrix component; i,j=1,2,3
$[Q]$	Reduced stiffness matrix
Q_{ij}	Reduced stiffness matrix component; i,j=1,2,6
m, n	Abbreviations of transformation matrix components
$[T]$	Transformation matrix
$[\bar{Q}]$	Transformed reduced stiffness matrix
$[\bar{Q}_{ij}]$	Transformed reduced stiffness matrix component; i,j=1,2,6
$[\bar{S}]$	Transformed reduced compliance matrix
E_i	Laminate Young modulus; i=x,y,z
G_{ij}	Laminate shear modulus; i,j=x,y,z; i≠j
N	Number of laminas
H	Laminate thickness
h	Lamina thickness
z_i	Lamina interface distance in thickness direction
u, w	Displacement in the x and y directions
k^0	Reference surface curvature
N_i	Forces acting on the laminate; i=x,y
N_{ij}	Forces acting on the laminate; i,j=x,y; i≠j
M_i	Moments acting on the laminate; i=x,y
M_{ij}	Moments acting on the laminate; i,j=x,y; i≠j
A_{ij}, B_{ij}, D_{ij}	Laminate stiffness matrix components ; i,j=1,2,6
a_{ij}, b_{ij}, d_{ij}	Inverse laminate stiffness matrix components ; i,j=1,2,6
$\bar{E}_i$	Effective elastic modulus of the lamiante; i=x,y
$\bar{G}_i$	Effective shear modulus of the laminate; i,j=x,y; i≠j
$\mathbf{u}$	Displacement vector
$\boldsymbol{x}$	Generic variable
$\mathbf{n}$	Unitary vector normal to the domain boundary
$\mathbb{R}$	Effective compliance tensor of the RVE
$\mathbb{C}^i$	Effective elastic tensor of teh RVE; i= material phase
$\mathbb{C}^{-1}(\mathbf{x})$	Compliance matrix
N	Number of phases within the RVE

3D	Three-dimensional
$\tilde{\mathbf{u}}$	Fluctuating displacement
V	Volume
$\mathbf{K}$	Interface stiffness tensor
n_{ij}	Unitary vector component
$\mathbf{e}_i$	Unitary basis vector; i=1,2
$\mathbf{u}^{(ij)}$	Displacement tensor component; i,j=1,2,3
$\mathbf{u}(\mathbf{x})$	Displacement tensor
u^i	Displacement fields in i^{th} domain
$\bar{\mathbb{C}}$	Elasticity tensor
$\bar{\mathbb{A}}$	Strain localization tensor
$\bar{\mathbb{B}}$	Stress localization tensor
$C_{pqij}(\mathbf{x})$	Elasticity tensor in matrix form
$A_{ijkl}(\mathbf{x})$	Localization tensor relating micro and macro strains
$B_{ijkl}(\mathbf{x})$	Localization tensor relating macroscopic to microscopic stress
u	Displacement in x direction
v	Displacement in y direction
$\mathbf{U}^e$	Matrix of the nodal unknowns
N_i	Applied load; i=1,2,3
$\mathbf{f}$	Body forces tensor
$\mathbf{F^*}$	Traction forces tensor
$\mathbf{R}$	Constraint equation in discrete form
$\mathbf{P}$	Matrix relating the coupled nodes indices to the whole set of nodes indices
$\mathbf{q}$	Vector form of ordered unknowns
$\mathbf{T}$	Constraint equations tensor
$\mathbf{K}$	Interface stiffness tensor
$u_i(\mathbf{x}^\alpha)$, $u_i(\mathbf{x}^\alpha)$	Node pairs on the opposite RVE faces
n, t	Normal, tangential to the fibre plane of the lamina
t, c	Tensile, compressive
$R^t_\parallel$, $R^c_\parallel$	Uniaxial tensile and compressive strengths of UD lamina parallel to fiber direction
$R^t_\perp$, $R^c_\perp$	Uniaxial tensile and compressive strengths of UD lamina perpendicular to fiber direction
$R_{\perp\parallel}$	In-plane shear strength of UD lamina
$R^t_\perp$,$R^t_\perp$	Tensile and compressive strength of UD lamina transverse to fibre direction
$R^A_{\perp\perp}$	Fracture resistance of an action-plane action parallel to the fibre direction against its fracture due to $\tau_{\perp\perp}$ stressing acting on it
$m_{\sigma,f}$	Normal stress magnification factor
$m_{\tau,f}$	Shear stress magnification factor
$E_{\parallel f}$, $E_{\perp f}$	Young's modulus of fiber for parallel or transverse to fibre direction
$E_\parallel$, $E_\perp$	Young's modulus of UD lamina for parallel or transverse to fibre direction
$G_{\perp\parallel}$	In-plane shear modulus
R^A	Stress on action plane
f_E	Stress exposure
f_S	Stretch factor
$p^t_{\perp\psi}$, $p^c_{\perp\psi}$	Inclination parameter in tension and compression for arbitrary fracture plane

c_1, c_2	Model parameters in Puck hypothesis
$p^{t}_{\perp\perp}$, $p^{c}_{\perp\perp}$	Inclination of (τ_{nt}, σ_n)-fracture curve at $\sigma_n = 0$; t for the range $\sigma_n > 0$; c for the range $\sigma_n < 0$
$p^{t}_{\perp\parallel}$, $p^{c}_{\perp\parallel}$	Inclination of (τ_{n1}, σ_n)-fracture curve at $\sigma_n = 0$; t for the range $\sigma_n > 0$; c for the range $\sigma_n < 0$
d_f	Fiber diameter
n_{DEG}	Degradation exponent
F^{IS}_{2t}	In-situ transverse strength correction
F^{IS}_{6t}	In-situ shear strength correction
G_{IC}, G_{IIC}	Critical fracture toughness values in mode I and mode II, respectively
V_{ff}	Volume ratio of fibers
D_{ft} , D_{fc}	Fiber damage in tension, compression
D_{mt} , D_{mc}	Matrix damage in tension, compression

Greek Symbols

Variable	Definition
ξ	Effective fiber strength coefficient
κ_{DEG}	Moduli degradation coefficient
σ_i	Normal component of the stress tensor; i=1,2,3
τ_{ij}	Shear component of the stress tensor; i,j=1,2,3; i≠j
$\bar{\sigma}$	Macroscale stress tensor component
ε	Normal component of the strain tensor; i=1,2,3
γ_i	Shear component of the strain tensor; i=1,2,3
$\bar{\varepsilon}$	Macroscale strain component
τ	Shear stress
ν_{ij}	Lamina Poisson ratio; i,j=1,2,3; i≠j
ϑ	Fiber closing angle
ν_{ij}	Laminate Poisson ratio; i,j=x,y,z; i≠j
η	Coefficient of mutual influence
ε^0	Strain of the reference surface
$\bar{\nu}_{ij}$	Effective Poisson's ratio of the laminate; i,j=x,y; i≠j
$\bar{\sigma}_i$	Effective normal stress in the laminate; i=x,y
$\bar{\tau}_{ij}$	Effective shear stress in the laminate; i,j=x,y; i≠j
Ω	Global domain
$\partial\Omega$	Global domain boundary
∂	Partial derivative
Γ	Constituent's interface boundary
$\sum$	Sum
$\int$	Integral
α_{norm}	Normalization parameter
$\bar{\boldsymbol{\sigma}}$	Homogenous stress field tensor
$\bar{\boldsymbol{\varepsilon}}$	Homogenous strain field tensor
$\tilde{\boldsymbol{\varepsilon}}$	Microscopic strain fluctuation
σ^i	Stress tensors in domain Ω^i; i=1,2

$\langle \boldsymbol{\varepsilon} \rangle$	Average local strain field
$\langle \boldsymbol{\sigma} \rangle$	Average local stress field
$\boldsymbol{\sigma n}$	Traction stress
σ_{1t}, σ_{1c}	Uniaxial tensile, compressive stress
ε_{1f}	Fiber strain
σ_{1f}	Fiber stress
$\nu_{\parallel\perp f}$	Poisson ratio of fiber
θ_{fp}	Angle of fracture plane
σ_n	Normal stress on an inclined action plane (action-plane strength criterion)
$\sigma_\perp$	Transversal stressing in UD lamina
$\sigma_\parallel$	Longitudinal stressing in UD lamina
σ_1, σ_2, τ_{12}	lamina stresses related to the local coordinate system
τ_{nt}	Transverse/transverse shear stress on an inclined action plane (action-p. strength criterion)
τ_{n1}	Transverse/longitudinal shear stress an on inclined action plane (action-p. strength criterion)
$\tau_{\perp\perp}$	Transverse/transverse shear stressing in the UD lamina
$\tau_{\perp\parallel}$	Transverse/longitudinal shear stressing in the UD lamina
$\tau_{\perp\perp}$	Out-of-plane shear stressing
θ	Inclination angle
ψ	Angle calculated from arctan (τ_{n1}/τ_{nt}) determined by the ratio τ_{n1}/τ_{nt}
ν	Poisson's ratio (for isotropic case)
$\nu_{\perp\parallel}$, $\nu_{\parallel\perp}$, $\nu_{\perp\perp}$	Poisson's ratios of UD lamina
ξ	Effective fiber strength coefficient
γ	Shear strain
β_i	Orientation of the supporting (off-axis) layer; i=quantity
λ_{12}	In-plane biaxiality ratio
κ_{DEG}	Degradation coefficient
Λ^0_{22}, Λ^0_{44}	In-situ calculation parameters acquired in dependence on material orthotropic properties

Mathematical Symbols

Symbol	Definition
∇	Divergence operator
$\forall$	Universal quantifier (meaning: for all the … example: $\forall$ (x) means for all the x values)
$\otimes$	Direct tensor product for tensors of any ranks
$\mathcal{L}$	Linear integral operator
∂	Differential operator
ϵ	Element of
$D_{\delta\mathbf{u}}$, $D_{\delta\boldsymbol{\Lambda}}$	Gateaux directional derivatives
$\boldsymbol{\Lambda}$	Lagrange multiplier
$\parallel$, $\perp$	UD-lamina coordinate system showing parallel (longitudinal) and transverse fiber directions
x-y-z	Global coordinate system
1-2-3	Local coordinate system

List of Abbreviations

AM	Additive manufacturing
*n*D	*n*-dimensional
C, G, K	Carbon, glass, aramid
RVE	Representative volume element
UMAT	User defined material model
DoE	Design of Experiments
EU	European Union
PA	Polyamide
PC	Polycarbonate
PET	Polyethylene terephthalate
PEEK	Polyether ether ketone
CFRP	Continuous fiber-reinforced polymer
UD	Unidirectional
CDM	Continuum damage mechanics
SEM	Scanning electron microscope
FIJI	Fiji is just ImageJ
WEKA	Waikato Environment for Knowledge Analysis
ASTM	American Society for Testing and Materials
UD-0	Specimen reinforced in direction of the applied load
UD-90	Specimen reinforced in perpendicular direction of the applied load
SH-45	$[45/-45]_{4s}$ specimen for in-plane shear properties acquisition in uniaxial tension
DIC	Digital image correlation
OH	Open hole specimen (specimen with circular stress concentrator)
OH-90	$[0/90_2/0/90_2]_S$ laminate with circular stress concentrator
OH-60	$[0/60_2/0/-60_2]_S$ laminate with circular stress concentrator
OH-45	$[0/45_2/0/-45_2]_S$ laminate with circular stress concentrator
LSS	Lamina stacking sequence
WWFE	Worldwide Failure Exercise
FRP	Fiber reinforced polymer
DDM	Discrete damage mechanics
EBM	Electron beam melting
SLS	Selective laser sintering
SHS	Selective hot sintering
DMLS	Direct metal laser sintering
DED	Direct Energy Deposition
LMD	Laser metal deposition
SLA	Stereo lithography
DPL	Digital light processing
PBIH	Powder bed and inkjet head
PP	Plaster-based 3D printing
MJM	Multi-jet modelling
LOM	Laminated object manufacturing
UC	Ultrasonic consolidation
FDM	Fused deposition modelling
FFF	Fused filament fabrication
BASS	Break-away systems
ABS	Acrylonitrile butadiene styrene
PLA	Polylactic Acid
UV	Ultraviolet
C/PA	Carbon-fiber reinforced polyamide

ISO	International standard organization
CFF	Continuous fiber fabrication
SLM	Selectively laser melting
*n*K fiber	Fiber tow with *n*·1000 individual fibers
CFC	Composite filament co-extrusion
PAN	Polyacrylonitrile
JIS	Japanese Industrial Standards
μCT	Micro CT
pre-preg	Pre-impregnated composite lamina
PP	Polypropylene
ILSS	Interlaminar shear strength
FEA	Finite element analysis
RoM	Rule of Mixture
CAE	Computer aided engineering
CZM	Cohesive zone model
XFEM	Extended finite element method
LEFM	Linear elastic fracture mechanics
FF, MF	Fiber failure, matrix failure
MMD	Micro-mechanic damage model
SDM	Synergistic damage mechanics
ERR	Strain energy release rate
CLT	Classical laminate theory
FSDT	First-order shear deformation theory
HSDT	Higher-order shear deformation theory
PBC	Periodic boundary conditions
SUBC	Statistically uniform boundary conditions
KUBC	Kinematically uniform boundary conditions
IFF	Inter fiber fracture
C-, G-, KFRP	Carbon, glass or aramid fiber-reinforced polymer
MFB	Master fracture body
LFD	Low-vacuum Secondary Electron Detector
BSED	Solid-state Diode Backscatter Electron Detector
SGM	Long splitting failure within the gauge mid-region
TGA	Thermogravimetric analysis
S4R	Conventional four-node shell element with reduced integration
thin, thick	Superscript to indicate in-situ properties calculation for thin or thick laminate
IS	Superscript indicating in-situ material property
SDV	Solution Dependent Variable
MS	Microsoft

List of Figures

List of Figures